NOTE TO USERS

This reproduction is the best copy available.

UMI®

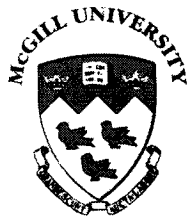

Wear Behaviour of Cobalt-Chromium-Molybdenum Alloys used in Metal-On-Metal Hip Implants

ROCCO VARANO
Department of Mining, Metals and Materials Engineering
McGill University
Montreal, Quebec, Canada

A thesis submitted to McGill University
in partial fulfillment of the requirements for the degree of
Doctor of Philosophy

© Rocco Varano
April, 2004

Library and Archives Canada

Published Heritage Branch

395 Wellington Street
Ottawa ON K1A 0N4
Canada

Bibliothèque et Archives Canada

Direction du Patrimoine de l'édition

395, rue Wellington
Ottawa ON K1A 0N4
Canada

Your file Votre référence
ISBN: 0-494-06347-5
Our file Notre référence
ISBN: 0-494-06347-5

NOTICE:
The author has granted a non-exclusive license allowing Library and Archives Canada to reproduce, publish, archive, preserve, conserve, communicate to the public by telecommunication or on the Internet, loan, distribute and sell theses worldwide, for commercial or non-commercial purposes, in microform, paper, electronic and/or any other formats.

The author retains copyright ownership and moral rights in this thesis. Neither the thesis nor substantial extracts from it may be printed or otherwise reproduced without the author's permission.

AVIS:
L'auteur a accordé une licence non exclusive permettant à la Bibliothèque et Archives Canada de reproduire, publier, archiver, sauvegarder, conserver, transmettre au public par télécommunication ou par l'Internet, prêter, distribuer et vendre des thèses partout dans le monde, à des fins commerciales ou autres, sur support microforme, papier, électronique et/ou autres formats.

L'auteur conserve la propriété du droit d'auteur et des droits moraux qui protège cette thèse. Ni la thèse ni des extraits substantiels de celle-ci ne doivent être imprimés ou autrement reproduits sans son autorisation.

In compliance with the Canadian Privacy Act some supporting forms may have been removed from this thesis.

While these forms may be included in the document page count, their removal does not represent any loss of content from the thesis.

Conformément à la loi canadienne sur la protection de la vie privée, quelques formulaires secondaires ont été enlevés de cette thèse.

Bien que ces formulaires aient inclus dans la pagination, il n'y aura aucun contenu manquant.

Canada

Abstract

The influence of carbon (C) content, microstructure, crystallography and mechanical properties on the wear behaviour of metal-on-metal (MM) hip implants made from commercially available cobalt-chromium-molybdenum (CoCrMo) alloys designated as American Society of Testing and Materials (ASTM) grade F1537, F75 and as-cast were studied in this work. The as-received bars of wrought CoCrMo alloys (ASTM F1537 of either about 0.05% or 0.26% C) were each subjected to various heat treatments to develop different microstructures. Pin and plate specimens were fabricated from each bar and were tested against each other using a linear reciprocating pin-on-plate apparatus in 25% by volume bovine serum solution. The applied normal load was 9.81 N and the reciprocating plate had a sinusoidal velocity with an average speed of 26 mm/s. The wear was measured gravimetrically and it was found to be most strongly affected by alloy C content, irrespective of grain size or carbide morphology. More precisely, the wear behaviour was directly correlated to the dissolved C content of the alloys. Increased C in solid-solution coincided with lower volumetric wear since C helps to stabilize the face-centred cubic (FCC) crystal structure thus limiting the amount of strain induced transformation (SIT) to the hexagonal close-packed crystal structure (HCP). Based on the observed surface twinning in and around the contact zone and the potentially detrimental

effect of the HCP phase, it was postulated that the MM wear behaviour of CoCrMo alloys in the present study was controlled by a deformation mechanism, rather than corrosion or tribochemical reactions.

Résumé

L'influence du carbone (C), la microstructure, la cristallographie et les propriétés mécaniques sur l'usure métal-sur-métal (MM) des implants fait d'alliages de cobalt-chrome-molybdène (CoCrMo) (ASTM F1537-94, F75-92 et en forme d'ingot) a été étudié dans ce travail. Aussi, les matériaux ASTM F1537-94 ont subi différents traitements thermiques. Des échantillons ont été usinés dans ces matériaux afin de mener des tests sur un appareil d'usure linéaire dans une solution faite avec 25% sérum de bovin. Une force normale de 9.81 N et une vitesse de 26 mm/s ont été utilisés. L'usure a été quantifiée par la perte en poids des échantillons et c'était trouvé que le C avait une influence prépondérante quelles que soient la taille des grains et la morphologie des carbures. En effet, la résistance à l'usure a été reliée au C en solution solide. L'augmentation du C en solution solide ce traduit par un réduction d'usure parce que le C stabilise la structure cubique face centré (CFC) du Co. En d'autres mots, la quantité de transformation de CFC en hexagonal compacte (HC) induite par la déformation a été réduite. La présence de macles sur et autour de la zone de contact ainsi que l'effet négatif de la phase HC tend à montrer que la résistance à l'usure MM des alliages CoCrMo est contrôlée par la déformation plutôt que des mécanismes de corrosion ou tribo-chimiques.

Acknowledgments

First and foremost, I thank God, above all else, for his one and only Son Jesus Christ who saved me from my sins and who gave me the strength to persevere during this thesis.

I would like to thank the excellent guidance given by Dr. Steve Yue and Dr. Dennis Bobyn. Their supervision and leadership have been excellent examples to me for my future endeavors. I am also very grateful for the support and guidance given by Dr. John Medley from the University of Waterloo, who was technically a third supervisor throughout all this. I am grateful for his input, constructive criticisms and insightful discussions. Without him this thesis could not be completed.

I would also like to thank the graduate students in the Yue/Jonas groups, in particular Abdel Elwazri and Gregg Stewart for their friendship and support. I thank the staff in the Department of Mining, Metals and Materials Engineering, namely Mr. Edwin Fernandez for his technical support and Ms. Lorraine Mello for her administrative assistance. They went out of their way to help me all these years and for that I am very grateful. I am also grateful for Mr. Jan Krygier at the Montreal General Hospital and Mr. Ernst Huber at the University of Waterloo for their technical assistance and support. I also thank Mr. Jan Brandt at the University of Western Ontario for his help with profilometry work. Finally, I would like to acknowledge Dr. Rob Hammond, Dr. Ian

Swainson and Mr. Lachlan Cranswick at Atomic Energy of Canada Ltd. for their time and assistance for the neutron diffraction studies conducted in this work.

In addition, this research would not have been possible without the financial support of the Canadian Institute of Health Research and the Natural Sciences and Engineering Research Council of Canada.

Nomenclature

A	Strain energy factor
a	Radius of circular contact area (m)
a_{hkl}	Lattice parameter of a cubic crystal (m)
$\vec{b}$	Burger's vector (m)
b_1, b_2	Partial dislocation Burger's vectors (m)
C_{YS}	Yield strength conversion factor
C_{UTS}	Ultimate tensile strength conversion factor
c	Half thickness of an ε nucleus in an α matrix (m)
D	Punch displacement (m)
d	Sliding distance (m)
d_f	Width of a faulted area (m)
d_{hkl}	Interplanar spacing of reflecting planes in a crystalline solid (m)
E'	Effective modulus of elasticity (Pa)
E_1, E_2	Moduli of elasticity of two contacting materials (Pa)
F_f	Frictional force (N)
F_N	Normal load (N)
F_R	Resultant load (N)

F_T Tangential load (N)

G Shear modulus (Pa)

H Hardness of a contacting material (kg/m^2)

h Depth of a wear groove (m)

h_c Central film thickness (m)

K Wear factor (m^3/Nm)

k Wear coefficient (s^2/m)

m Mass loss (kg)

L Number of surface heights

P Punch load (N)

R Topologically close-packed phase in Co

R_a Center line roughness (m)

R_q Root mean square roughness (m)

R_c Radius of the acetabular cup (m)

R_{eff} Effective radius (m)

R_H Radius of the femoral head (m)

r Radius of punch (m)

r_a Radius of an asperity (m)

r_p Radius of an ε particle in an α matrix (m)

t Thickness of shear punch specimen (m)

V Wear volume (m^3)

y_i Particular surface height (m)

$\bar{y}$ Average surface height (m)

α Face-centered cubic Co structure

α_t Take-off angle (°)

γ Shear strain

γ_d Level divergence angle (°)

γ_{SFE} Stacking fault energy (J)

ΔG Gibb's free energy (J)

ΔG_c Gibb's chemical free energy per unit volume associated with the phase transformation from FCC to HCP (J/m^3)

ΔG_m Gibb's mechanical free energy per unit volume associated with phase transformations (J/m^3)

ε Hexagonal close-packed Co structure

ε_e Axial engineering strain

θ Scattering angle (°)

θ_a Angle of the asperity surface to the direction of motion (°)

θ_m Angle of monochromator in a neutron diffractometer (°)

λ Lambda ratio

λ_{hkl} Wavelength of incident neutron beam (m)

μ Topologically close-packed phase in Co

ν_1, ν_2 Poisson's ratio of two contacting materials

ρ Theoretical density (kg/m^3)

σ Topologically close-packed phase in Co

σ_1, σ_2 Roughness of two contacting surfaces (m)

σ_i interfacial energy per unit area (J/m^2)

σ_{YS} Yield strength (Pa)

σ_{UTS} Ultimate tensile strength (Pa)

ϕ Scattering angle in neutron diffraction (°)

ψ Angle of rotation of specimen in neutron diffraction (°)

Contents

Figures

Tables

CHAPTER 1

Introduction

Total hip arthroplasty (THA) involves the replacement of both the acetabular cup and femoral head of the hip joint (Figure 1.1) with an implant made from common materials. The current dominant problem affecting the longevity of THA is periprosthetic osteolysis.[1] This "disease" is caused by macrophage-induced bone resorption or destruction[2,3] at the bone-implant interface due to the ingress of particulate debris in this area.[1] Macrophages are cells which react to the foreign wear particles by enveloping them and fusing with other macrophages to form cysts. Studies conducted on the macrophages present in the area of bone resorption were found to contain large amounts of particulate polyethylene wear debris.[4,5]

The utilization of conventional ultra-high molecular weight polyethylene (UHMWPE) as the bearing surface of the acetabular cup was first introduced in the 1960's by Sir John Charnley who suggested that it reduced the overall friction of the joint[6] while maintaining low wear. Prior to the implementation of metal-on-polyethylene components, the earlier generation artificial hip implants were composed entirely of metal. At that time, biocompatibility and strength were the governing issues in THA and metal alloys met these criteria. In particular, as-cast Co alloys were used as the joint material due to their very high strengths and resistance to various forms of corrosion.[7]

The cast material contained a relatively coarse microstructure, including element segregation leading to the formation of coarse carbide precipitates in certain areas of the microstructure.[8] As a result, the mechanical properties were poor and they varied from implant to implant manufactured under the same processing conditions. In addition, the acetabular cups and femoral heads were not very round, had quite rough surfaces and were often paired to produce very low clearance articulations that produced high frictional torques due to the large contact zones. Furthermore, the cups had thin walls and tended to wrap around the heads. As a result implant seizure occasionally occurred due to frictional fusion near the equator.[9,10] One solution to high friction was the introduction of UHMWPE cups.

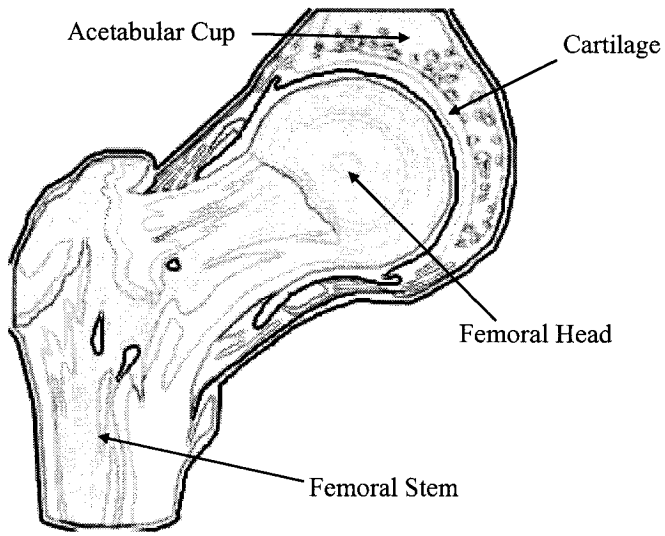

Figure 1.1. Diagram of the human hip joint

Although the problem of high frictional torques was effectively eliminated with conventional UHMWPE, a new problem arose with respect to wear particle-induced osteolysis as discussed above. Interestingly, retrievals of some cast CoCrMo metal-on-metal hip implants which did not experience seizing (some in situ for over 25 years) revealed very low wear of the articulating surfaces compared with metal-UHMWPE

implants. As a result, a renewed interest has developed regarding the optimization of the wear performance of CoCrMo metal-on-metal (MM) implants used in THA.

Modern MM hip implants (Figure 1.2) are made from investment cast (and later subjected to hot isostatic pressing) or machined from wrought alloys.[11] The wrought state of these alloys is achieved through thermomechanical processing of the cast material by hot rolling or forging into bar stock. Thermomechanical processing of the material refines the grain structure and removes any macrodefects that are present, thus improving the overall mechanical properties of the alloy.[12] In addition, the precision surface grinding that is used in manufacturing the head and cup components has allowed implants to have precise clearance ranges that effectively eliminated any problems associated with implant seizing at the joint equator.

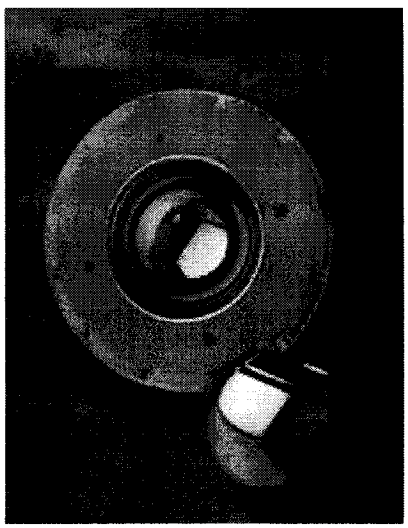

Figure 1.2. A modern metal-metal hip implant (made by Centerpulse Orthopedics, now part of Zimmer) [11]

Although MM implants have been shown to exhibit much less wear than their conventional UHMWPE-on-metal counterparts, research is required to further reduce the volume of wear debris, which is generated at the joint interface. Since implants made from different CoCrMo alloys exhibit different amounts of wear, it is necessary to investigate the role of microstructure (in the case of metal components) on the wear of

these implants in order to increase the longevity of THA. As a prerequisite, a better understanding of the parameters controlling wear is required.

CHAPTER 2

Literature Review

2.1. Introduction

In order to tackle the potential problems of wear particle-induced osteolysis and ion release in CoCrMo THA, it is necessary to have a fundamental metallurgical background of Co and its alloys with the aim of addressing the materials issues that may influence the tribological behaviour of MM implants. Subsequently, an understanding of the overall tribology of these joints is essential in order to help identify the wear mechanisms that may control MM articulation. This chapter will address the areas of Co structure and properties, and the tribology of artificial hip joints.

2.2. Properties of cobalt

Since alloys composed mostly of cobalt (Co) are exclusively used in MM THA and since this study involves a materials approach to the problem of wear, an understanding of the materials characteristics of Co is important.

2.2.1. Crystallography of cobalt

Cobalt undergoes a martensitic (or diffusionless) transformation from a face-centered cubic (FCC) structure to a hexagonal close-packed (HCP) structure when cooled below 450°C in the pure form. However, due to the slow transformation kinetics from FCC to HCP the prominent phase at room temperature is a metastable FCC structure.[13]

The sluggish kinetics of the martensitic transformation in Co can be explained by the low Gibb's free energy change (ΔG) from FCC to HCP (which is approximately -12 J/mole). Comparatively, the ΔG for the martensitic transformation from FCC to body-centered tetragonal in steel is -1213 J/mole (approximately 100 times greater than that of Co).[14]

As previously mentioned, martensitic transformations are diffusionless phase transformations. In other words, there are no compositional changes from the starting phase to the end phase. However, there are changes to both the lattice orientation (as in twinning) and in the structure of the crystal lattice.[15] For the transformation to proceed from FCC to HCP, the overall ΔG for the transformation must be less than or equal to zero. The free energy requirements for the transformation in Co to occur can be divided into two parts: one is the chemical free energy change (ΔG_c) from the FCC phase to the HCP phase and the second involves various forms of mechanical energy (ΔG_m), which oppose the chemical energy component of the reaction (i.e., $\Delta G_m=|\Delta G_c|$).[14] If an oblate spheroid of the HCP phase were to nucleate in a perfect crystal of the FCC phase, the free energy change of that event could be described by the following equation:[16]

$$\Delta G = \left(\frac{4\pi}{3}\right) r_p^{\,2} c \Delta G_c + \left(\frac{4\pi}{3}\right) r_p^{\,2} c \left(\frac{Ac}{r}\right) + 2\pi r_p^{\,2} \sigma_i \qquad (2.1)$$

where ΔG is the free energy change for the overall phase transformation, r_p is the radius of the particle, c is the half-thickness of the particle, ΔG_c is the chemical free energy change per unit volume, Ac/r is the elastic strain energy per unit volume, A is the strain energy factor and σ_i is the interfacial energy per unit area.

The nucleation of an HCP particle in the Co system is based on the hypothesis that a stacking fault in the FCC matrix is actually an embryo of the HCP phase.[14,17] A

stacking fault is literally a fault or "error" in the layering sequence of the close-packed atom planes for a particular crystal structure. In the case of FCC metals, the stacking sequence is ABCABCABC. A stacking fault in the FCC sequence can act as an embryo for the HCP phase as suggested by Figure 2.1 (the HCP structure has a stacking sequence of ABABABAB).[18]

The existence of a stacking fault in a crystal lattice is inversely related to the stacking fault energy (SFE) in metals. In the case of pure Co, the SFE is approximately 20 mJ/m^2, which is relatively low when compared to other metals such as Al (which has a SFE of 250 mJ/m^2).[19] This translates to a high probability of a stacking fault to occur in pure Co.

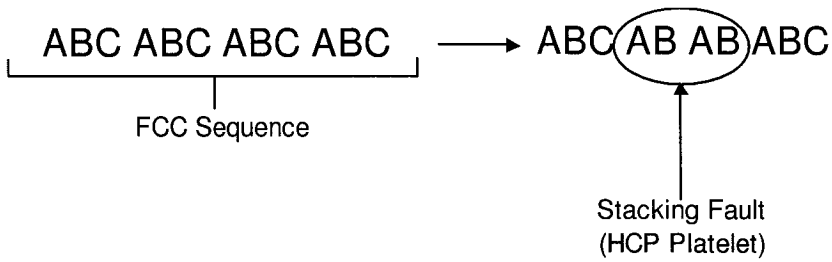

Figure 2.1. Fault in the FCC stacking sequence

It is believed that when the transformation temperature from FCC→HCP is approached, the SFE decreases and the width of the faulted region increases. The growth mechanism of the HCP phase is explained as the movement of partial dislocations along the (111) planes in the FCC lattice.[14] The resultant dislocation along the (111) planes possess the Burger's vector:

$$\frac{a_{hkl}}{2}[\bar{1}10]$$

and the partial dislocations possess the Burger's vectors:

$$\frac{a_{hkl}}{6}\left[\bar{1}2\bar{1}\right]$$

and

$$\frac{a_{hkl}}{6}\left[\bar{2}11\right]$$

where a_{hkl} is the lattice parameter in a cubic crystal.[20,21]

Figure 2.2 illustrates this growth mechanism.[21] Firstly, a stacking fault lies between two partial dislocations shown above. Secondly, the width of the faulted area increases as the transformation temperature is approached and is inversely proportional to the SFE, as shown in the following expression:

$$d_f = \frac{G(b_1 b_2)}{2\pi\gamma_{SFE}} \tag{2.2}$$

where d_f is the width of the faulted area, G is the shear modulus, b_1 and b_2 are the partial dislocation Burger's vectors and γ_{SFE} is the SFE.

Thirdly, the partial dislocation lines 1 and 2 move in opposite directions (due to repulsive forces) in the (111) screw plane about the dislocation line 3. In essence, the partial dislocations are the interfaces across which the atoms are displaced from an FCC to an HCP lattice structure.

2.2.2. Cobalt-chromium-molybdenum alloys

In the design of total hip replacements, materials selection is very important since there are many functional requirements to fulfill. In particular, mechanical and chemical requirements. A total hip implant must be able to support the weight of the individual and withstand millions of cycles of use, just as the healthy natural hip joint can. In addition, a total hip implant should minimize any biological dangers to the patient.

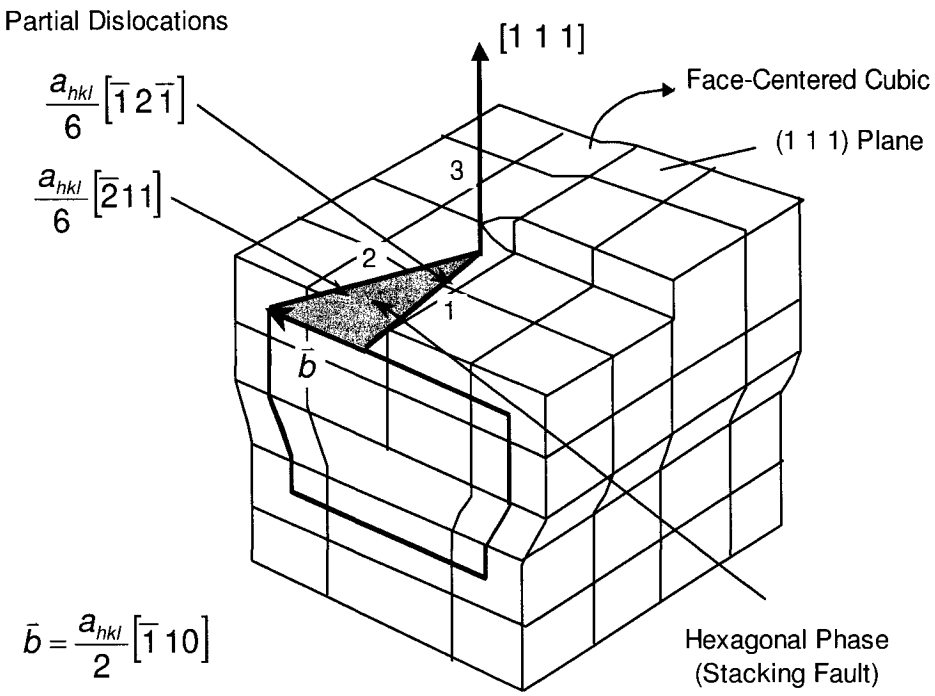

Figure 2.2 Transformation mechanism from FCC→HCP in Co[21]

Since metals can be tailored to satisfy a variety of needs, alloy design is the initial step in producing an effective material to be used for THA. Metallurgical techniques which have been used in the development of nickel (Ni) alloys and austenitic stainless steels have been used in the design of cobalt-chromium-molybdenum (CoCrMo) alloys.[22] Nominal amounts of alloying elements used in Ni alloys and stainless steels are applied to the Co system. In order to avoid the formation of certain intermetallic phases common to Co-based alloys, which have shown to be detrimental to the materials properties,[23] a phase computational technique known as PHACOMP has been used to verify the alloy composition.[22]

CoCrMo alloys used in THA can be manufactured by various techniques. Each technique will result in a material with a different microstructure and materials properties. The ASTM F75 alloy is a cast CoCrMo alloy containing roughly 27-30 wt% Cr, 5.0-7.0 wt% Mo, < 1.0 wt% Ni, < 0.75 wt% iron (Fe), < 1.0 wt% silicon (Si), < 1.0 wt% manganese (Mn) and < 0.35 wt% C.[24] However, limitations in the casting process

impose some microstructural features that may alter the mechanical properties. In the early generation implants, as-cast CoCrMo alloys were used. The process produced a coarse structure with non-uniform properties as mentioned previously in Chapter 1. Therefore, other processing steps were added in order to improve the materials properties, such as hot isostatic pressing and solution-annealing of the as-cast alloy.

Another, more widely used CoCrMo alloy is the ASTM F1537.[25] This is a wrought alloy and the rolling process used in during manufacturing helps to eliminate void defects and refines the microstructure, thus improving the mechanical properties (Table 2.1).[8] A comparison of the properties of the cast and wrought CoCrMo alloys shows a definite increase in both the yield and fatigue strengths of the material as a result of thermomechanical processing.

Table 2.1. Mechanical properties of implant metals[8]

Material	Young's Modulus (GPa)	Yield Strength (MPa)	Fatigue Strength (MPa)
30% Cold Worked Stainless Steel	190	792	310-448
Cast CoCrMo Alloy	210	448-517	207-310
Wrought CoCrMo Alloy	210	896-1200	600-896
Titanium (Ti) Alloy (Ti6Al4V)	116	896	620

In terms of corrosion resistance, pure Co is essentially a passive metal. However, the corrosion and high temperature oxidation resistance are greatly improved through the addition of Cr.[26,27] Chromium is also a carbide former and usually forms $M_{23}C_6$ type carbides.[23,28-30] This is beneficial for strengthening but detrimental to corrosion resistance because the formation of carbides removes valuable amounts of Cr from solid solution. Since these carbides have a high Cr to C ratio, high Cr contents in the alloy (of up to 30 wt%) are required to establish enough Cr in solid. solution to attain good corrosion resistance. In addition, Cr acts as a solid solution strengthener and HCP stabilizer.

Mo is added based on its carbide forming tendency and its solid-solution strengthening effect. When Mo is added in quantities of 3 wt% - 4 wt% in stainless steels (e.g., 316L stainless steel), the alloy exhibits better resistance to pitting, sulfuric acid and hot organic acids.[31] The same features can be applied to Co alloys, making it a more attractive material for biomedical applications. Similar to Cr, Mo is also a solid solution strengthener and an HCP stabilizing element. The addition of C aids in strengthening the alloy in two ways:

1. By forming a solid solution with Co
2. Through carbide precipitation

Although, the effect of C as a solid-solution strengthener is 100 times that of Ni when used in stainless steels, its solubility, is however, low. Carbon is an FCC stabilizer (like Ni), but is 30 times more effective than Ni in austenitic stainless steels.[32] In addition to strengthening the material, the above alloying elements also affect the crystallographic characteristics of Co. In particular, different alloying elements can serve to lower or raise the transformation temperature from HCP to FCC, but the kinetics of the transformation remain relatively unchanged, for a given driving force. Additions of Cr and Mo tend to stabilize the HCP-Co structure by lowering the SFE of the crystal lattice. Stacking faults are believed to be the source of the transformation from HCP to FCC in Co. Elements which raise the SFE (such as Ni) stabilize the FCC-Co structure (Figure 2.3) because the probability of finding an ε nucleus is decreased.[23] It was also found that the poor ductility and workability of Co alloys are due to the formation of stacking faults in the structure.[23,33] Thus, Ni is usually added in quantities of 5 wt% - 15 wt% to counteract the effects of Cr and Mo in order to stabilize the FCC structure and improve the ductility and workability of the material.

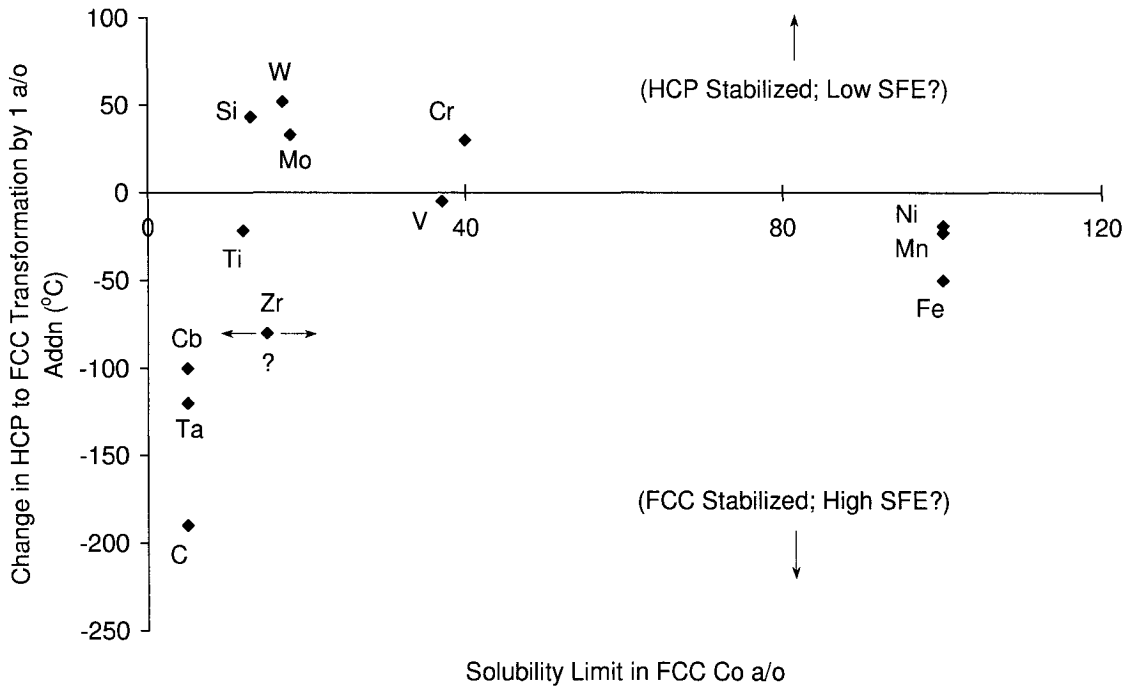

Figure 2.3. Effect of alloying additions on the HCP→FCC transformation temperature in Co[23]

2.2.3. Microconstituents of cobalt-chromium-molybdenum alloys

Up to this point, the literature has focused on the characteristics of pure Co. In summary, pure Co has a high temperature HCP crystal structure which undergoes a martensitic transformation below 450°C to a low temperature FCC structure. However, in the CoCrMo system, the transformation temperature from HCP to FCC is raised to approximately 815°C. In an alloy system, one must also consider the existence of other phases present in the microstructure that affect the properties of the material.

Carbide precipitates are very common secondary phases whenever C is present in metal alloy systems. The presence of carbides throughout the matrix increases the difficulty of dislocation motion through the crystal lattice (during plastic deformation), thus increasing the strength. Alternatively, little strengthening has been associated with the presence of grain boundary carbides, since grain boundaries act as barriers to dislocation motion themselves.[34] Various carbide types may form depending on the alloying elements present (Figure 2.4).[23] As stronger carbide formers are added, the

stability of the carbide increases and the following changes to the carbide composition occur:

$$M_3C_2 \rightarrow M_7C_3 \rightarrow M_{23}C_6 \rightarrow M_6C \rightarrow MC$$

The M_3C_2 and M_7C_3 carbide types form at low Cr to C ratios in alloys containing less than 5 wt% Cr.[33] However, the presence of these carbides is relatively uncommon in most contemporary alloys for two main reasons:

1. Most contemporary alloys contain over 5 wt% Cr and
2. The instability of the M_3C_2 and M_7C_3 carbide phases leads to the decomposition of these two carbide species into $M_{23}C_6$ carbides during precipitation heat treatment

The $M_{23}C_6$ is the next most stable carbide type and it readily forms in alloys containing more than 5 wt% Cr. The formation of these carbides can be attributed to a direct reaction of Cr with C (i.e., $23Cr+6C \rightarrow Cr_{23}C_6$) or can be formed as a result of decomposition reactions of the M_3C_2 and M_7C_3 carbides (e.g., $23M_7C_3 \rightarrow 7M_{23}C_6+27C$).[23] The M_6C carbides have been mainly observed in alloys containing appreciable amounts of Mo (~6-8 wt%) and/or W (~15 wt%). These carbides form more stable grain boundary precipitates than the $M_{23}C_6$ type and are found to be beneficial in preventing high temperature creep deformation.[23] However, in the newer Co alloys, which contain strong carbide formers such as Ti, zirconium, niobium and tantalum, the prominent carbide phase is the MC carbide. This carbide type is the most stable of the other carbide types already mentioned and it has a more profound effect on the strength of the material.[23]

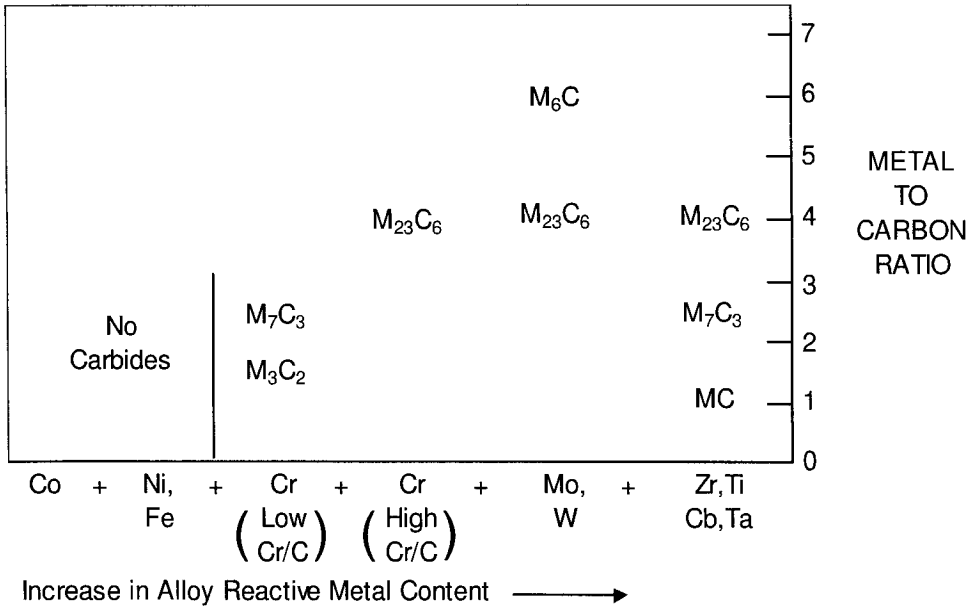

Figure 2.4. Effect of alloying elements on the types of carbides formed[23]

In the more common CoCrMo surgical implant alloys, such as the cast F75 and the wrought F1537 alloys, the carbides present in the microstructure are mainly of the $M_{23}C_6$ type, which are very stable, as previously mentioned. However, studies have shown that complete dissolution of these precipitates can be achieved through a solution anneal treatment at 1230°C ± 20°C for various holding times. In some cases, complete dissolution was achieved in 4 hr, whereas in other instances, complete dissolution required a 72 hr heat treatment,[35] depending on the temperature and alloy chemistry.[36]

Apart from the carbide phases, which are commonly found in CoCrMo alloys, other secondary phases, such as σ, μ and R, may also be present in the microstructure, depending on the composition of the alloy and the thermal processing conditions (as shown in Figure 2.5).[37] These intermetallic phases have a topologically closed packed (TCP) crystal structure composed of close-packed atom layers, which are displaced from one another by larger atoms, resulting in a characteristic topology.[38] These phases have been found to negatively affect the mechanical properties of the material (e.g., strength and ductility).[38,39] The deterioration in the mechanical properties is due to the morphology of the TCP phases. They tend to form acicular or plate-like precipitates and

act as stress concentrators, thus lowering the rupture strength of the material.[23,40] In addition, the formation of TCP phases removes precious amounts of Cr and other refractory metal atoms from solid-solution, which would otherwise serve to strengthen the Co matrix.[23]

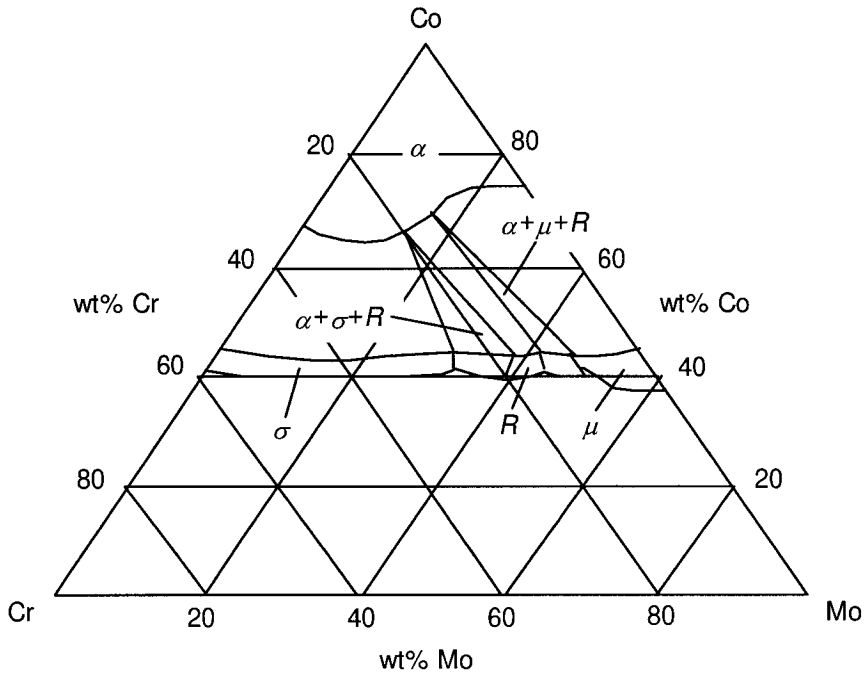

Figure 2.5. Isothermal CoCrMo ternary phase diagram at 1200°C[37]

Of the various intermetallic phases that may form, the σ phase is a commonly occurring TCP phase, especially in alloy systems that contain transition elements, such as Cr and Mo.[38,41,42] The general stoichiometry for the σ phase is $Co_x(Cr,Mo)_y$, where x = 1-7 and y = 1-7.[23] The μ phase is characterized by the general formula $Co_7(Mo,W)_6$ in the CoCrMo alloy system.[38] However, unlike the σ phase, the formation of the μ phase is not of great concern, since the Mo and W contents are usually not high enough for its formation to occur. In fact, the occurrence of μ requires over 25 wt% Mo, which makes its presence in CoCrMo alloys unlikely, since the maximum Mo content is ~7 wt%. The

R phase is a ternary intermetallic phase occurring in ternary alloy systems, such as the CoCrMo system. The composition range for this phase is small and contains the elements in the approximate ratio $Co_{23}Cr_{15}Mo_{15}$.[43]

2.3. Tribology

A tribological system involves two contacting bodies moving in relative motion to each other in a specific medium, incorporating the science and technology of friction, lubrication and wear processes.

Friction is the resistance to the relative motion between two surfaces. Contact occurs at discrete points on the surfaces, known as asperities and often plastic deformation occurs at the asperity tips while subsurface deformation is elastic (Figure 2.6).[44-46] Under static conditions, when a normal force is applied to two metal surfaces, these discrete points of contact will deform and work harden, according to the bulk properties of the materials. Due to the high pressures at these points, cold welding or adhesion of the contact surfaces also occurs. The resistance involved in separating these cold-welded joints via an applied tangential force is known as "shearing",[47] which is a static form of friction. Another component of friction, known as "plowing", occurs when one surface digs into another surface (due to a difference in hardness), thus forming a groove or scratch in the softer material. This is considered to be a kinetic form of friction.

Lubrication involves placing a substance (usually a liquid) between the surfaces in order to influence (usually reduce) the friction and wear. This can be achieved by various combinations of either a flowing "fluid film" that physically separates the surfaces to some extent or by "boundary" molecules with chemical attachments to the surface that are capable of influencing the adhesion and sometimes even the abrasion.

Wear can be described as the progressive loss of material from the operating surface of a body occurring as a result of relative motion at the surface from another body in contact.[48] Under lubricated conditions (such as in the hip joint) wear can occur when there is a breakdown in fluid film and/or boundary lubrication, resulting in direct asperity-asperity interaction.

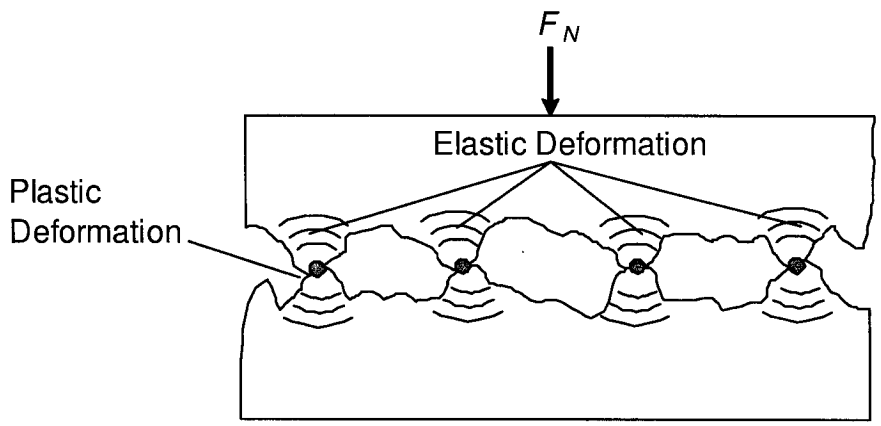

Figure 2.6. Asperity contact between two surfaces under an applied normal load F_N[45]

2.4. Factors affecting wear and its mechanisms

Several factors, other than lubrication, can greatly affect wear. They include component macro-geometry, load, speed, temperature, surface roughness, hardness and surface microstructure.

Generally, the wear rate increases with increasing loads and speeds. However, over a wide range of loads and speeds transition points in the equilibrium wear rate are often found in which the wear pattern can change from mild wear to severe wear and vice versa. A similar effect of temperature on the wear rate can be seen due to softening of the material and the changes in lubricant properties.

Highly rough surfaces have also been found to increase the wear rate in both abrasive and adhesive wear conditions. As wear progresses, there is a subsequent change in the surface roughness. Often, the initial wear rate is relatively high but it gradually reduces to a lower equilibrium or "run-in" rate. Although smoother surfaces would tend to lower the wear rate, very smooth surfaces can become rough over time when subjected to wear.

Usually, harder materials resist wear more than softer ones. Since hardness is a mechanical property, the microstructural features of a material, such as crystal structure and secondary phases, may affect the wear rate.[49,50]

2.4.1. Adhesive wear

Adhesive wear, one of the most common forms of wear which occur under sliding conditions, involves a transfer of material from one surface to another. This process of material transfer is also referred to as "mechanical mixing".[50] Contacting surfaces have a tendency to adhere to one another due to attractive forces existing between the atoms of the two materials. When the two surfaces are separated, either normally or tangentially (as in sliding), then the attractive forces between the two try to pull one material to the other, thus producing an adhesive wear fragment. This is illustrated in Figure 2.7,[51] where two asperities from opposite surfaces are in contact. If the strength of the joint is greater than the strength of the bulk material, then fracture occurs at some distance away from the interface.

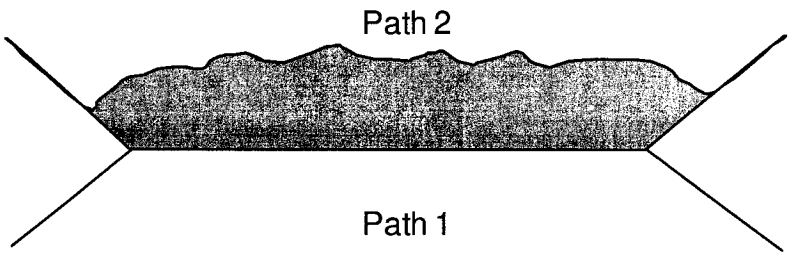

Figure 2.7. Joining of two asperities under an applied normal load. If the strength of the joint along path 1 is much greater than the bulk strength of the top surface, then fracture will occur along path 2 due to tangential forces[51]

In repetitive transverse sliding (as in a reciprocating wear tester), this transfer of material can occur over several stages before an actual particle is pulled free of both surfaces. The transferred or "mixed" material is usually harder than the parent material due to a significant amount of deformation and detached particles of this mixed material often act as third-body abrasive wear particles. However, it is believed that the interaction of asperities only occasionally leads to the production of a wear particle because:

1. The cross-sectional area of the junction is smallest (therefore higher stresses are present there)
2. The large number of vacancies which are likely to be present in these areas, lower the strength of the interface
3. The presence of oxide layers, contaminants or other surface layers at the interface also contribute to fracture along the interface

Since early experiments on adhesive wear were conducted on metals, the process of adhesion was given the term "welding". In metallurgy, the term "welding" is usually used for joining metals at high temperatures, essentially removing the interface between the two surfaces by diffusion processes (Figure 2.8a).[52] This is quite different to adhesive contact, where microstructural changes at the interface are not readily visible and the interface itself is very distinct (Figure 2.8b).

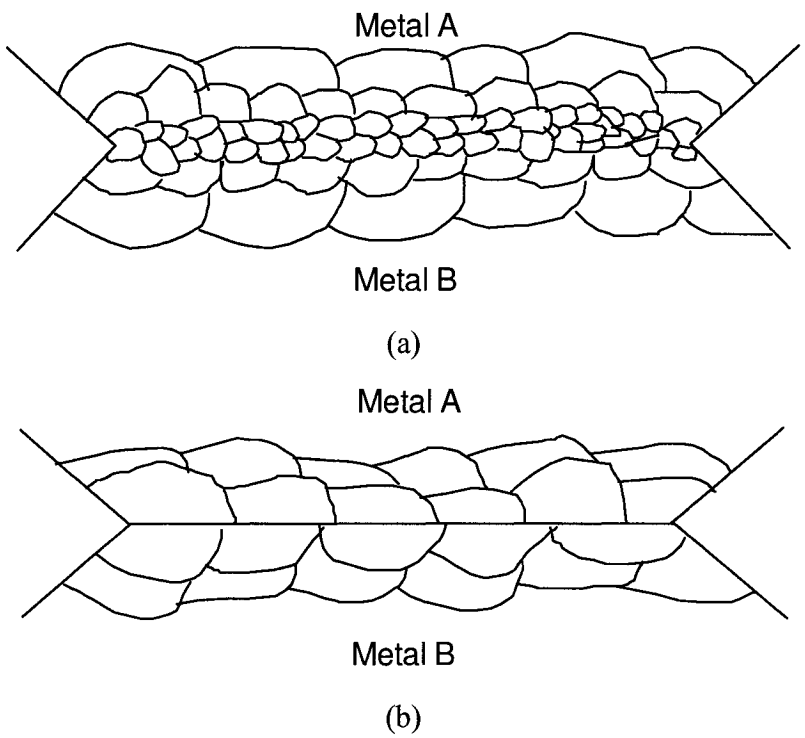

Figure 2.8. Joining of two surfaces: (a) a typical metallurgical joint formed by welding and (b) an adhesional joint[52]

2.4.2. Abrasive wear

Abrasive wear occurs when a hard surface slides against a softer surface, removing material in the form of a groove. These grooves can be produced by a "ploughing" action (Figure 2.9),[53,54] where harder material displaces softer material, forming two mounds on either side of the groove track. The material in the mounds is then subject to removal from the surface. This type of material removal is a multi-step process and one extreme of abrasive wear known as "smooth sliding."

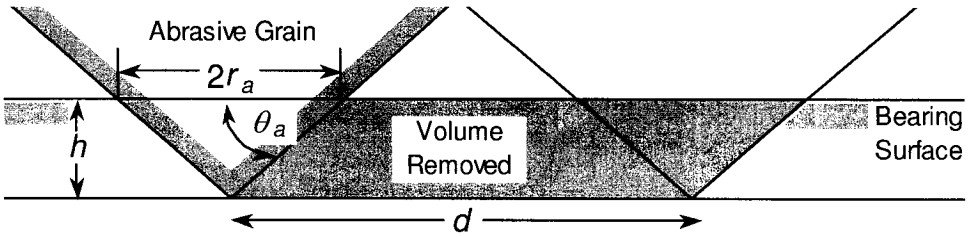

Figure 2.9. A simplified example of abrasive wear by a cone-shaped asperity removing material from a counterface, where d is the distance traveled, h is the depth of the groove, $2r_a$ is the diameter of the asperity at distance h from the apex and θ_a is the angle of the asperity surface to the direction of motion[54]

The other extreme is direct removal or "microcutting"[53] of the softer material by the harder material and is dependent on surface roughness and the morphology of surface particles. Rough surfaces and sharp particles protruding from the surface contribute to this type of abrasive wear but this mode of abrasion can change as surfaces become smoother. The reverse can also occur when changes in the microstructure caused by mechanical mixing or strain-induced transformation (SIT) increase the hardness of the surface material.[55] An example of this is when a tool steel is slid against 304 stainless steel, which has a metastable austenitic structure.[50] The wear is normal at first, but when martensite is produced by SIT the extremely hard surface abrades the tool steel. In the case of 310 stainless steel, where the austenite is stable, the wear behavior is like that of many simple metals.

2.4.3. Delamination wear

Delamination wear is also referred to as "surface fatigue wear." It is a fatigue process whereby cyclical loading of the contacting surfaces produces cracks in the surface or near surface material (Figure 2.10).[56] It is believed that the initiation of cracks in these areas are in response to an unstable or deleterious microstructure which can evolve during plastic deformation of the surfaces.[57] Some examples of microstructural evolution during sliding are: shear banding, twinning, SIT, wedge cracking and, under certain conditions, dynamic recrystallization. These local discontinuities in the microstructure, as well as the presence of precipitates, inclusions and pores act as stress raisers where cracks are likely to form and propagate, leading to the formation of wear debris.

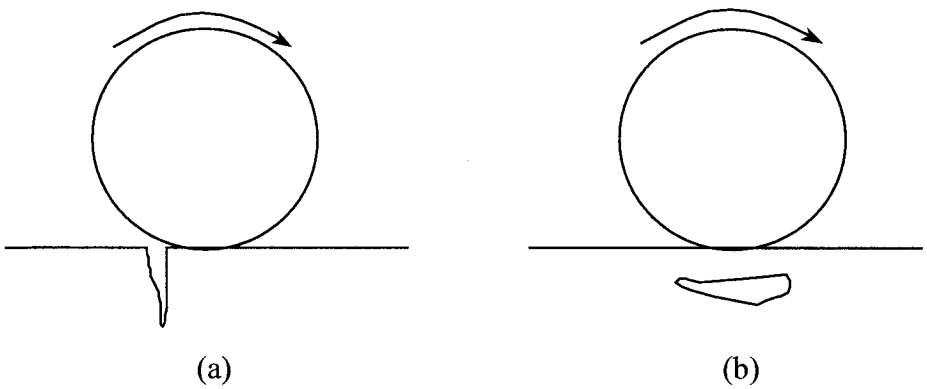

Figure 2.10. Example of surface fatigue related to wear of a rolling contact in the early stages of development: (a) surface crack and (b) subsurface crack[56]

2.4.4. Oxidational wear

In the previous sections, the focus was on the mechanical mechanisms of wear, which are considered more "severe" forms of wear. However, wear can still occur under "mild" conditions where the surface stresses are relatively low and/or a lubricating environment is present. In such cases, material loss may be caused by a mild wear, which occurs through an oxidational wear mechanism.[58] Oxygen from the atmosphere or even the lubricant can react with the metal surface to produce an oxide layer—this process being enhanced due to frictional heating of the contact zone or high fluid pressures in the

lubricant. It is believed that oxides can form and grow to a critical thickness, which inevitably fail mechanically, producing wear debris. This process can occur cyclically as metal surfaces oxidize and become exposed after the oxides are removed and reoxidize. When any other components of the environment attack a surface, the wear may be influenced and this is often called corrosive wear.

2.5. Measurement of wear

Wear is commonly measured by studying the contact surfaces before and after testing using various techniques, such as: gravimetric, mechanical and analytical methods.[59]

Gravimetric analysis is the most accepted method for quantifying the extent of wear in the area of orthopaedics. Wear can be calculated directly as a mass loss or, by dividing the mass by the density of the material, as a volumetric loss. This is the most straightforward method of measurement, but care must be taken to ensure proper cleaning of the specimens prior to weighing in order to remove any unwanted material (i.e. material or lubricant residues), which may affect the accuracy of the results. In some cases, the amount of wear is too small to resolve. For the more advanced methods, the resolving capabilities are usually in the order of 10^{-4} g. This wear measurement method is good for obtaining a single value for weight loss, but to determine the distribution of wear over a surface then other methods should used. One such method is the mechanical method which takes into account the topography of the surface (at the asperity level) and the overall shape of the contact surface. One way to measure the topography of the surface is with a profile measuring device or "profilometer." A small needle rides along the surface of the material and fluctuations in the vertical displacement are recorded. The output from this device is a two dimensional trace of the surface which can be used to estimate roughness of the surface and perhaps the volume loss of material. This method of analysis can therefore be used for both qualitative and quantitative measurements.

For qualitative analyses of worn surfaces, devices such as scanning electron microscopes and atomic force microscopes, can give very detailed three dimensional views of the surfaces at very high magnifications. They are also useful for compositional analysis in the case of determining transferred material from one surface to another.

2.6. Wear studies conducted on total hip implants

2.6.1. Hip joint simulator

In the design and testing of hip implants, hip joint simulators (Figure 2.11) are used as the preferred testing method,[60] since they usually predict the wear phenomena that occur in vivo—better than the less expensive, small-scale screening devices, which utilize simpler specimen geometries.[61] Although in vivo testing of hip implants would provide the most realistic results, the large patient-to-patient variation in many of the. factors that influence wear, the time limitations and potential health risks involved make this form of testing impractical, illegal and unethical. However, simulators can be used to test a variety of materials under representative but controlled conditions in a relatively quick manner.

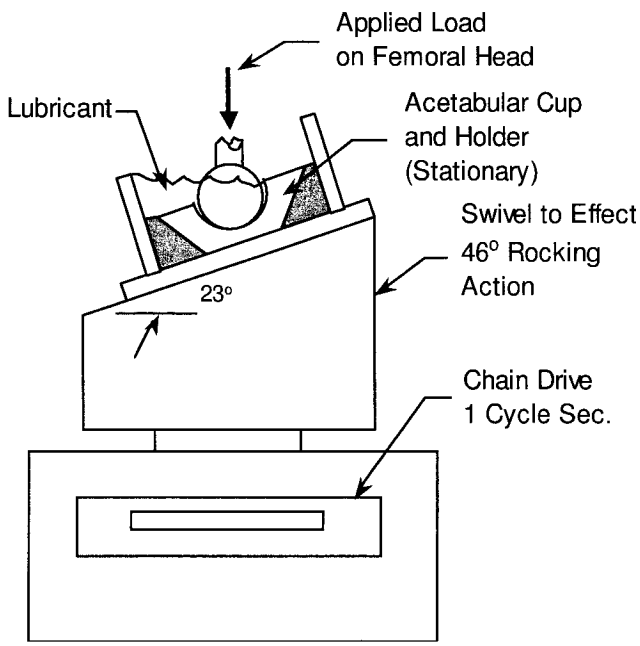

Figure 2.11. Schematic diagram of a hip joint simulator[60]

Hip joint simulator studies have been conducted on various implant couples, such as metal-on-polyethylene, ceramic-on-polyethylene, MM and ceramic-on-ceramic pairs and have been compared to the results obtained clinically. Metal-on-polyethylene THA was introduced by Charnley in the 1960's and it was observed that these implant pairs

generated the highest volumetric wear per year (30-90 mm^3/year).[62] With the introduction of ceramic balls articulating against polyethylene cups, they suggested that the polyethylene cups had less wear than with metal balls (6-60 mm^3/year). However, the best results were obtained from the CoCrMo MM and ceramic-on-ceramic implant couples, which they found exhibited relatively low wear rates (1.5-6 mm^3/year and 3 mm^3/year, respectively). However, it has been observed that under certain conditions, ceramic cups had the tendency to wear rapidly and consequently fracture.[62]

According to one European surgeon,[63] CoCrMo MM implants have been shown to be the most promising of these different material couples with their relatively low wear rates, high strength and high fracture toughnesses. Due to the success of several earlier generation MM implant pairs, there has been a renaissance of these implants in Europe with several companies developing new generation MM bearings.

Currently, hip joint simulator studies conducted on MM hip implants have paid particular attention to several control parameters, such as: kinematics of the simulator, roughness of the joint surfaces, diametral clearance between the head and cup components and alloy design. In the past, implants tested in the simulator experienced lower volumetric wear, even an order of magnitude lower than the results obtained clinically. Some explanations for the discrepancies in the results are as follows: the kinetics of the simulator are different from what actually is happening in the human hip, the new generation MM implants have better surface finishes than their earlier counterparts, the diametral clearances between the head and cup allow for better fluid film lubrication and the new CoCrMo alloys have better mechanical properties. Current studies have shown that changing the simulator kinematics from a continuous motion to a "start-stop" motion (i.e., a more realistic representation of human hip movement) increases the volumetric wear) [64]—approaching the values obtained in vivo (Figure 2.12).

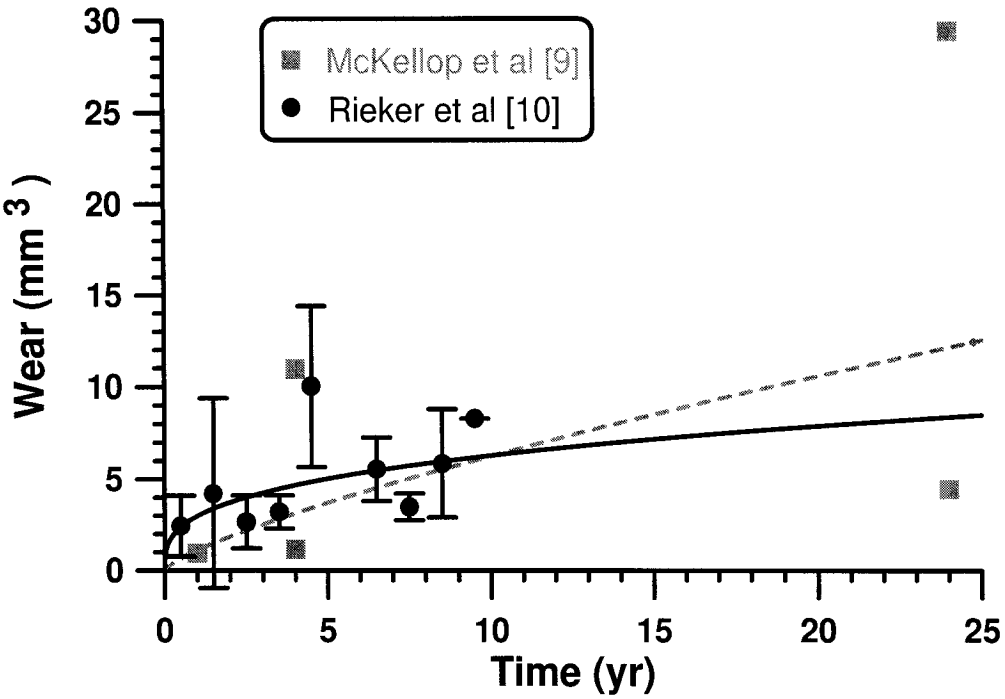

(a)

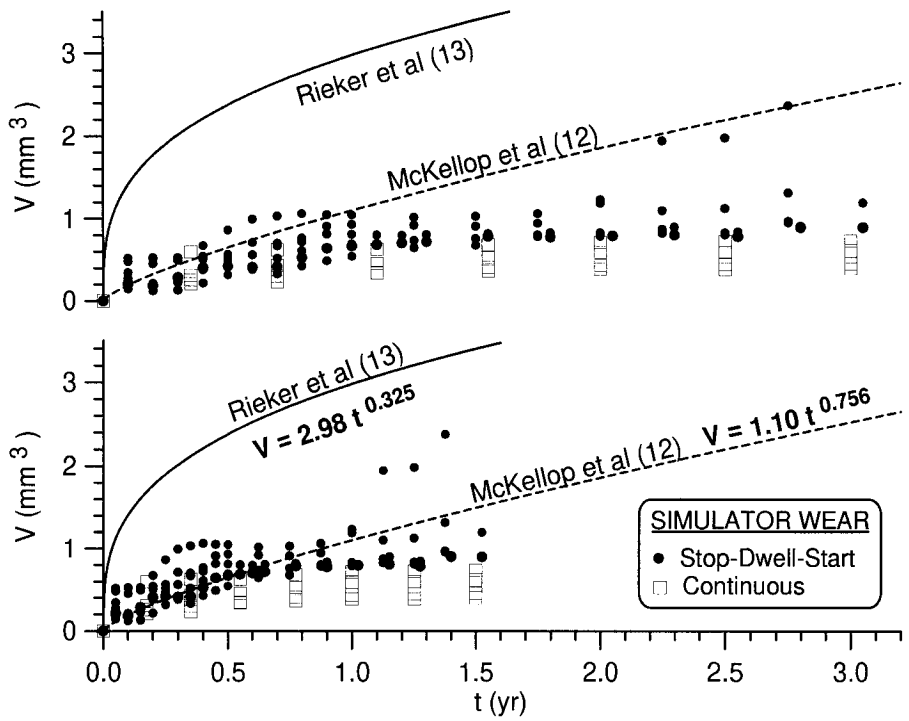

(b)

Figure 2.12. (a) Prediction of clinical volumetric wear (scatter bars equal one standard deviation) [65] and (b) simulator wear of MM hip implants compared with estimates of clinical wear from retrievals (assuming 1 Mc = 1 yr for upper graph and 2 Mc = 1 yr for lower graph)[64]

Hip joint simulator work has provided much insight in the problem of wear in THA. However, an in depth materials study would be beneficial in understanding the effects of microstructure on wear, since wear processes involve material removal. Such information would be very useful in further minimizing the volumetric wear in MM implants (since the clinical results still reveal substantial wear).

Thus far, work has been done to study the evolution of the joint surfaces in MM implants tested in a hip joint simulator in order to gain understanding of the wear characteristics of CoCrMo alloys.[66] Prior to testing, it was found that carbides were proud of the surface in the cast and high C wrought alloy specimens. After testing for 3.0 million cycles (Mc) and 6.0 Mc, the carbides were found to be worn below the matrix surface (in the case of the high C wrought alloy) or pulled out completely (as in the cast alloy), the latter potentially acting as potential third-body abrasive particles.

Some recent MM studies have attempted to focus on the materials aspect of wear. It was clearly seen that C content had an effect on the wear performance of these alloys.[67] In addition, it was found that the as-cast alloy (without any post-treatments) out-performed the high C wrought alloy.[68] Although both alloys have high C contents, an explanation for the discrepancy in wear behaviour was not given. It may be concluded that a difference in wear could be attributed to the differences in their microstructures. However, in another simulator study conducted on cast components it was found that microstructure had no significant effect on the wear behaviour.[69]

In this study, one group of cast components were hot isostatically pressed producing a coarse carbide structure while another group was solution heat treated resulting in a fine carbide structure. This demonstrates that the role of materials in MM THA may not be the predominant one, but it does not negate the fact that they may have an underlying effect on the overall tribological behaviour of these implant couples. Thus, in order to isolate and identify the role of materials on wear, more dramatic contact scenarios may required to do so.

2.6.2. Screening devices

As mentioned in the previous section, small-scale screening devices are also used in the study of wear in THA since they are relatively easy to build and can provide valuable wear data more quickly than the other, more elaborate devices.[70] As of yet, no standard test method has been devised. For small screening devices, making such a comparison is very difficult because of the different kinematics and geometry of each device. One approach to this difficulty is to calculate a wear factor. If load and sliding distance are the main parameters governing wear in two screening tests and if the wear increases in a linear fashion from zero, it may be meaningful to compare their wear factors. The wear factor is determined from the following equation:

$$K = \frac{V}{F_N d} \tag{2.3}$$

where K is the wear factor, V is the volume loss of material, F_N is the applied normal load and d is the sliding distance.

However, as research into all-metal hip joints increases, it is worthwhile to consider the implementation of standardized tests using such devices. These devices are intended to mimic the sliding conditions occurring in vivo by simulating similar surface pressures, sliding speeds and lubrication. In a typical pin-on-plate wear test, careful consideration must be given to the contact geometry. For instance, in MM contacts, elastic deformation in the testing equipment is inevitable. In the case of a flat-ended pin on a flat surface the slightest deflection of the pin can cause plowing of the edge, leading to artificially high wear rates.[71] Therefore, subtle changes in the contact conditions will have a significant effect on the wear behavior. As a result, the use of a flat-ended pin on a flat surface is greatly discouraged in MM wear testing. The use of a pin with a spherical tip is more favorable since this configuration eliminates the problem of edge effects during testing (Figure 2.13).[72]

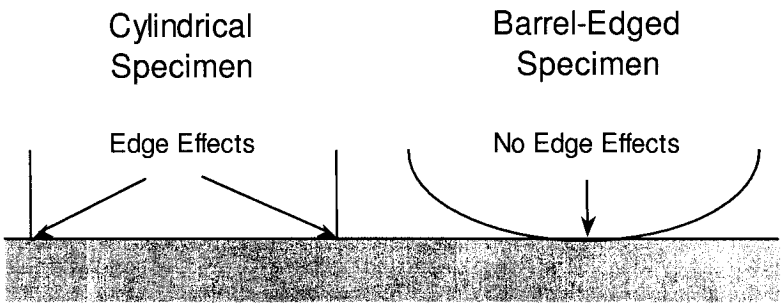

Figure 2.13 Schematic diagram of different pin geometries against a flat surface

In addition to specimen geometry, other considerations such as contact zone kinematics has been found to have a significant effect on the wear behavior, in particular those made of UHMWPE. Higher wear rates were observed when an additional pin rotation was implemented on the device (Figure 2.14),[73] producing a biaxial motion versus the more common uniaxial motion in a standard reciprocating pin-on-plate apparatus. Contrary to this, biaxial wear tests conducted on MM contacts were found to reduce the amount of wear when compared to the results obtained in a uniaxial wear apparatus (Figure 2.15).[74,75]

2.7. Microstructural considerations of wear

2.7.1. Role of matrix crystal structure

In many wear processes, deformation of the surface is almost inevitable. In fact, sliding wear in metal systems produces very large shear strains ($\gamma > 10$) at the interface and large strain gradients in the near surface material.[57,76] Therefore, the crystal structure of the matrix is important since it will dictate its deformation characteristics and, in turn, affect its wear behavior.

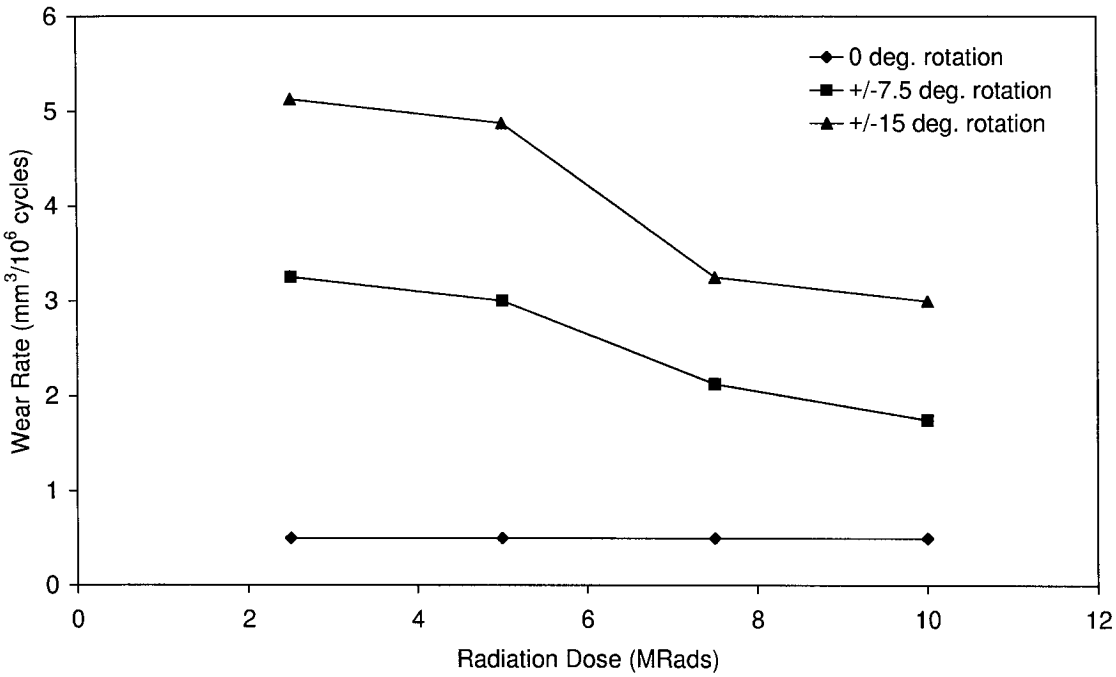

Figure 2.14. Wear rate of UHMWPE against CoCrMo. The wear rate increased with increasing degree of rotation. 0 deg. implies uniaxial motion. As the absolute value of the degree of rotation is increased, the motion becomes biaxial[73]

In general, it is believed that increasing the strength of the matrix will increase the adhesive and abrasive wear behaviour of the materials in a particular contact. This can be achieved through solid-solution strengthening and strain-hardening techniques. As a surface is worn, local strain-hardening will occur as a result of the stresses which are imposed at the contact zones. The presence of solute atoms, prior dislocations and grain boundaries will increase the resistance to dislocation motion and thus improve the resistance to wear.[77] In addition, improving the strength of the matrix may be beneficial in supporting secondary phases in the microstructure, which also contribute to the wear resistance of the material.

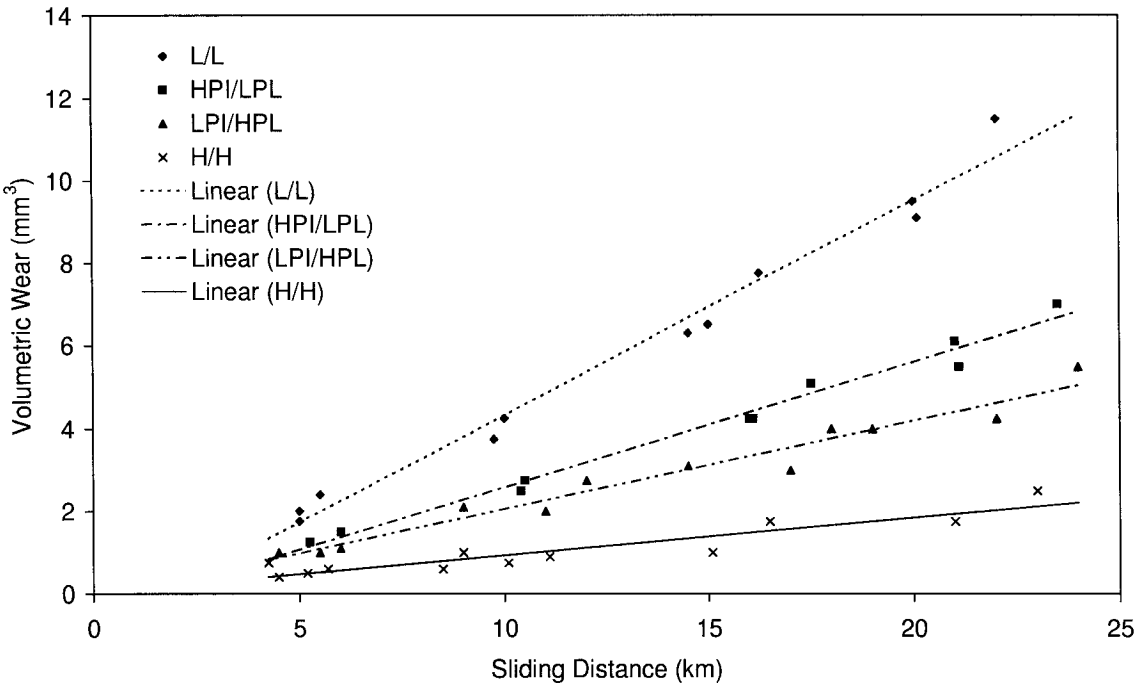

(a)

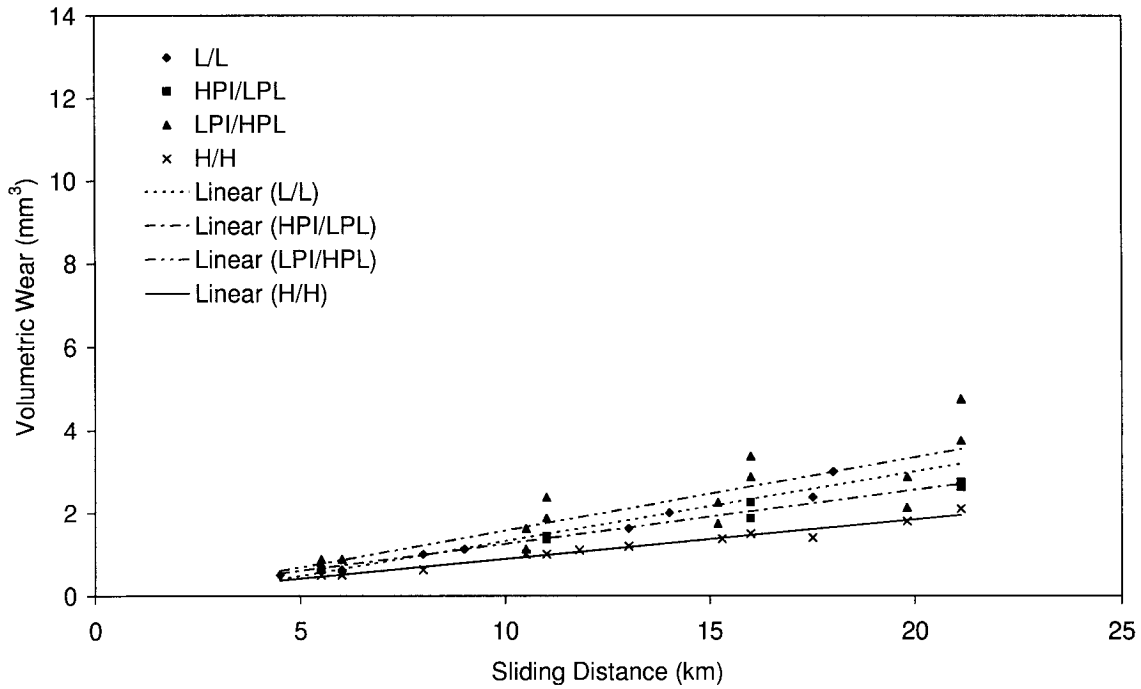

(b)

Figure 2.15. Volumetric wear of CoCrMo MM pin-on-plate test: (a) uniaxial and (b) biaxial motion. In the legend, L/L = low C pin on low C plate, HPI/LPL = high C pin on low C plate, LPI/HPL = low C pin on high C plate and H/H = high C pin on high C plate[74]

Some researchers attribute the attractive wear properties of Co-based alloys to their unusual deformation characteristics. Co is an allotropic metal that undergoes a martensitic transformation from an FCC structure to an HCP structure when cooled below 450°C. The HCP phase is the thermally stable structure at room temperature. However, due to the slow transformation kinetics from FCC to HCP the prominent crystal structure at room temperature is a metastable FCC structure, even after slow cooling.[13] The HCP phase can be obtained isothermally, athermally[78] or through strain-induced transformation (SIT).[79,80]

The transformation produces HCP platelets in an FCC structure. Depending on the mode of transformation, the volume fraction of these HCP platelets will vary according to: heat treatment time, temperature gradients, the amount of strain applied and on the stability of the FCC phase. In the case of SIT, when the FCC phase is stabilized, deformation occurs primarily by twinning and slip. Therefore, when the FCC phase is not fully stabilized a combination of deformation mechanisms occurs [81] that greatly increases the work-hardening rate, which may explain the superior wear properties of Co-based alloys.[77]

2.7.2. Role of secondary phases

In multicomponent materials, wear resistance depends on the individual phases present in the microstructure with regards to volume fraction, size, and morphology. In the case of carbides, as the volume fraction is increased, there is a subsequent increase in the abrasive wear resistance due to the higher hardness of the carbides relative to the matrix. However, under circumstances where the carbides detach, break or spall, wear resistance is found to decrease. Therefore, the assumption that better wear performance can be achieved through an increase in the carbide volume fraction may not always be the case.[77]

In addition, wear resistance was found to be greater for microstructures containing coarse carbides.[77,82] Diamond scratch tests conducted on alloys containing different carbide sizes revealed carbide cracking and ploughing to have occurred. But for quartz scratch tests, only cracking was observed suggesting that greater damage is incurred if the

abrasive material is harder than the carbides.[83] For microstructures containing fine carbides, scratches are relatively large compared to the carbide size and thus, extensive cutting and plastic deformation of the matrix around the carbide can occur, leading to the detachment of such particles. In fact, it has been observed that fine carbides were completely removed within chunks of debris.[83,84] This is contrary to the wear behaviour of coarse carbides, where the scratch dimensions are smaller than the carbides themselves, making them difficult to remove.

Therefore, it would seem that the optimum conditions for wear resistance would be large volume fractions of coarse carbides in a high strength matrix. However, other factors, such as the strength of the carbide/matrix interface and carbide spacing must also be considered.

2.7.3. Formation of wear particles

There are several mechanisms responsible for the formation of wear debris. For the most part, wear mechanisms are studied with respect to the worn surfaces. However, information on wear mechanisms can also be obtained by analyzing the wear particles that are formed and the morphological attributes of wear particles (Figure 2.16) can be linked to the mechanism which produced them.[85]

One of these mechanisms is known as "delamination" wear, a fatigue process resulting in the accumulation of strain at the surface and subsurface region of the bearing material due to cyclical loading.[76,86] Under such conditions, material detachment is caused by crack initiation and propagation in the near surface material,[87,88] producing thin platelets of wear debris. Surface defects and discontinuities in the microstructure (such as grain boundaries, secondary phases, inclusions and voids) act as potential sites where crack initiation may occur. The propagation of these cracks will then depend on the direction and magnitude of the stresses involved and on mechanisms which shield the advancing crack tip. Such mechanisms include: crack deflection and meandering by hard particles (e.g., carbides) in the microstructure, zone shielding due to a transformation in the crystal structure or strain-hardening and contact shielding in the form of unbroken ligaments across the fracture plane (Figure 2.17).[89] An interesting feature of Co is the low

stacking fault energy of the FCC crystal structure responsible for SIT to the HCP phase, which can act as a barrier to fatigue crack propagation.

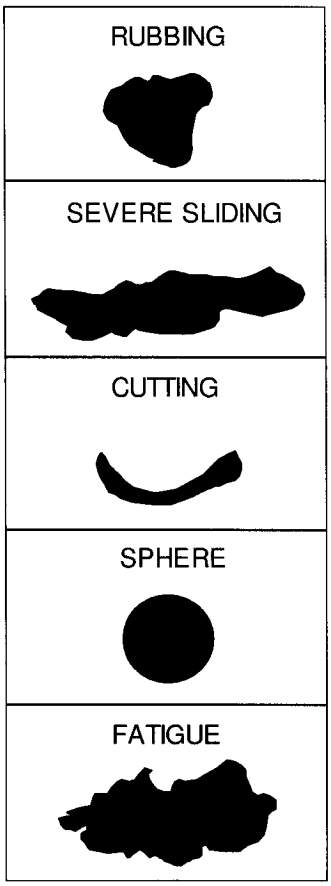

Figure 2.16. Morphology of different types of wear particles[85]

According to adhesion theory, material removal is caused by fragmentation of cold welded asperities due to surface shearing at the contact zone.[90] In adhesion, wear debris may be formed after a complex series of steps involving material transfer from one surface to another or mechanical mixing. As a result, the debris formed will have a different composition and microstructure than that of the base material.

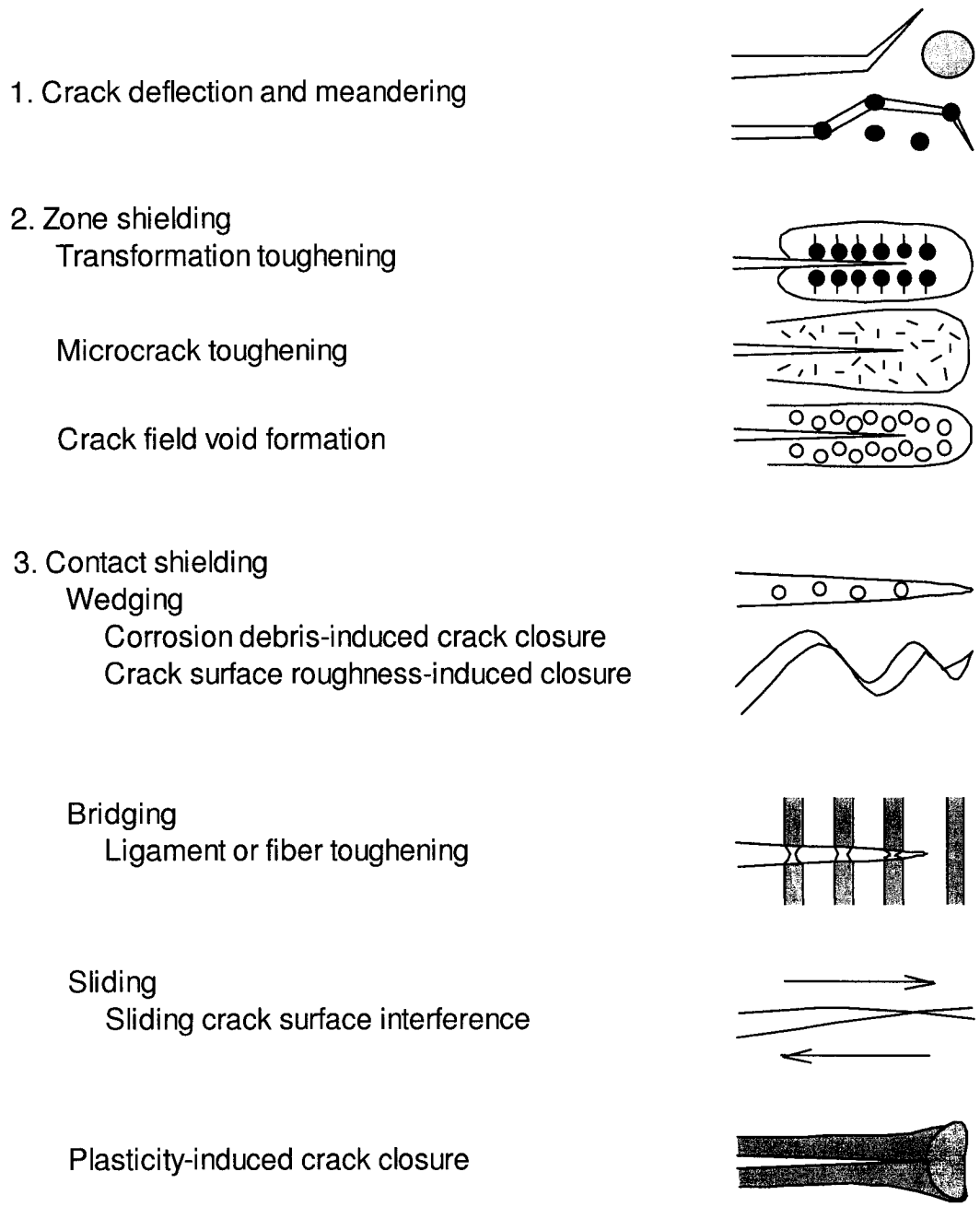

Figure 2.17. Different types of crack-tip shielding mechanisms in solids[89]

Under abrasive conditions, wear particles are produced when one surface "digs into" another surface due to a difference in hardness, effectively removing material in the form of cutting chips. This form of wear is also referred to as "microcutting". In

microcutting, wear particles are generated directly from the base material and will tend to have the same composition and microstructure as the parent material.[50] In the case of corrosive wear, particulate debris is formed by the removal of surfaces layers formed by chemical reactions with the environment. In metal systems, corrosive wear debris can often be identified as oxide particles.

Another source of wear particles is the detachment or fragmentation of secondary phases (e.g., carbides) from the matrix, which may then act as third body wear particles.[77] The ease with which carbides detach from the matrix depends on the fatigue resistance of the particle itself and on the strength of the carbide/matrix interface. Large carbides may themselves crack when subjected to repetitive loading thus producing a number of detached carbide fragments. The main factor influencing the interfacial bonding of carbide particles to the matrix would be incoherencies in the lattice structure between the carbides and the matrix, resulting from differences in crystal structure or local strain-hardening of the matrix surrounding the carbide particles. Therefore, poor carbide/matrix bonding or crack initiation at the interface will result in particle detachment.

2.8. Concluding remarks

From the literature it has been found that Co alloys possess interesting characteristics, namely their ability to undergo SIT. This ability may influence the wear behaviour of MM hip implants. In addition, the tribological studies conducted on CoCrMo alloys have shown a strong effect of kinematics and implant characteristics (geometry, surface roughness, etc.) on the wear behaviour and have touched on the materials component in the wear phenomena. In particular, the wear volume was found to decrease with increased C content in these alloys.

CHAPTER 3

Research Objectives

In light of the problems of wear debris induced osteolysis and metal ion release on the longevity of THA, the main objective of this work is to improve the wear behaviour of CoCrMo alloys used in MM hip orthopaedics. Although considerable work has been done on some of the mechanical and tribological aspects of artificial hip implants (and to a degree, alloy design) this study is focused on the materials issues involved in MM THA with the aim of further understanding the wear mechanisms involved and improving the wear behaviour. The premise is that the removal of material due to various wear mechanisms is directly related to the properties of the materials themselves. Therefore, an understanding of the relationship between material properties and wear will allow further advancement toward the goal of reducing the number of wear particles formed. Since materials properties are related to the microstructure of the material, the present study examines the effect of microstructure on the wear behaviour of Co-based alloys. This effect will be assessed quantitatively (through wear testing) and qualitatively (using optical and electron imaging techniques and diffraction studies). The wear testing will involve a particular apparatus with conditions chosen to be representative of in vivo conditions but then held constant so that only material microstructure varies. Such an approach allows the microstructural effects to be isolated but remains susceptible to the

problem that the links found between wear mechanisms and microstructure may change with very subtle changes in the test conditions.

CHAPTER 4

Experimental Procedure

4.1. Materials

Since THA involves implantation of a foreign material in the body, the acceptance of a new material for implantation involves extensive testing (in vitro and in vivo) over a long period of time, in order to ensure its safety. In response to the time constraints involved, this study mainly focused on materials currently accepted for use in THA.

Four as-received CoCrMo alloys were characterized in this study and their compositions are shown in Table 4.1. The ASTM F1537 alloys came in the form of wrought bar stock,[25] the F75 alloy in the form of cast and solution annealed bar stock[24] and the as-cast alloy in the form of cylindrical tensile specimens. The as-cast material (without solution-annealing) is not currently used, but is included in the present study because it was used with some success in the first MM hip implants (such as the McKee-Farrar).

Table 4.1. Chemical composition of CoCrMo alloys (in wt%)

Alloy	Cr	Mo	C	Fe	Si	Mn	Co
F1537 Low C (LC)	28	5.7	0.051	0.18	0.66	0.57	Bal.
F1537 High C (HC)	27	5.7	0.23	0.36	0.66	0.57	Bal.
F75	29	5.7	0.27	0.38	0.59	0.50	Bal.
As-cast	Similar to F75						

4.2. Equipment

4.2.1. High temperature furnace

All thermal treatments of the as-received material were carried out in a Blue M electric furnace. The furnace chamber was lined with silica bricks and heat was generated through resistance heating of the silicon carbide elements. The temperature in the furnace was regulated by a digital controller connected to a close-ended thermocouple, which was situated at the center of the furnace chamber. It was therefore possible to control the rate of heating, the holding temperature and the rate of cooling of the furnace.

4.2.2. Metallography equipment

Specimens were cut for microstructural analysis using an Extec low concentration diamond cutting blade. The low concentration blade (as opposed to the high concentration blade) is essential in cutting hard materials, such as Co based alloys and martensitic steels. The low concentration of diamond is sufficient for cutting Co alloys, but if used on softer materials, the areas between the diamond particles tend to clog up and reduce the cutting capacity of the wheel. As a result, high concentration blades are used for softer materials. The samples were mounted in a LECO PR 10 hot mounting press and polished using a Leco VP-150 automatic polisher. Etching of the specimen was carried out in an automatic Buehler Electromet 4 electropolisher, which was used for electroetching.

4.2.3. Image analysis system

Particle size measurements of the carbide phases present in the various microstructures were conducted using a Nikon Epiphot 200 optical microscope, which was connected to a Clemex Vision image analysis software. The software has the capability of measuring up to 8 different phases simultaneously, including area fractions and grain size measurements.

4.2.4. Scanning electron microscope

Microstructural analysis of the specimens was done using a JEOL 840A scanning electron microscope (SEM). The microscope was equipped with an EDAX PV9756/38 ME x-ray detector for energy dispersive spectroscopy (EDS), an EDAX Genesis x-ray analysis system for chemical analysis and quantifiable x-ray mapping and image analysis.

4.2.5. Neutron powder diffractometer

Crystallography measurements were conducted on all the test specimens using a C2 Dualspec powder diffractometer. This technique provides crystallographic information of the bulk material and requires no surface preparation as in x-ray diffraction, since neutrons penetrate the entire volume of the specimen. The apparatus was attached to a nuclear reactor, which supplied the needed neutrons for the experiments. A beam of neutrons was directed from the reactor source through a filter (which suppressed any neutrons with wavelengths less than 0.06 nm), to a monochromator, as shown in Figure 4.1.[91]

At the monochromator, the incident neutrons were diffracted by a known angle 2θ and passed through two collimator slits, forming a coherent beam. The beam then hit the sample and was diffracted according to the crystal structure of the material. Since the Dualspec was equipped with an 800 multi-channel position-sensitive detector, the diffracted beam was analyzed every 0.10° over a total span of 80°.

The DUALSPEC was controlled by a Unix-based program (called DSCAN), which also stored the data from the detector in a compressed binary file. In addition, the data

from the detector were collected using a personal computer located at the spectrometer. A multi-channel software package, known as APTEC MCA, read the detector memory and displayed the data in real time.[91] Finally, the data from the output file were analyzed using a Unix-based software package, known as General Structure Analysis System (GSAS), which can calculate the volume fractions and lattice parameters of the different crystal structures present in the materials.

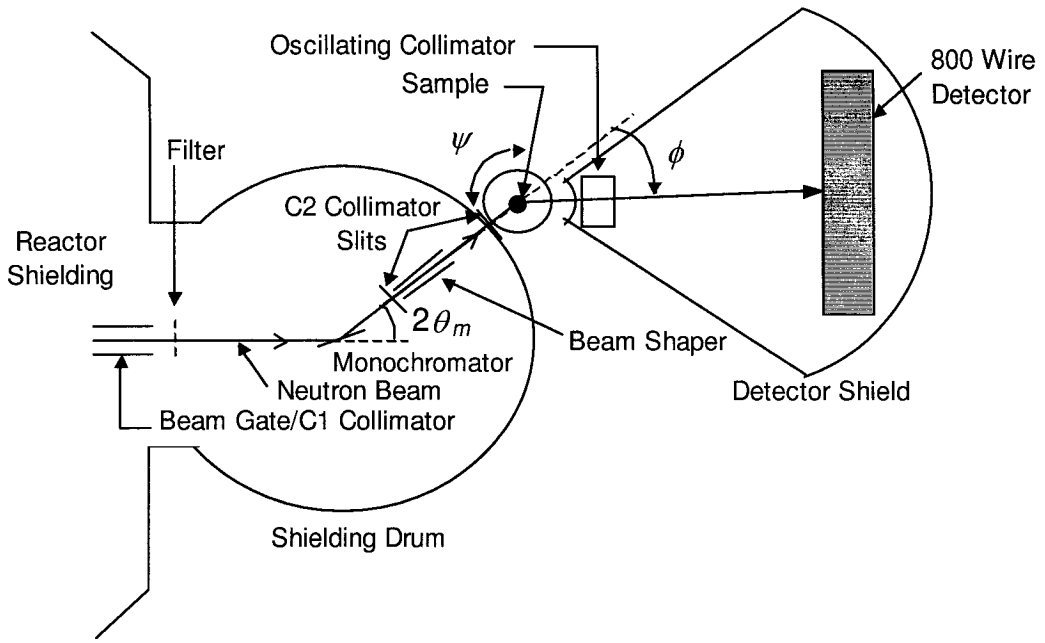

Figure 4.1. Schematic diagram of neutron diffractometer device

4.2.6. X-ray diffractometer

Although neutron diffractometry was effective in determining the bulk crystal structure of the material, x-ray diffraction was used in order to characterize the crystal structure of the contact surfaces. Surface crystallography measurements were conducted on a Rigaku Rotaflex x-ray diffractometer, equipped with a 50 kV rotating Cu anode as the x-ray source (Figure 4.2). The x-rays leaving the anode passed through a barium window followed by a series of slits:

1. Divergence soller* slit and
2. Divergence slit (respectively)

producing a coherent beam. The incident x-rays struck the specimen at an angle θ relative to the beam. Prior to reaching the detector, the scattered x-rays passed through another set of slits:

1. Receiving slit
2. Receiving soller slit
3. Scatter slit (respectively)

Finally, the scattered x-rays were collected by a 1D detector which moved at an angle of 2θ relative to the incident beam thus allowing for the acquisition of characteristic diffraction peaks.

4.2.7. Shear punch apparatus

The device used for mechanical testing of the material was a Materials Testing System (MTS), which consisted of a load frame assembly (capable of delivering a 100 kN load), a closed looped servo-hydraulic system, a hydraulic power supply and an outer loop computerized data acquisition system (Figure 4.3). The force and linear displacement of the hydraulic actuator (which was moved by a servo-valve) were measured via a load cell and a linear variable differential transformer (LVDT). The data acquisition system utilized the TestStar software package, which ran on a personal computer, and controlled the hydraulic actuator.

The shear punch apparatus consisted of two main components, which were fitted onto the hydraulic actuator and the stationary base of the frame assembly on the MTS. The upper component was essentially a cylindrical flat-head pin (or punch) made of tool steel which was clamped inside a metal housing.

* A soller slit consists of a set of closely spaced, thin metal plates parallel to the plane of the diffractometer circle.

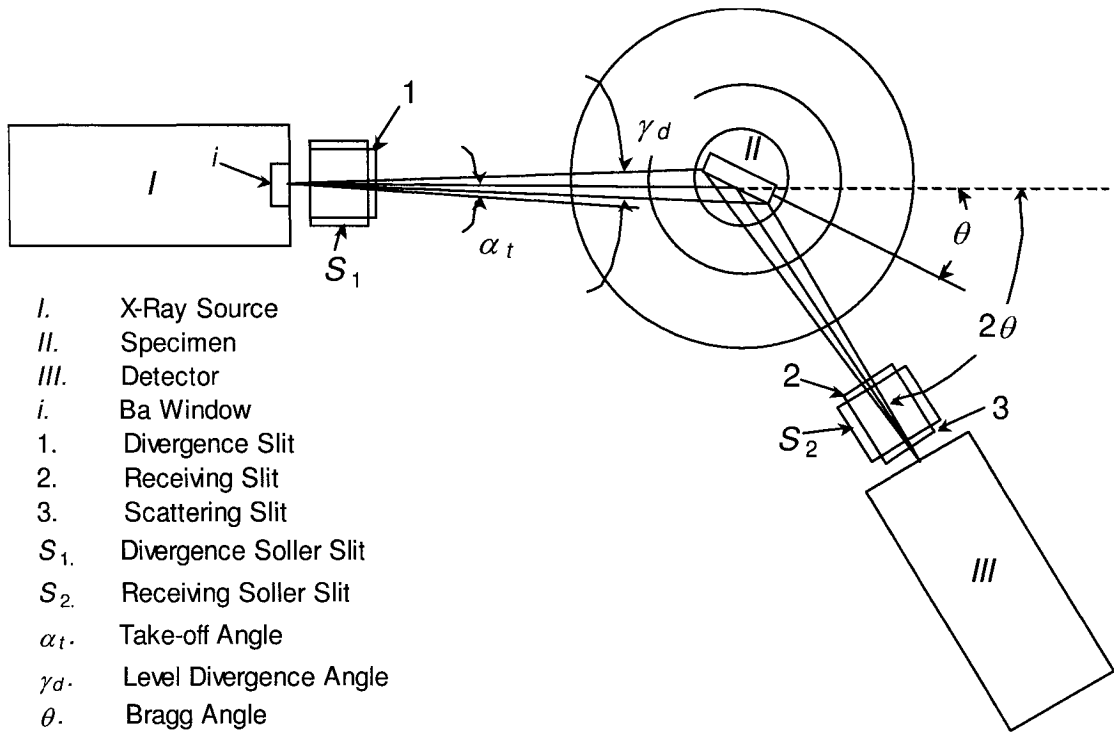

Figure 4.2. Schematic diagram of a Rigaku Rotaflex x-ray diffractometer

Although the punch head could be fabricated in different sizes, the head diameter used in this study was approximately 3 mm. The lower component was a cylindrical die made of the same material as the punch and was also clamped inside a metal housing. In the center of the die was a hollow tube, having a diameter slightly larger than that of the punch head, so that the punch would have room for insertion during testing. The test specimen was a disc of thickness 300 μm and a diameter large enough to fit over the cylindrical die of the lower component.

4.2.8. Wear apparatus

Wear tests were conducted using a reciprocating pin-on-plate wear apparatus (Figure 4.4). The apparatus consisted of a reciprocating baseplate supported by two linear bearing tracks. The reciprocating motion of the baseplate was provided by a scotch yoke mechanism and was driven by a variable speed DC motor. On the baseplate, nine

chambers which held the plate specimens and the test lubricant were screwed into position, while nine corresponding pin specimens remained fixed relative to the moving baseplate via a stationary bridge. A more detailed view of the wear configuration can be seen in Figure 4.5.

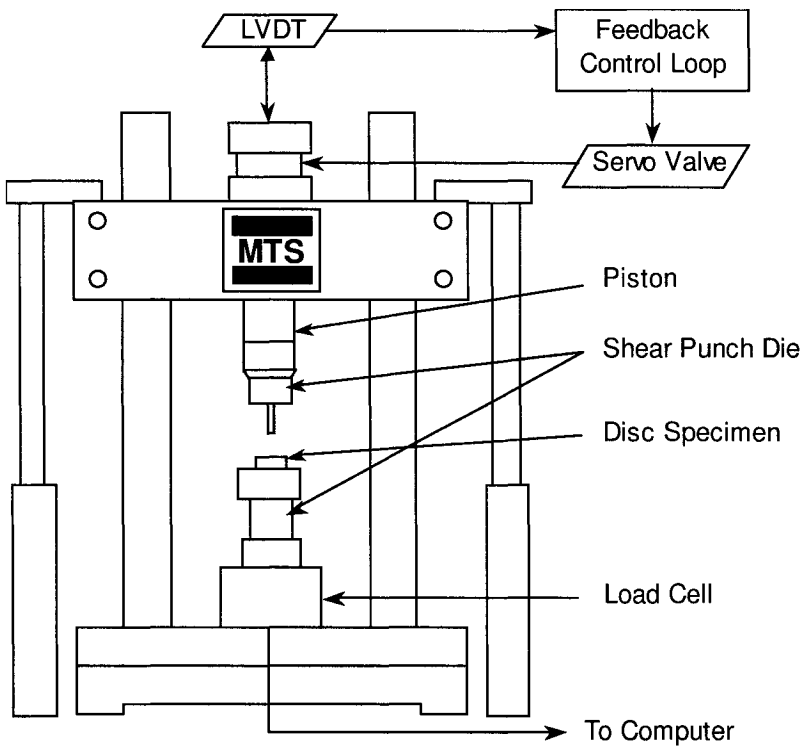

Figure 4.3. Schematic diagram of the shear punch apparatus

Round holders for the flat specimens were machined from AISI 304 stainless steel. The plate specimens were inserted into recesses of similar dimensions and held into position with four set screws. Sectioned tubes of transparent plexiglass were fitted onto these holders in order to contain the lubricant and allow easy viewing of the contact. The pin holders consisted of a metal shaft made of tool steel with one hollow end and the other end connected to an aluminum cup. The pins were inserted into the hollow end and held into position with one set screw and a known mass was placed in the aluminum cup, acting as the applied normal load for the wear tests. The pin holders were inserted

through a polymer (Delrin) sleeve connected to a stationary bridge and were free to move vertically but not horizontally. Also, a holding pin in a vertical slot was used to prevent any rotational movement of the pin holder.

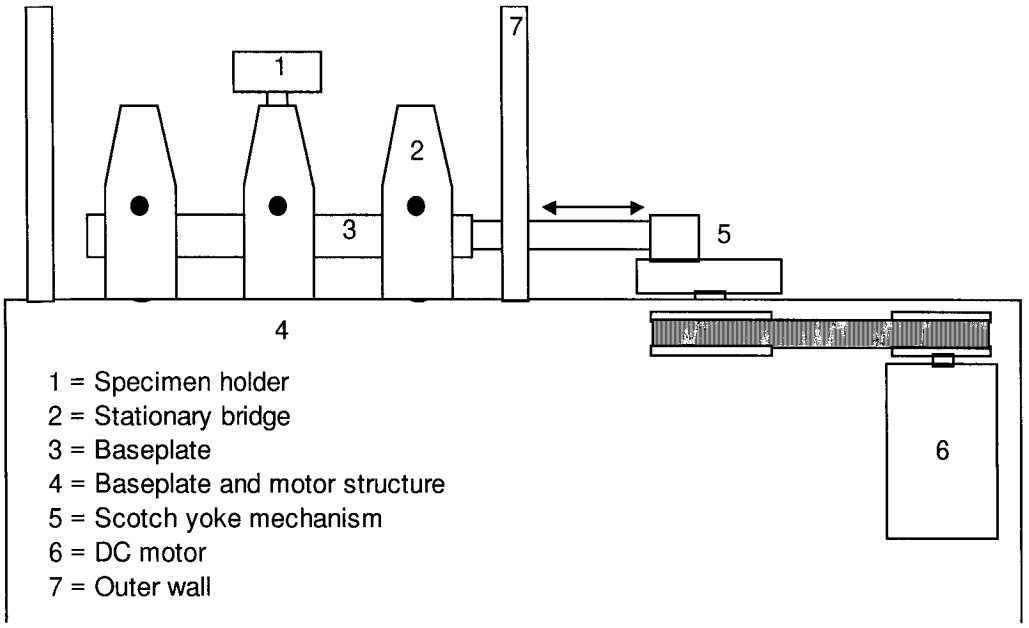

Figure 4.4. Linearly reciprocating pin-on-plate wear apparatus

4.2.9. Profilometer

As part of the surface analysis of the contact zones, micro-geometry measurements (i.e. surface profiles) were taken using a Tencor P-10 profilometer. The device utilized a contacting stylus (pin with a radius of curvature in the order of 1 μm) fine needle recorder that ran over the surface of the specimens, measuring relative heights and depths in the surface to a vertical resolution of $1.0x10^{-5}$ μm. The device was connected to a computer acquisition system and was capable of generating 2D and 3D surface profiles. The 3D surface profiles must require multiple parallel passes over a particular surface region and some sort of surface fitting software. The analysis system also generated

statistical roughness parameters (e.g. R_a, R_q) for the surface region involved in the measurements.

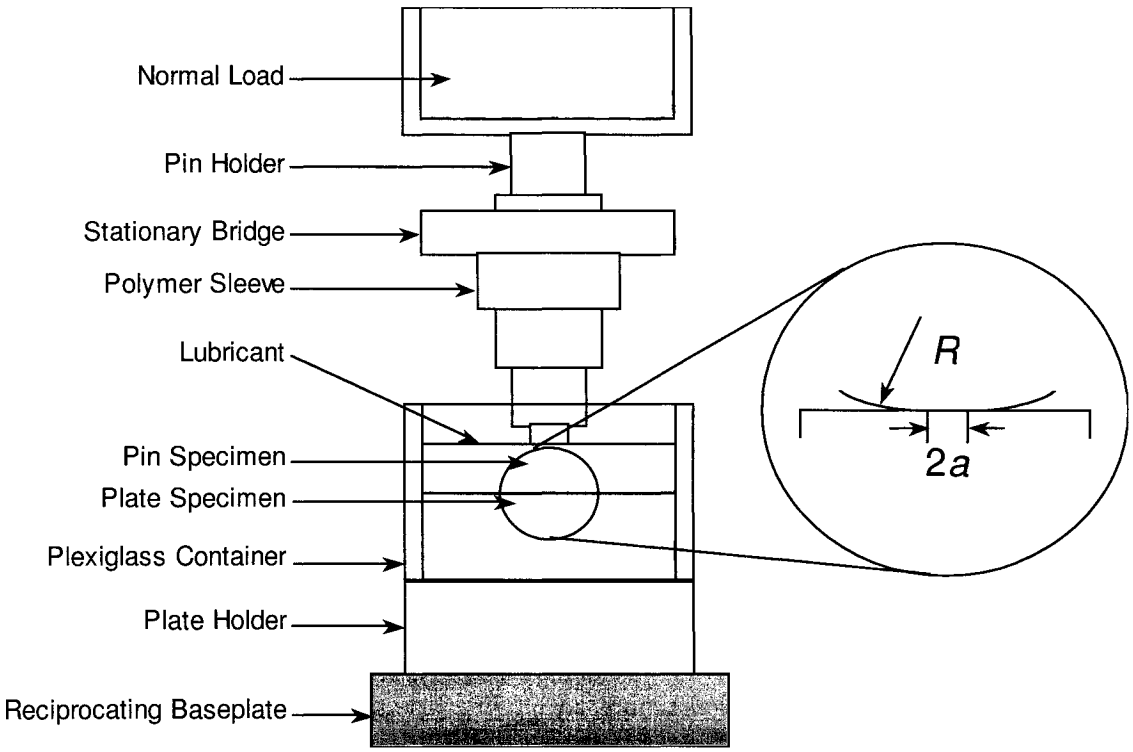

Figure 4.5. Schematic diagram showing the details of the wear configuration, where R is the radius of the pin head and a is the radius of the circular contact area

The centerline average (R_a) and the root mean square (R_q) surface roughness parameters can be used to characterize the surface heights. The surface roughness are calculated as follows:

$$R_a = \frac{1}{L}\sum_{i=0}^{L}|y_i - \bar{y}| \tag{4.1}$$

$$R_q = \sqrt{\frac{1}{L}\sum_{i=0}^{L}(y_i - \bar{y})^2} \tag{4.2}$$

$$\bar{y} = \frac{1}{L}\sum_{i=1}^{L} y_i \tag{4.3}$$

where R_a is the center line average roughness, R_q is the root mean square roughness, L is the total number of surface heights, y_i is a particular height and $\bar{y}$ is the average of all the heights over an entire sampling length.[92]

The use of these parameters to describe a surface can be helpful for modelling and comparative purposes. However, one drawback in using only a surface height parameter to characterize a surface is the fact that R_a or R_q cannot define a surface uniquely. Figure 4.6 illustrates how different surface topographies may result in the same R_a or R_q values.[93] Additional surface roughness parameters are needed to characterize the asperities (or summits of the surface heights) in terms of their radii of curvature and distribution over a measured surface region.

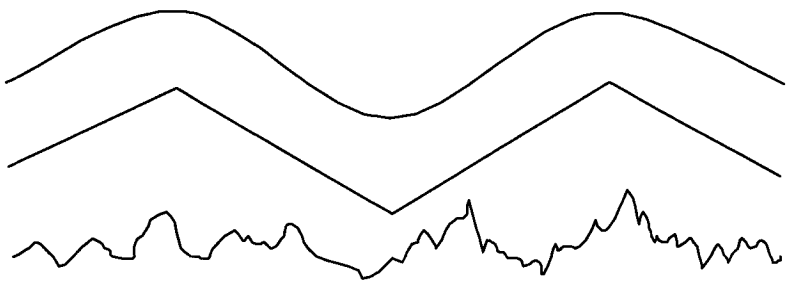

Figure 4.6. Surfaces with varying topographies

4.3. Protocols

4.3.1. Heat treatment

Thermal treatments were conducted on the as-received F1537 (wrought) alloys using several electric furnaces. The temperature in each furnace was regulated by a digital controller connected to close-ended thermocouple, making it possible to control the rate of heating, the holding temperature and the rate of cooling of the furnace chamber.

Many of the heat treatments conducted in this work were adapted from studies done by Weeton and Signorelli.[35] A solution-anneal heat treatment was used to dissolve the carbides in order to achieve a homogeneous FCC microstructure. The furnace was heated to a temperature of 1200°C and the material was held at that temperature for 24 h and then quenched in water. Due to the slow kinetics of the Co alloy system, complete carbide dissolution would require a 72 hr heat treatment in a vacuum furnace.[35] Geometric constraints of the wear specimens and limitations in the furnace equipment required that the material be heat treated under atmospheric conditions. However, excessive oxidation of the specimens would occur after 72 h at 1200°C. Therefore, a shorter treatment time was necessary. A 24 hr treatment time seemed adequate for considerable carbide dissolution and minimal oxidation. Heat treatments at 1200°C were conducted for various times and the carbide fraction in the microstructure was determined and plotted versus time (Figure 4.7).

For the aging (transformation) heat treatments the as-received F1537 specimens were either transferred from one furnace (after being held at 1200°C for 24 h) to another furnace held at 650°C for 72 h and then quenched in water (Figure 4.8) or simply heated from room temperature to 650°C for 72 h without any prior heat treatment. The solution-anneal and aging heat treatments were designed to produce a relatively homogeneous HCP microstructure in the absence of carbide precipitates. The simple aging treatments should produce an HCP structure with carbide precipitates similar to the as-received F1537 alloys.

4.3.2. Microstructural characterization

In order to characterize the microstructures, the materials were cut using a low concentration diamond cutting blade. The samples were then mounted in a hot mounting press and polished using an automatic polisher. The automatic polisher was set to provide a load of 23 N per specimen at a polishing speed of 320 rpm. The mounted specimens were ground using SiC paper for 2 min in water with the following grit sizes: 120, 240, 320, 600, 800 and 1200. The specimens were then polished in a 3.0 μm diamond

suspension for 3 min and a final polishing step of 1.0 μm diamond suspension for 1.5 min. After each step, the polished surfaces were washed in soap and water.

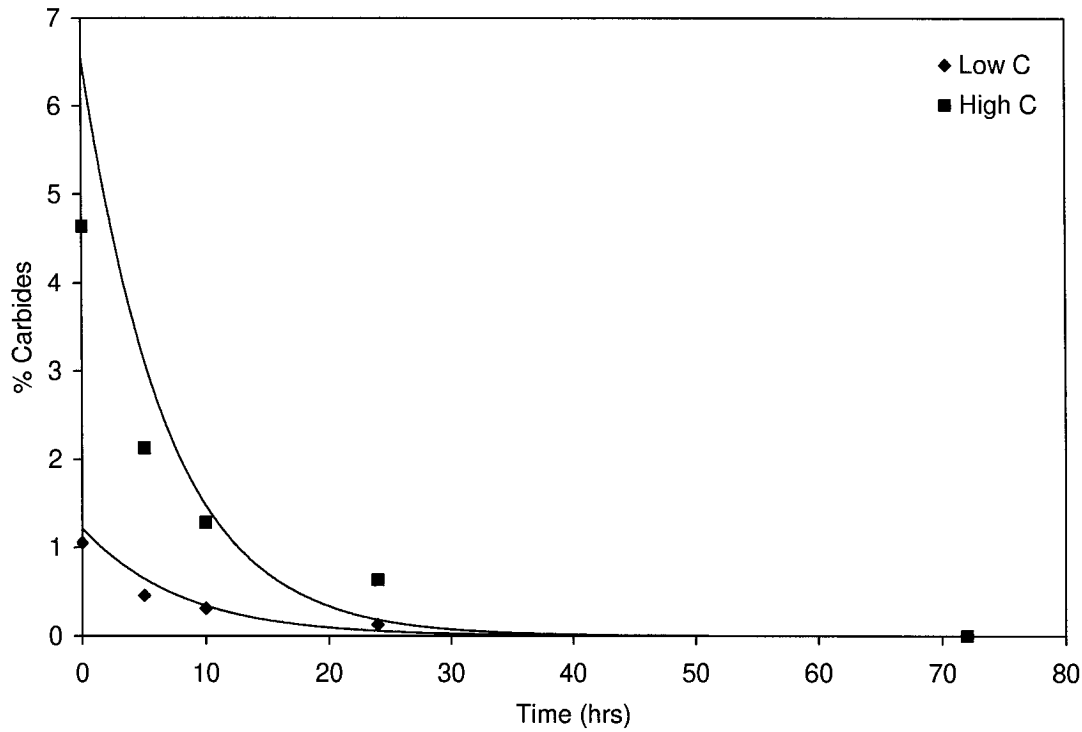

Figure 4.7. ASTM F1537 low and high C alloys heat treated at 1200°C for 5hrs, 10 h and 24 h. Within the first 5 h of treatment there is a significant drop in the percent carbides in the material (most prevalent in the high C alloy)

The specimens were electroetched in an acid solution containing 60 vol% nitric acid and 40 vol% distilled water in order to reveal the grain structure.[94] The etching device was set to a voltage of 5 V for 10-25 s. The microstructures were then analyzed using a JEOL 840A scanning electron microscope (SEM). The microscope was equipped with an energy dispersive x-ray detector and an x-ray analysis system for qualitative and quantitative chemical analysis. As part of the microstructural analysis, microhardness measurements were taken of the various phases in the materials using a Microhardness Tester.

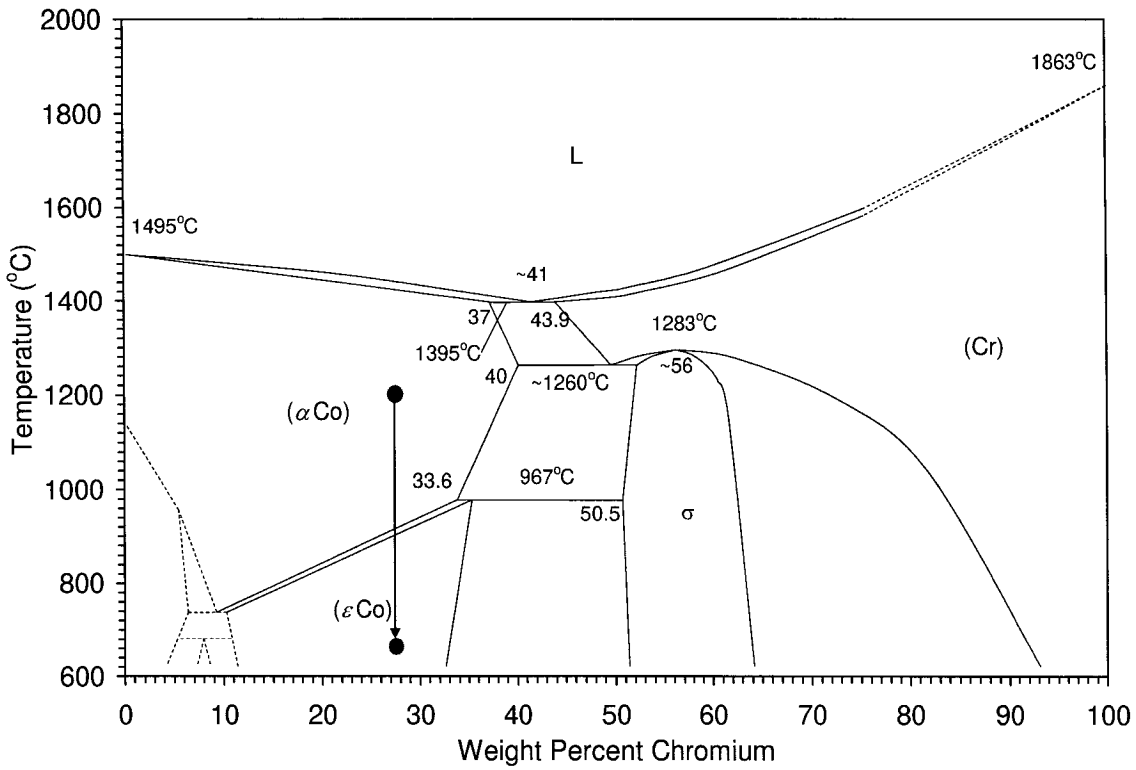

Figure 4.8. Co-Cr Phase diagram showing phase transformation from 1200°C to 650°C (denoted by arrow)

The specimens were also stain-etched in order to identify and quantify the carbide phases. Prior to stain-etching, the specimens were lightly electroetched in a solution of 2.0 vol% CrO_3 in distilled water for 1 second at 5.0 V. Then the etched surfaces were immersed in a staining solution containing 1 part 20 Vol% $KMnO_4$ in distilled water and 1 part 8.0 vol% NaOH in distilled water for 7.0 s.[35]

Microstructural features were measured quantitatively using a Windows™-based imaging software, which was connected to an optical microscope. The software interface allowed for live acquisition of an optical image under various magnifications of x25, x50, x100, x200 and x500. The image could later be manipulated through the software in order to enhance any particular feature of the microstructure for subsequent quantitative measurement. The software utilized a coloring scheme in order to isolate and measure the desired areas. In this study, the microstructures were imaged for grain size, carbide size and carbide fraction.

4.3.3. Crystallography measurements

In neutron diffraction, no sample preparation was required, due to the fact that neutrons penetrate the entire volume of the sample (i.e. not only a surface, as is the case in conventional x-ray diffraction). In fact, larger sized specimens were encouraged, since larger specimen volumes reduce the analysis time required. The wavelength of the incident neutron beam was calibrated using Bragg's law for a sample of alumina:

$$\lambda_{hkl} = 2d_{hkl} \sin\theta \tag{4.4}$$

where λ_{hkl} is the wavelength of the incident neutron beam, d_{hkl} is the known interplanar spacing of the reflecting planes of the sample and θ is the known diffraction angle of the corresponding reflective plane.

The cylindrical specimens were placed on a rotating stand in the specimen chamber. In that way, any effect of texture due to heat treatment or prior thermomechanical processing was eliminated. In the DSCAN program, the scan time for each specimen was set at 1 hr (based on the specimen volume). The final step involved opening the beam gate to turn on the neutron beam.

X-ray diffraction, on the other hand, is a surface analysis technique (unlike neutron diffraction, which takes into consideration the entire volume of the specimen). Sample preparation requires a highly polished surface. In this study, the worn plates, which were mechanically polished prior to wear testing were analyzed. More precisely, x-ray scans were taken of the worn and unworn areas in order to assess any crystallographic differences before and after wear was introduced. It should be noted that x-ray analysis of the worn areas could have been influenced by the roughened surfaces (perhaps causing deviations in the Bragg angles). In order to assess the effect of mechanical polishing to the x-ray diffraction behaviour, some specimens were prepared using a Buehler Vibromet 2 polisher. After mechanically polishing the specimens using a 1.0 μm diamond suspension, the specimens were subjected to vibrational polishing in a colloidal SiO_2 solution for 2.0-4.0 h. Vibrational polishing is used to remove the deformed layer on the surface caused by mechanical polishing. The quantity of surface material removed is dependant on the polishing time. Due to the geometric restrictions of the Vibromet 2,

only the plate specimens were vibrationally polished. Once the specimens were ready for analysis, they were placed in the x-ray diffractometer and scanned for a period of 1.0 hr. The 2θ scan range for all the specimens was from 38°-101° at 0.1° intervals.

4.3.4. Mechanical testing

Sample preparation for the shear punch test involved cutting thin sections of approximately 500 μm in thickness. The thin sections were then ground using 600 grit silicon carbide paper to a final thickness of 250-300 μm. Both sides of the specimens were ground, so that both surfaces were reasonably parallel. For each test, a thin specimen was placed onto the center of the cylindrical die (covering the hole where the punch would be inserted) and it was then clamped into place. At the end of each test, the punched portion of each specimen was collected and its average thickness was measured using a standard micrometer.

The initial test setup involved configuring the data acquisition software system. In the TestStar software, a template procedure for room temperature compression was used and the desired input parameters were entered. The input parameters included: data acquisition time, punch speed, punch displacement, load detection limit and LVDT detection limit. The input parameters used for mechanical testing are shown in Table 4.2.

Table 4.2. Input values for shear punch tests

Input parameter	Amount
Data Acquisition Time (s)	0.20
Punch Speed (mm/min)	-0.50
Punch Displacement (mm)	-1.5
Approach Detection Limit (kN)	-0.030
Load Detection Limit (kN)	-98

The data acquisition time was the time at which each reading was taken from the LVDT and load cell sensors. The sensors would give a value for the displacement of the actuator and the applied load every 0.20 s. The punch speed was simply the speed at which the specimen was deformed and the compression displacement was the change in height of the specimen. The equivalent strain rate for this compression speed was 0.065/s. The punch displacement was -1.5 mm, greater than the thickness of the specimens in order to ensure complete penetration through the sample. The approach detection limit was used to pause the test as the actuator made initial contact with the specimen, thus allowing the displacement sensor to be set to zero. The load detection limit halted the test if the load in the MTS exceeded the specified limit (in this case, the specified limit was -98 kN). The load-extension data acquired from the shear punch test were converted into equivalent uniaxial tensile stress-strain values, using the following relationships for yield strength, ultimate tensile strength and strain:[95]

$$\sigma_{YS}=\frac{P-F_f}{C_{YS}2\pi rt} \tag{4.5}$$

$$\sigma_{UTS}=\frac{P-F_f}{C_{UTS}2\pi rt} \tag{4.6}$$

$$\varepsilon_e=\frac{D}{C_{EL}t} \tag{4.7}$$

where σ_{YS} is the yield strength, σ_{UTS} is the ultimate tensile strength, P is the load of the punch, F_f is the load due to friction, C_{YS} is the yield strength conversion factor, C_{UTS} is the ultimate tensile strength conversion factor, C_{EL} is the elongation to fracture conversion factor, r is the radius of the punch, t is the thickness of the specimen, ε_e is the engineering strain and D is the displacement of the punch.

The conversion factors (C_{YS}, C_{UTS}, C_{EL}) were obtained as a part of a calibration process in which materials of known tensile properties were subjected to shear punch testing. Then the effective stresses and strain from the shear punch tests were plotted as a

function of their tensile counterparts. The slopes were then determined and used as the conversion factors. Figure 4.9 illustrates this point.[95]

4.3.5. Wear testing

The hip joint is a tribological system having a ball-in-socket configuration. In order to determine the head and cup contact area, an equivalent area was calculated using classical Hertzian theory. In theory, the contact geometry of the hip joint could be simplified into a sphere-on-flat configuration resulting in a circular contact area.

This equivalent contact area could then be calculated using the following equation:

$$a = \left[\frac{3FR_{eff}}{2E'}\right]^{\frac{1}{3}} \tag{4.8}$$

where a is the radius of the circular contact area, F is the normal load, R_{eff} is the effective radius and E' is the effective modulus of elasticity of the materials.

The effective radius of the sphere could be found using equation 4.6:

$$R_{eff} = \frac{R_C R_H}{R_c - R_H} \tag{4.9}$$

where R_C is the radius of the acetabular cup and R_H is the radius of the femoral head.

In addition, E' was determined by:

$$\frac{1}{E'} = \frac{1}{2}\left[\frac{\left(1-\nu_1^2\right)}{E_1} + \frac{\left(1-\nu_2^2\right)}{E_2}\right] \tag{4.10}$$

where E_1 and E_2 are the moduli of elasticity of two contacting materials and ν_1 and ν_2 are the their respective Poisson's ratios.

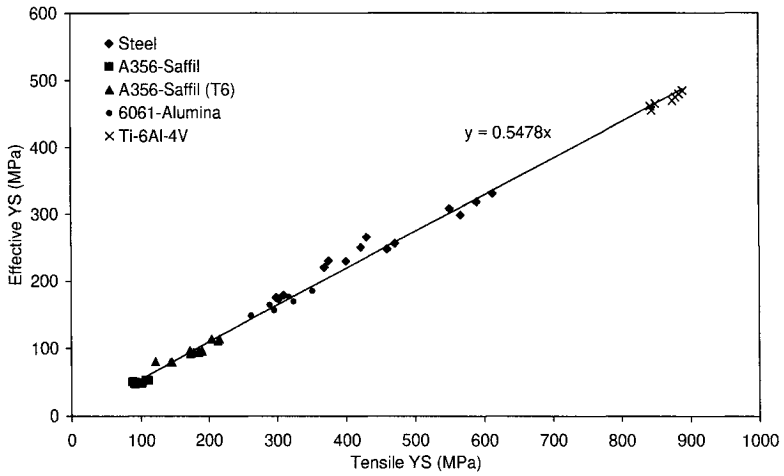

(a)

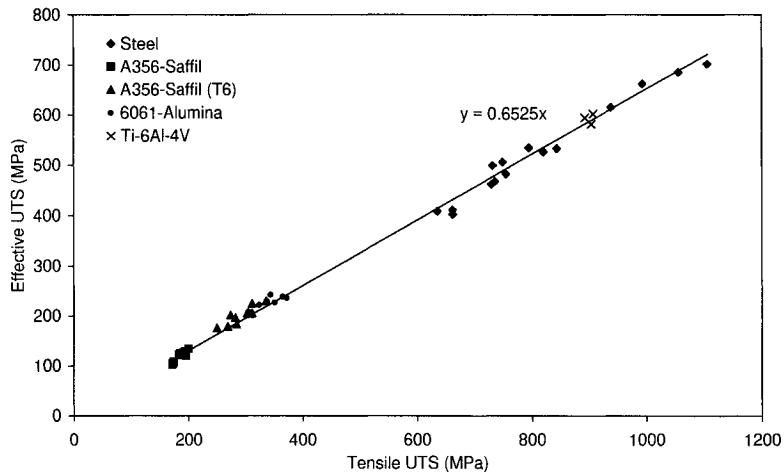

(b)

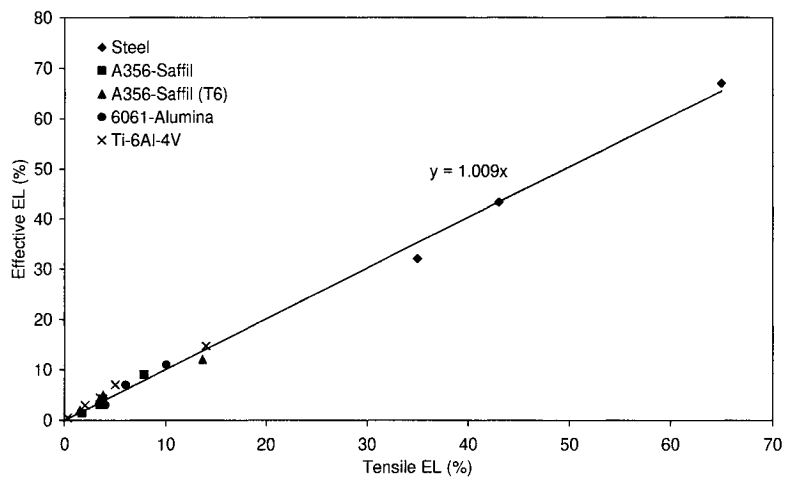

(c)

Figure 4.9. Calibration curves used for the determination of various shear punch conversion factors[95]

The above equations helped determine the appropriate spherical tip radius of the pin and the appropriate normal load in order to achieve similar contact stresses measured in the hip joint simulator. The advantage of using a spherical tip versus a flat-ended pin would the elimination of edge effects (Section 2.5.2) and effect of misalignment resulting in non-parallel surface contact.[72]

Cylindrical pins were machined from the various materials with 12 mm diameters and 100 mm spherical tip radii. The corresponding plates were machined of the same material (and microstructure) with 24 mm diameters and 13 mm thicknesses. After machining, the contact surfaces were ground using 600 grit emery paper and polished using 9.0 μm, 3.0 μm and 1.0 μm diamond suspension, manually. Each test pin was loaded to 9.8 N, resulting in a contact stress of 97 MPa, which was similar to the stresses applied in the hip simulator. The stroke length of the reciprocating baseplate was set to 11 mm and the average reciprocating velocity was set to 26 mm/s, which was also similar to the sliding velocity in the hip simulator.

The test lubricant used in these experiments was a 25 vol% bovine calf serum* in distilled water with the following additives: 0.95 % ethylenediaminetetraacetic acid† (EDTA), 0.24% Fungizone, 0.14% Streptomycin. *EDTA* is a chelating agent and is used as a film suppressant. It has been found that protein deposits (such as calcium phosphate films) may form on CoCrMo surfaces without the presence of EDTA.[96] These films may contribute to artificially low wear rates, not normally seen in vivo. Therefore, in order to better simulate sinovial fluid found in the human joint, EDTA is added to bovine serum. *Fungizone* is an anti-fungal agent and *Streptomycin* is an anti-bacterial agent used to preserve the quality of the serum, preventing degradation and maintaining its lubricating properties.

Bovine calf serum is commonly used as the lubricating medium in hip joint simulator testing and thus, it was also used in this study for comparative purposes with

* Bovine calf serum is the standard lubricant used in current THA studies and is used to simulate synovial fluid, which is found in the human hip joint cavity.
† EDTA has the chemical composition of $C_{10}H_{16}N_2O_8$.

respect to fundamental tribological behaviour. However, the lubrication regimes for the hip joint simulator and the pin-on-plate apparatus are not identical. A method of determining the lubrication regime is through the *lambda ratio* (λ).

Boundary lubrication occurs when the load is carried by asperity contacts through thin surface layers ($\lambda < 1$). In *Fluid film* lubrication, the load is carried by a film separating the surfaces, allowing for no asperity contact to occur ($\lambda > 3$). *Mixed film* lubrication lies in between boundary and fluid film lubrication ($1 < \lambda > 3$). In this regime, the load is carried by both asperity contacts and fluid film. In the case of hip joint simulators, the lambda ratio may range between 0.25 and 9.0, with varying amounts of fluid film action. The lambda ratio can be calculated through the following expression:[97]

$$\lambda = \frac{h_c}{\sqrt{\sigma_1^{\,2} + \sigma_2^{\,2}}} \tag{4.11}$$

where h_c is the central film thickness and σ_1 and σ_2 are the roughnesses of two contacting surfaces. The central film thickness can be calculated from the following equation modified by Medley *et al*:[61]

$$h_c = 5.083 \frac{(\eta u)^{0.660} R_{eff}^{\;\;0.767}}{(E')^{0.447} F^{0.213}} \tag{4.12}$$

where η is the lubricant viscosity and u is the entrainment speed.

In this study, the lambda ratio was determined by incorporating the following parameters: η = 0.0010 Pa·s, u = 13 mm/s, R_{eff} = 100 mm, E' = 252 GPa, F = 9.8 N, σ_1 = 7.4 nm and σ_2 = 19 nm. According to equation 4.12 the central film thickness (h_c) was 2.6 nm and using this value in equation 4.11 the lambda ratio (λ) was determined to be 0.13, which is < 1. Therefore, the predominant lubrication regime for the pin-on-plate testing used in this study was boundary lubrication. This is the desired regime since material interaction would be promoted and the influence of microstructure on wear could be determined.

The lubricant was replaced with fresh serum after every 24 h of testing or 0.10 Mc and the tests ran for a total of 1.0 Mc. The extent of wear was then quantified gravimetrically. After every 0.10 Mc of testing, the specimens were thoroughly washed in antibacterial soap, rinsed in alcohol and air dried. They were then weighed in a microbalance with a resolution of 0.10 mg. The microbalance was calibrated prior to each specimen through an internal calibration system. Subsequently, five weight measurements were taken per specimen and the balance was zeroed between each measurement. The volumetric wear was then calculated using the following equation:

$$V = \frac{m}{\rho} \tag{4.13}$$

where V is the volumetric wear loss, m is the mass loss and ρ is the theoretical density of Co.

In addition, the wear surfaces of the specimens were characterized using the SEM. The microscope operated at an accelerating voltage of 5 kV and a working distance of 15 mm in order to accentuate the topography of the surfaces and to permit qualitative chemical analysis of various surface features, respectively. Backscattered electron imaging was also used for qualitative chemical analysis. All the wear tests were done in triplicate for repeatability purposes and the average volumetric wear measurements were reported.

4.3.6. Surface profile measurements

Specimens of various heights and surface characteristics could be mounted on a rotating table and held in place with clay. The specimen chamber was closed in order to minimize dust formation on the surface and any background noise caused by circulating air in the room. The rotating table made it possible to align the wear scar in any desired orientation relative to the needle recorder.

The 2D profiles were set over a linear path length of 8.0 mm for both the pin and plate specimens. The data were collected over 4.0×10^3 points over the surface and all the

data were normalized in order to graphically plot the articulating surfaces parallel to one another. In the case of the 3D plots, the surface recorder scanned an area of the surface 2.0 mm x 2.0 mm in size. The scan time required for the 2D profiles was 60 s/specimen whereas the acquisition time for the 3D plots was 30 min/specimen.

CHAPTER 5

Results

Prior to wear testing, a first study was conducted on characterizing various CoCrMo alloys used in THA, including microstructure and mechanical properties, and the effect of heat treatment on these characteristics. This was followed by a second study, which focused on the wear behaviour of the materials.

5.1. Microstructures

5.1.1. As-received materials

Thermomechanical processing of these alloys during the manufacturing process produced a relatively fine grain structure (Figure 5.1). The average grain size for the LC alloy was approximately 3.1 μm. Due to the LC content of the alloy a strong electro-etch was required to reveal the grain boundaries. As a result, massive pitting also occurred as shown by the glowing areas in the SEM micrographs. These were most likely prior carbide precipitates which were removed by the etching process. These "holes" however, were not indicative of the size of the carbides. Several of the alloying elements in the wrought material (such as Co, Cr, Mo) have the tendency to form carbides in the presence of C. This was verified through energy dispersive spectroscopy. A typical scan

of a carbide precipitate can be seen in Figure 5.2. It should also be noted that annealing twins could be seen in the microstructure. Annealing twins are commonly found in metals with low SFE, such as Co.

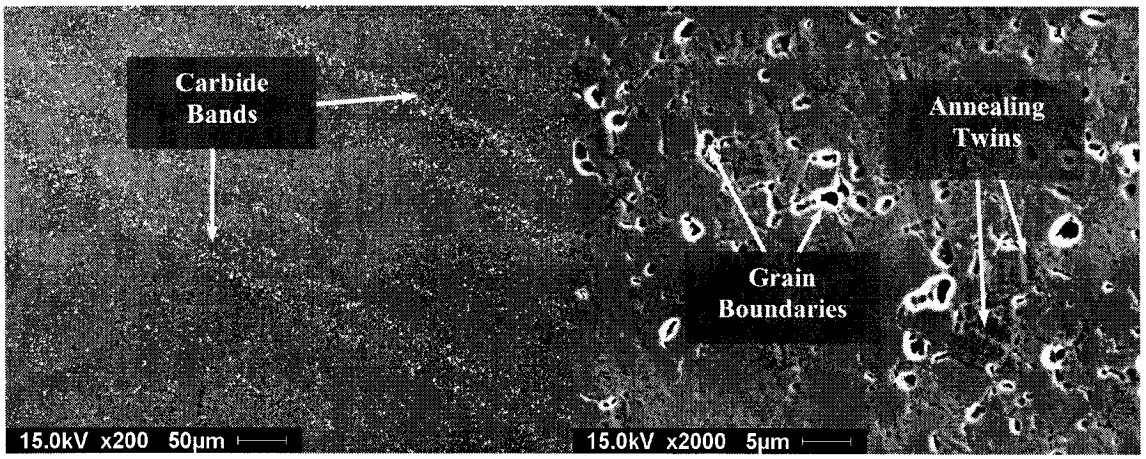

(a) (b)

Figure 5.1. Microstructures of F1537 LC alloy: (a) x200 and (b) x2000

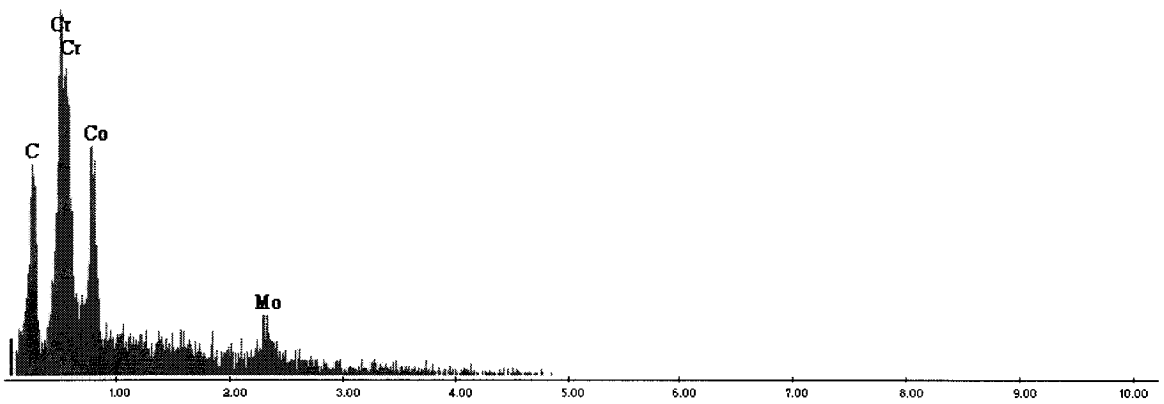

Figure 5.2. Chemical analysis of white or "glowing" areas in SEM micrographs

In order to determine the presence of intermetallic phases and to differentiate between different carbide types and to quantify them, stain-etching techniques were used (see Section 4.3.2). The stain-etching techniques described by Weeton and Signorelli[35]

verified that no TCP phases (such as σ phase) were present in any of the microstructures, but they also revealed the presence of different carbide types (as described in Section 2.1.3). The carbides appeared as discrete particles with a circular morphology (Figure 5.3). Their chemical compositions revealed the presence of Co, Cr and Mo, and they were distributed within the structure in the form of long "bands." The average carbide size was measured to be approximately 0.55 μm and the carbide volume fraction was 1.1 %.

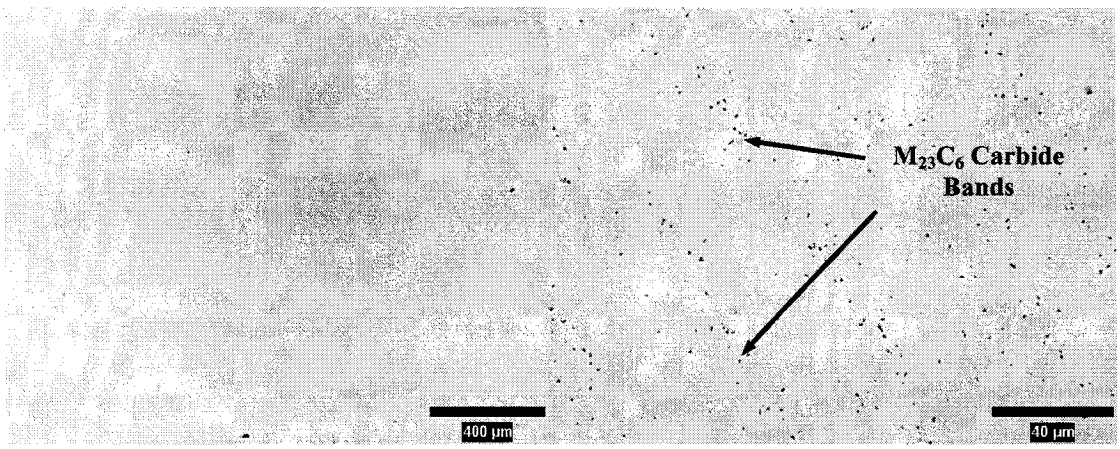

(a) (b)

Figure 5.3. Stain-etched micrograph of F1537 LC alloy: (a) x50 and (b) x500 magnification

According to the stain-etching method outlined by Weeton and Signorelli,[35] different carbide types should be discernable based on color differentiation. Pale yellow to light tan particles are considered to be M_7C_3 carbides, brown particles correspond to the $M_{23}C_6$ carbides and red, green or blue particles pertain to the M_6C carbides. This stain-etch method required a light electro-etch in order to bring out only the carbides and no other feature of the microstructure. As a result, only a few carbide particles were exposed in the LC alloy. The distinction between different carbide species can be seen more clearly in the F1537 HC alloy. At low magnification (Figure 5.3a) the carbides were difficult to resolve, but at higher magnification (Figure 5.3b) they were more clearly seen. In this micrograph, the yellow background was the Co matrix and the carbide particles were most likely the $M_{23}C_6$ carbides.

In the HC alloy, carbides were also observed and seemed to occur more profusely throughout the microstructure, as expected (Figure 5.4). At lower magnifications (Figure 5.4a) carbide bands were visible, but the band widths were greater than in the LC alloy. Despite electro-etching, the larger carbides remained in the microstructure and were clearly seen in Figure 5.4b. In addition, the grain boundaries were more evident and the measured grain size was 1.8 μm, almost half the size of the LC alloy. Although annealing twins were visible in the LC alloy, this was not the case for the HC alloy.

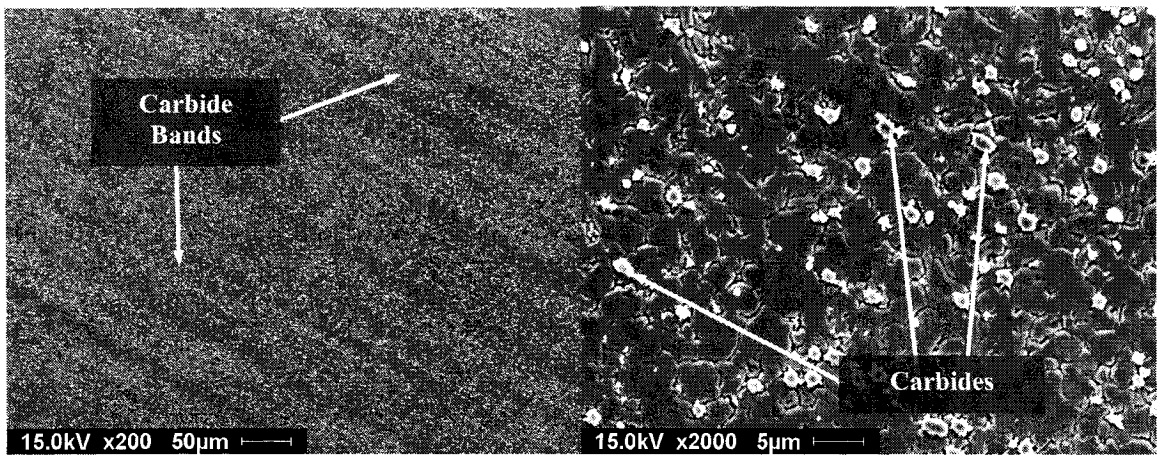

(a) (b)

Figure 5.4. Microstructures of F1537 HC alloy: (a) x200 and (b) x2000

The average measured carbide size was 1.1 μm and the carbide phase covered 4.8 % of the microstructure (Figure 5.5). This was almost 3 times that of the LC alloy. In this image, the carbides can be clearly identified as $M_{23}C_6$ (brown) and M_6C (red or green). The $M_{23}C_6$ carbides seem to occupy a wide range of sizes from very fine to very coarse, whereas the M_6C carbides are relatively fine.[98]

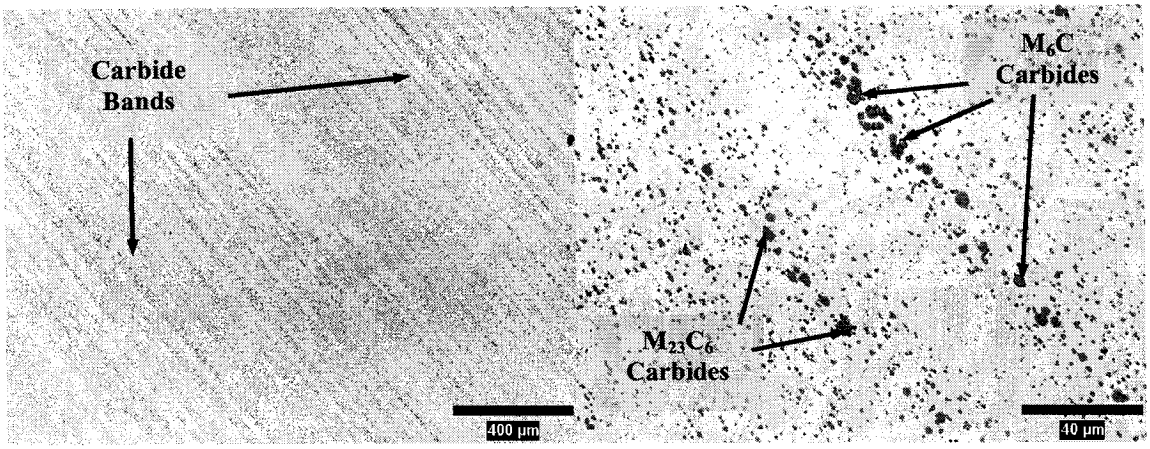

(a) (b)

Figure 5.5. Stain-etched micrograph of F1537 HC alloy under x1000 magnification

The F75 alloy (Figure 5.6) is the newer generation cast alloy currently being used in THA. This is essentially an as-cast alloy which has been subjected to a solution-anneal heat treatment and hot isostatic pressing in order to modify the structure and to remove most of the porosity inherent in casting processes, thus improving the overall mechanical properties of the alloy. Through metallographic analysis it was found that the F75 alloy contained large primary carbide colonies having a lamellar structure, surrounded by smaller secondary or "satellite" carbide precipitates.

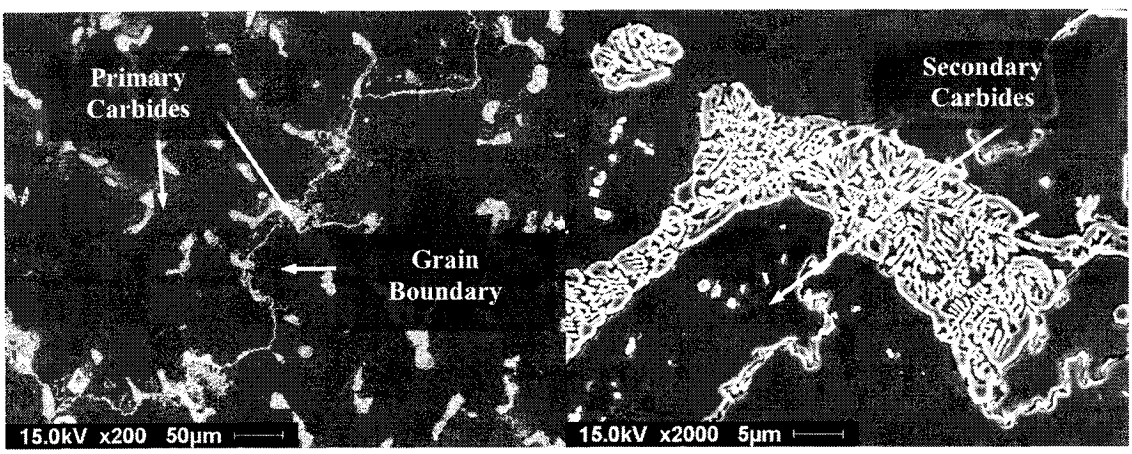

(a) (b)

Figure 5.6. Microstructures of F75 alloy: (a) x200 and (b) x2000

The grain structure was also very coarse with a grain size > 1000 μm. Stain-etching of the F75 alloy (Figure 5.7) identified the carbides as a mixture of $M_{23}C_6$-M_6C carbides for the coarse eutectic carbide islands (based on the reddish-brown appearance)[23] and fine $M_{23}C_6$ satellite carbides, shown in brown. The primary carbide colonies were acicular in morphology (26 μm long and 12 μm wide), whereas the satellite carbides appeared as fine discrete particles (0.31 μm). Through image analysis, the carbides fraction was measured and the carbides were found to comprise 5.3 % of the overall microstructure.

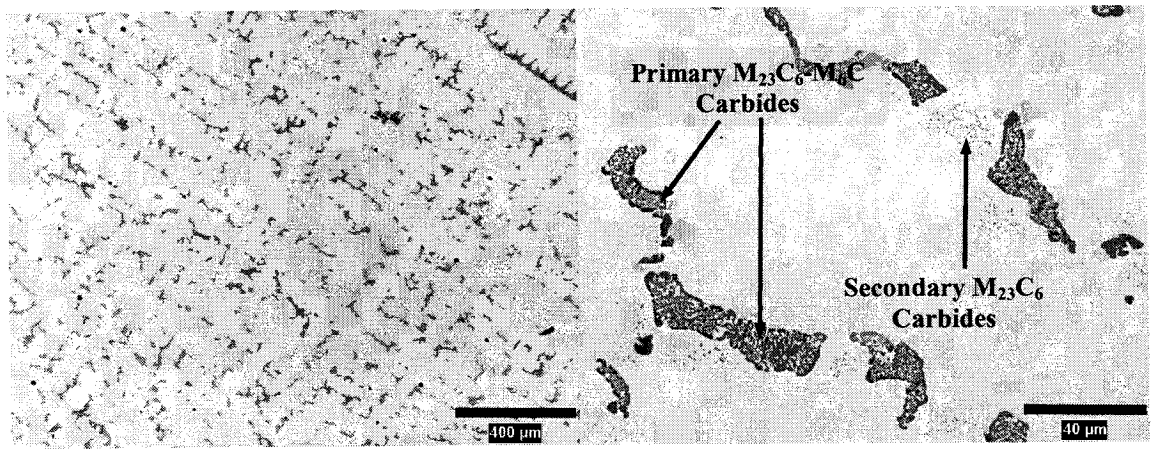

(a) (b)

Figure 5.7. Stain-etched micrograph of F75 alloy under x1000 magnification

The as-cast alloy (Figure 5.8) was used in the early generation hip implants. It had a very coarse microstructure (average grain size > 1000 μm) with a grain boundary carbide phase and interdendritic carbides. From stain-etching the samples, the carbides were found to have an acicular morphology (as in the case of the F75 alloy) with an average length of 14 μm and width of 7.7 μm and occupied 3.6 % of the microstructure.

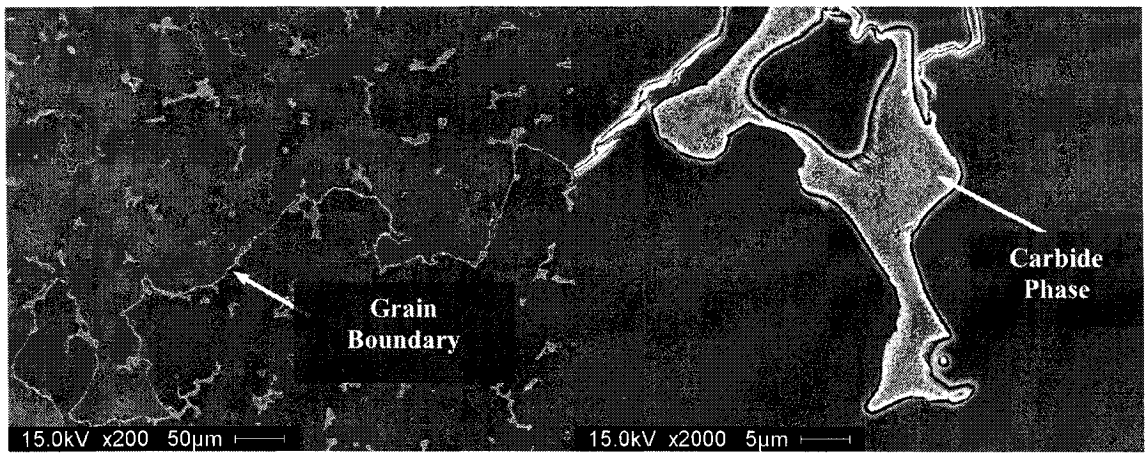

(a) (b)

Figure 5.8. Microstructures of as-cast alloy: (a) x200 and (b) x2000

There was also evidence of porosity throughout the material, an inherent feature of many casting processes and could be detrimental to the mechanical properties of the material. The porosity and inhomogeneous microstructure were believed to be the cause of many stem fractures in the earlier generation MM hip implants. Stain-etching the as-cast alloy helped to determine the carbide type as a mixture of $M_{23}C_6$-M_6C, as was found in the F75 alloy. The carbides were a eutectic phase which formed during investment casting (as in the manufacturing of orthopaedic devices), thus having a lamellar structure.[99] This was confirmed in Figure 5.9c, where a fine lamellar structure was seen under high magnification using the SEM.

5.1.2. Heat treated materials

5.1.2.1. Solution-annealed

The first heat treatment consisted of a solution-anneal at 1200°C for 24 h. Holding the specimens at 1200°C for 24 h successfully dissolved most of the precipitates and also coarsened the grain structure of the LC alloy (Figure 5.10). Due to the heat treatment, the grain size increased to 73 µm and the annealing twins were more evident, which helped to define the grain boundaries.

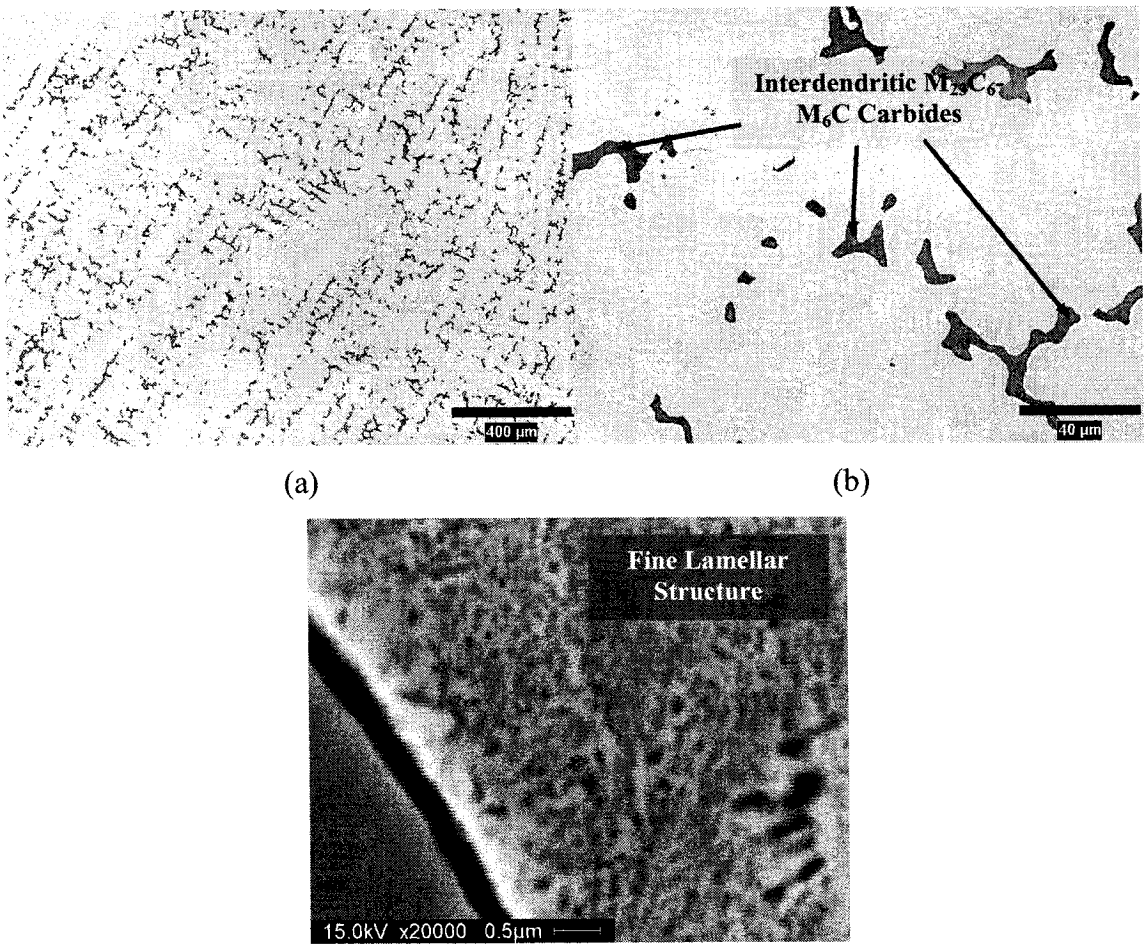

Figure 5.9. Micrographs of as-cast alloy: (a) stain-etched micrograph under x50 magnification, (b) stain-etched micrograph under x500 magnification and (c) high magnification (x20000) SEM micrograph

As a result of the solution-anneal of the LC alloy, the remaining carbides in the microstructure reduced in size to 0.65 µm and the carbide fraction was measured to be 0.13 %. Since the carbide volume fraction was quite low, it became more difficult to identify the carbides through stain-etching. However, it was possible to isolate a few carbides, as shown in Figure 5.11b. Although the material was heat treated for an extended period of time, the $M_{23}C_6$ carbides can still be found in the microstructure.

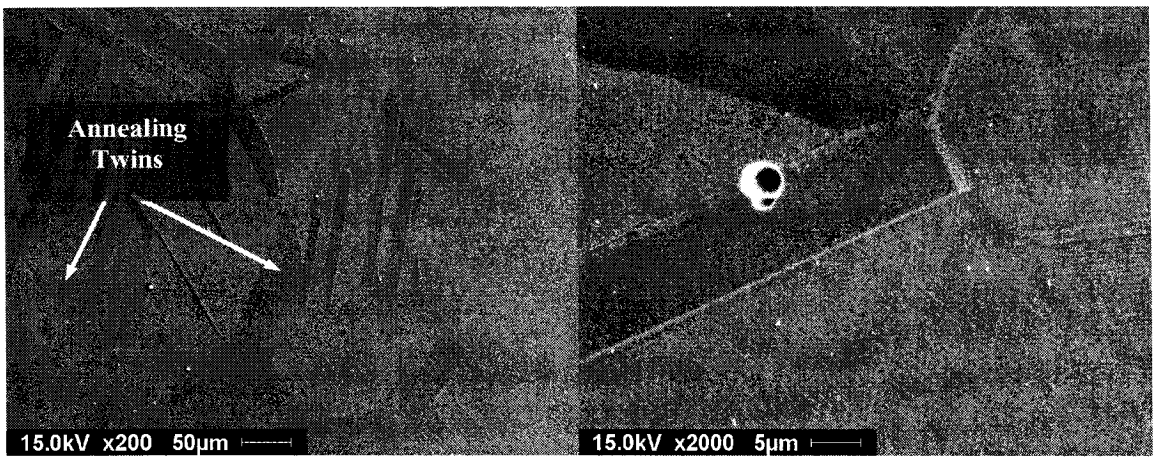

(a) (b)

Figure 5.10. Microstructures of F1537 LC alloy heat treated at 1200°C for 24 h, then water quenched: (a) x200 and (b) x2000

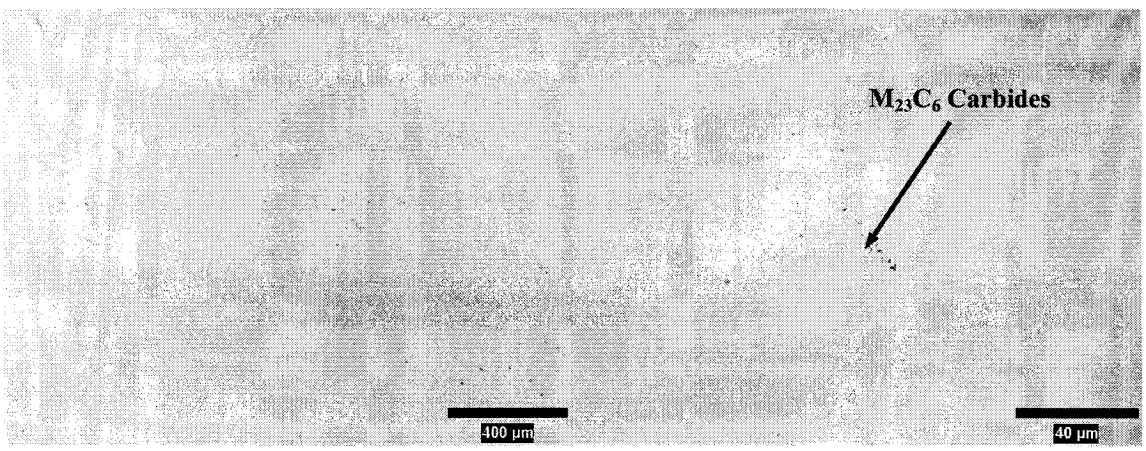

(a) (b)

Figure 5.11. Stain-etched micrograph of F1537 LC alloy solution-annealed at 1200°C for 24 h: (a) x50 and (b) x500 magnification

Similar to the LC alloy, the grain size of the HC alloy also increased as a result of the heat treatment to 60 µm and annealing twins were also more visible than in the as-received condition, but not as defined as in the LC alloy (Figure 5.12). In addition, there were remnants of the carbide bands as seen in the as-received microstructures. The carbide size was 1.5 µm and was greater than in the LC alloy, as was the carbide fraction

for the HC alloy (0.63 %). The higher fraction was expected since the treatment time was not sufficient for 100 % dissolution of all the precipitates in the microstructure (Figure 4.6). Nevertheless, the higher carbide fraction allowed for better identification of the carbides through stain-etching. Figure 5.13 confirmed the presence of only $M_{23}C_6$ carbides after heat treatment. The M_6C carbides (which were found in the as-received microstructures) were still identifiable, although the amount seemed to decrease.

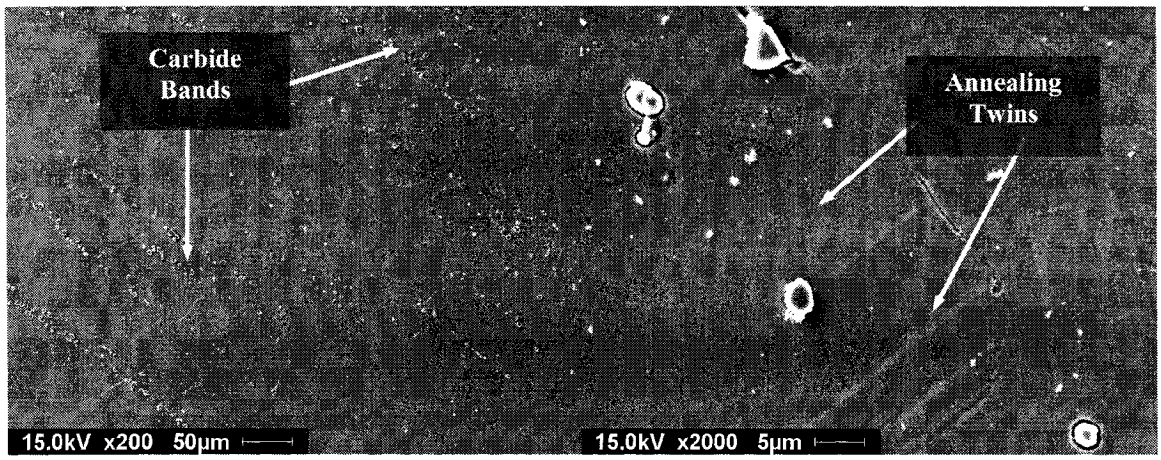

(a) (b)

Figure 5.12. Microstructures of F1537 HC alloy heat treated at 1200°C for 24 h, then water quenched: (a) x200 and (b) x2000

5.1.2.2. Solution-annealed and aged

Following the solutionizing treatment, the specimens were transferred directly to a furnace held at 650°C. The specimens were aged for 72 h below the transformation temperature, in the ε region of the Co phase diagram (Figure 4.7). The relatively low isothermal transformation temperature was used in order to discourage any further grain growth or precipitation of the carbide phase during transformation in order to assess the effect of crystal structure on wear. The solution-annealed and aged specimens (Figures 5.14-5.17) revealed a similar coarse microstructure to Figures 5.10 and 5.12. It is assumed that the solutionizing step had similar effects on the carbide phase, as previously mentioned.

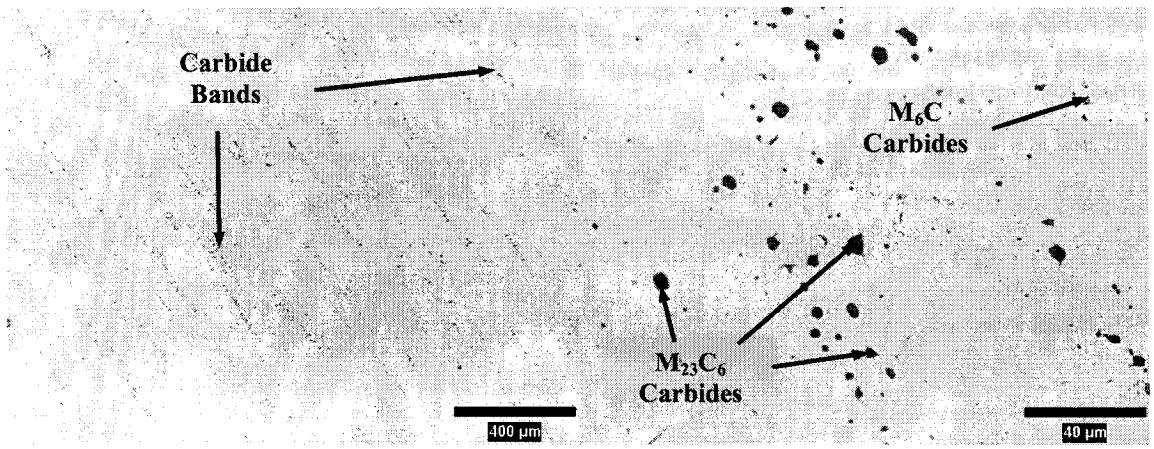

(a) (b)

Figure 5.13. Stain-etched micrograph of F1537 HC alloy solution-annealed at 1200°C for 24 h: (a) x50 and (b) x500 magnification

For the LC alloy (Figure 5.14), the overall heat treatment coarsened the structure resulting in an average grain size of 89 µm. However, one noticeable difference in the microstructure was the formation of a continuous carbide phase at the grain boundaries (when compared to the solution-annealed microstructure—Figures 5.10). There was also evidence of intragranular carbides and the annealing twins (which were very pronounced in the solution-annealed microstructure) were still present after aging. The stain-etching technique revealed that the continuous grain boundary phase and the intergranular carbides were both $M_{23}C_6$ carbides (Figure 5.15). The measured carbide size and fraction were 0.61 µm and 0.15 %, respectively.

The solution-annealed and aged HC microstructures are shown in Figure 5.16. Compared with the solution-anneal treatment, the additional aging process slightly coarsened the grain size to 68 µm. Extensive carbide precipitation can be seen at the grain boundaries and intergranularly (as shown by the pitting). In fact, the intergranular carbides are more prevalent in HC and than in the LC alloy (Figure 5.14). These intergranular carbides seem to be remnants of the carbide chains witnessed in the as-received structures (Figure 5.4). However, it should be noted that in the HC alloy (Figure 5.16b) there was evidence of carbide precipitation along twin boundaries. It was also found that a continuous carbide phase also formed at the grain boundaries, as in the LC

alloy (Figure 5.14). Stain-etching (shown in Figure 5.17) identified the grain boundary carbides as $M_{23}C_6$, as in the case of the LC alloy and the intergranular carbides were also identified as $M_{23}C_6$. The carbide size was 1.5 μm and the carbide fraction was 1.5 %.

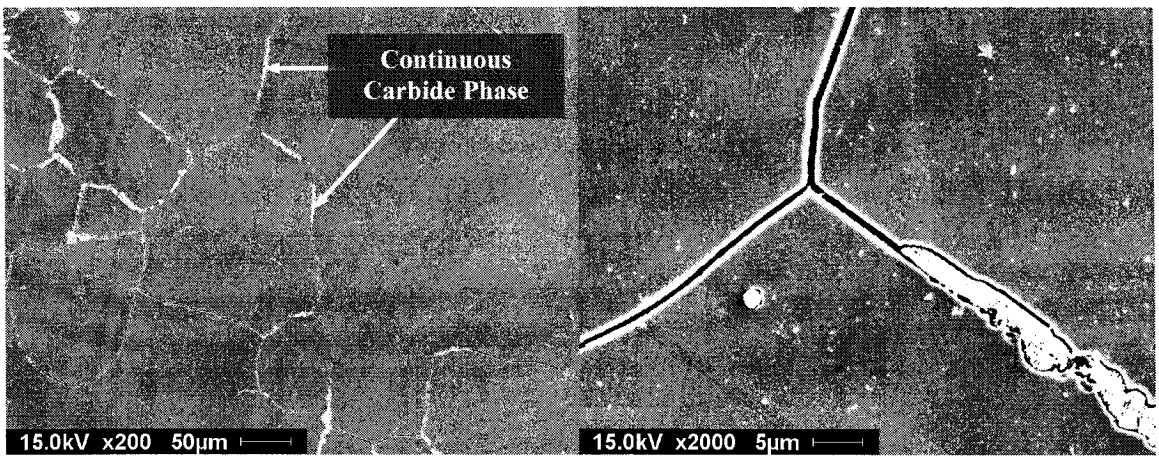

(a) (b)

Figure 5.14. Microstructures of F1537 LC alloy solution-annealed at 1200°C for 24 h and aged at 650°C for 72 h, then water quenched: (a) x200 and (b) x2000

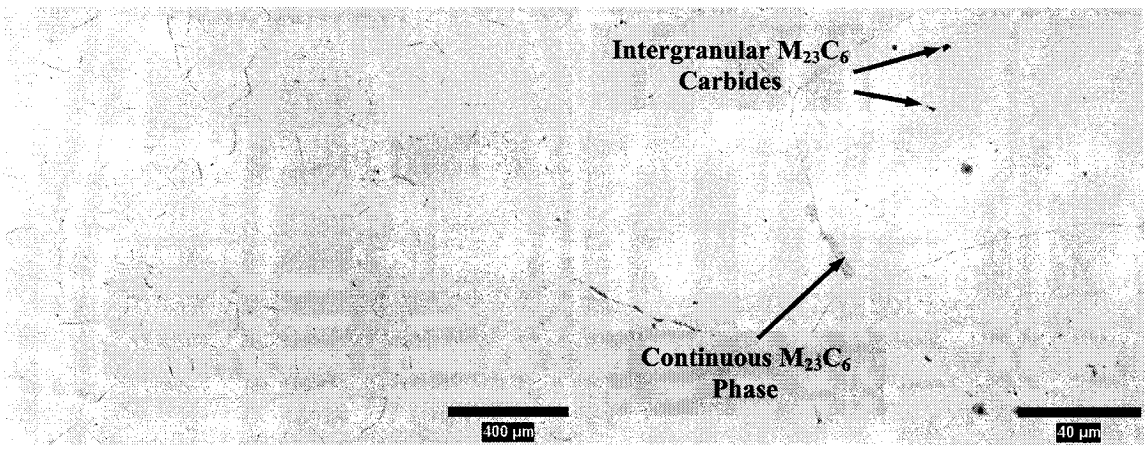

(a) (b)

Figure 5.15. Stain-etched micrograph of F1537 LC alloy solution-annealed at 1200°C for 24 h and aged at 650°C for 72 h

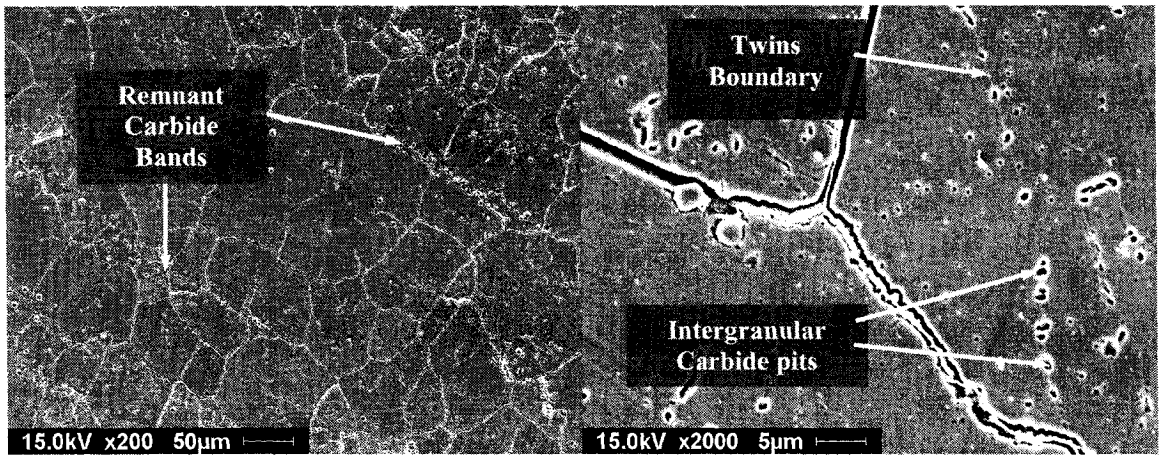

(a) (b)

Figure 5.16. Microstructures of F1537 HC alloy solution-annealed at 1200°C for 24 h and aged at 650°C for 72 h, then water quenched: (a) x200 and (b) x2000

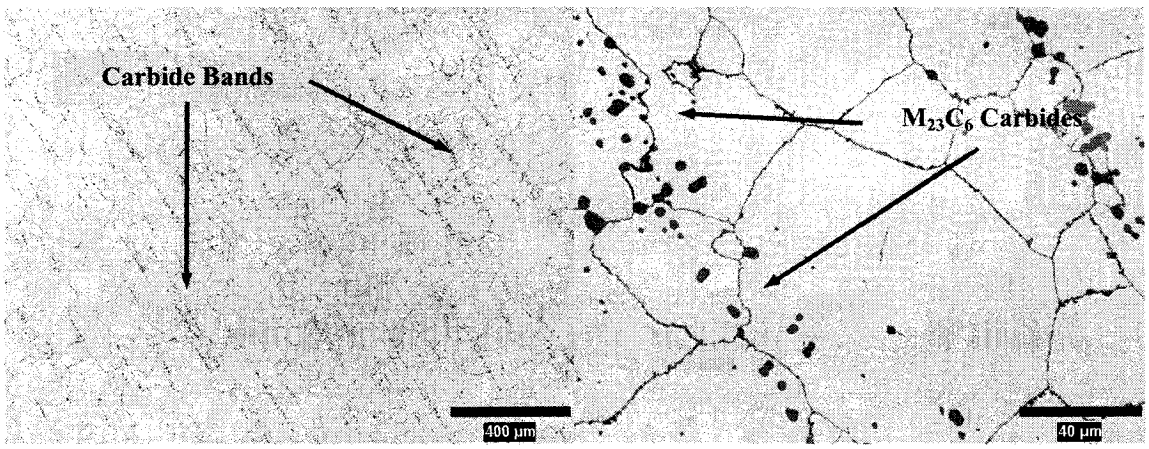

(a) (b)

Figure 5.17. Stain-etched micrograph of F1537 HC alloy solution-annealed at 1200°C for 24 h and aged at 650°C for 72 h: (a) x50 and (b) x500 magnification

5.1.2.3. Aged

The final set of microstructures involved a simple aging treatment at 650°C for 72 h, followed by a water quench (Figures 5.18-5.21). Despite the extended treatment time, the materials seemed to maintain a fine grain size (in comparison to the as-received microstructures—Figures 5.1 and 5.4).

Figure 5.18 shows the LC alloy and entire microstructure seemed to be engulfed in white, indicative of the carbide phase. This can be seen by the extensive charging effect of the non-conductive carbide phase in Figure 5.18b. Apart from the dramatic increase in grain boundary carbides, other microstructural features can still be seen—namely, intergranular carbides and annealing twins. The average carbide size was 0.58 μm and the total carbide phase constituted 1.2 % of the microstructure. Although the materials was aged for 72 h at 650°C, the grain size only increased slightly to 3.3 μm. Although the SEM micrographs revealed considerable carbide precipitation at the grain boundaries, they became difficult to resolve through stain-etching techniques. However, the stain-etched micrograph (Figure 5.19) seemed to reveal an $M_{23}C_6$ phase at the grain boundaries and M_6C intragranular carbides.

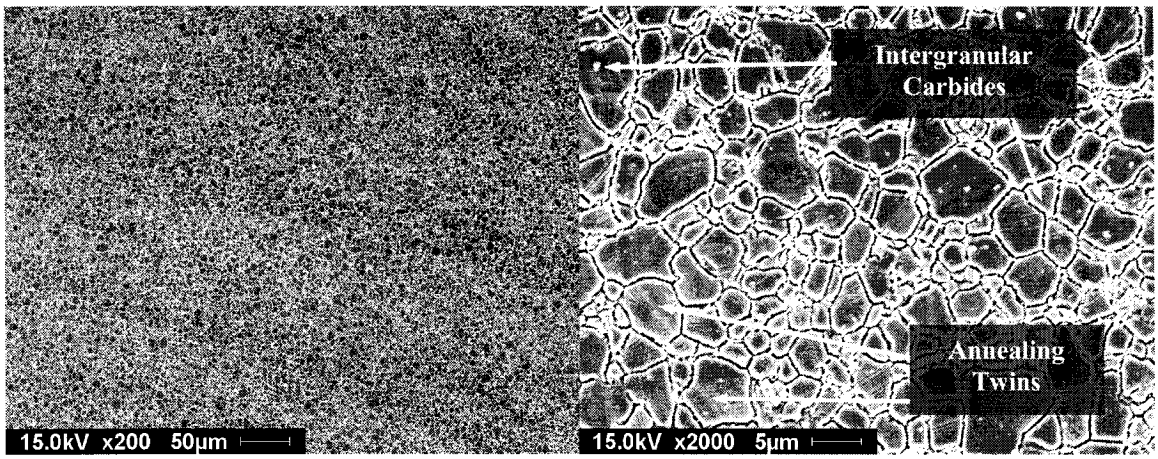

(a) (b)

Figure 5.18. Microstructures of F1537 LC alloy aged at 650°C for 72 h, then water quenched: (a) x200 and (b) x2000

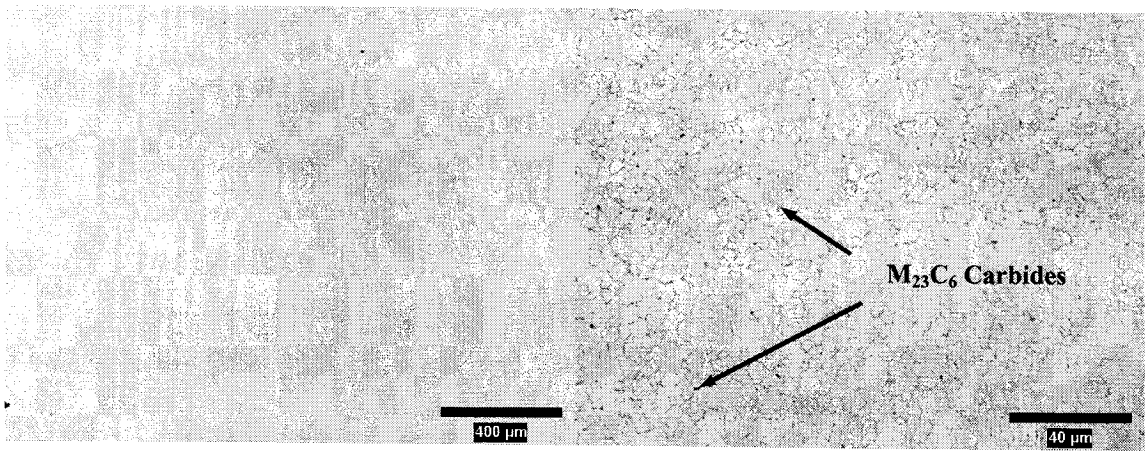

(a) (b)

Figure 5.19. Stain-etched micrograph F1537 LC alloy aged at 650°C for 72 h

In the case of the HC alloy aged at 650°C for 72 h, the measured grain size was 2.0 µm—only 0.2 µm greater than the as-received microstructure despite the extended heat treatment time (Figure 5.20). The carbide size was 1.1 µm and the carbide fraction increased to 5.1 %, compared to 4.6 % in the as-received condition. Although the carbide fractions increased considerably, there was still evidence of carbide bands, which could be seen at higher magnifications (see Figure 5.11b). These bands were remnants from the as-received state. However, this was not the case for the LC alloy in which the bands were no longer visible.

Similar to the LC alloy, stain-etching of the HC alloy revealed the presence of both $M_{23}C_6$- and M_6C-type carbides in the microstructure (Figure 5.21). Since these carbides are located along the bands, it is most likely that they are remnants from the as-received condition. A summary of all the microstructural features for the different alloys (with respect to composition and treatment condition) can be seen in Table 5.1 for comparative purposes.

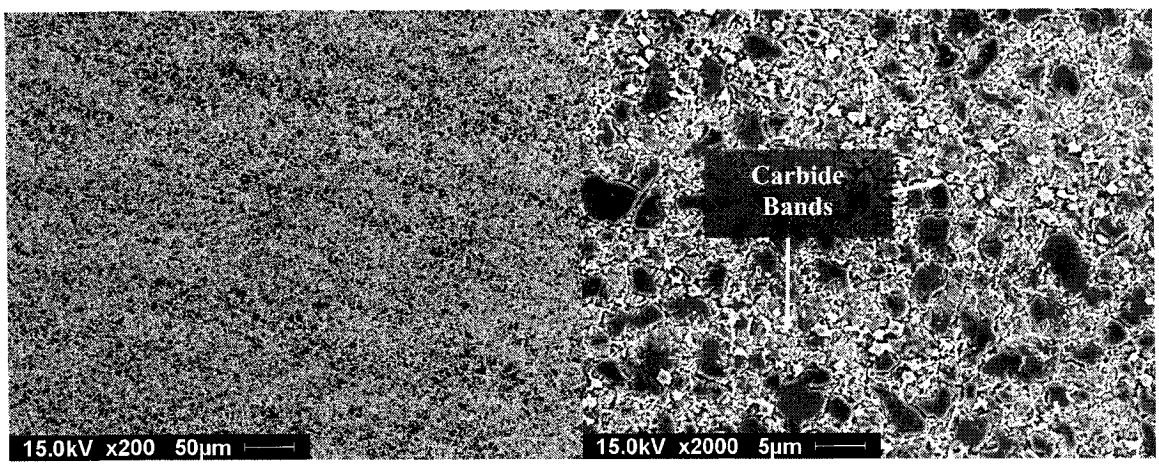

(a) (b)

Figure 5.20. Microstructures of F1537 HC alloy aged at 650°C for 72 h, then water quenched: (a) x200 and (b) x2000

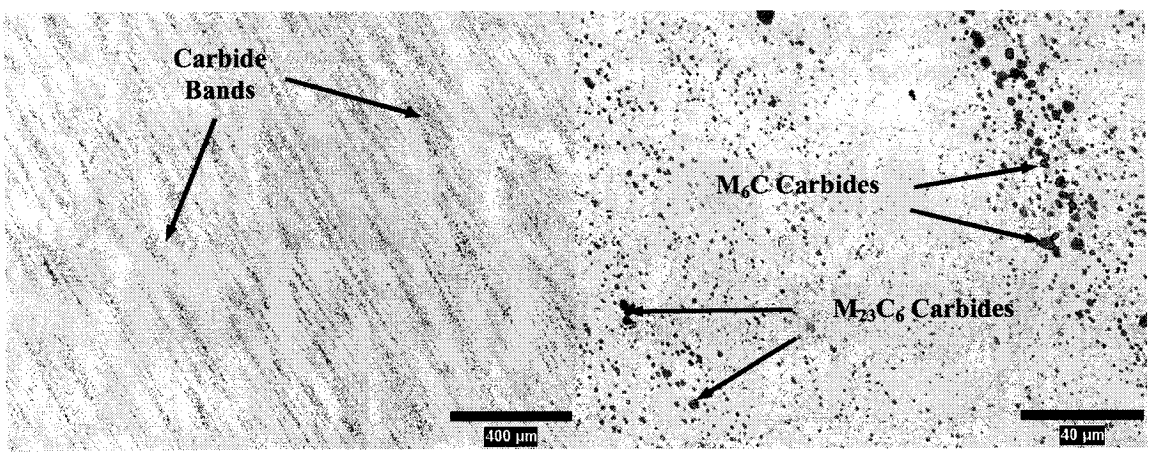

(a) (b)

Figure 5.21. Stain-etched micrograph of F1537 HC alloy aged at 650°C for 72 h: (a) x50 and (b) x500 magnification

Table 5.1. Summary of microstructural features

Alloy	Grain Size (μm)	Carbide Size (μm)	Carbide Fraction (%)
As-Received			
F1537 LC	3.1	0.55	1.1
F1537 HC	1.8	1.1	4.8
F75	>1000	Large: L=26, W=12; Small: 0.31	5.3
As-Cast	>1000	L=14, W=7.7	3.6
Solution-Annealed (1200°C, 24 h)			
F1537 LC	73	0.65	0.13
F1537 HC	60	1.5	0.63
Solution-Anneal and Aged (1200°C, 24 h + 650°C, 72 h)			
F1537 LC	89	0.61	0.15
F1537 HC	68	1.5	1.5
Aged (650°C, 72 h)			
F1537 LC	3.3	0.58	1.2
F1537 HC	2.0	1.1	5.1

5.2. Crystallography

Although metallographic analysis of the various alloys gave an idea of the basic microstructure of the materials (i.e. grain size, carbide size and carbide fraction) one important aspect, that could not be attained metallographically, was the crystal structure(s) of the material. Neutron diffractometry was used on each alloy to determine the bulk crystal structure(s) and the relative amounts of each crystal structure. As described previously in Chapter 4, the incident neutron beam was diffracted at characteristic angles for each crystallographic phase present in the alloys.

As was mentioned in Section 4.3.3, the specimens were mounted onto rotating stands in the neutron specimen chamber. This was done in order to minimize any texture effects, which would affect the quantitative analysis of the various phases present (i.e. FCC and HCP). If a specimen has a texture or a preferred crystal orientation, then the results from the diffraction analysis would be affected by the relative angle of the specimen to the incident beam. In x-ray diffraction, a specimen is cut and the surface of

the cut is polished and analyzed for its crystal structure. If the specimen has a texture, then different angular cross-sections of the sample may yield different results. Since neutrons penetrate the entire volume of the specimen and due to the rotating action of the specimen holders and the polycrystalline nature of the materials, any texture effects were for the most part removed.

5.2.1. As-received materials

Neutron scans were taken of the as-received materials and the results are shown in Figure 5.22. The intensity of the diffracted beam (in counts) was plotted versus the diffraction angle (2θ). The wavelength of the incident beam used in this study was 0.1329 nm and it should be noted that the position of these peaks will vary with wavelength of the incident neutron beam. From Figure 5.22, it can be ascertained that the crystal structure of the as-received materials was almost entirely FCC. This is based on the fact that no HCP peaks are visible at the 2θ angles specified in Table 5.2.

At certain angles, there is an overlapping of FCC and HCP peaks, making it difficult to calculate the volume fraction of each phase separately. As a result, the data were analyzed using the GSAS software package, which fits all the peaks at once and calculates the relative volume fraction of each phase and the new unit cell lattice parameter for each phase. Neutron diffraction data of the as-received materials which were fitted using the GSAS program can be seen in Figure 5.23.

The measured data points are shown as red "+" symbols and the fitted curve is represented by the green line. By inputting all the necessary information about the materials into the program (such as FCC-Co and HCP-Co space groups, unit cell composition(s), diffractometer constants, absorption coefficients, etc) an iterative least squares curve fit was performed. As can be seen in Figure 5.23, the fitted curves agree quite closely with the measured data.

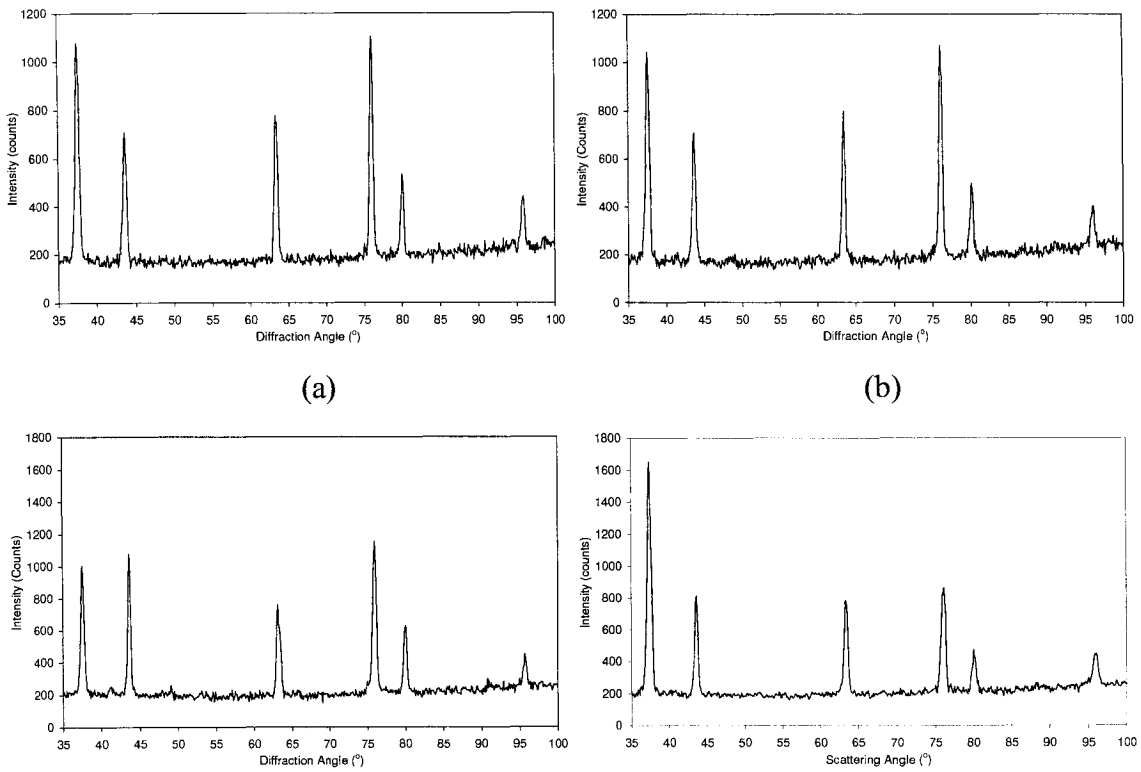

Figure 5.22 Neutron diffraction of the as-received materials: (a) F1537 LC, (b) F1537 HC, (c) F75 and (d) as-cast

Table 5.2. Overlapping FCC and HCP diffraction peaks in pure Co (λ = 0.1329 nm)

FCC		HCP	
Peak (hkl)	Angle (2θ)	Peak ($a_1a_2a_3c$)	Angle (2θ)
111	37.5°	0002	37.9°
220	63.3°	$10\bar{1}3$	63.4°
311	76.1°	0004	76.2°

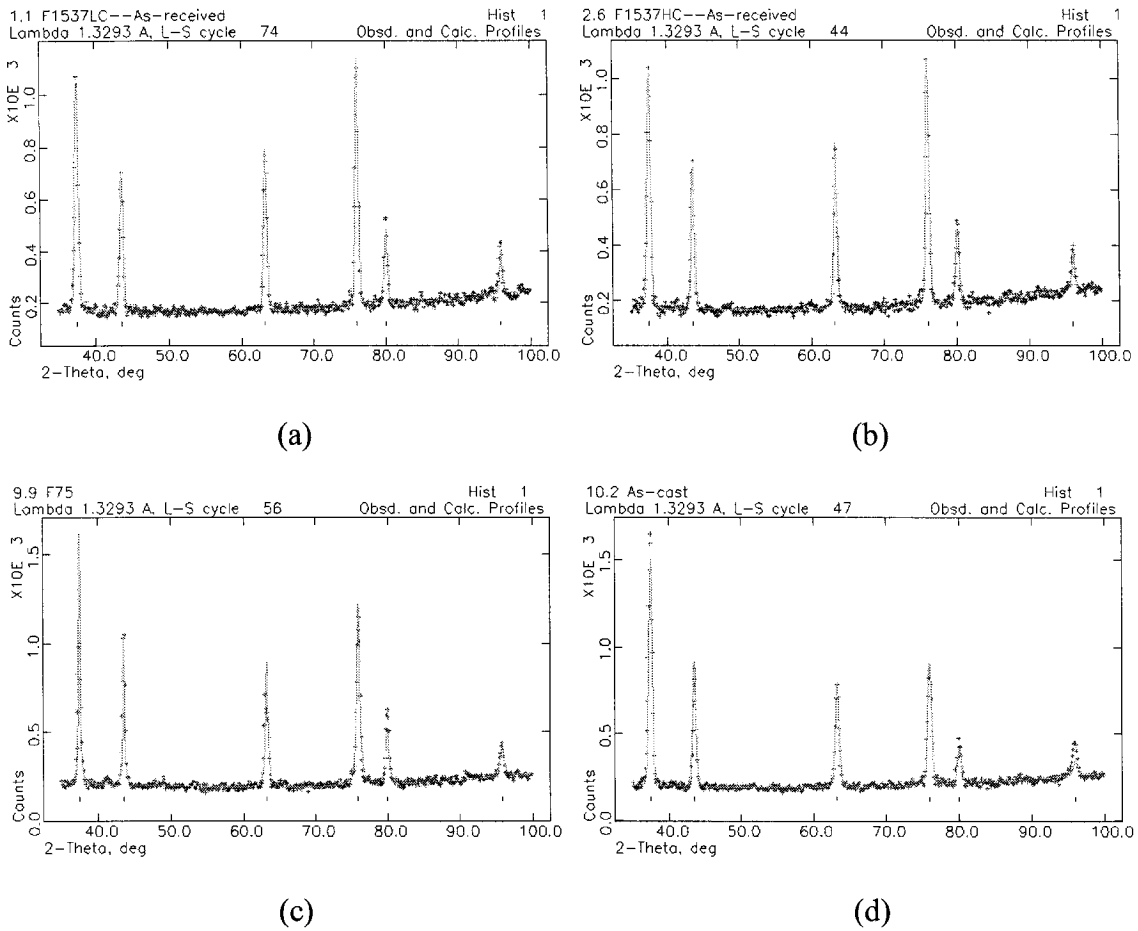

Figure 5.23. GSAS modeled neutron diffraction of as-received materials: (a) F1537 LC, (b) F1537 HC, (c) F75 and (d) as-cast

Through the GSAS program it was verified that there was no detectable bulk HCP phase in any of the as-received materials. It was also verified by the GSAS program that there was an increase in the FCC-Co lattice parameter "a_{hkl}" with respect to pure FCC-Co, as expected. The lattice parameter for pure FCC-Co is 0.3537 nm, whereas the average lattice parameter for the CoCrMo alloys used in this study was 0.3574 nm.

5.2.2. Heat treated materials

5.2.2.1. Solution-annealed

The neutron diffraction data for the materials solution-annealed at 1200°C for 24 h are shown in Figures 5.24 and 5.25. The purpose of this heat treatment was to homogenize the microstructure in the single-phase α-Co region of the CoCrMo ternary system, producing a bulk FCC solid-solution (see Section 4.3).

From the neutron diffraction data, it can be seen that the bulk crystal structure after heat treatment was FCC. In addition, the measured data which were modeled using the GSAS software confirmed that there was no detectable amount of HCP phase in the structure (as was intended by the heat treatment).

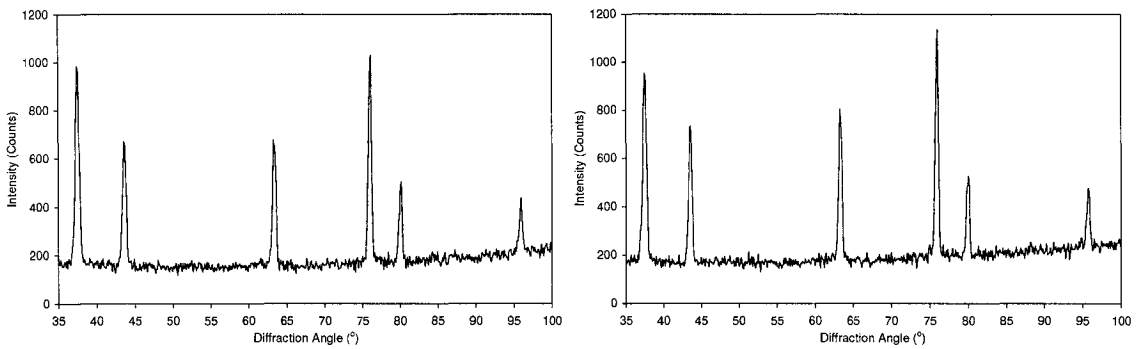

Figure 5.24. Neutron diffraction of F1537 alloys solution-annealed at 1200°C for 24 h: (a) LC and (b) HC

5.2.2.2. Solution-annealed and aged

Neutron diffraction of the materials solution-annealed at 1200°C for 24 h and aged at 650°C for 72 h can be seen in Figures 5.26 and 5.27. The purpose of the first heat treatment was to produce a single phase microstructure through the dissolution of carbides in the Co matrix. The second heat treatment was conducted in order to transform the FCC-Co solid-solution to a single phase HCP-Co structure. In this way, the effect of crystal structure on wear may be ascertained.

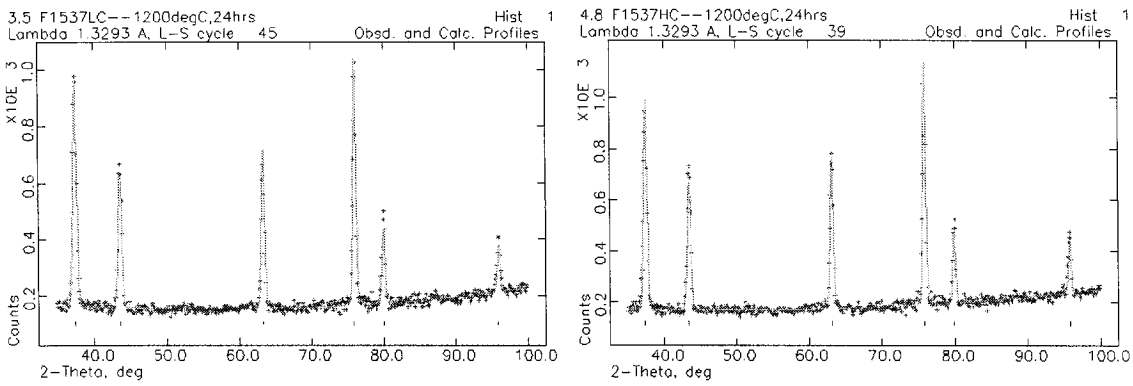

(a) (b)

Figure 5.25 GSAS modeled neutron diffraction of F1537 alloys solution-annealed at 1200°C for 24 h: (a) LC and (b) HC

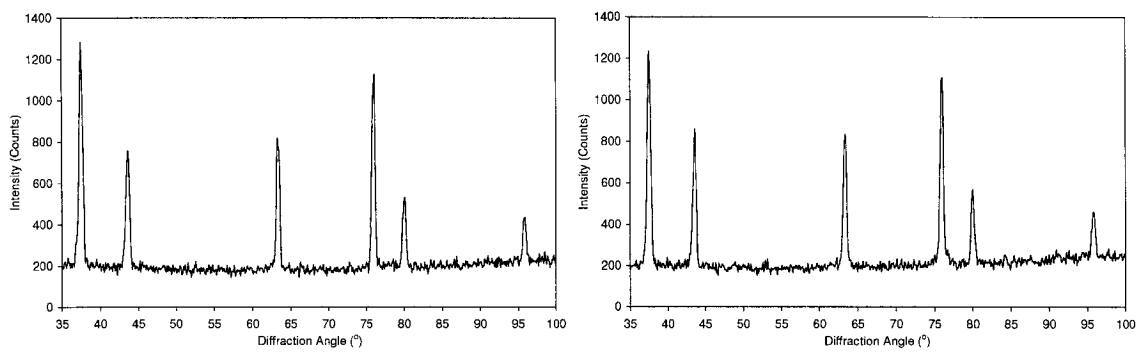

(a) (b)

Figure 5.26 Neutron diffraction of F1537 alloys solution-annealed at 1200°C for 24 h and aged at 650°C for 72 h: (a) LC and (b) HC

However, as can be seen in Figure 5.26, the temperature or time of heat treatment was insufficient to transform the bulk crystal structure to HCP. In fact, it was verified through GSAS (Figure 5.27) that the bulk crystal structure was FCC-Co. The transformation temperature for these CoCrMo alloys was estimated at ~ 820°C. Although at this temperature the crystal structure was successfully transformed from FCC to HCP, considerable precipitation also occurred (Figures 5.28 and 5.29). Therefore, a lower transformation temperature would be required in order to minimize the kinetics of

precipitation of carbides in the microstructure. According to the work conducted by Weeton and Signorelli,[35] a 650°C transformation temperature was used and resulted in little precipitation of secondary phases after solution-treatment. Nevertheless, the aging heat treatment at 650°C was not successful in transforming the FCC matrix to HCP after the solution-anneal treatment.

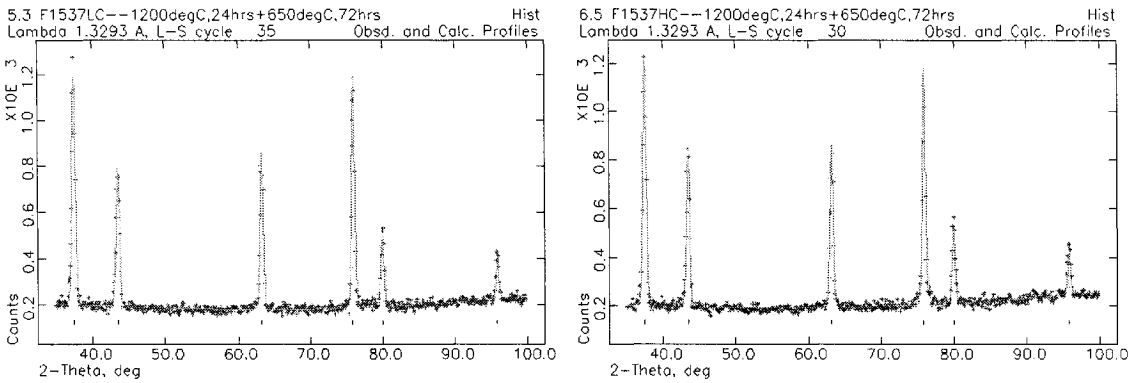

(a) (b)

Figure 5.27. GSAS modeled neutron diffraction of F1537 alloys solution-annealed at 1200°C for 24 h and aged at 650°C for 72 h: (a) LC and (b) HC

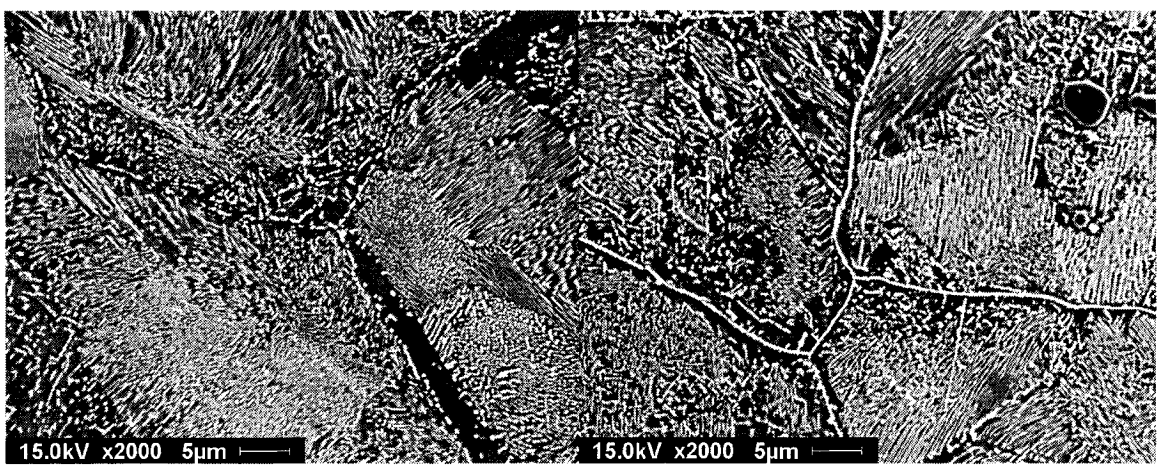

(a) (b)

Figure 5.28. SEM micrographs of F1537 alloys solution-annealed at 1200°C for 24 h and aged at 820°C for 72 h showing considerable precipitation at the grain boundaries and intragranularly: (a) LC and (b) HC

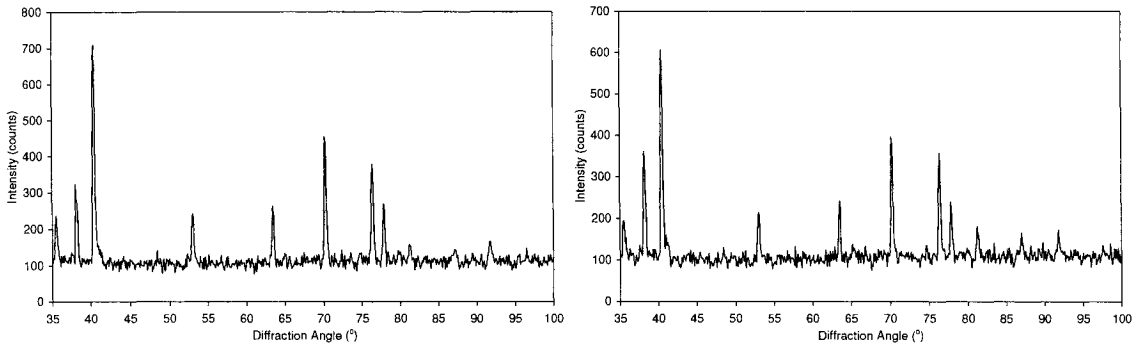

(a) (b)

Figure 5.29. Neutron diffraction of F1537 alloys solution-annealed at 1200°C for 24 h and aged at 820°C for 72 h revealing a bulk HCP structure: (a) LC and (b) HC

5.2.2.3. Aged

The aging treatment was done in order to achieve a fine grained HCP microstructure. The neutron diffraction data for the specimens aged at 650°C for 72 h are shown in Figure 5.30. In this case, the F1537 alloys were placed directly in a furnace at 650°C without any prior solution-anneal step. As can be seen in Figure 5.30, the aging treatment was successful in transforming the bulk FCC structure to a predominantly HCP structure.

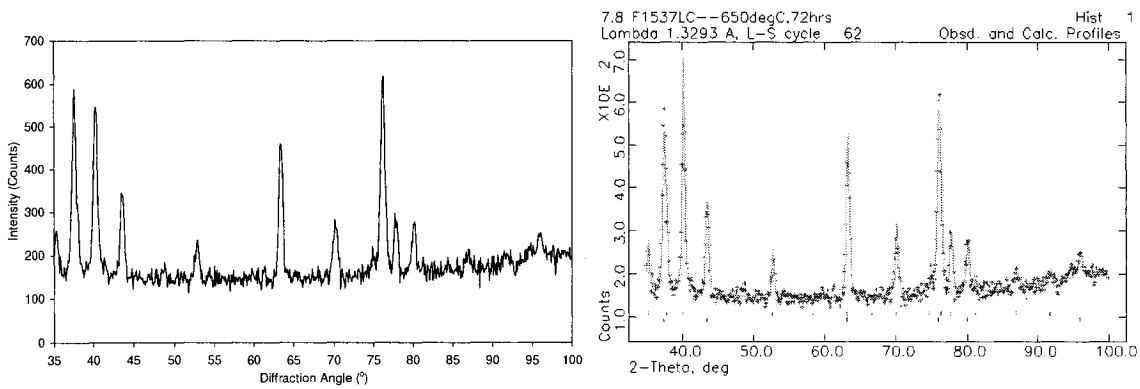

(a) (b)

Figure 5.30. Neutron diffraction of F1537 LC alloy aged at 650°C for 72 h: (a) measured data and (b) GSAS output file of measured data

In fact, it was determined through the GSAS software that the aging heat treatment produced a dual matrix structure composed of 16 vol% FCC and 84 vol% HCP. (Note: Only neutron diffraction data for the LC alloy is available. However, x-ray analysis of the HC alloy revealed a predominantly HCP structure, similar to the LC alloy—Figure 5.31.)

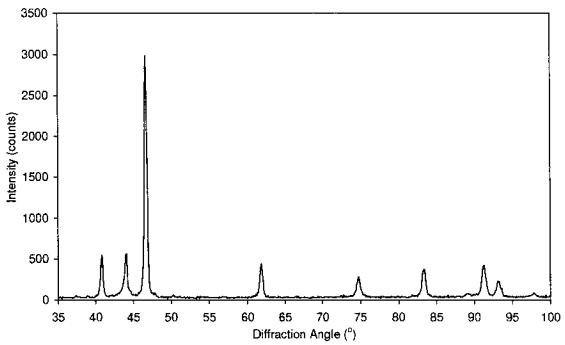

Figure 5.31. X-ray diffraction of F1537 HC alloy aged at 650°C for 72 h

5.3. Mechanical properties

Determination of the mechanical properties of the material was achieved through shear punch testing. Specimens were cut into thin 300 μm sections and the size of the cross-sections allowed for 3 punches to be performed per slice. From the punch tests, load-displacement curves were acquired and the data were then converted into tensile stresses and strains, using the appropriate conversion factors as described in Section 4.3.4. From the stress-strain curves, the yield strength (YS), ultimate tensile strength (UTS) and elongation to fracture (EL) were determined. The shear punch test is particularly attractive due to the small average specimen volume subjected to deformation (therefore high sensitivity to microstructure) and the nature and ease of analysis of raw data and properties. It should be noted that the shear punch test is not recommended by ASTM as standard test for Co alloys. It is true that there are slight variations between different test methods, however, the shear punch test has been shown to produce quite accurate tensile values in other areas of study.[95]

5.3.1 As-received materials

The strength results obtained for the as-received specimens are shown in Figure 5.32. It was found that with increasing C content the YS increased (in the case of the F1537 alloys) and there was a slight increase in the UTS. It was also observed that the LC alloy experienced relatively large amounts of work hardening compared to the HC alloy, indicated by the difference between the YS and UTS.

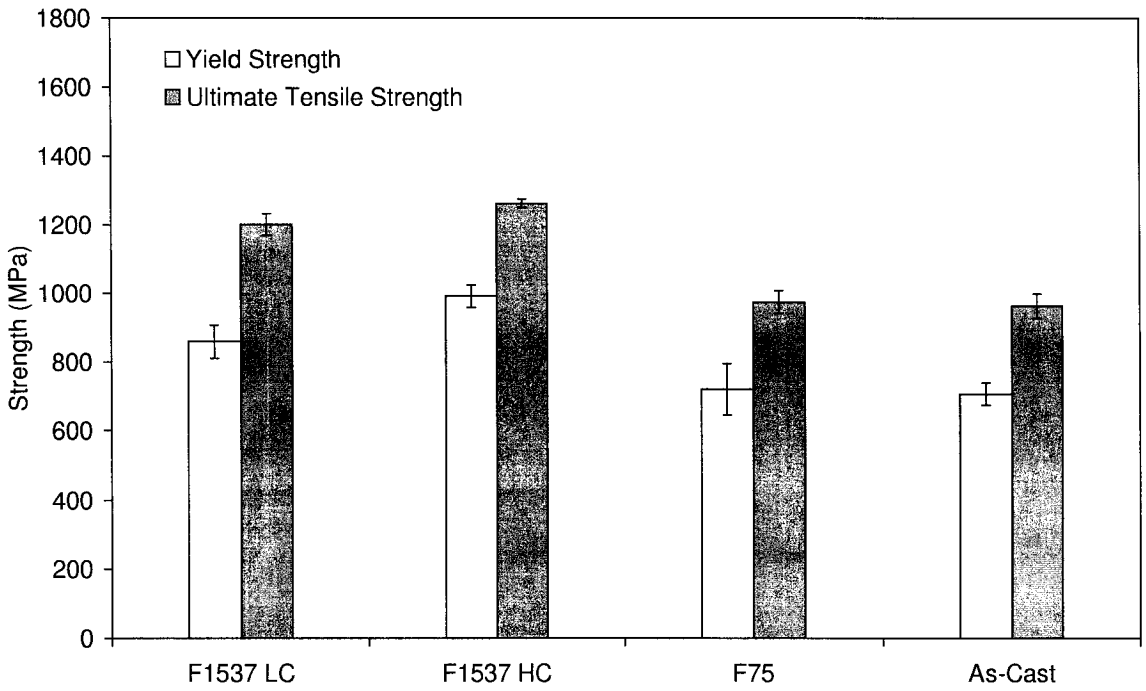

Figure 5.32. Strength properties for as-received specimens

As previously mentioned, the use of the as-cast alloy in MM hip implants was terminated due apparently to its undesirable mechanical properties. As a response to this, the as-cast alloy was subjected to a solution-anneal process in order to enhance the mechanical properties of the material. This post-treatment of the as-cast alloy according to ASTM specifications generates the F75 alloy. However, from Figures 5.32 and 5.33 it can be seen that the post-treatment process of the as-cast alloy did not produce any

significant improvement in the mechanical properties of the F75 material. Nevertheless, when compared to the ASTM specifications, the as-received materials meet all the strength requirements, as shown in Table 5.3.

Table 5.3. ASTM minimal mechanical requirements for as-received alloys

Alloy	Condition	Yield Strength (MPa)	Ultimate Tensile Strength (MPa)	Elongation (%)
F1537	Annealed	520	900	20
	Warm Worked	830	1170	12
F75	As-Cast	450	650	8.0

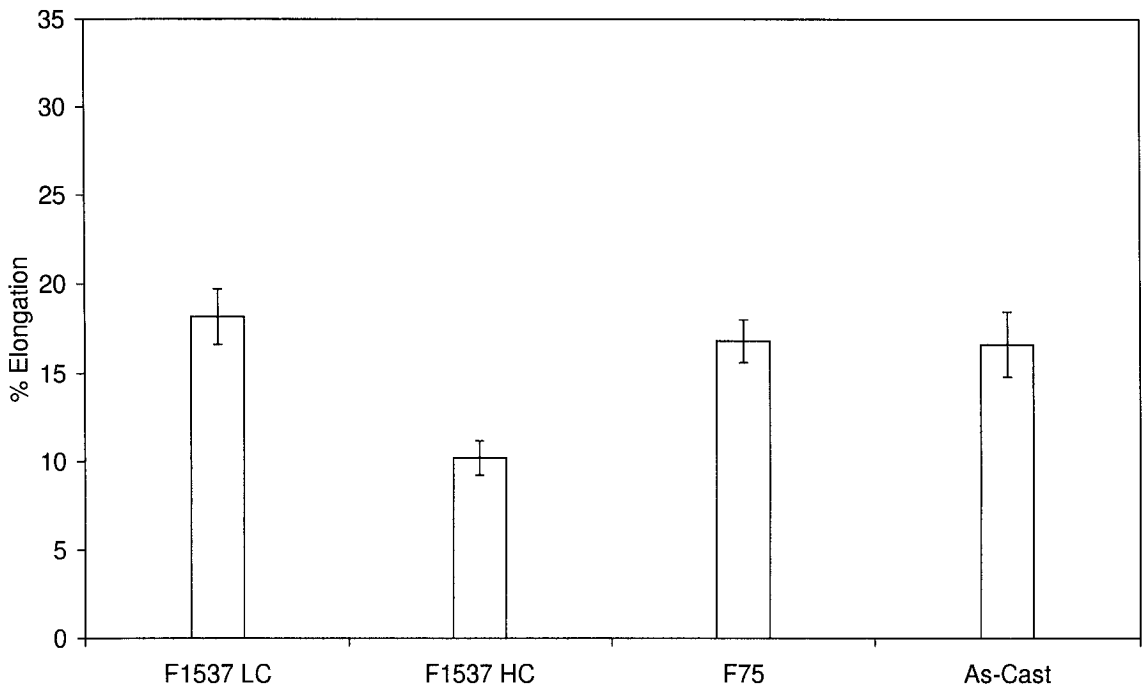

Figure 5.33. Elongation to fracture measurements of as-received specimens

The results for the EL are shown in Figure 5.33. The EL's for cobalt-based alloys were quite low when compared to other more ductile biomaterials such as polyethylene or Ti6Al4V. The EL for the wrought HC F1537 alloy was unexpectedly low. In addition, the EL's for the cast alloys were unexpectedly high, even 1.5 times higher than the HC alloy. In general, the ductility values obtained for the as-received alloys met the ASTM requirements, except for the HC alloy which had an EL below 12 %. The other three materials tested were well above their respective ASTM specifications.

5.3.2. Heat treated materials

The results from the punch tests for the LC and HC heat treated specimens are shown in Figures 5.34 and 5.35. As previously mentioned, all heat treatments were conducted on the as-received F1537 alloys since these are the most commonly used CoCrMo alloys in THA. The heat treatments were conducted in order to alter the microstructure of the as-received F1537 alloys and, in doing so, alter their mechanical properties.

The solution-anneal treatment, which involved a holding temperature of 1200°C for a period of 24 h, lowered the YS of both the LC and HC alloys below 700 MPa (which was less than the 830 MPa minimum of the ASTM specification as shown in Table 5.3). The UTS's also decreased to 1130 MPa, but they were within the ASTM specifications for the annealed condition. Despite their difference in C content, the LC and HC alloy possessed similar strength values after solution-annealing.

For the specimens which were solution-annealed and aged, the aging step taken at 650°C for 72 h promoted some carbide precipitation (as seen in Figures 5.15 and 5.17). However the strength properties for the LC alloy seemed lower than the solution-annealed specimens, although, the scatter was greater as can be seen by the error bars in Figure 5.34. On the other hand, the aging step seemed to produce a marked increase in the strength properties for the HC alloy. Both alloys met all the ASTM strength requirements for the annealed condition (Table 5.3).

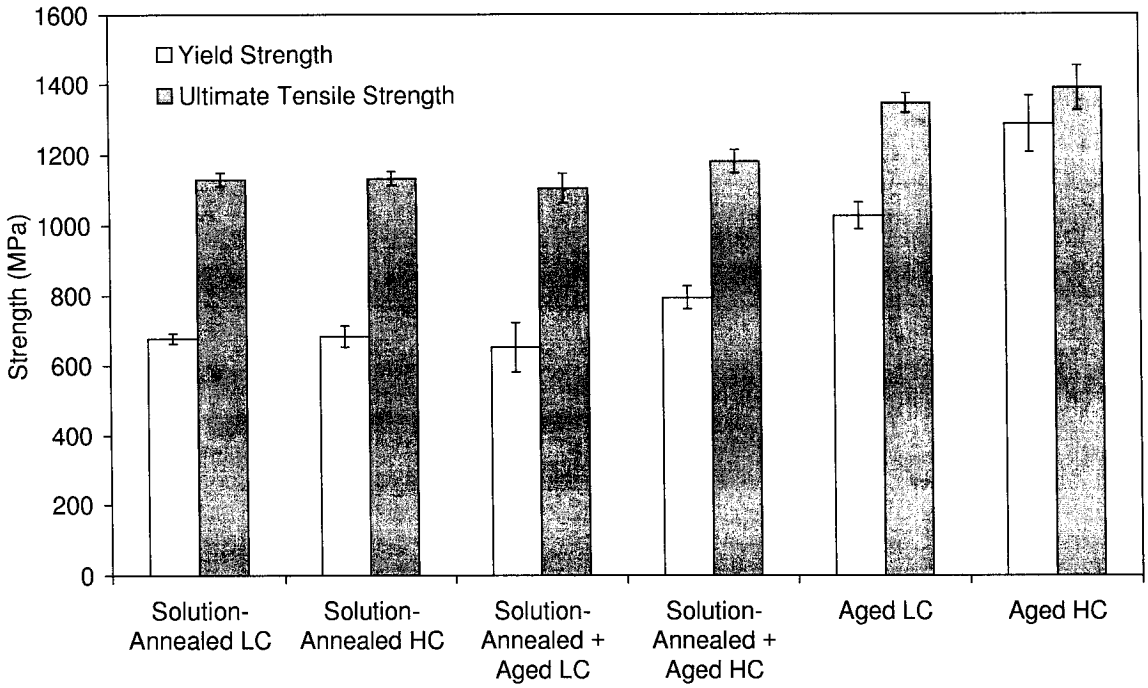

Figure 5.34. Strength properties for heat treated specimens

The last set of specimens underwent a simple aging treatment at 650°C for 72 h without any prior solutionizing step. As was seen in the micrographs in section 5.1.2 (Figures 5.19 and 5.21) noticeable carbide precipitation occurred during heat treatment, while the materials maintained a relatively fine grain structure. As a result, their strength properties (as shown in Figure 5.34) revealed a considerable increase in YS and UTS for both the LC and HC alloys. Both YS's and UTS's were well above the ASTM specification, the lowest being the LC alloy whose YS and UTS were 1030 MPa and 1350 MPa, respectively. The HC alloy had the highest YS and UTS of all the other alloys (both as-received and heat treated) of 1290 MPa and 1390 MPa, respectively.

With respect to the effect of heat treatment on ductility, the EL values for the various heat treated conditions can be seen in Figure 5.35. For the solution-annealed specimens, the LC alloy had the highest EL of all the other alloy conditions tested, with a value of 26 % and the HC alloy was significantly lower at 22 %. Nevertheless, both alloys were above the ASTM standard (> 20 %).

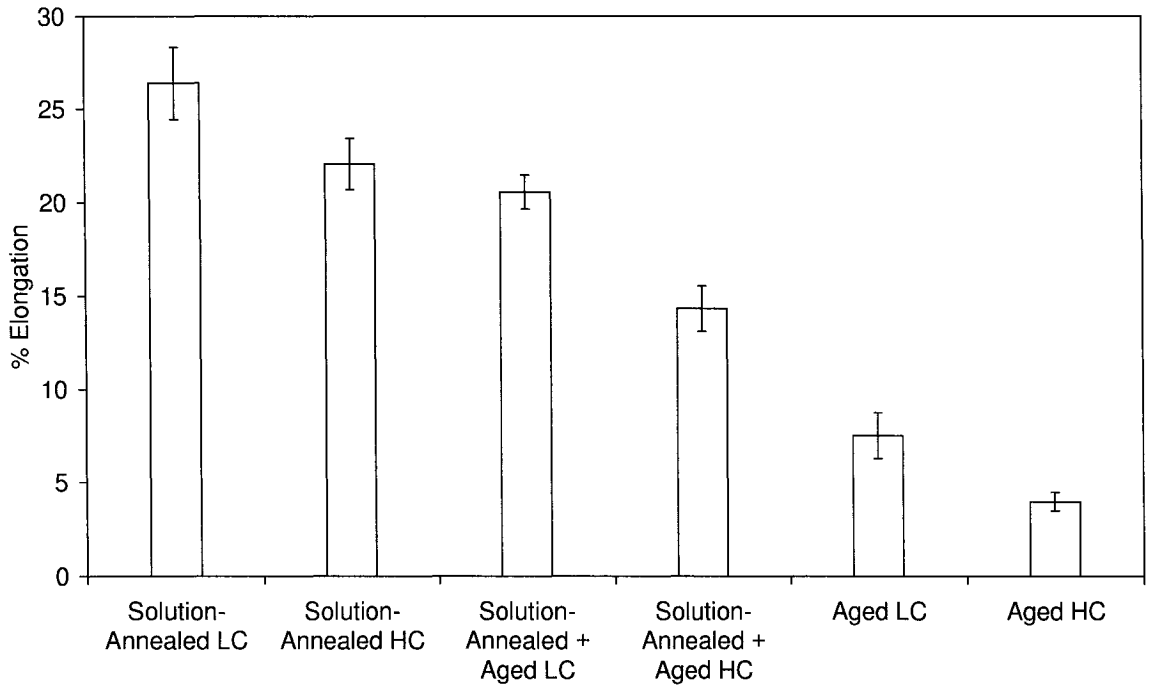

Figure 5.35. Elongation to fraction measurements of heat treated specimens

Incorporating the aging step after solution-annealing reduced the EL for the low and HC specimens, as expected. Compared to the solution-annealed specimens, the EL for the LC alloy decreased by 22 %, while the EL for the HC alloy was reduced by 35 %. Yet only the LC alloy had an average value that was above the specifications with an EL of 21 %, while the HC alloy dropped to a 14 % EL (which was below the ASTM specification of 20 %).

When the as-received F1537 alloys were subjected to a simple aging treatment at 650°C for 72 h, it was seen that the strengths of the materials dramatically increased (Figure 5.34). Conversely, with increasing strength there was a decrease in the ductility due to the aging treatment. Compared to the as-received materials, the EL for the aged specimens decreased by 60 %, with values of 7.5 % and 4.0 % for the LC and HC alloys, respectively.

5.3.3. Microhardness

Since classical wear theory partly attributes the wear resistance of a material to its hardness, microhardness measurements were taken as a supplement to the mechanical properties data. Due to the scale of these tests, microhardness measurements were taken in different features of the microstructures, such as: the alloy matrix and carbide phases (size permitting). Table 5.4 provides a list of the materials examined in this study and their corresponding hardness values for various microstructural features. An average of eight measurements was taken for each condition.

Table 5.4. Vickers microhardness measurements (kg/mm^2)

Alloy	Matrix	Carbide	Matrix+Carbide
	As-received		
F1537 LC	N/A*	N/A	470 ± 14
F1537 HC	N/A	N/A	554 ± 29
F75	348 ± 14	493 ± 43	N/A
As-Cast	393 ± 16	611 ± 62	N/A
	Heat treated		
Solution-Annealed LC	345 ± 10	N/A	N/A
Solution-Annealed HC	408 ± 28	N/A	N/A
Solution-Annealed and Aged LC	372 ± 26	N/A	N/A
Solution-Annealed and Aged HC	409 ± 7.0	N/A	N/A
Aged LC	N/A	N/A	540 ± 18
Aged HC	N/A	N/A	771 ± 46

Among the as-received materials, it was found that the F1537 alloys had the highest hardness (Note: separate measurements for the matrix and carbides phases could not be attained due to the fine microstructure). For the cast alloys, in which the coarse microstructure allowed for microhardness measurements of the individual phases, the Co-

*Due to limitations in the indentor size, microhardness measurements for certain microstructural features could not be attained.

rich matrix was found to be 1.5 times softer than the carbide phase. And for the as-cast alloy, the carbide phase was found to be almost 25% harder than the carbide phase in the F75 microstructure. Referring to Figures 5.7 and 5.9 and Table 5.1, the carbides in the as-cast alloy were relatively different in structure, size and morphology. For the solution-annealed and solution-annealed and aged alloys, it was found that the hardness values of the Co-rich matrix were in the same range, if not slightly higher than the cast materials. For the alloys which were simply aged without any prior solution-annealing, their hardness values increased by 15% for the LC and 40% for the HC materials when compared to the as-received F1537 alloys.

5.4. Wear

The wear behaviour of all the materials in this study was monitored over time by determining the mass loss for each specimen couple (pin and plate) at various cyclic intervals (0.050, 0.10, 0.20, 0.30, 0.40, 0.50, 0.75 and 1.0 Mc) and converting this mass loss into volumetric wear. In a study conducted by Tipper *et al*,[74] in which a pin-on-plate tester was used, an linearly increasing wear behaviour was found for all the materials tested (Figure 2.15 of the present thesis).

Again, in a similar study by Scholes and Unsworth,[75] an increasing linear wear behaviour was seen throughout the 1.0 Mc of testing for all the materials. On the other hand, in some wear simulator testing of hip implants, two distinct wear trends were found. According to the work conducted by Chan *et al*,[100] a period of "run-in" or rapid wear was seen in the early stages of testing (between 0 and 1.0 Mc) followed by an extended period of "steady-state" or low wear from 1.0 to 3.0 Mc. This wear behaviour was also seen in a study conducted by Anissian *et al.*[101]

5.3.1. As-received materials

In the present study, a similar wear behaviour to that of some of the wear simulator testing of hip implants was observed. It would seem that prior to 1.0 Mc of testing, run-in wear was taking place, while the on-set of steady-state wear coincided at around 1 Mc of

testing (Figure 5.36). This was mainly observed in the HC alloys, and was not the case for the LC material, which seemed to remain in the run-in stage even at 1.0 Mc of testing. This was consistent with Chan *et al* [100] in which the LC implants seemed to achieve steady-state wear rates after 2.0 Mc of testing on average. In fact, in addition to a different wear behaviour between the LC and HC alloys, there was also a significant difference in the extent of wear between the F1537 LC alloy (1.1 ± 0.093 mm^3) and F1537 HC, F75 and as-cast alloys (average = 0.23 ± 0.091 mm^3) after 1.0 Mc of testing. However, it should be noted that the LC components had lower clearances and higher roughness values which may have dominated the wear behaviour. In addition, during the run-in period, there was a noticeable discoloration in the bulk lubricating fluid as was observed in the hip joint simulator.[102] However, at 1.0 Mc of testing this discoloration was less noticeable.

Although there were similarities between this simple pin-on-plate study and the hip joint simulator, there remained one major difference—the ability to differentiate the wear behaviour with respect to different materials. In the simulator it was only found that the HC CoCrMo alloys may be better than the LC alloy, and even this finding was far from conclusive. However, in the present study it was found that even in the realm of HC alloys there were significant differences in wear behaviour. Somewhat similar behaviour was found by Tipper et al [74] and by Scholes and Unsworth.[75] In particular, the as-cast alloy had the lowest volumetric wear of all the others, followed by the F75 alloy and then the F1537 HC alloy. Even though the HC alloys shared similar compositions (Table 4.1) they behaved differently under lubricated sliding conditions. This would suggest that some aspect of the materials (namely the microstructure) might have affected the wear behaviour. In order to explore the acting wear mechanisms in the present wear tests and to compare them with those that may be acting in MM THA, surface analysis of the specimens was required. Figure 5.37 presents a set of SEM micrographs of the as-received materials prior to wear testing.

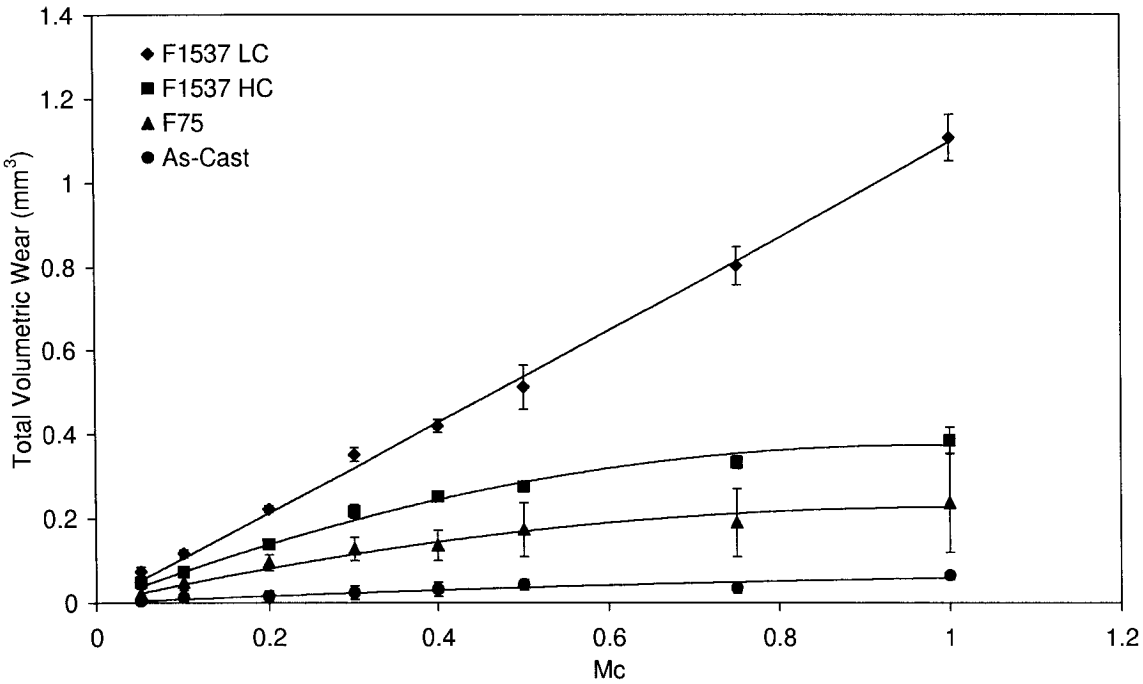

Figure 5.36. Wear curves of as-received materials after 1.0 Mc of testing

As mentioned in Section 4.3, the surfaces were ground and polished manually and any prior machining marks were reduced to fine scratches visible only in the electron microscope. In addition, for all the SEM examinations a low accelerating voltage of 5.0 kV was used in order to accentuate the surface characteristics. It was found that at such low accelerating voltages the near surface carbides (represented by the dark-gray areas) could be observed (denoted by the arrows) and their sizes and morphologies were in agreement with the previous microstructural findings (see Section 5.1). Another interesting feature which was only observed in the F75 and as-cast materials was the presence of round particles distributed throughout the as-polished surfaces (Figure 5.38). These particles were also observed by Wang *et al* [103] in a surface analysis study conducted on CoCrMo MM implants tested in a simulator up to 6.0 Mc. These particles were mainly identified as Si-rich residual grinding stones embedded in the surface as a result of the manufacturing process of these components.

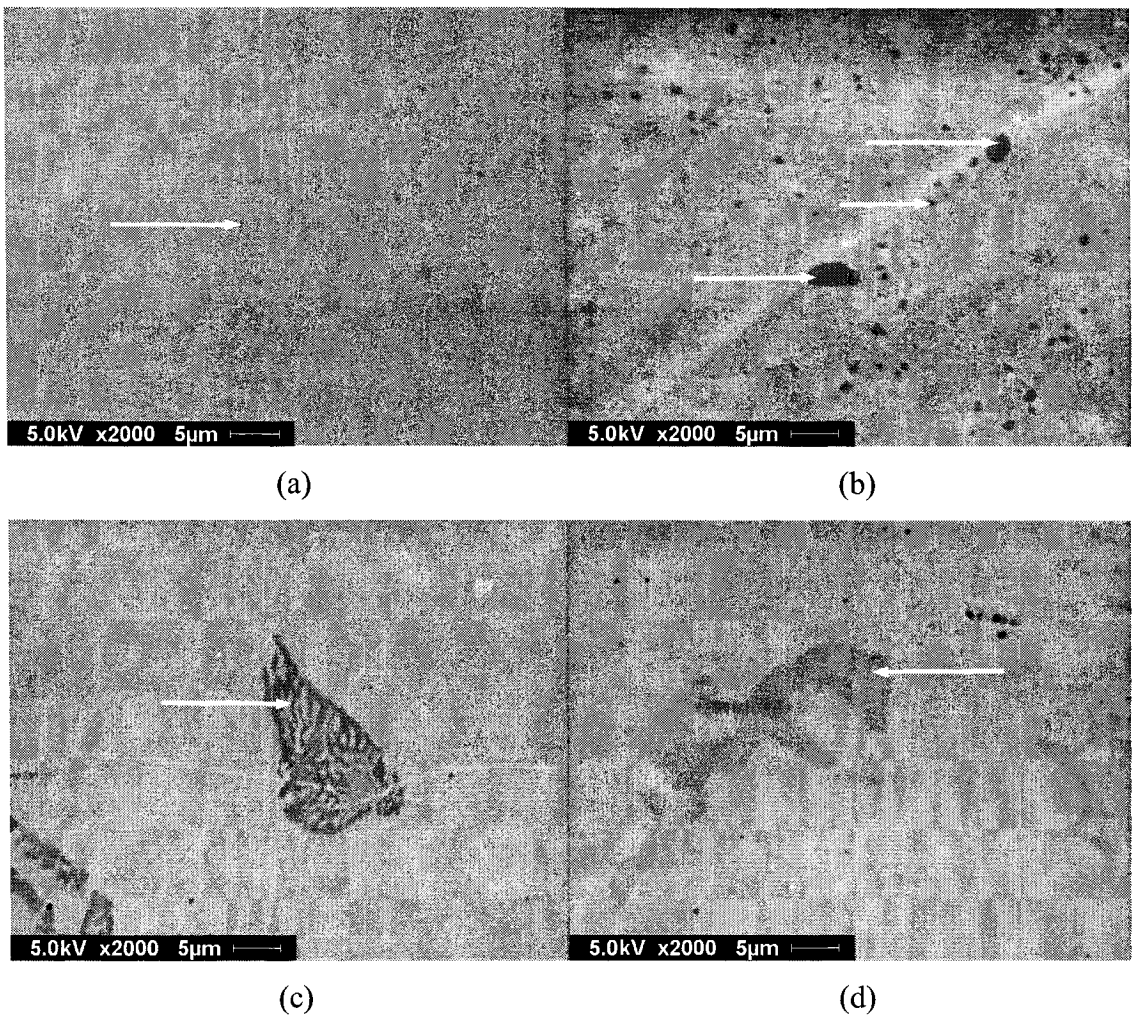

Figure 5.37. Initial surfaces of as-received materials: (a) F5137 LC, (b) F1537 HC, (c) F75 and (d) as-cast (carbides are arrowed)

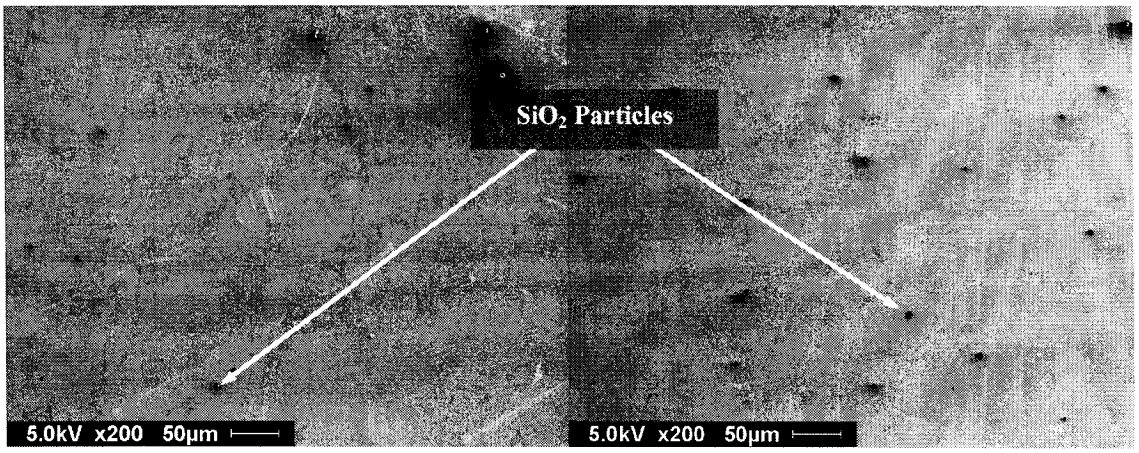

(a) (b)

Figure 5.38. As-polished surfaces at x200 magnification: (a) F75 and (b) as-cast

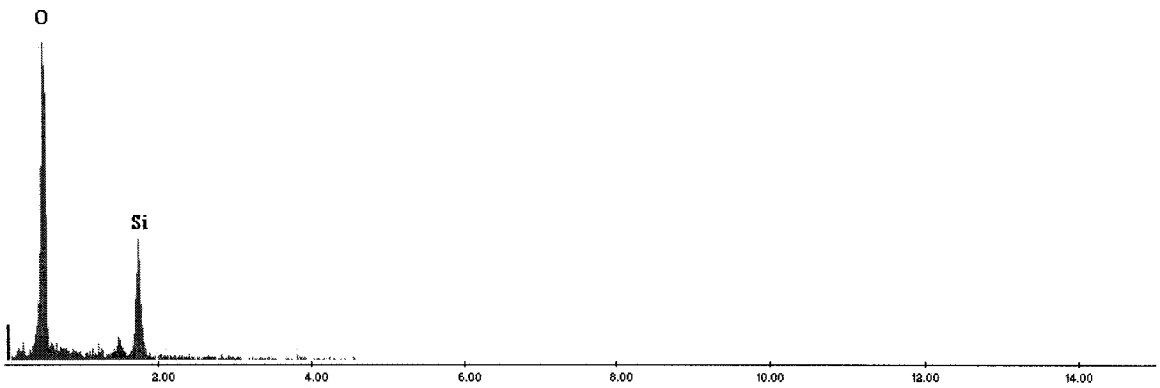

Figure 5.39. Chemical analysis of particles observed in as-polished cast specimens

EDS analysis of the specimens in Figure 5.38 revealed the particles to be SiO_2 (Figure 5.39) and they were not observed in any of the as-received or heat treated F1537 alloys. This was similar to Wang *et al* who found an abundance of these particles in the F75 material, but very few in the F1537 alloys. The sighting of these particles in both studies (which used very different surface preparation protocols) would suggest that these particles are not residual grinding stones from the finishing process, but a part of the materials' microstructures.

From the onset of wear until the end of testing, all the specimens (both as-received and heat treated) exhibited linear grooves on the contact surfaces coinciding with the linear motion of the wear apparatus. Some attribute these grooves as a direct result of scratch abrasion originating from second or third-body particles. However, it is still unclear what the dominant cause may be. Typical wear scars can be seen in Figure 5.40.

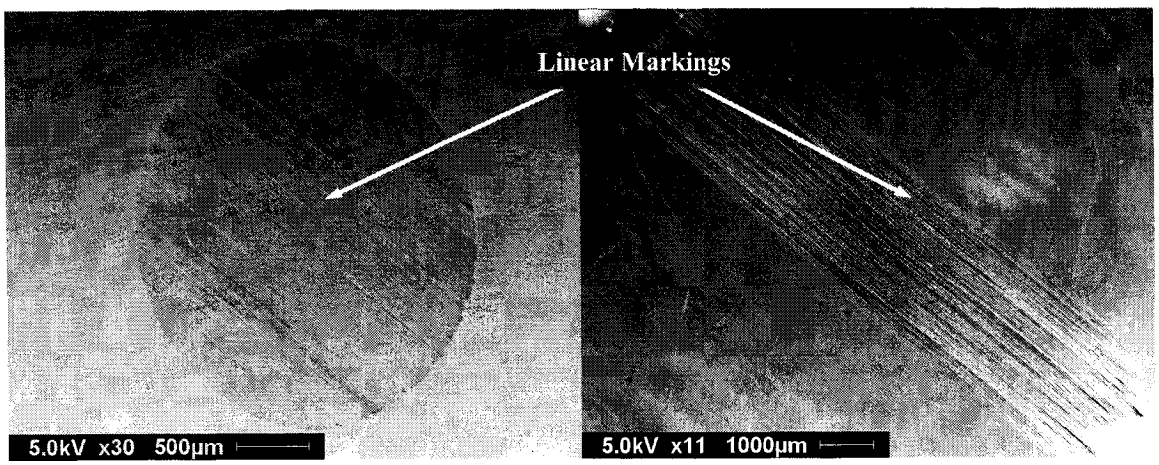

(a) (b)

Figure 5.40. Linear wear scars after 0.05 Mc of testing: (a) pin and (b) plate specimens

At higher magnifications, other wear features could be observed on both the pin and plate surfaces. Unique wear features for the F1537 LC alloy included sharp, fragmented grooves mixed with areas of a dimpled surface, as was found in the hip simulator.[104] These features were seen on the plate specimens in the earlier stages of testing (up to 0.40 Mc), but later were no longer visible on approaching 1.0 Mc. However, the grooves maintained a sharp-edged appearance (see Figure 5.41).

For the pin specimens the linear markings had a rounder appearance and there was occasional evidence of surface pitting early on. Toward the end, the grooves became sharper, surface dimples were no longer observed and surface voids (i.e. areas that seemed to have material which was fractured off) were prevalent mainly at 0.50 Mc (see Figure 5.42).

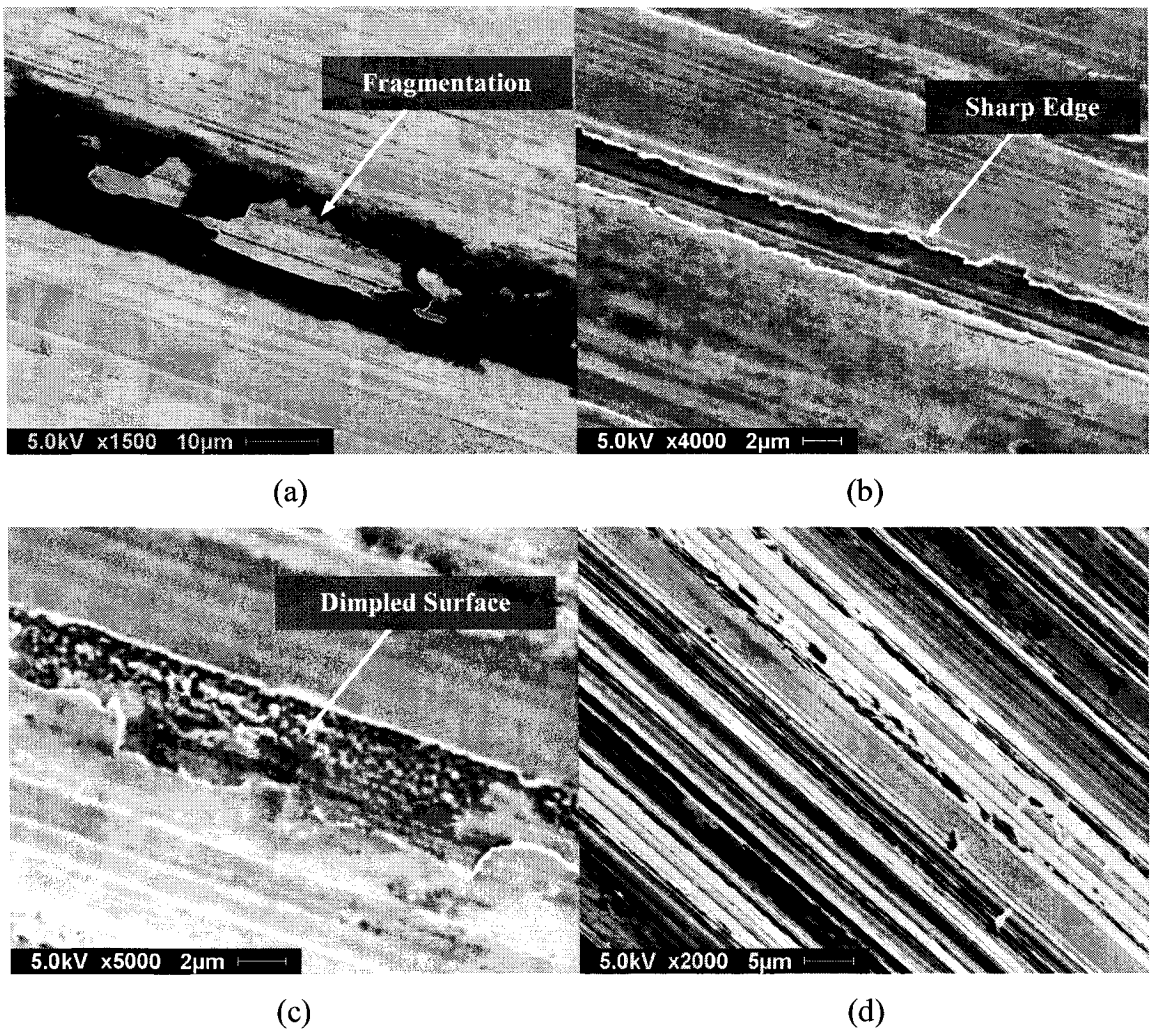

Figure 5.41. Wear surfaces of as-received F1537 LC plate specimens after: (a) 0.20 Mc, (b) 0.20 Mc, (c) 0.20 Mc and (d) 1.0 Mc

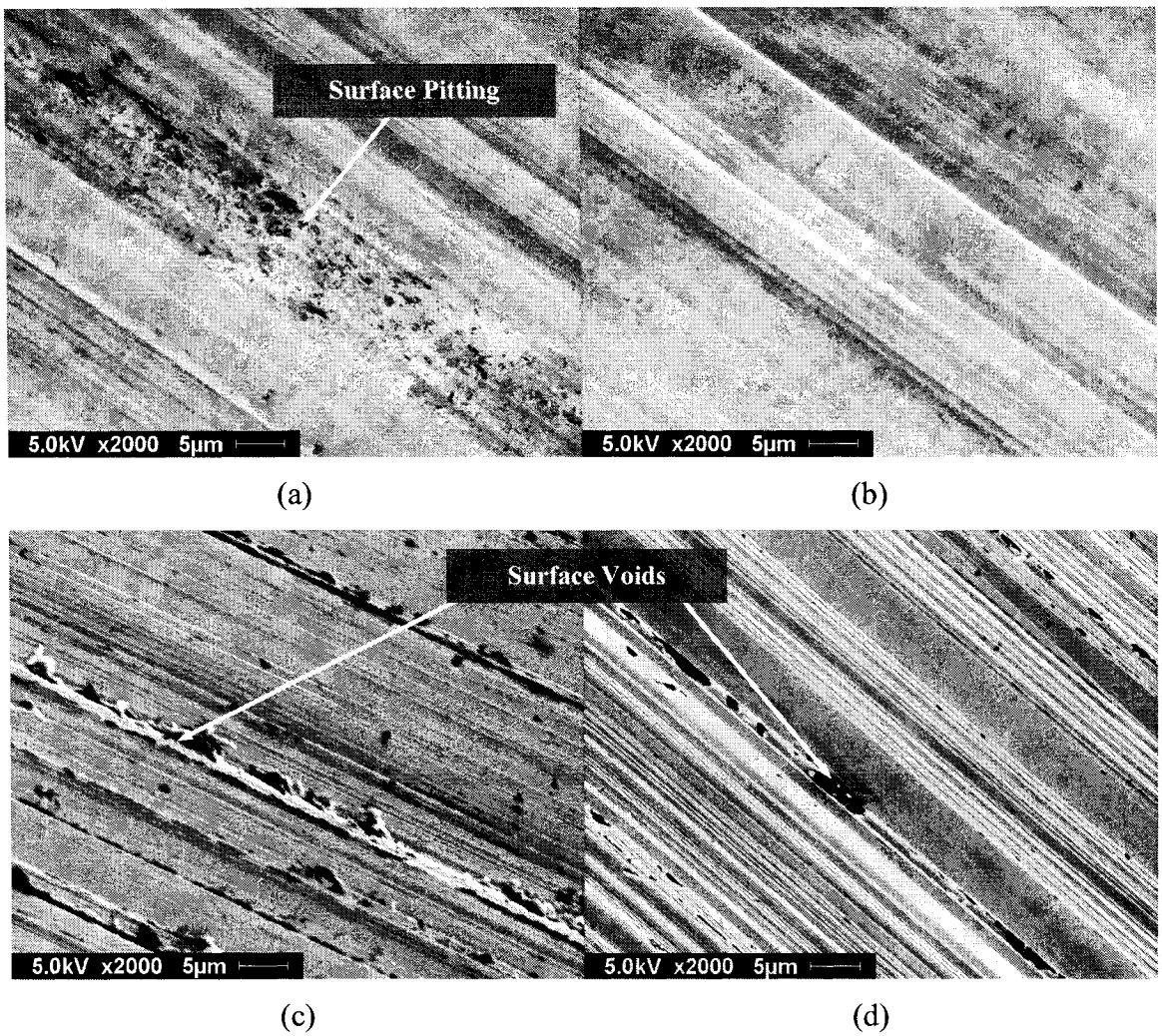

Figure 5.42. Wear surfaces of as-received F1537 LC pin specimens after: (a) 0.20 Mc, (b) 0.20 Mc, (c) 0.50 Mc and (d) 1.0 Mc

A characteristic feature of the as-received F1537 HC alloy and the other as-received HC alloys (F75 and as-cast) was the presence of massive pitting,[104] particularly on the wear surface of the plate specimens (see Figure 5.43). This however was not the case for the pin specimens, which only exhibited occasional pitting (see Figure 5.44).

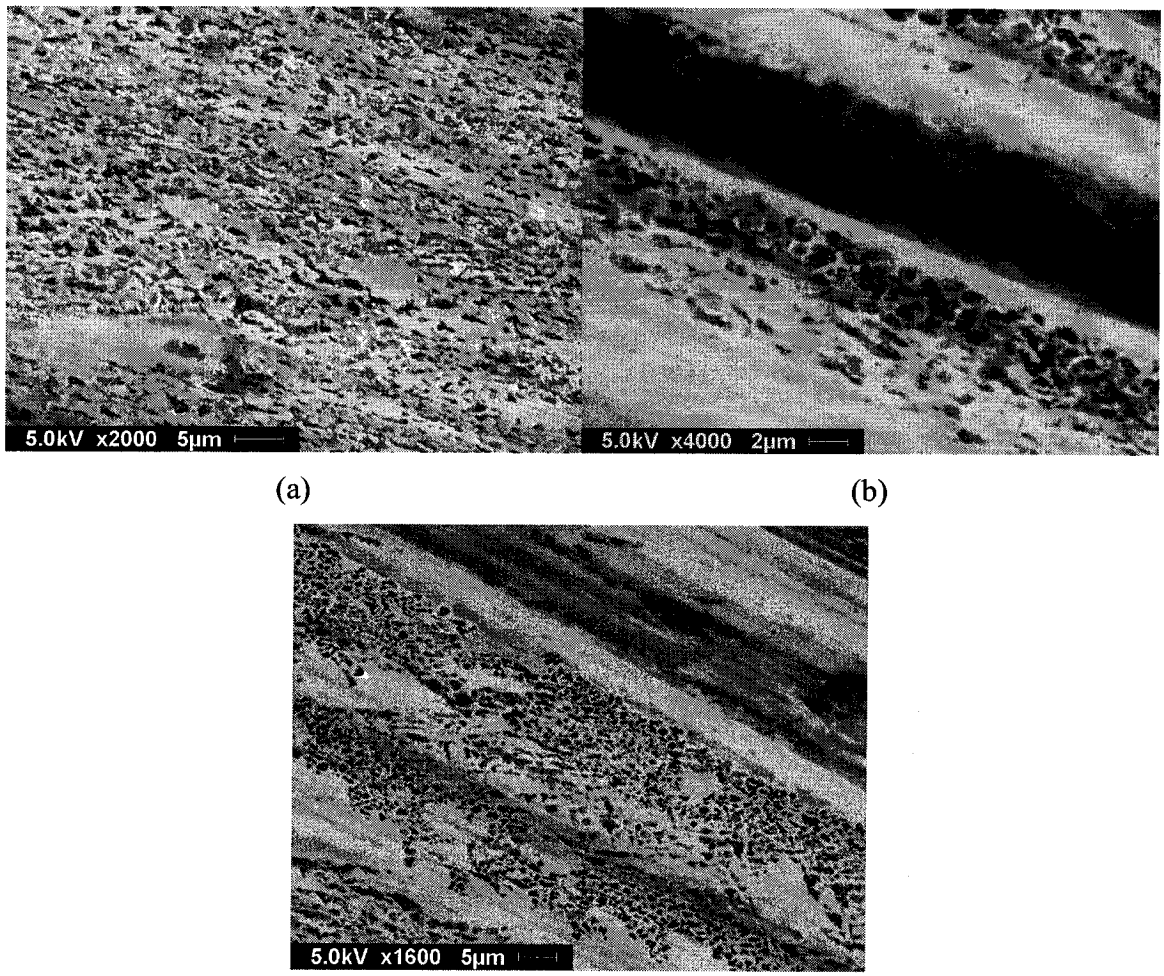

Figure 5.43. Surface pitting along contact zone in as-received HC plate specimens after 0.20 Mc: (a) F1537 HC, (b) F75 and (c) as-cast

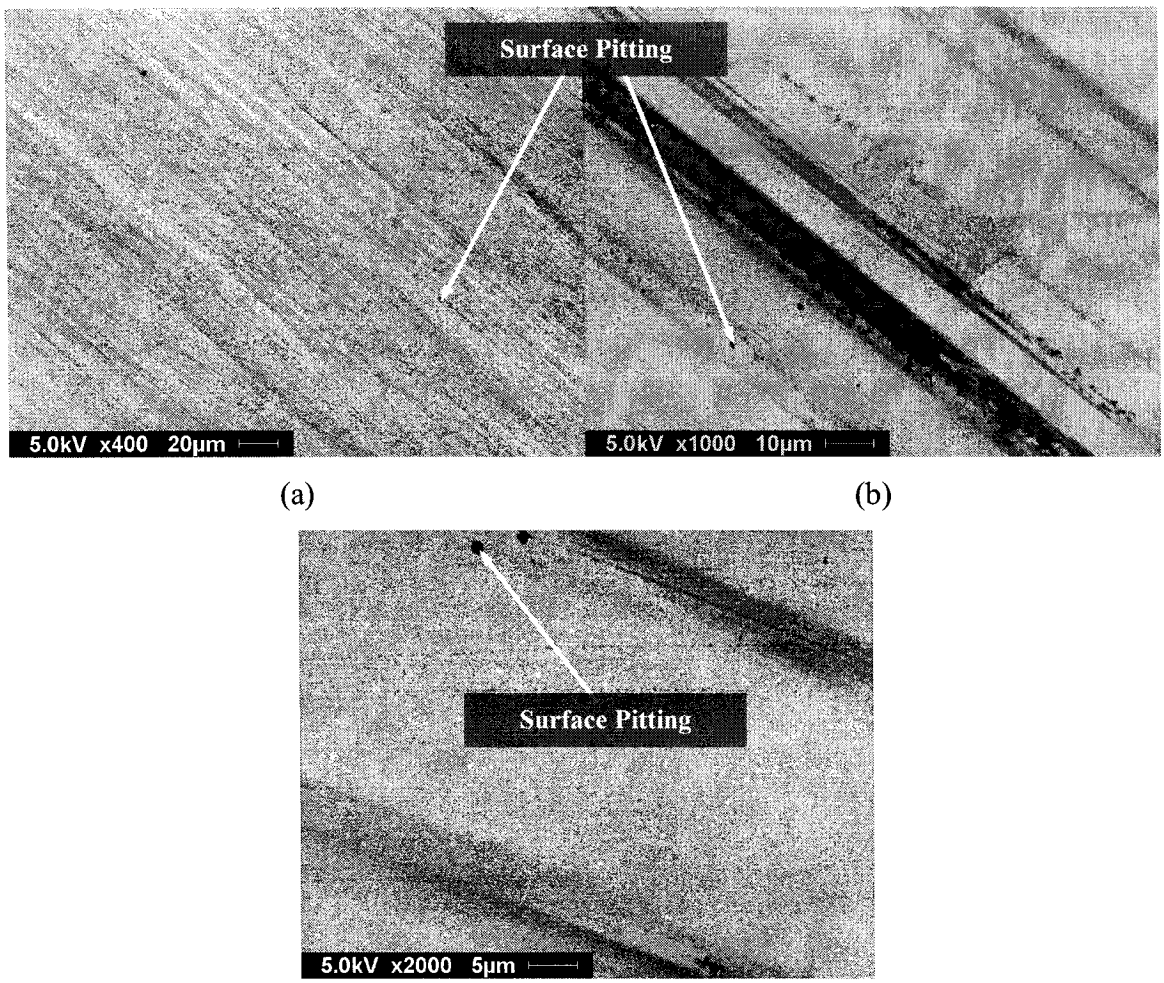

Figure 5.44. Wear surfaces of as-received HC pin specimens after 0.30 Mc revealing occasional surface pitting: (a) F1537 HC, (b) F75 and (c) as-cast

In general, the linear markings had rounder edges and in the case of the cast alloys, the wear surfaces had a "smeared" appearance. Regardless of the linear markings, the carbide precipitates could still be observed on the surface and near surface material of all the HC alloys, and the Si-O particles observed on the as-polished surfaces of the cast specimens were still visible in the wear zone (Figure 5.45).

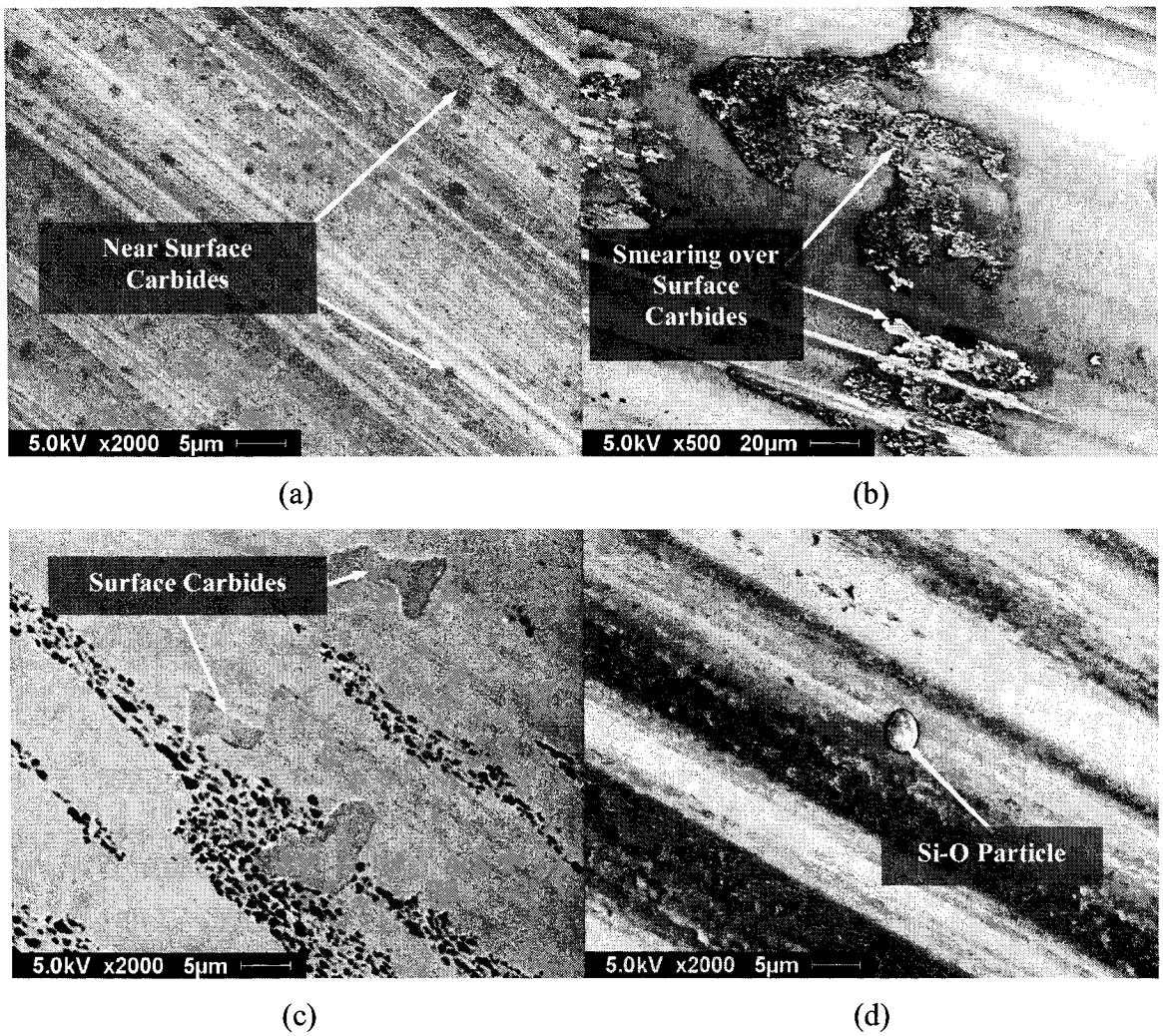

Figure 5.45. Carbides shown on surface or near surface material of HC alloys: (a) F1537 HC pin at 0.20 Mc, (b) F75 Plate at 0.050 Mc, (c) as-cast plate at 0.50 Mc. (d) Si-O particle in wear zone of F75 plate at 0.50 Mc.

Profilometry measurements of the as-received specimens were taken in 2D and 3D after 1.0 Mc of testing. (Note: 3D profilometry measurements of only the as-received plate specimens were conducted due to time constraints.). From Figure 5.46 it can be seen that the pin and plate surfaces conformed well to one another (i.e. one surface was a mirror image of the other). Although the starting surface of the plates was flat, profilometry measurements revealed that after 1.0 Mc of testing the contact zone adopted a curved surface with a radius of curvature greater than the starting pin radius of 100 mm. In addition, higher wear seemed to correspond to a wider or smaller contact curvature

(i.e. a measure of the radius of curvature of the contact zone). A flatter contact zone corresponded to lesser volumetric wear.

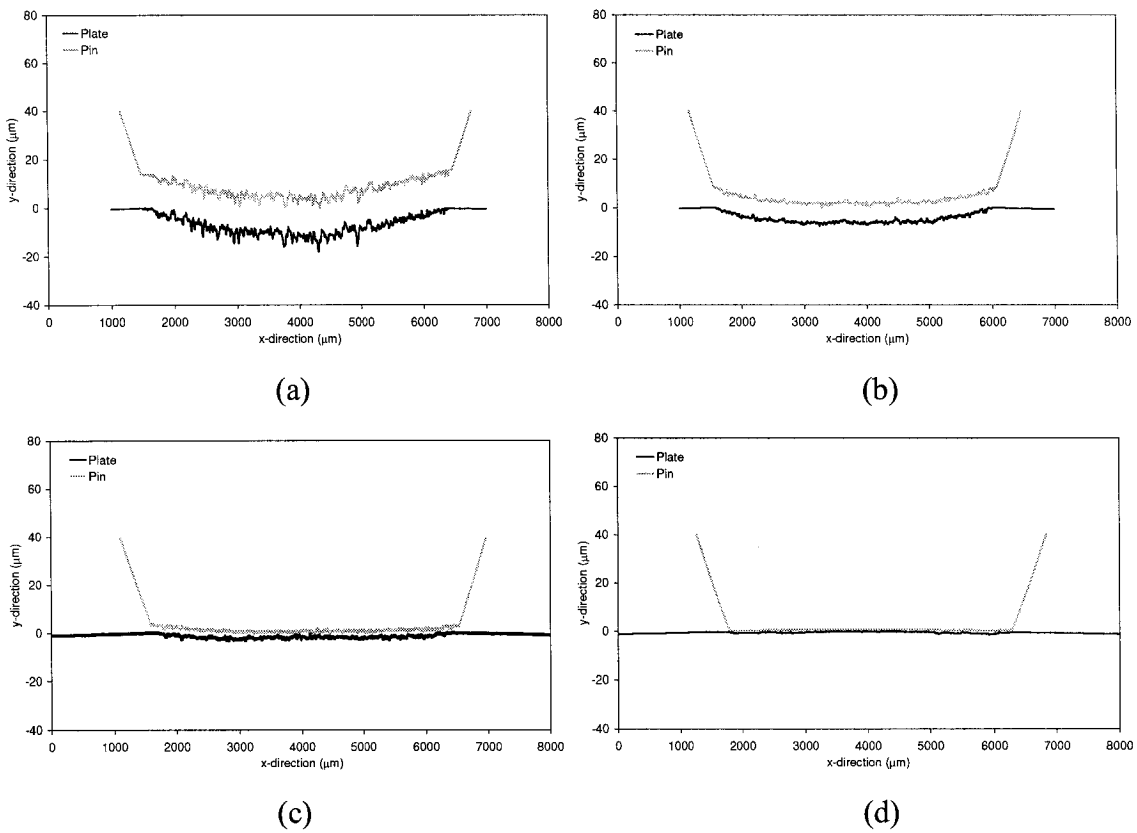

Figure 5.46. 2D profilometry measurements of as-received pin and plate specimens: (a) F1537 LC, (b) F1537 HC, (c) F75 and (d) as-cast

It was also found that with decreasing wear (Figure 5.36) there was also a notable decrease in the surface roughness of the contact zone for the as-received specimens. This is illustrated in the 3D profilometry measurements shown in Figure 5.47. In general, the contact zones had roughness values at least one order of magnitude greater than the as-polished surfaces, with the exception of the as-cast pin which was in the same range for both the as-polished and worn conditions and the F1537 LC plate which had a roughness value two orders of magnitude greater than the as-polished condition (see Table 5.5).

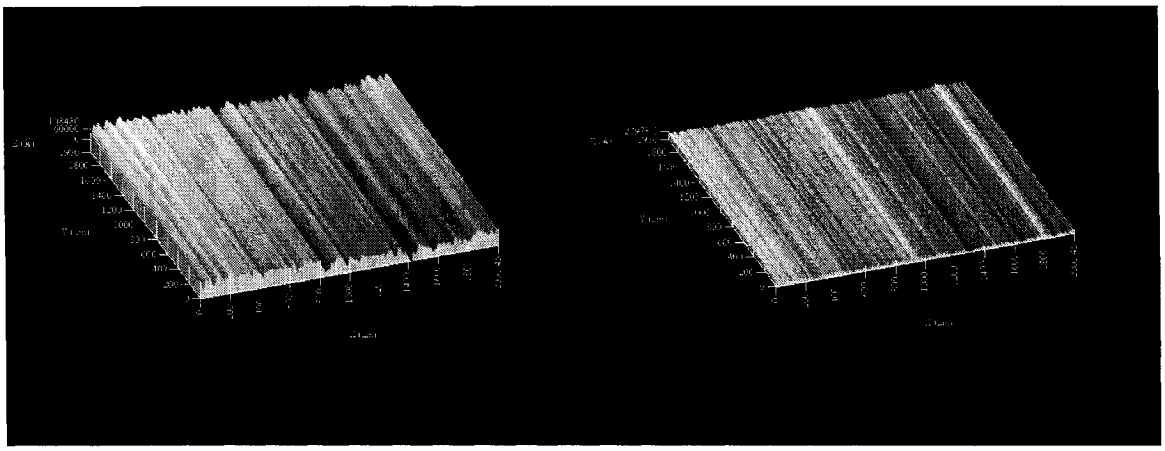

(a) (b)

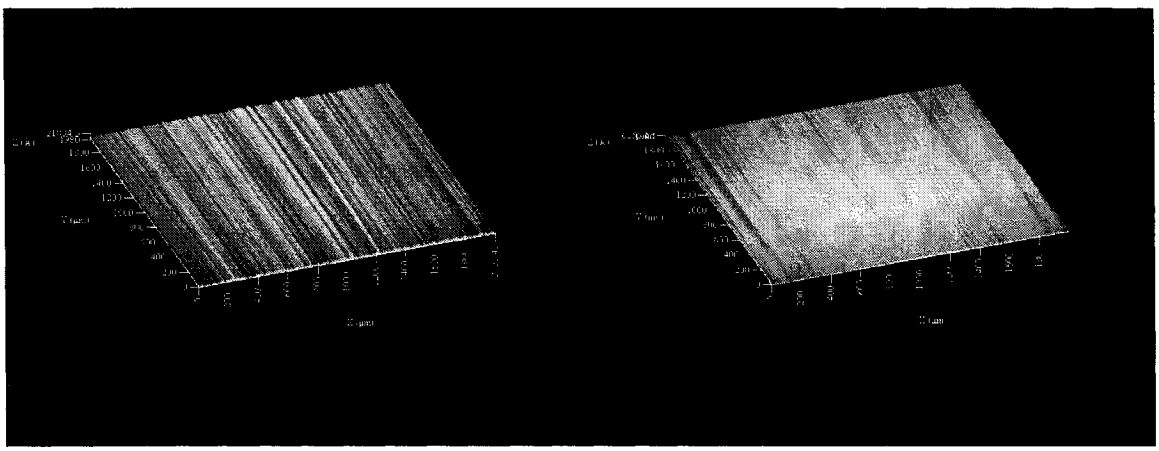

(c) (d)

Figure 5.47. 3D profilometry measurements of as-received plate specimens: (a) F1537 LC, (b) F1537 HC, (c) F75 and (d) as-cast

Table 5.5. R_q (root mean square) roughness values for the as-received specimens

Alloy	Pin Surface		Plate Surface	
	As-Polished (μm)	Worn (μm)	As-Polished (μm)	Worn (μm)
F1537 LC	0.025	1.5	0.0053	1.7
F1537 HC	0.027	0.60	0.0058	0.46
F75	0.033	0.34	0.020	0.45
As-Cast	0.014	0.054	0.0051	0.076

Further surface analysis included x-ray diffraction of both the worn and as-polished sections of the plate specimens (Figures 5.48 and 5.49). The pin specimens were not analyzed due to certain geometric constraints, namely the spherical shape of the pin tip and the size of pin itself. Recalling the crystallographic data from neutron diffractometry (section 5.2), the bulk crystal structure of the as-received materials was FCC. However, since wear processes affect the surface and near surface material, changes to the surface crystal structure may have taken place.

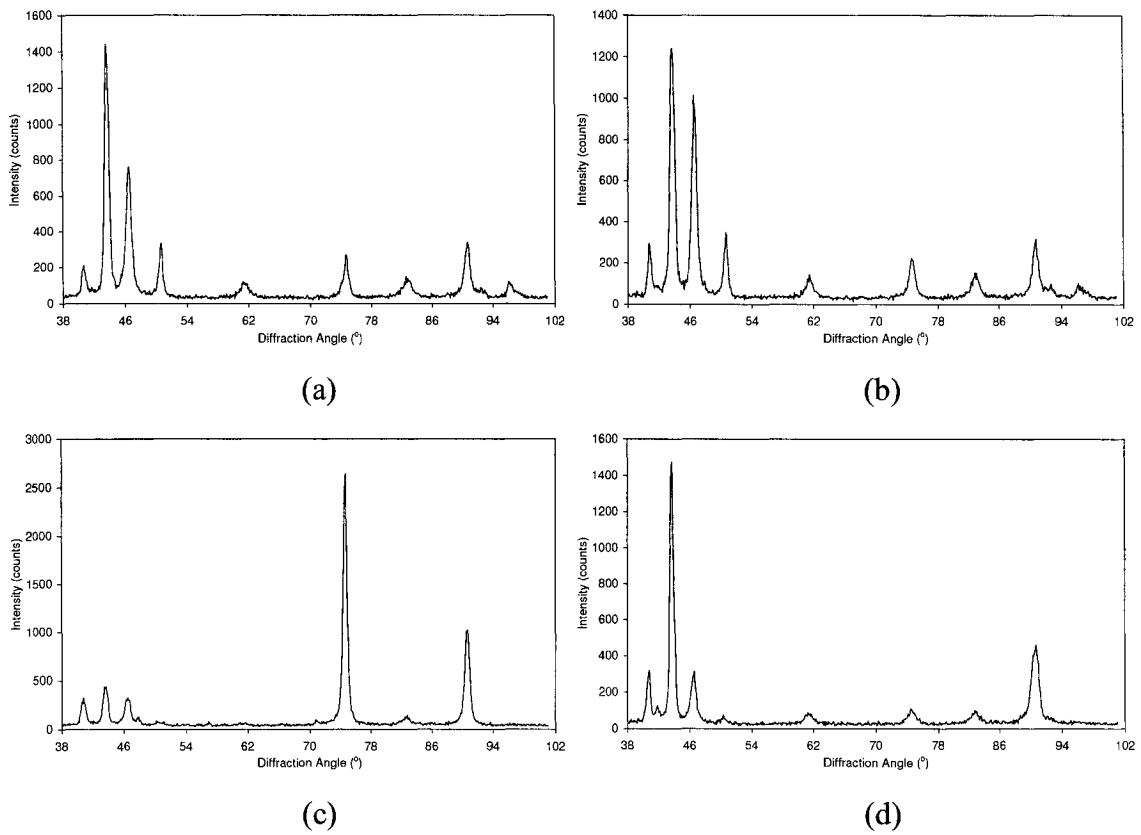

Figure 5.48. X-ray diffraction data for worn surfaces of as-received plate specimens: (a) F1537 LC, (b) F1537 HC, (c) F75 and (d) as-cast (note: characteristic HCP peak at 46.5°)

For the most part, x-ray diffraction was used as a qualitative analysis tool and it confirmed a predominately FCC structure with the presence of the HCP phase on the worn and as-polished surfaces of the plate specimens. In both cases one can see that the

surfaces consisted of a dual-phase FCC and HCP structure and were consistent with the findings of a surface analysis study conducted on CoCrMo alloys tested in a hip joint simulator.[104]

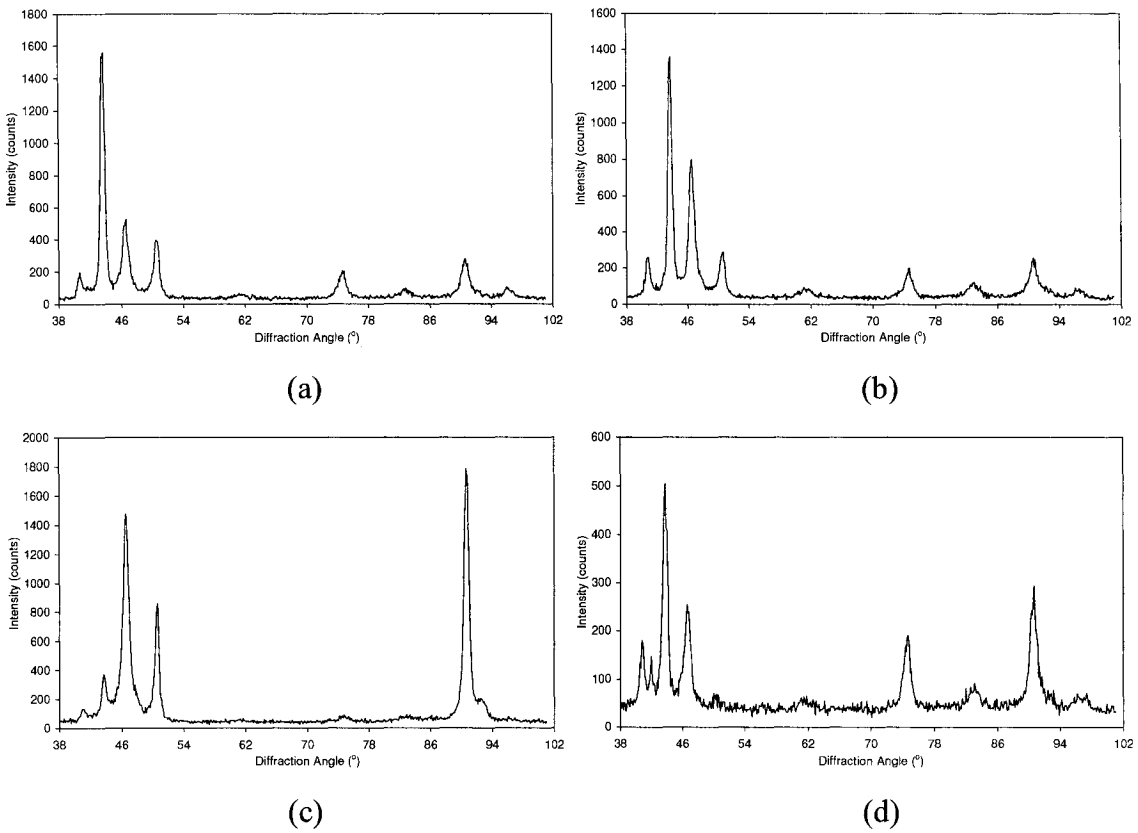

Figure 5.49. X-ray diffraction data for as-polished surfaces of as-received plate specimens: (a) F1537 LC, (b) F1537 HC, (c) F75 and (d) as-cast (note: characteristic HCP peak at 46.5°)

5.4.2. Heat treated materials

Since all the heat treatments in this study were conducted on the F1537 alloys, the following wear results for the heat treated specimens were compared to the as-received condition.

5.4.2.1. Solution-annealed

For the specimens which were solution-annealed at 1200°C for 24 h, the total volumetric wear after 1.0 Mc of testing can be seen in Figure 5.50. As in the case of the as-received specimens there was a clear separation between the LC and HC alloys, before and after heat treatment. The LC alloys seemed to experience a steady increase in volumetric wear throughout the entire 1.0 Mc, with the solution-annealed LC alloy showing an overall lower wear rate than the as-received LC alloy.

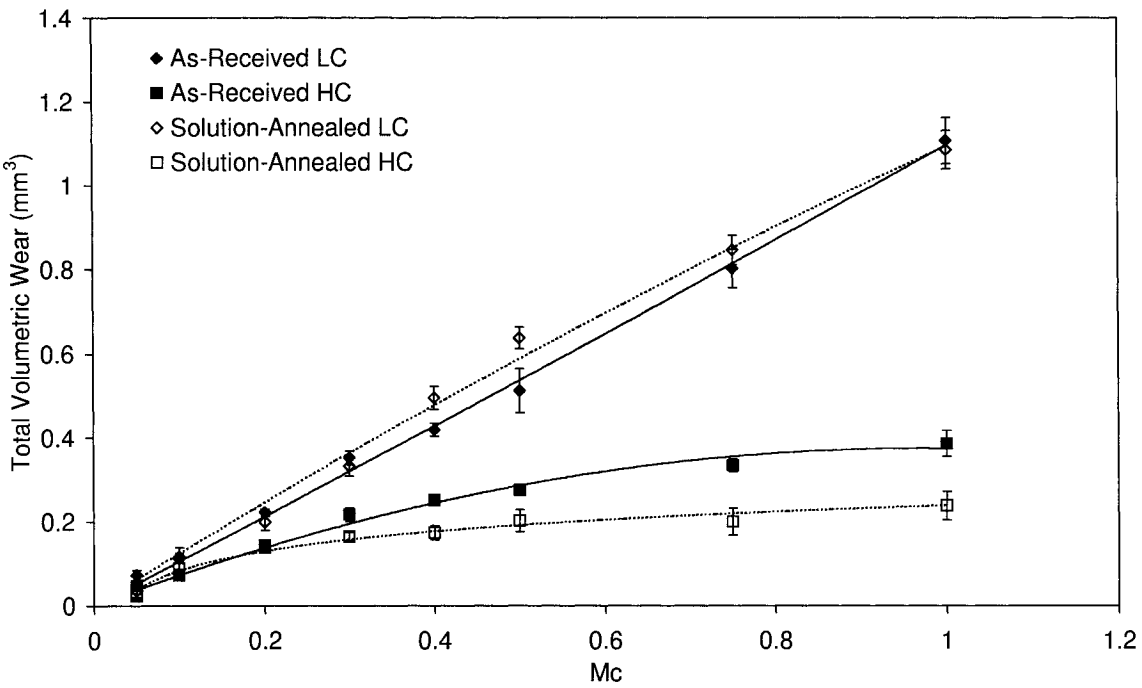

Figure 5.50. Wear curves of F1537 alloys solution-annealed at 1200°C for 24 h after 1.0 Mc of testing compared to the as-received condition

The wear behaviour of the HC alloys seemed to exhibit a decreasing wear rate prior to 1.0 Mc followed by the onset of steady-state wear. It was also found that the solution-annealed HC alloy experienced substantially lower wear than the as-received HC alloy. This was unexpected since the heat treatment reduced the volume fraction of carbides in

the microstructure and was therefore expected to lower the wear resistance. According to wear theory, higher hardness and even the presence of hard phases are believed to improve the wear properties of metallic materials according to the following relationship:[50]

$$V = \frac{kF_N d}{H} \tag{5.1}$$

where V is the wear volume, k is the wear coefficient, F_N is the normal load, d is the sliding distance and H is the hardness of one of the interacting materials.

As was the case for the as-received LC alloy, the solution-annealed LC alloy showed the characteristic feature of occasional surface voids on the pin specimen and surface dimples in the case of the plate specimen in the middle stages of testing (Figures 5.51a and 5.51b). For both cases, in the latter part of testing, these features were less visible (Figures 5.51c and 5.51d). Rather, only the common wear grooves remained at 1.0 Mc.

For the solution-annealed HC specimens there was evidence of occasional pitting in the early stages of testing, but much less than what was observed in the as-received HC alloys throughout the 1.0 Mc of testing. However, after 1.0 Mc these pits were no longer visible (see Figure 5.52).

2D profilometry measurements of the solution-annealed LC and HC specimens can be seen in Figure 5.53. The results show that the larger diameter and width of the wear zones for the pin and plate specimens, respectively, correspond to increased wear, as was observed earlier. In addition, it would seem from the surface profile of the wear zone for the solution-annealed LC alloy that the surface roughness was much less than the as-received LC alloy. However, in the case of the solution-annealed HC alloy, the roughness was slightly greater than the as-received HC alloy (see Table 5.6). Through x-ray diffraction it was confirmed that even in the solution-annealed condition, a dual FCC and HCP structure exists at the worn and as-polished specimen surfaces (see Figure 5.54).

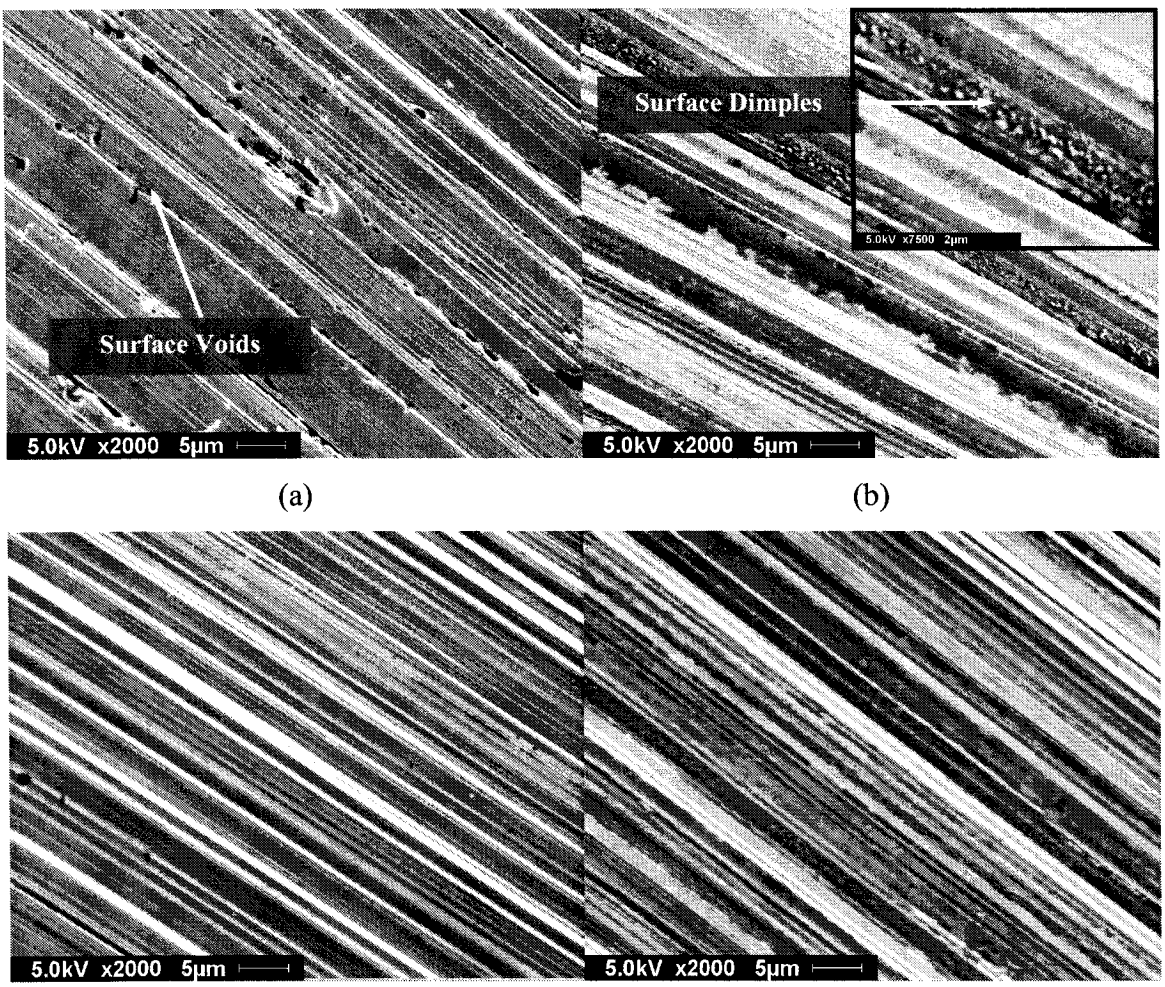

Figure 5.51. Wear surfaces of F1537 LC alloys solution-annealed at 1200°C for 24 h: (a) pin specimen after 0.20 Mc, (b) plate specimen after 0.40 Mc, (c) pin specimen after 0.75 Mc and (d) plate specimen after 1.0 Mc

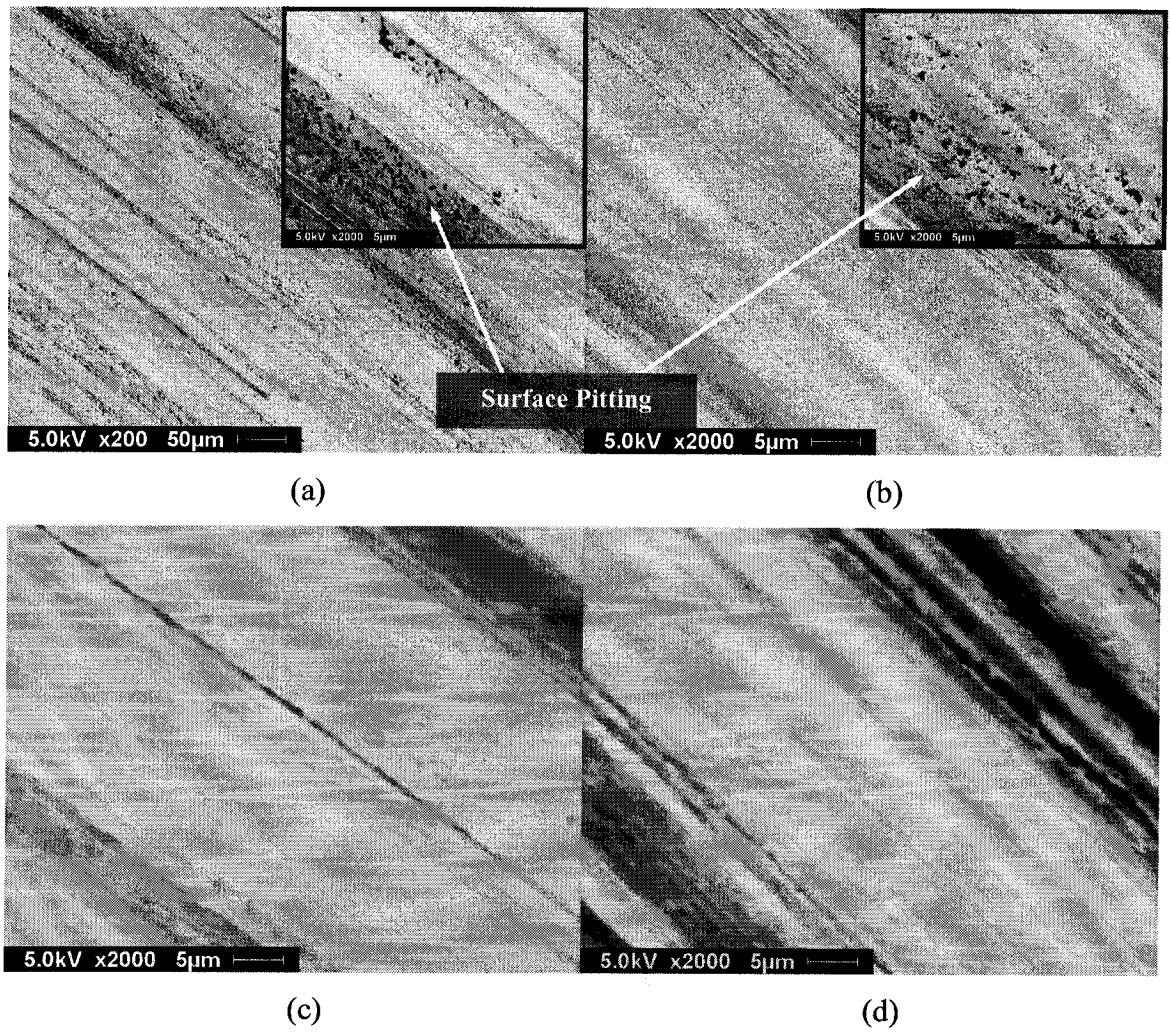

Figure 5.52. Wear surfaces of F1537 HC alloys solution-annealed at 1200°C for 24 h: (a) pin specimen after 0.40 Mc, (b) plate specimen after 0.40 Mc, (c) pin specimen after 1.0 Mc and (d) plate specimen after 1.0 Mc

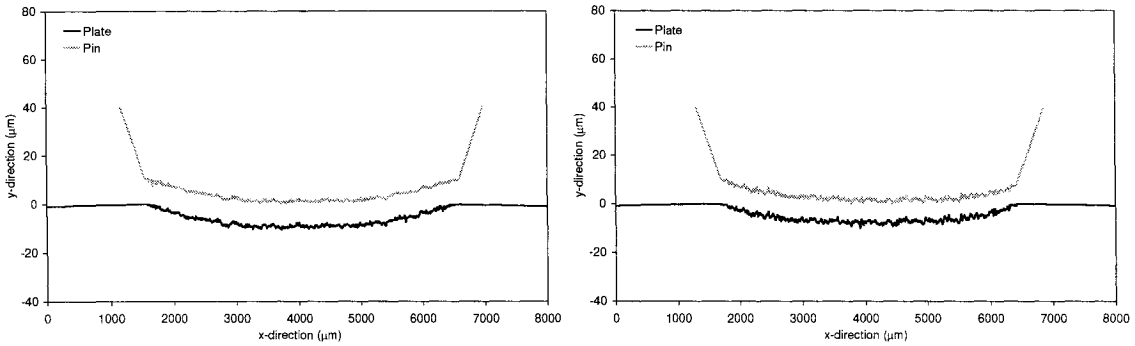

(a) (b)

Figure 5.53. 2D profilometry measurements of F1537 alloys solution-annealed at 1200°C for 24 h: (a) LC and (b) HC

Table 5.6. R_q roughness values for the F1537 alloys solution-annealed at 1200°C for 24 h

Alloy	Pin Surface		Plate Surface	
	As-Polished (μm)	Worn (μm)	As-Polished (μm)	Worn (μm)
Solution-Annealed LC	0.0077	0.55	0.0065	0.58
Solution-Annealed HC	0.015	0.71	0.0064	0.69

5.4.2.2. Solution-annealed and aged

The wear results of the alloys solution-annealed at 1200°C for 24 h and aged at 650°C for 72 h are shown in Figure 5.55. As mentioned previously (Section 4.3.1), the solution-anneal and aging heat treatments were designed to produce a homogeneous HCP microstructure, but it was verified through neutron diffraction in Section 5.2.2 that the microstructure maintained a bulk FCC crystal structure. Nevertheless, there was a difference in wear behaviour due to the added aging treatment when compared to a simple solution-annealing step (compared to Figure 5.50).

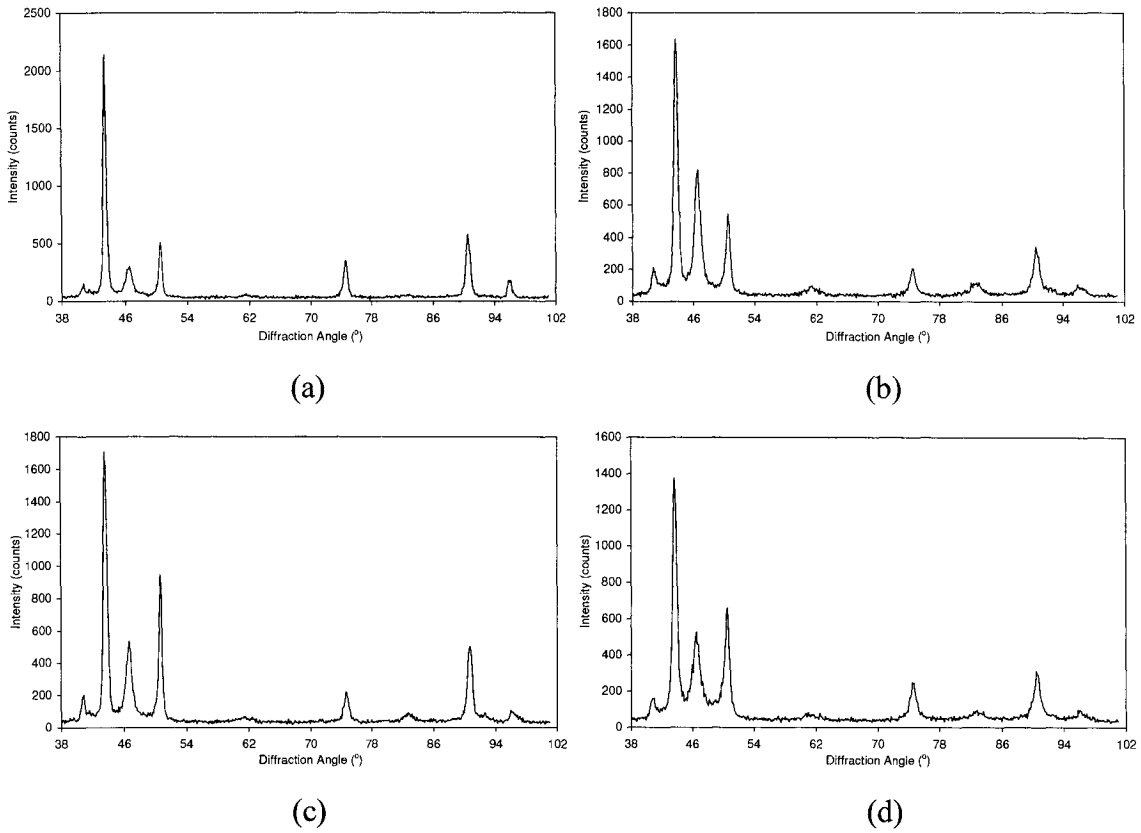

Figure 5.54. X-ray diffraction data for F1537 alloys solution-annealed at 1200°C for 24 h: (a) LC worn specimen, (b) HC worn specimen, (c) LC as-polished specimen and (d) HC as-polished specimen (note: characteristic HCP peak at 46.5°)

As previously mentioned, there was a clear separation between the LC and HC alloys, before and after heat treatment. For the LC specimens there seemed to be no significant difference in the amount of wear with respect to the solution-anneal and aging treatment. However, the solution-annealed and aged specimens exhibited a slight decrease in the wear rate (although not as dramatic a decrease as with LC specimens which were simply solution-annealed).

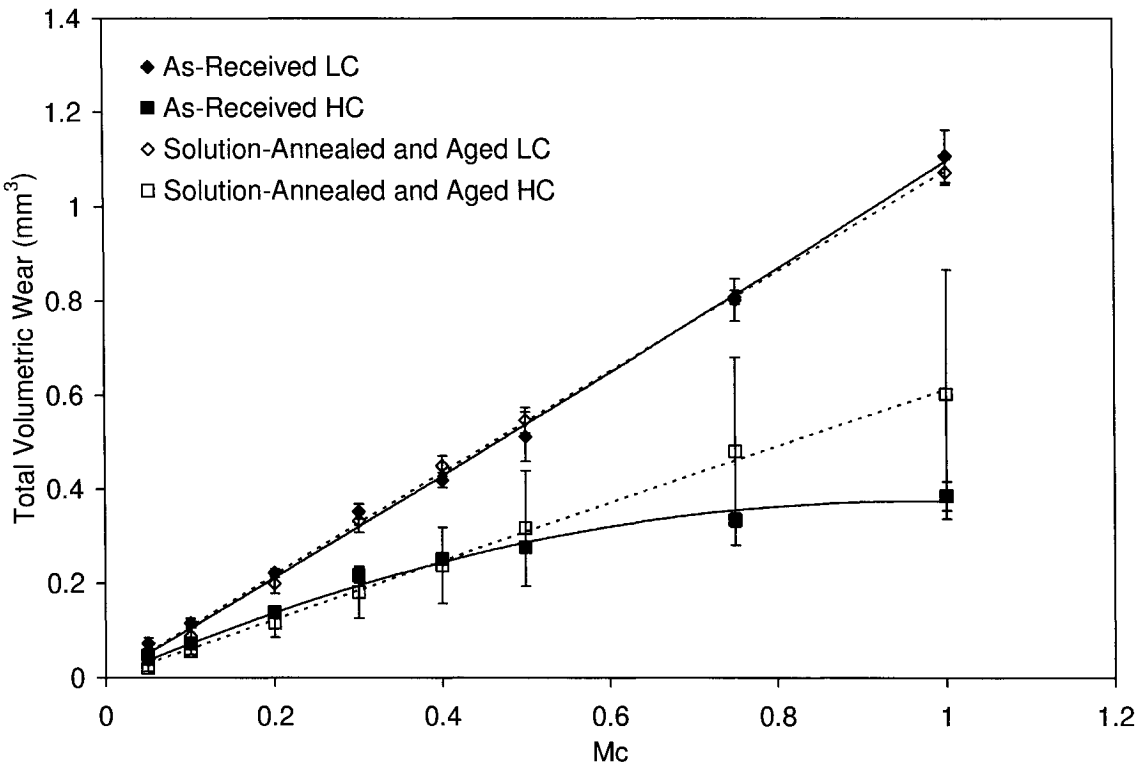

Figure 5.55. Wear curves of F1537 alloys solution-annealed at 1200°C for 24 h and aged at 650°C for 72 h after 1.0 Mc of testing compared to the as-received condition

In regards to the solution-annealed and aged HC specimens, it was found that the aging step had a significant adverse effect on the wear behaviour. Although a simple solution-anneal improved the wear properties of the HC alloy (Figure 5.50), further aging below the transformation temperature (allowing for some precipitation of carbides) had a detrimental effect on wear. SEM analysis of the solution-annealed and aged LC specimens revealed surface voids on both the pins and plates, while surface dimples were only observed on the plates as shown in Figure 5.56 (these features were prevalent prior to 0.50 Mc). However, by 1.0 Mc the surface voids on the pins were noticeably reduced and the surface dimples on the plates were no longer evident.

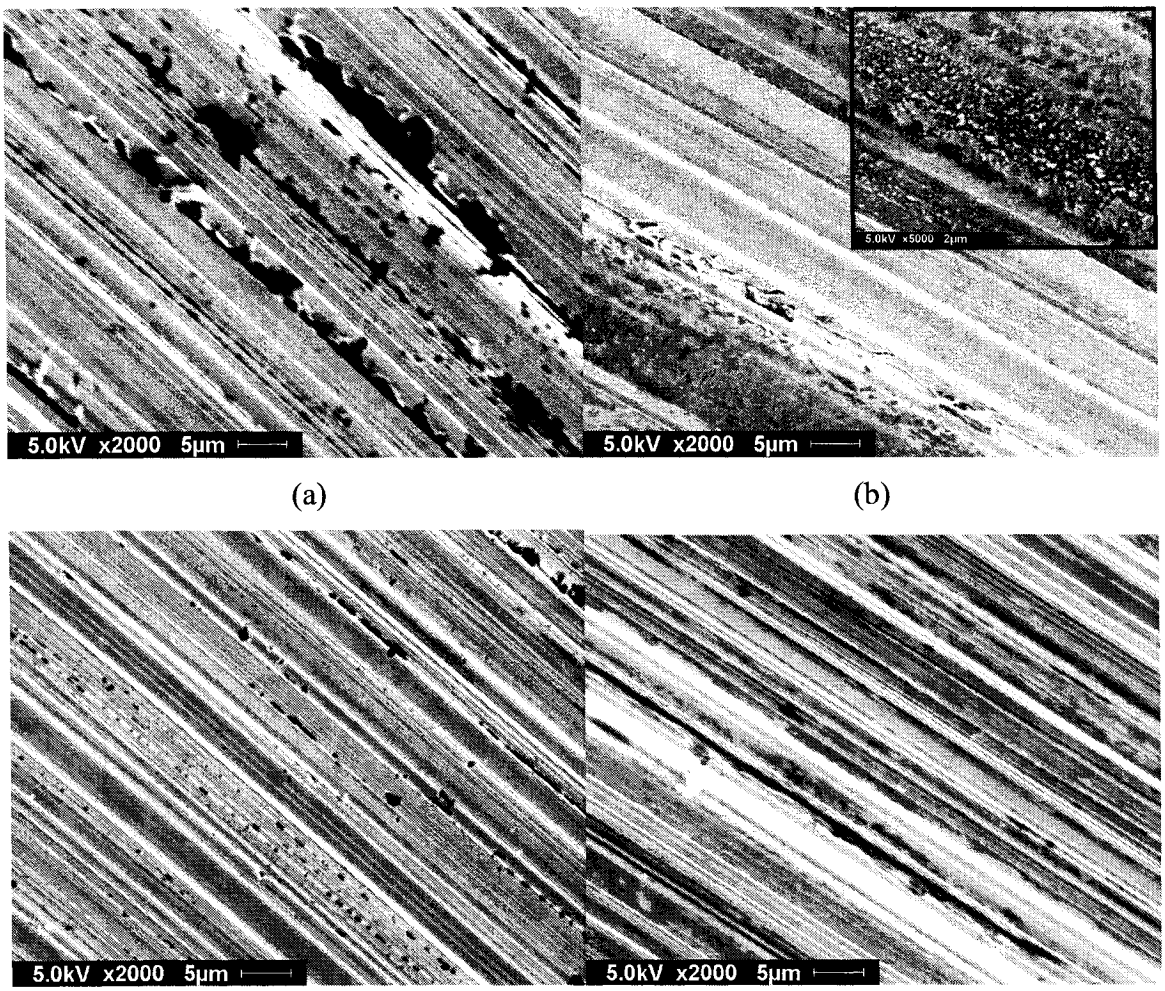

Figure 5.56. Wear surfaces of F1537 LC alloys solution-annealed at 1200°C for 24 h and aged at 650°C for 72 h: (a) pin specimen after 0.40 Mc, (b) plate specimen after 0.10 Mc, (c) pin specimen after 1.0 Mc and (d) plate specimen after 1.0 Mc

Analysis of the solution-annealed and aged HC specimens (shown in Figure 5.57) revealed isolated pitting on the pin surfaces and more extensive pitting on the plate surfaces in the earlier stages of testing (similar to Figure 5.52a and 5.52b). By the end of 1.0 Mc, the surface damage seemed to increase in the form of more pronounced groove marks, although the surface pitting on the plate specimens seemed to diminish.

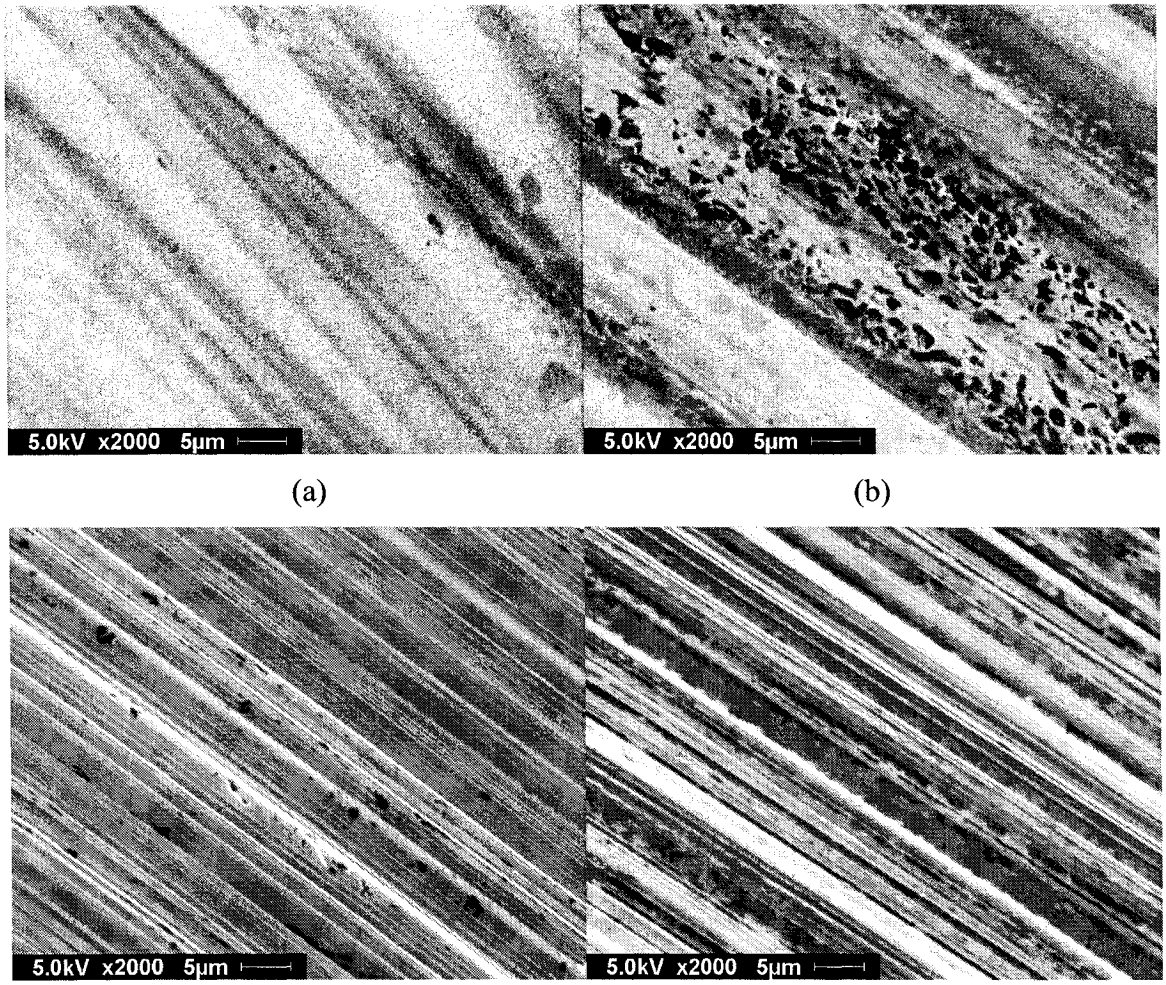

Figure 5.57. Wear surfaces of F1537 HC alloys solution-annealed at 1200°C for 24 h and aged at 650°C for 72 h: (a) pin specimen after 0.50 Mc, (b) plate specimen after 0.050 Mc, (c) pin specimen after 1.0 Mc and (d) plate specimen after 1.0 Mc

Profilometry measurements of the solution-annealed and aged LC and HC specimens can be seen in Figure 5.58. It was found that the surface profile of the wear zone for the solution-annealed LC alloy had the highest surface roughness of all the other as-received and heat treated alloys conducted in this study (see Table 5.7).

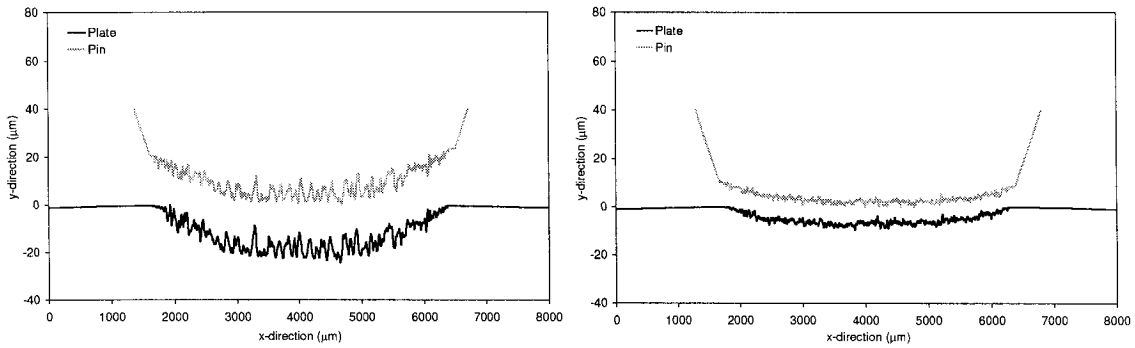

(a) (b)

Figure 5.58. 2D profilometry measurements of F1537 alloys solution-annealed at 1200°C for 24 h and aged at 650°C for 72 h: (a) LC and (b) HC

Table 5.7. R_q roughness values for the F1537 alloys solution-annealed at 1200°C for 24 h and aged at 650°C for 72 h

Alloy	Pin Surface		Plate Surface	
	As-Polished (µm)	Worn (µm)	As-Polished (µm)	Worn (µm)
Solution-Annealed and Aged LC	0.021	2.7	0.0059	3.0
Solution-Annealed and Aged HC	0.020	0.85	0.0060	0.82

In addition, the solution-annealed and aged HC alloy had a smaller contact curvature and a slightly higher roughness than the as-received HC alloy. As with all the other specimen conditions, x-ray diffraction revealed a dual FCC and HCP structure for both the worn and as-polished surfaces (Figure 5.59).

5.4.2.3. Aged

The final heat treatment which was studied in this work involved an aging treatment at 650°C for 72 h. It must be noted that only the aged LC alloy was tested for its wear behaviour in this work since machining of the aged HC alloy was not possible due to the extremely brittle nature of the material. As a result, only the wear data for the aged LC

alloy are reported. From the wear curves in Figure 5.60 it was found that there was no significant difference in the amount of wear when compared to the as-received condition. However, it was found that the aged LC alloy had the highest average wear rate of all the other alloy conditions in this study.

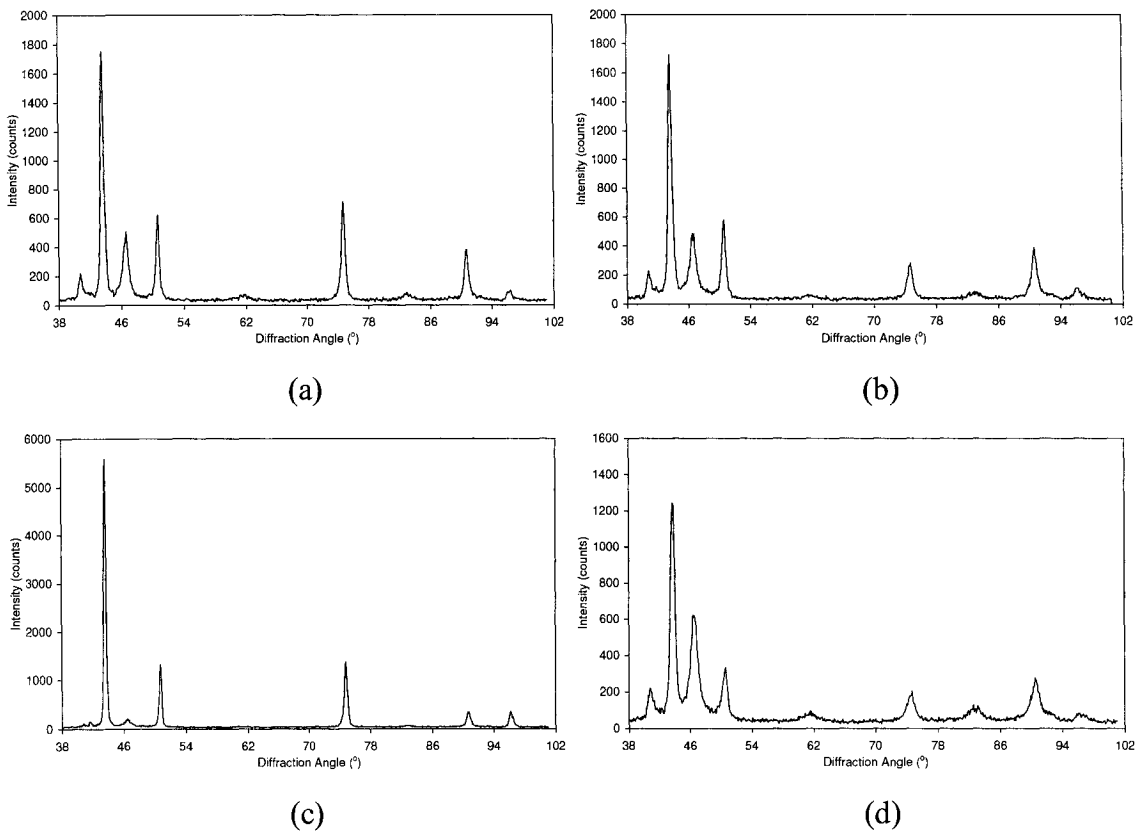

Figure 5.59. X-ray diffraction data for F1537 alloys solution-annealed at 1200°C for 24 h and aged at 650°C for 72 h: (a) LC worn specimen, (b) HC worn specimen, (c) LC as-polished specimen and (d) HC as-polished specimen (note: characteristic HCP peak at 46.5°)

SEM analysis of the wear surfaces revealed characteristic features inherent in the other LC alloys, such as surface voids and dimples (note: the surface dimples were only observed on the plate specimens). Figure 5.61 shows the presence of these features in the early stages of testing, but toward the end, the dimples were no longer visible and the surface voids were still prevalent on the pin specimens.

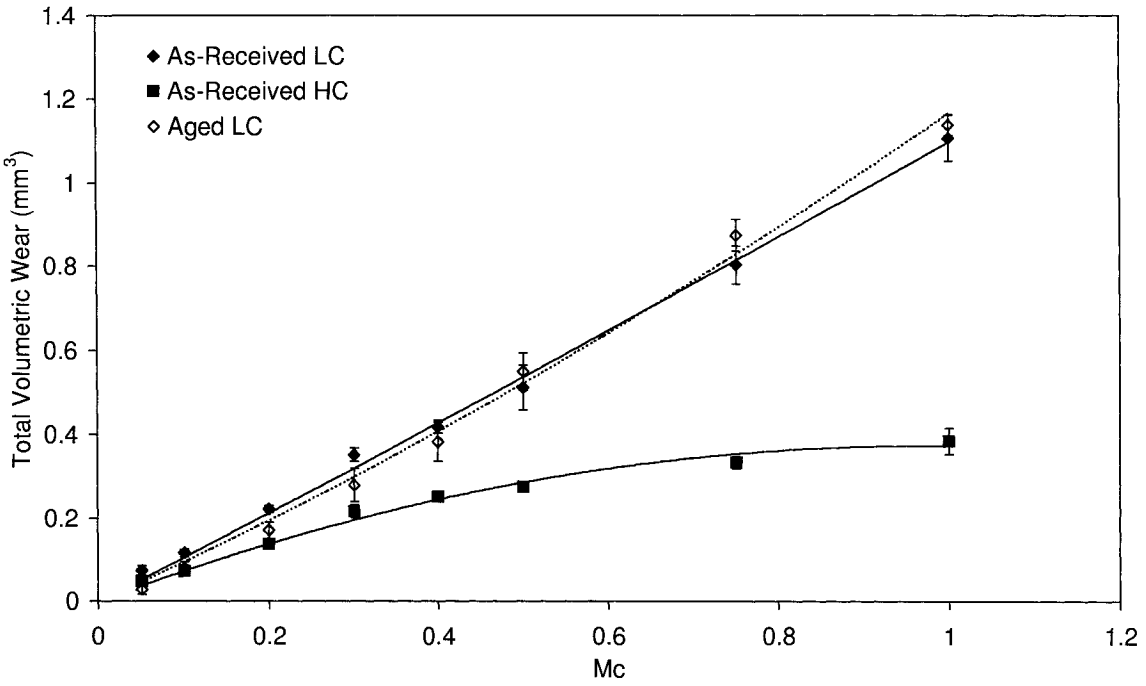

Figure 5.60. Wear curves of F1537 alloys aged at 650°C for 72 h after 1.0 Mc of testing compared to the as-received condition

The 2D profilometry measurements (Figure 5.62) of the aged specimens showed a relatively smooth surface (Table 5.8) in spite of the fact that the aged LC alloy had the highest amount of wear of all the as-received and heat treated materials tested. However, the width of the contact zone was slightly larger than that of the as-received condition and, in addition, the contact curvature was less than the as-received specimens, indicating an increase in wear volume. Finally, x-ray diffraction of the worn and as-polished surface revealed a predominately HCP structure that was similar to the neutron diffraction data for the bulk material (Figure 5.63). A complete summary of the wear results can be found in Table 5.9 for comparative purposes.

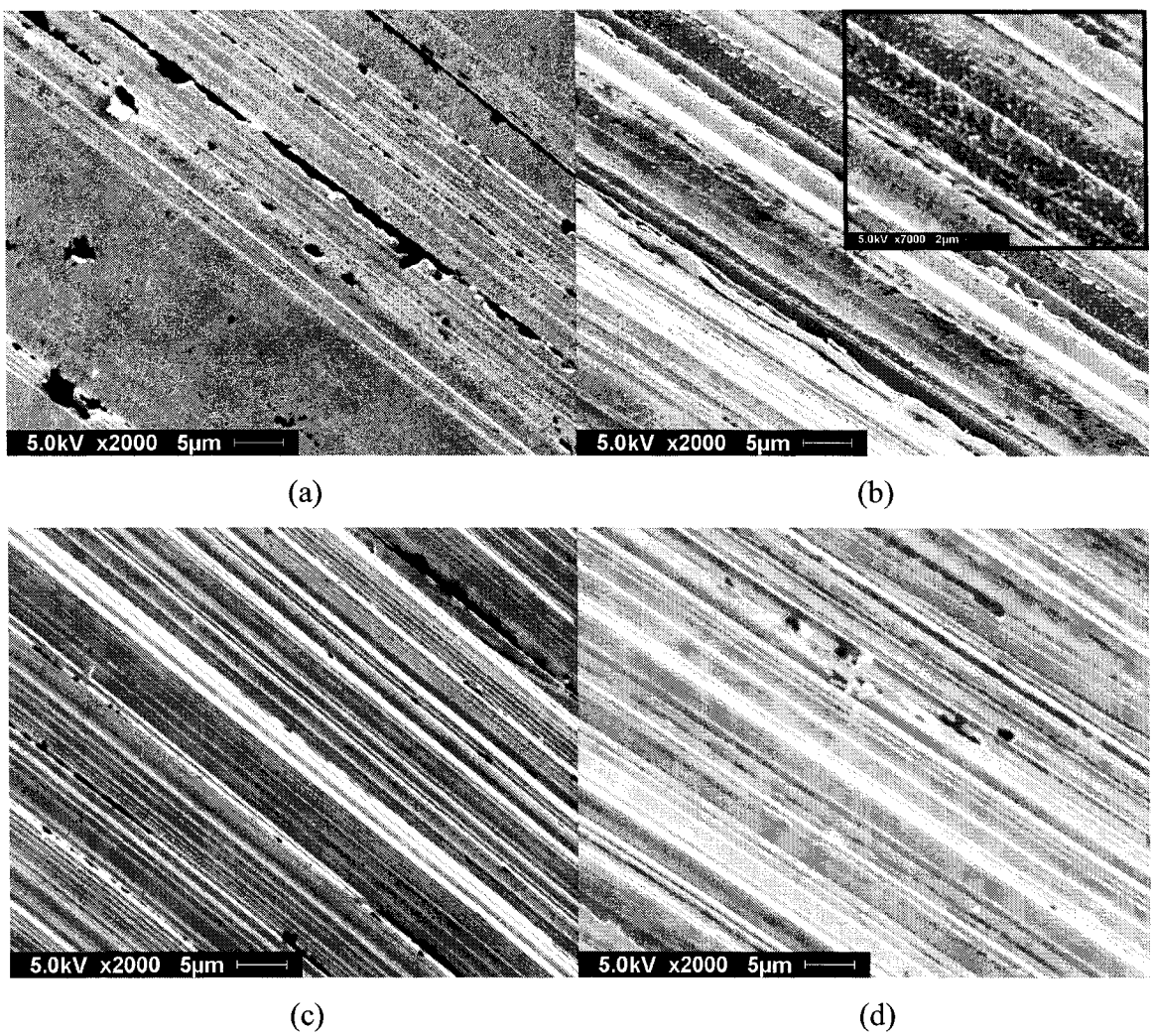

Figure 5.61. Wear surfaces of F1537 LC alloys aged at 650°C for 72 h: (a) pin specimen after 0.20 Mc, (b) plate specimen after 0.050 Mc, (c) pin specimen after 1.0 Mc and (d) plate specimen after 1.0 Mc

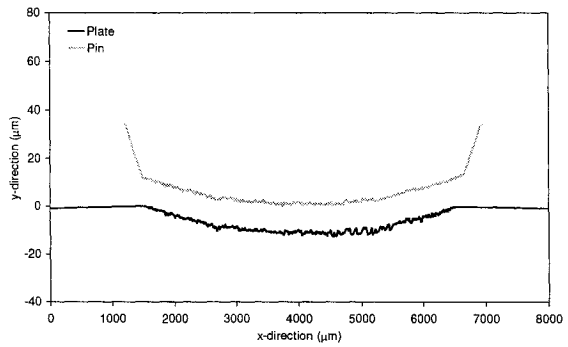

Figure 5.62. 2D profilometry measurements of F1537 alloys aged at 650°C for 72 h

Table 5.8. R_q roughness values for the F1537 LC alloys aged at 650°C for 72 h

Alloy	Pin Surface		Plate Surface	
	As-Polished (μm)	Worn (μm)	As-Polished (μm)	Worn (μm)
Aged LC	0.011	0.73	0.0057	0.50

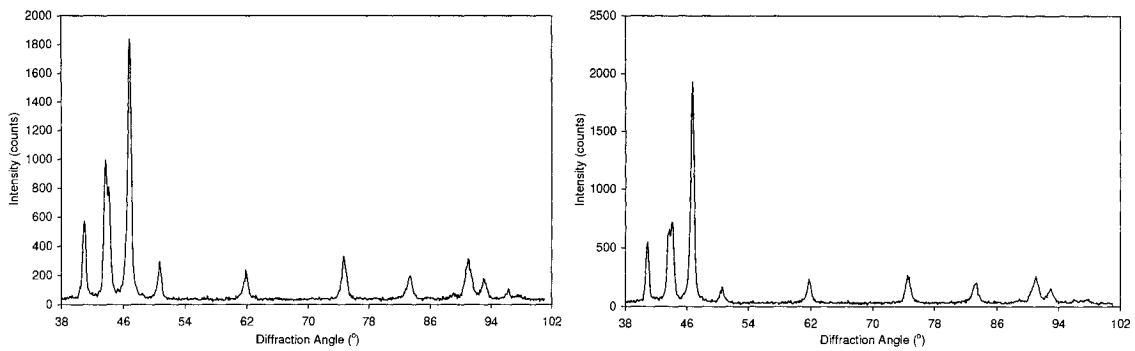

(a) (b)

Figure 5.63. X-ray diffraction data for F1537 alloys aged at 650°C for 72 h: (a) LC worn specimen and (b) LC as-polished specimen

Table 5.9. Summary of wear results

Alloy	R_q Roughness				Total Volumetric Wear (mm^3)
	Pin		Plate		
	As-Polished (μm)	Worn (μm)	As-Polished (μm)	Worn (μm)	
F1537 LC	0.025	1.5	0.0053	1.7	1.11
F1537 HC	0.027	0.60	0.0058	0.46	0.39
F75	0.033	0.34	0.020	0.45	0.24
As-Cast	0.014	0.054	0.0051	0.076	0.06
Solution-Annealed LC	0.0077	0.55	0.0065	0.58	1.09
Solution-Annealed HC	0.015	0.71	0.0064	0.69	0.24
Solution-Annealed & Aged LC	0.021	2.7	0.0059	3.0	1.07
Solution-Annealed & Aged HC	0.020	0.85	0.0060	0.82	0.60
Aged LC	0.011	0.73	0.0057	0.50	1.14

CHAPTER 6

Discussion

The microstructure of a material will dictate its mechanical properties, such as strength and ductility. In the following discussion, a correlation will be attempted between microstructure and wear.

6.1. As-received materials

6.1.1. Microstructure

Upon investigation of the as-received F1537 alloys, several microstructural features were noticed, in particular a fine grain structure, carbides (including carbide bands) and annealing twins. As previously mentioned, the as-received material was a thermomechanically processed CoCrMo alloy. Although, the precise steps in the manufacturing of the material were not readily available, the fact that the alloy was hot-worked would explain the fine grain structure. The fine equiaxed grains were a result of recrystallization during mechanical deformation, due to the elevated processing temperatures. The carbide precipitates identified in F1537 alloys were of the $M_{23}C_6$ and M_6C types. Several of the alloying elements in the material have a tendency to form carbides in the presence of C. Based roughly on the relative amounts of each element (see

Table 4.1), Cr, Mo and Co would be the most likely candidates to form carbides with a range of compositions. Of these three, Cr has the highest affinity for C and usually dominates the carbide composition as shown in Figure 5.2.[23] These carbide particles were mainly distributed at the grain boundaries, forming long bands, perpendicular to the circular cross section of the specimen. This inhomogeneous distribution of the second phase could be explained by the formation of deformation bands, due to the materials properties and the forging method used. This accumulation of strain may induce precipitation of carbides at elevated temperatures, by increasing the diffusion of C to the grain boundaries or it might be due to solidification. Due to prior mechanical and thermal processing of the as-received material, annealing twins were observed in the microstructure. Under the SEM, they had a different contrast, because of the different crystal orientation relative to the grain, affecting the scattering of the electrons from the microscope. Annealing twins are common in metals which have low SFE, as in Co and its alloys, and occur in association with recrystallization and growth of new grains, as a result of pre-existing stacking faults in the old grains.[105]

In the case of the cast structures a very coarse microstructure was observed, in contrast to the fine structures of the wrought F1537 alloys. The cast grain sizes were > 1000 μm and thus visible with the naked eye after polishing and etching the samples. The F75 alloy consisted of a dendritic structure and coarse interdendritic and grain boundary eutectic $M_{23}C_6$ carbides due to the solidification process. The eutectic carbides are usually comprised of $M_{23}C_6$ and M_6C lamellae [23] (giving a reddish-brown appearance in the stain-etched micrographs) and are intermixed with the α-Co matrix. The coarseness of the lamellar carbide colonies and the presence of satellite $M_{23}C_6$ carbides are indicative of a post heat treatment process of the as-cast material. Heat treatment of the as-cast alloy probably resulted in solutionization and reprecipitation of more $M_{23}C_6$ carbides as very fine secondary particles surrounding the primary carbides.[23] In the as-cast condition a coarse grain structure was also observed. The interdendritic and grain boundary carbides had a blocky morphology and were comprised of a fine eutectic structure of $M_{23}C_6$-M_6C/α-Co having a reddish-brown appearance and no fine satellite carbides. Thus, confirming the as-cast condition. The coarse grain size (> 1000 μm) and the absence of M_7C_3 carbides would suggest that a slow cooling rate was used in the

solidification process. M_7C_3 is a relatively uncommon carbide phase in contemporary Co-based alloys. However, it has been found that M_7C_3 carbides can occur in contemporary cast Co alloys (such as the F75) under rapid cooling conditions.[106]

6.1.2. Crystallography

Based on the neutron diffraction studies it was found that the crystal structure of the as-received materials were entirely FCC, even though the stable structure at room temperature is HCP. Due to the slow transformation kinetics from FCC to HCP (see section 2.1.1), cooling rates even as low as 0.01°C/s (i.e., furnace cooled) do not allow the material enough time to thermally transform. Hence, thermomechanical processing (which is normally performed at elevated temperatures in the α-Co region of the phase diagram) would ultimately yield a bulk FCC crystal structure.

6.1.3. Mechanical properties

The results from the punch test have shown that the mechanical properties of the as-received materials met all the strength requirements specified in the ASTM handbook. It should be noted that although the punch test is not an ASTM standard test for Co alloys, it has been shown to produce values that are quite similar to tensile values.[95] Of the four alloys tested, the as-received F1537 alloys had the highest YS's and UTS's, as expected. This is due to the wrought nature of the F1537 alloys and their fine grain structure. The YS of a material is dependent on several parameters, as shown in the Hall-Petch relationship:

$$\sigma_{YS} = \sigma_i + k_y d^{-\frac{1}{2}} \tag{6.1}$$

where σ_{YS} is the yield strength, σ_i is the overall resistance of the lattice to dislocation motion, k_y is the relative hardening contribution of grain boundaries and d is the grain size.

When comparing the two as-received F1537 alloys, both had similar UTS's with the HC alloy having the higher YS. Recalling Equation 6.1, the HC alloy had a smaller grain size than the LC alloy (~ half the size) which could account for the higher YS. In addition, the HC alloy had over four times the carbide fraction, which would also create higher resistance to dislocation motion, enhancing the strength of the material. From the results, it was found that the amount of work hardening in the LC alloy was almost twice that of the HC alloy based on the following equation:

$$Work\ Hardening = \frac{UTS - YS}{YS} \tag{6.2}$$

where *UTS* is the ultimate tensile strength and *YS* is the yield strength.

A list of work hardening values for the as-received materials is shown in Table 6.1. In previous work conducted by Varano et al.[80] it was shown that SIT from FCC to HCP can occur in Co-based alloys and that C is an FCC stabilizer by raising the stacking fault energy of the Co matrix. In that work it was found that the LC alloy experienced more SIT than the HC alloy when plastically deformed. And it may be possible that this change in structure during deformation may account for the higher UTS and EL by offsetting the inhomogeneous deformation that leads to failure.[107] This phenomenon has also been observed in certain steels which undergo transformation induced plasticity (TRIP) due to SIT.[108]

In the case of the cast alloys, both the F75 and as-cast alloys had strength properties inferior to the wrought alloys. In comparison to the F1537 HC alloy, the YS's and UTS's of the cast alloys was ~ 1.4 times lower. The main factors which account for the poor properties of the cast alloys are: very coarse grain sizes, dendritic structures, element segregation and porosity. The coarse grain sizes would reduce the YS strength according to Equation 6.1. The dendritic structure would present poor resistance to dislocation motion or advancing cracks prior to failure (i.e. transgranular cracks would arise causing catastrophic failure). In other words, element segregation and prior porosity could act as nucleation sites for microvoids leading to crack initiation, lowering the strength and overall elongation of the alloys.

In addition, the F75 is a modified cast material subjected to heat treatments in order to improve on the mechanical properties of the material. However, as can be seen in Figures 5.32 and 5.33, the F75 and as-cast alloys exhibited the same properties, regardless of post-treatment of the F75 alloy.

Table 6.1. Work hardening values for the as-received materials

Alloy	YS (MPa)	UTS (MPa)	EL (%)	Work Hardening (UTS-YS)/YS
F1537 LC	860	1200	18	0.40
F1537 HC	990	1260	10	0.27
F75	720	980	17	0.36
As-Cast	710	960	17	0.35

For the microhardness measurements direct comparisons could not be made between the wrought and cast alloys due to the microstructural differences (i.e. grain size and carbide size differences). However, between the F1537 alloys it was found that the microhardness of the HC alloy was significantly higher than the LC alloy. Considering the similar grain sizes between the LC and HC alloy, resistance to local indentation was probably due to the higher carbide fraction of the HC alloy. Even though their tensile strengths were similar (Diff. = 5.1 %), there was a greater difference in their microhardness values (Diff. = 18 %). For certain materials, such as steel, hardness can be a good indication of tensile strength. But the correlation between strength and hardness for Co alloys is not well established. The discrepancy between the tensile and microhardness values for the LC and HC F1537 alloys may be an indication that the alloys are sensitive to the mode of deformation (i.e tension versus compression). For the cast alloys, comparisons could be made with respect to the matrix and carbide microhardness values due to the coarse microstructure. The matrix microhardness was found to be higher for the as-cast alloy than the F75 alloy, which was probably due to the post-treatment of the F75 alloy, which reduced the overall solute content of the matrix via

carbide precipitation and possibly decarburization (if post-treatment was conducted under atmospheric conditions). In terms of the carbide phases, it was found that the carbides in the as-cast alloy were significantly higher than those found in the F75 alloy. In section 5.1.1 it was shown how the carbide structures for the as-cast and F75 alloy differed. Both carbide phases were identified as eutectic $M_{23}C_6$-type carbides. However, there was a difference in the eutectic structure. The as-cast alloy was shown to have had a very fine eutectic structure which could only be resolved at high magnification in the SEM (Figures 5.8 and 5.9). The fineness of the eutectic carbide structure in the as-cast alloy is what probably accounted for its relatively high hardness in comparison to the F75 alloy. For the F75 alloy, the primary carbides had a coarse lamellar structure of $M_{23}C_6$-M_6C plates interlayed with matrix FCC-Co (Figures 5.6 and 5.7). This carbide structure was seen in more recent studies [109] and described as a "depleted carbide" because it was believed that the carbides were partially dissolved and reprecipitated due to post heat treatment of the as-cast alloy.[23]

6.2. Effect of heat treatment

6.2.1. Microstructure

Solution-annealing of the LC and HC alloys at 1200°C for 24 h resulted in grain growth (including coarse annealing twins) and successfully dissolved most of the carbides, due to atom diffusion and grain boundary movement. The smaller grain size of the HC alloy relative to the LC alloy can be explained by the higher volume fraction of carbides, which may inhibit grain boundary movement to some degree. In the case of the LC alloy, the treatment eliminated the carbide bands, which were observed in the as-received material, but remnants of the bands were still present in the HC microstructure (again due to the higher fraction of carbides prior to heat treatment). Recalling Section 4.3.1, long treatment times were required in the Co system for transformation and diffusion to occur. Even at elevated temperatures such as 1200°C, the 24 hr treatment was insufficient to fully dissolve all the carbide precipitates in the HC alloy. This retardation in the precipitation kinetics at 1200°C is not thought to be a diffusion problem but a carbide stability issue.[110] $M_{23}C_6$ and M_6C are relatively stable carbides (M_6C having the highest

stability). As was shown in Figure 4.6, there was an initially high rate of carbide dissolution within the first 24 h of treatment, followed by a decreased dissolution rate. It is believed that the initial high rate of dissolution is related to the $M_{23}C_6$ carbides dissolving into the matrix leaving the more stable M_6C carbides to dissolve at a slower rate. Also, an additional rate-limiting step in the dissolution of carbides is the transformation of the $M_{23}C_6$ to M_6C during heat treatment. Since in this work the treatment time used was within the time of high rate of dissolution, a combination of $M_{23}C_6$ and M_6C carbides were observed in the microstructures.

Solution-annealing at 1200°C for 24 h followed by aging at 650°C for 72 h resulted in additional grain growth in the LC microstructure which maintained a larger grain size over the HC microstructure. Despite the 72 hr treatment time at 650°C the grain sizes only increased slightly and the carbide sizes remained relatively unchanged. Nevertheless, there was a slight increase in the carbide fraction for the LC alloy and an order of magnitude increase for the HC alloy. In the case of the HC microstructure, precipitation of carbides was observed intragranularly along twin boundaries. Twin boundaries, although different from grain boundaries, can act as potential sites for the nucleation and growth of secondary phases.[111] And at such low temperatures, short range diffusion of C to twin boundaries may be preferred over longer range diffusion to grain boundaries. An increase in the carbide fraction with the aging process was expected, however it was not desired. In any case, considering the length of aging time (72 h), precipitation of carbides was still approximately four times less that of the as-received condition.

When the as-received F1537 alloys were simply aged at 650°C for 72 h from room temperature minor changes in the microstructures were observed. For the LC and HC alloys the grain sizes only increased by 0.20 μm and there was an increase in carbide fraction (which was more prevalent in the HC microstructure), although the carbide sizes remained relatively constant. Carbide precipitation at the grain boundaries may have been facilitated by the fine grain size. In addition, grain growth did not occur probably due to grain boundary pinning and insufficient energy for grain growth due to the low temperature.

6.2.2. Crystallography

The neutron diffraction data for the alloys solution-annealed at 1200°C for 24 h revealed that the bulk material had an FCC crystal structure. In fact, it would be expected that the solutionizing treatment would increase the metastable FCC phase and the stability of the FCC structure through carbide dissolution (Section 6.1.3). In addition, heat treatment would also reduce the precursors to transformation, namely prior defects such as: dislocations and stacking faults. It is believed by some researchers that the motion of single partial dislocations in the close-packed plane of the FCC lattice can form intrinsic stacking faults and that a series of intrinsic stacking faults can act as an HCP embryo, leading to the nucleation and growth of the HCP phase.[78,112] Thus, by reducing the dislocation density and already present stacking faults through heat treatment, the nucleation sites for HCP formation are also reduced.

Solution-annealing at 1200°C for 24 h followed by aging at 650°C for 72 h was intended to produce a coarse homogenized microstructure with HCP grains. From the neutron diffraction results, it was found that the material maintained a bulk FCC crystal structure despite the 72 hr transformation treatment. This was unexpected since previous studies have found that 72 h at 650°C was sufficient in transforming the crystal structure entirely to HCP.[35] In addition, since no transformation took place after 72 h, it was felt that perhaps a longer aging time was required. Therefore, another heat treatment was conducted on the F1537 LC alloy which involved a solution-anneal at 1200°C for 24 h followed by aging at 650°C for 144 h (or 6 days) in order to see the effect of time on the transformation kinetics. From this treatment it was found that even after aging for 144 h at 650°C (with a prior solution-annealing step) the material maintained a bulk FCC structure, as shown from the neutron diffraction analysis in Figure 6.1.

The ineffectiveness of the transformation treatment may be explained by the prior solution-anneal treatment which may have stabilized the FCC structure to the point that the activation energy for transformation through the subsequent aging treatment at 650°C may have been energetically unfavourable. More specifically, grain growth would decrease the grain boundary area and possibly reduce the nucleation sites for transformation to occur, in addition to reducing the dislocation and stacking fault densities. This is supported by the fact that in two concurrent studies conducted on SIT in

CoCrMo alloys, it was found that the volume fraction of HCP was reduced with increasing grain size.[79,113] Nevertheless, in an athermal HCP study conducted by Huang and López [78] it was found that larger grain sizes increased the volume fraction of the HCP phase. The reason being that by increasing the grain size, the defect and stacking fault densities within the grain were increased, thus increasing the nucleation sites for HCP formation.

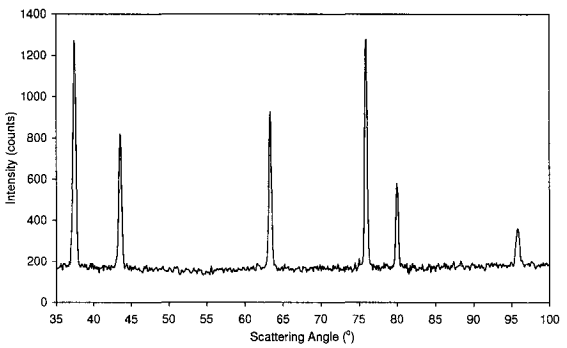

Figure 6.1. Neutron diffraction of F1537 LC alloy solution-annealed at 1200°C for 24 h and aged at 650°C for 144 h revealing a bulk FCC structure

However, in their study the crystallography measurements were conducted using x-ray diffraction techniques (a surface technique) and all their specimen surfaces were mechanically polished prior to analysis. Mechanical polishing of the wear specimens conducted in the present study suggested the occurrence of SIT due to the presence of the HCP phase through x-ray diffraction for all alloy conditions whether as-received or heat treated. In addition, despite the fact that all the specimens heat treated at 1200°C in this study were quenched in water (which should produce athermal HCP), neutron diffraction analysis revealed no HCP phase.

When the as-received alloys were directly aged at 650°C for 72 h, the intention was to produce a fine grain HCP structure with carbides. Through neutron diffraction analysis it was found that the LC alloy indeed experienced a transformation in crystal structure. However, the bulk crystal structure was not entirely HCP. Rather, the material had a dual

structure of 84 vol% HCP and 16 vol% FCC. As mentioned earlier, even though the alloy was aged for a period of 144 h, it would seem that prior solution-annealing hindered the transformation from occurring. But when aged directly from the as-received state, the transformation was able to occur. Coming from the as-received state (i.e. having a prior thermomechanical history) the alloys may have had a higher propensity for transformation due to higher defect and stacking fault densities, smaller grain sizes and residual stresses from the prior deformation process. Thus, providing the needed driving force for transformation to take place at 650°C. The extent of the transformation was quantifiable for the LC alloy using neutron diffraction, but the HC alloy could not be quantified since it was not analyzed using this technique. However, x-ray diffraction revealed qualitatively that the HC alloy did have a predominately HCP structure (although the exact volume fraction was not determined). It has not been well documented but the presence of HCP crystals in Co may be restricted to tiny particles or platelets within pre-existing FCC grains. This is unlike other SIT materials, such as TRIP steels, in which entire grains of retained austenite are transformed to martensite. In the case of SIT in bulk FCC-Co, it has been found that 100% transformation from FCC to HCP was unattainable. In fact a maximum of ~ 60% HCP was achieved in uniaxial room temperature compression tests ($\geq$ 0.25 strain) after which fracture occurred. Neutron diffraction studies revealed peak broadening with the development of the HCP phase in deformed Co specimens, suggesting large strain fields associated with the nucleation and growth of tiny platelets.[114] The limitation in the extent of transformation may be due to competing events of FCC twinning and slip (which do not lead to HCP formation) during deformation. During deformation dislocations and stacking faults are created which may lead to twinning due to the local stability of the FCC lattice. This may explain why, when the alloys were simply aged at 650°C for 72 h, a higher volume fraction of HCP (84%) resulted through isothermal transformation compared to SIT, since no new dislocations or twin embryos were being created. Thus, allowing the transformation to proceed to a larger extent, although not completely.

6.2.3. Mechanical properties

The solution-anneal heat treatment at 1200°C for 24 h resulted in a decrease in YS (21% change for LC and 31% for HC) and UTS (5.8% for LC and 10% for HC), and improved the EL (44% for LC and 120% for HC) of the alloys. The reduction in the YS in comparison to the as-received condition may be due to grain coarsening and a reduction in the carbide fraction by at least an order of magnitude for the LC and HC alloys. The similar grain sizes and carbide fraction after heat treatment may have accounted for the similar YS's between the LC and HC alloys. In terms of the deformation behaviour, it has been previously found that increasing the grain size and increasing C in solution may suppress the SIT to HCP due to fewer sites for heterogeneous nucleation, lower dislocation and stacking fault densities and higher stacking fault energy. It is believed that when SIT is suppressed then deformation may occur by twinning (depending on the stacking fault energy).[81,115] However, considering the localized phenomenon of SIT in Co-based alloys (i.e. the production of fine HCP platelets rather than bulk grains of HCP) a combination of SIT and twinning may occur—all leading to higher UTS, EL and increased work hardening.[77]

For the alloys which were solution-annealed at 1200°C for 24 h and aged at 650°C for 72 h it was found that the YS and UTS decreased, while the EL increased compared to the as-received condition. The most obvious contribution to this reduction is the larger grain sizes and the lower carbide fractions. In the previous case, where the alloys were simply solution-annealed, there seemed to be no significant difference in strength between the LC and HC alloys. However, in this case (where the materials were aged after solution-annealing) the LC alloy maintained similar strength levels with the previous heat treatment, while the HC alloy experienced a significant improvement in both YS and UTS, as well as a significant reduction in EL. The major difference between the LC and HC alloys after solution-annealing and aging was their carbide fraction. The HC alloy had over an order of magnitude higher carbide fraction (1.5%) than the LC alloy (0.15%). It is clear that the increased presence of carbides will impede dislocation motion and increase the strength of the material while lowering its EL.

The final heat treatment involved simply aging of the materials at 650°C for 72 h. From the strength results it was found that the YS's and UTS's for both the LC and HC

alloys dramatically increased while the EL's decreased. From previous microstructural and crystallographic analysis, several factors may have contributed to this, namely: grain size, carbide fraction and matrix crystal structure. Despite the extended heat treatment time, the microstructures retained a fine grain size (increasing the grain boundary fraction) which would increase the local dislocation density and resistance to dislocation motion, giving rise to higher strength levels. In addition, the higher carbide fractions would also have a positive contribution to the strength of the materials. Finally, and what is probably of greater influence on the strength and ductility of the materials is the crystallographic transformation of the matrix phase from FCC to HCP. Recalling Section 5.2.2.3, the volume fraction of HCP was 84%. Such a change in the bulk crystal structure would definitely have an effect on the strength of the material since FCC and HCP crystals deform differently under plastic strain. From deformation theory, twinning is the most prevalent mode of deformation in HCP materials. This is due to the fact that the HCP crystal has an insufficient number of slip systems to satisfy the necessary shape change for plastic flow to occur. This is not to say that all HCP materials are more difficult to deform compared to other materials having different crystal structures, since alloys of Mg, Ti and Zn are known to possess reasonable ductility. However, twinning in HCP-Co may be relatively more difficult than twinning or slip in FCC-Co due to the nature of the HCP phase. This may be due to the nature of the HCP phase which forms as tiny platelets in the FCC matrix. Discrete particles of HCP bound by an FCC lattice or surrounded by other HCP platelets may inhibit the rotation necessary for deformation twinning to occur.[116]

6.3. Wear

The following sections attempt to correlate the influence of the microstructure and its constituents on the wear behaviour of Co based alloys used for orthopaedic surgical implants. As previously mentioned in Section 2.3, classical wear theory states that load, speed, temperature, surface roughness and hardness all influence the wear behaviour of two contacting surfaces. In the context of the present study, the influence of hardness

would best relate to the microstructural effect on wear, since hardness is a material property.

6.3.1. Effect of microstructure

In this section, the more obvious microstructural features, such as grain size, carbides and matrix structure will be considered in the wear analysis. It must be noted that isolating certain microstructural features for comparison was difficult since the heat treatments would often alter more than one parameter at once. In any case, a correlation will still be attempted.

6.3.1.1. Grain size

Many crystalline materials are polycrystalline in nature. This means that they are composed of many crystals, each having a specific orientation relative to one another. Of course, there are also single crystal materials. Usually, single crystal materials are anisotropic in their properties (i.e. different crystallographic directions will yield different properties). However, polycrystalline materials will be isotropic if the crystals (or grains) in the microstructure are randomly oriented. Since grain size will affect the hardness (or strength) of a material, grain size may have a strong influence on the wear behaviour of MM surfaces? In Figure 6.2 the wear behaviour of the F1537 LC and HC alloys is plotted with respect to grain size (for both the as-received and heat treated conditions). The scatter in the results suggest that there is no direct influence of grain size on wear. Nevertheless, grain size may have a secondary effect on the underlying mechanism controlling the wear behaviour of these materials (e.g. work hardening and SIT characteristics). At this point, no definitive explanation can be given on this observation.

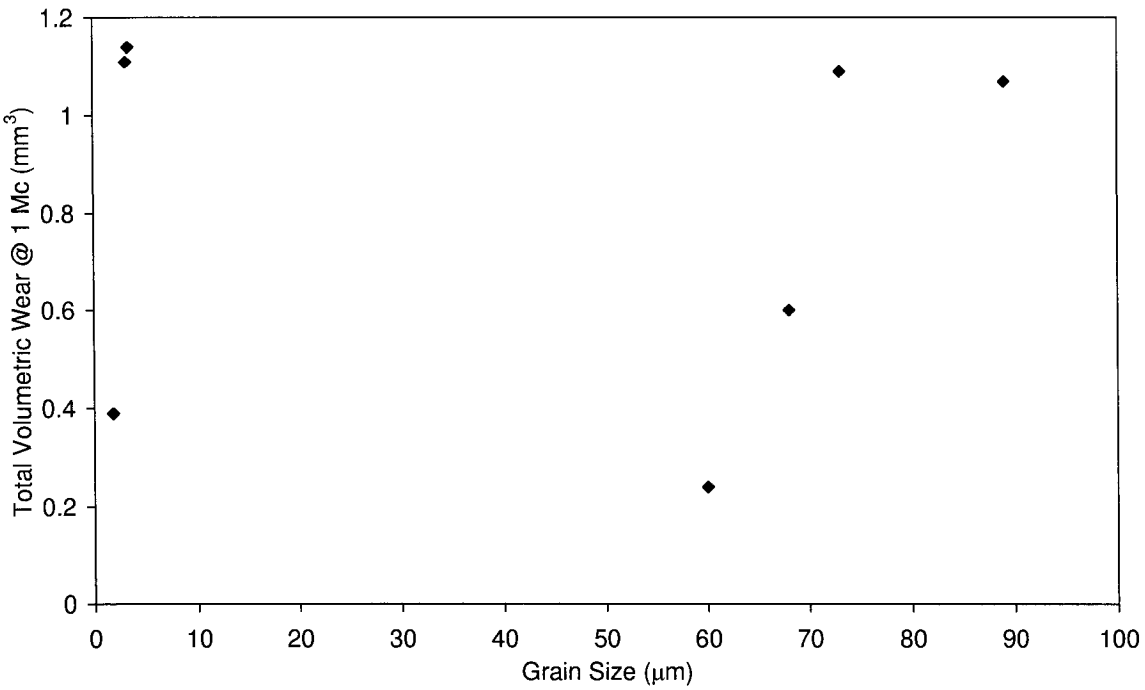

Figure 6.2. Wear behaviour of as-received and heat treat alloys after 1.0 Mc as a function of grain size

6.3.1.2. Carbides

Carbides are considered a very important second phase material with respect to wear due to their relatively hard nature. In metal alloy systems carbides have been found to have a beneficial effect on the strength of a material. In terms of wear resistance, carbides are believed to enhance the wear behaviour of materials not solely due to their high hardness characteristics, but as a protective barrier against matrix delamination.[83] This protective nature of the carbide phase will depend on the nature of the contacting surfaces (i.e. similar or dissimilar surfaces), the carbide fraction, shape and morphology. In this study identical surfaces were in contact with one another (having more or less identical microstructures). Therefore, it is unclear if the carbide particles will act as a protective barrier in this situation. However, it is clear that the presence of carbides in a material will cause abrasive damage to a counter surface.

Due to the nature of carbides it is also clear that these hard phases may experience cracking, sustain wear damage and may be pulled out entirely by opposing hard phases or

other acting wear mechanisms. Thus, the question remains: do carbides have a beneficial effect on the wear behaviour of MM surfaces? Figures 6.3a and 6.3b attempt to answer this question by plotting the wear as a function of the carbide fraction in the microstructure and average carbide size, respectively. From this set of Figures it would seem that there may be a general decrease in wear with increasing carbide fraction, although there seemed to be no direct correlation since there was a wide scatter in the data.

For example some specimens with relatively low carbide fraction exhibited low wear and conversely, some specimens with relatively higher carbide fraction exhibited higher wear, as shown in Figure 6.3a. On the other hand, Figure 6.3b reveals a stronger effect of carbide size on the wear behaviour, suggesting that larger carbides may be more beneficial to the wear resistance of the material as explained in Section 2.6. From 0.55 to 1.6 μm there seemed to be a dramatic decrease in the volumetric wear as the carbide size increased by an order of magnitude.

However, when the carbide size increased by another order of magnitude, the wear seemed to decrease and then increase. The scatter in the data at larger carbide sizes may be an indication that there is some optimum carbide size for reduced wear or that there may still remain some other parameter controlling the wear behaviour. The argument that larger carbides may be better against wear, since they are more difficult to gouge out compared to smaller carbides (although fracture of large carbides may occur), may not be an accurate conclusion for the present scenario of self-mated materials.[77] Actually, in the present study it was found that for the F75 and as-cast alloys (which contained the coarsest carbides of all the other materials) had carbides which were damaged and even pulled out (Figure 6.4). Thus, carbide phases, regardless of size, may be ineffective against wear in self-mating applications such as this.

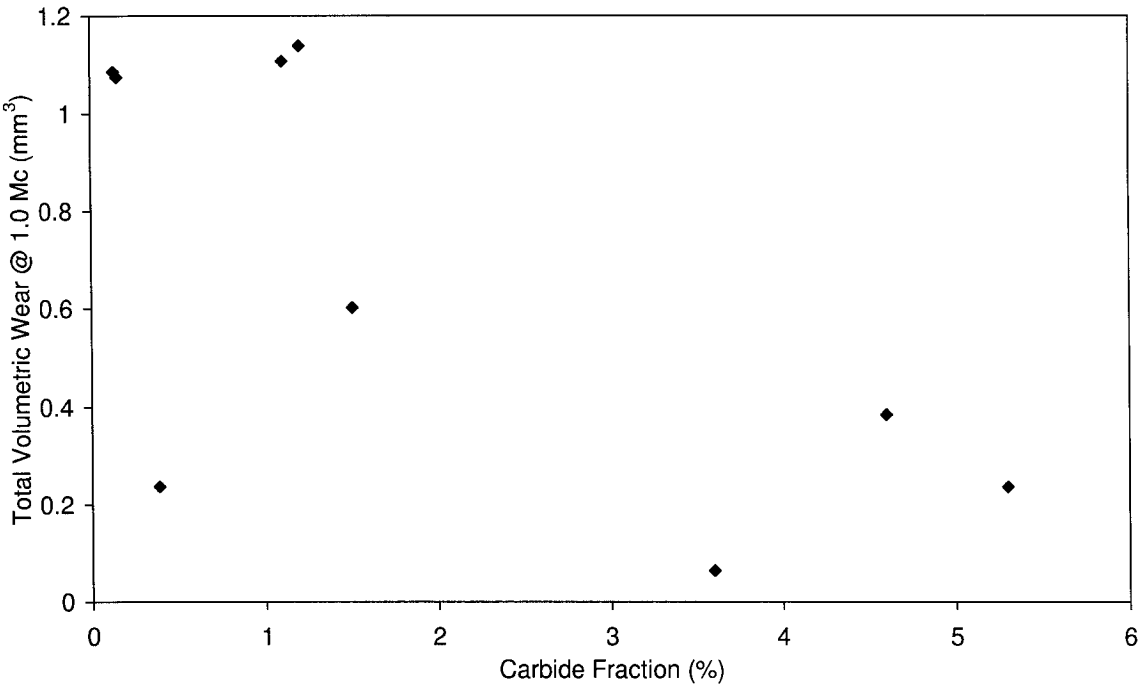

(a)

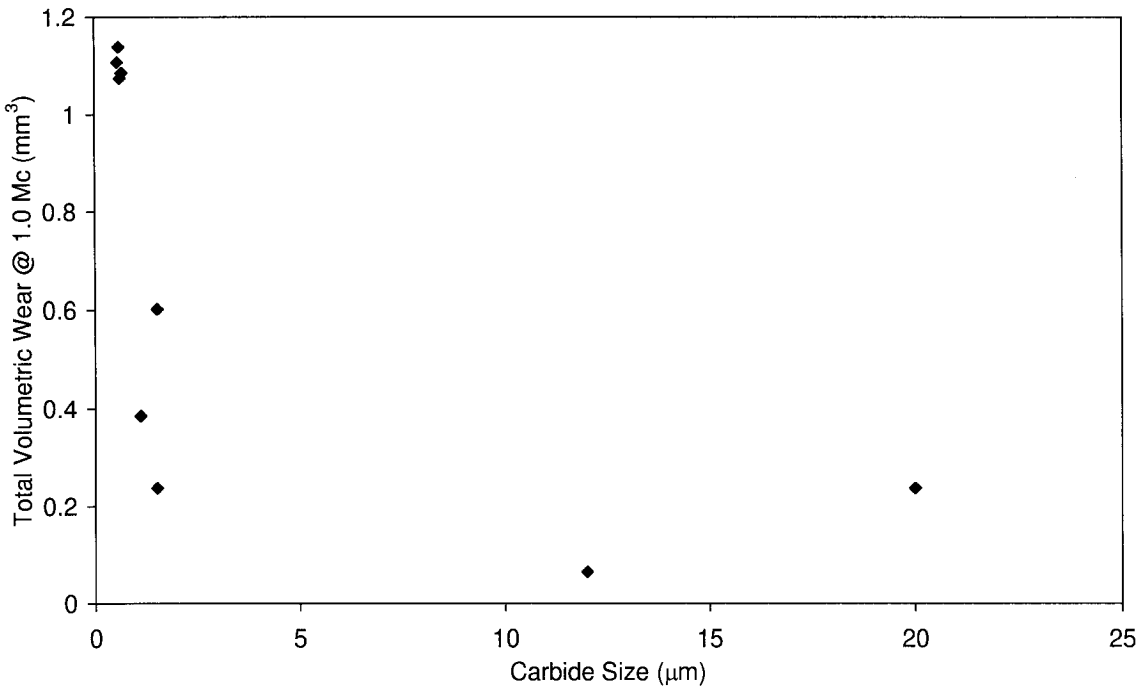

(b)

Figure 6.3. Wear behaviour of as-received and heat treat alloys after 1.0 Mc as a function of (a) carbide fraction and (b) carbide size

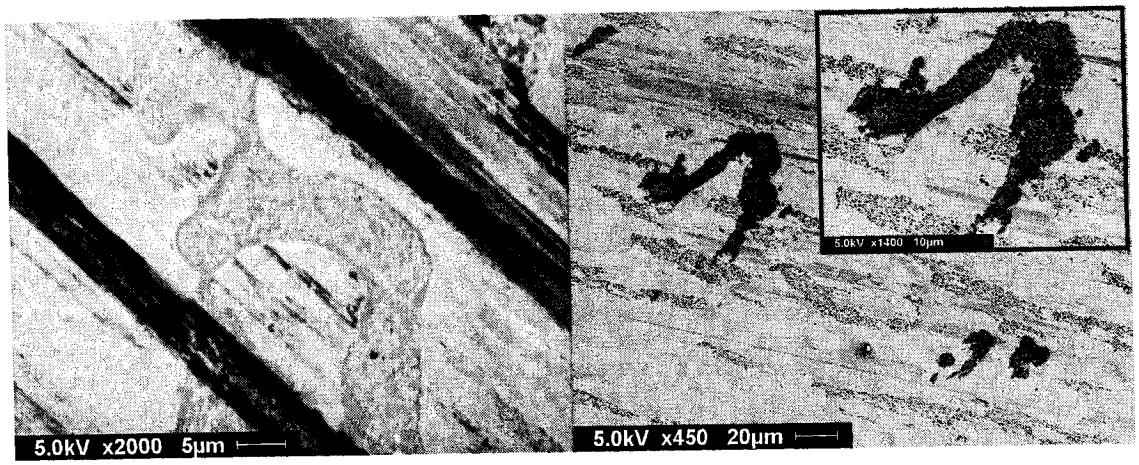

(a) (b)

Figure 6.4. SEM micrographs of carbide damage and pullout: (a) F75 and (b) as-cast specimens

6.3.1.3. Matrix structure

It was mentioned in the previous section that carbides may act as a protective barrier against abrasive wear of the matrix. At the same time, the matrix helps to support the discontinuous carbides. Thus, there is an interdependence between matrix and carbide phases. If carbides are beneficial against wear then it is desirable that the carbide particles remain attached to the matrix phase. This is difficult since many processes can lead to carbide detachment, resulting in third-body wear.

In the present study, all the materials (both as-received and heat treated) were primarily FCC, with the exception of the specimens which were directly aged from the as-received condition at 650°C for 72 h. These latter specimens experienced isothermal transformation with a final HCP volume fraction of 84 %. In addition, the carbide phases identified were primarily of the $M_{23}C_6$-type mixed with M_6C-type carbides. Both carbide types were cubic having a complex FCC structure. In general, carbides have good coherency with the surrounding matrix. Even though there are crystal structure differences between the carbides and matrix, good coherency is still attained.[117] Problems may arise when local changes occur at the carbide/matrix interface due to deformation, SIT and environmental changes which may weaken the bond between the carbide and matrix, since it is at these interfaces where stress and corrosion can concentrate and initiate. An attempt was made to compare the effect of the Co matrix crystal structure on

the wear behaviour of these alloys. Unfortunately, only one of the heat treatments resulted in a thermal transformation from FCC to HCP. In addition, the transformation was incomplete since only 84 % of the bulk crystal structure transformed.

Recalling Figure 5.61, the wear curves for the as-received LC alloy and the aged LC alloy showed no significant difference in the total volumetric wear except for the fact that the wear after 1.0 Mc was highest for the aged LC alloy. However, when comparing the wear rates for both alloys over the 1.0 Mc test period, it was found that the aged LC alloy was significantly higher as shown in Figure 6.5b. In fact, except for the as-received LC and aged LC alloy conditions, all the other materials exhibited a decrease in wear rate over the 1.0 Mc test period. This observation may be an indication that the HCP phase is detrimental to the wear behaviour of the material.

As previously mentioned, the aged LC alloy was the only material which had a bulk HCP structure prior to wear testing (84 vol%). All the other materials were entirely FCC, according to the neutron diffraction data (see Section 5.20). In addition, surface contact due to wear testing may have resulted in SIT of the remaining FCC structure, which may have worsened the wear behaviour—thus, the observed high wear rate.

With respect to the other materials, each had a starting bulk FCC structure. However, the susceptibility to SIT from FCC to HCP may have been different for each one. For example, solution-annealing may have added some stability to the FCC matrix through grain growth, the elimination of potential sites for HCP nucleation and through carbide dissolution.

On the other hand, aging the alloys below the transformation temperature may have reduced the stability of the FCC matrix even though transformation did not occur (in the case of the materials which were aged after prior solution-annealing). In addition, quenching all the materials after heat treatment may have also lowered the stability of the FCC structure, even though athermal martensite did not occur, by introducing defects in the lattice (acting as potential HCP nucleation sites).

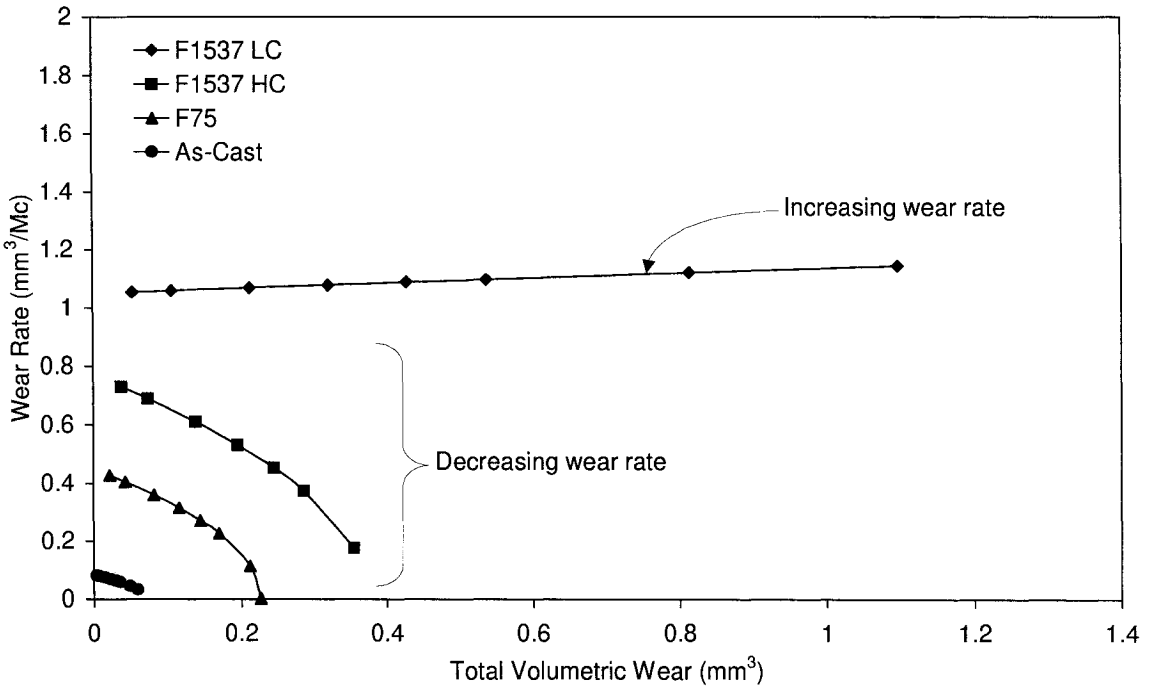

(a)

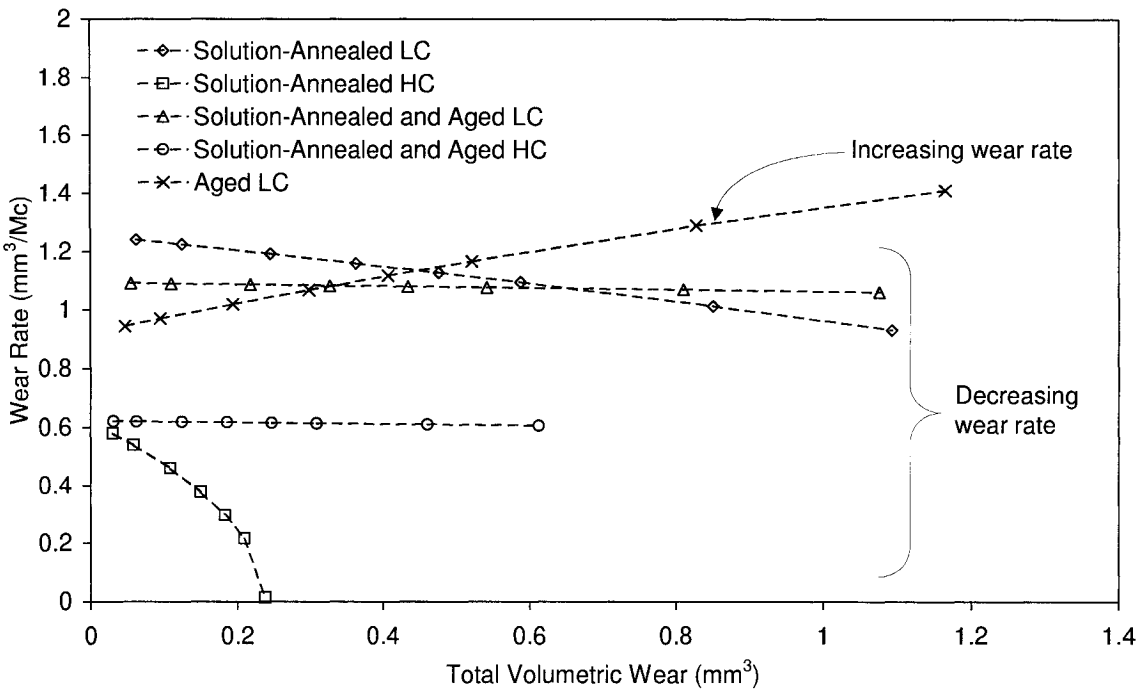

(b)

Figure 6.5. Comparison of wear rates between: (a) as-received and (b) heat treated alloys. Of interest are the F1537 LC and the aged LC alloys which show an increase in the wear rate as a function of total volumetric wear—the aged LC alloy having the highest wear rate

Despite the many factors which would seem to affect the stability of FCC-Co, there may be an overriding parameter controlling the stability of the FCC matrix and thus controlling the wear behaviour of these alloys. Nevertheless, if the HCP phase (occurring through SIT) is responsible for the wear behaviour of Co alloys this would imply that wear may be controlled by some form of deformation mechanism.

6.3.2. Mechanical properties

For a structural application such as THA, mechanical properties of the implant materials are very important with respect to the load bearing conditions of the hip joint. As a result, the implant materials must meet certain specifications in order to achieve successful functionality (Table 5.3). Therefore, one obvious reason for determining the mechanical properties of the materials in this study was to verify whether or not the materials met the required specifications, even though the microstructures were altered through heat treatment. The second reason was to determine if a relationship existed between mechanical properties and wear behaviour. Interestingly enough, when comparing the wear curves for the various materials tested in this study (Section 5.4), it was found that the alloys with poorer mechanical properties, such as the cast alloys and the solution-annealed HC alloy exhibited better wear behaviour than the as-received F1537 alloys and the other LC alloys in general. In fact, when wear is plotted against the strength and ductility of the materials, no clear relationship can be found (Figure 6.6).

This observation may be attributed to the fact that wear is a surface phenomenon and not dependant on the bulk properties of the material. It is evident that during the wear process many changes can occur to the contact surfaces as a result of mechanical and environmental conditions. Of equal importance is the fact that surfaces are often altered prior to implementation through manufacturing and processing technique which may explain why the bulk properties of the materials do not reflect the wear behaviour.

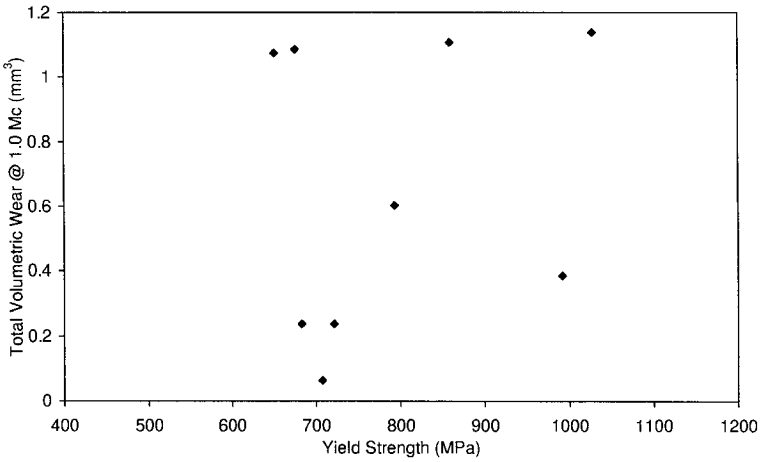

(a)

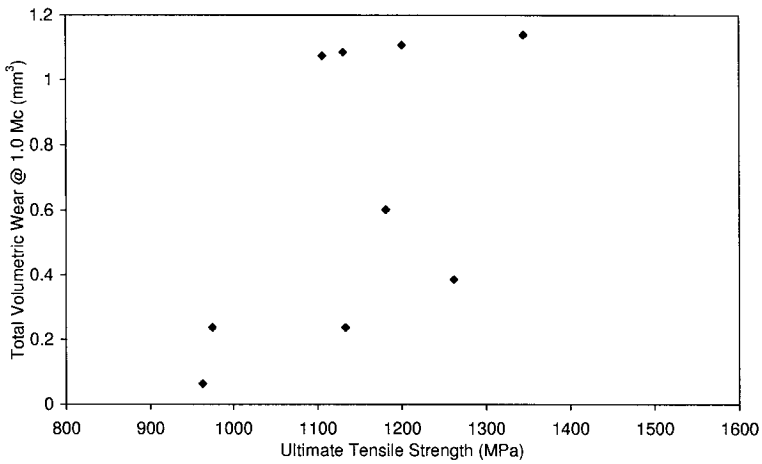

(b)

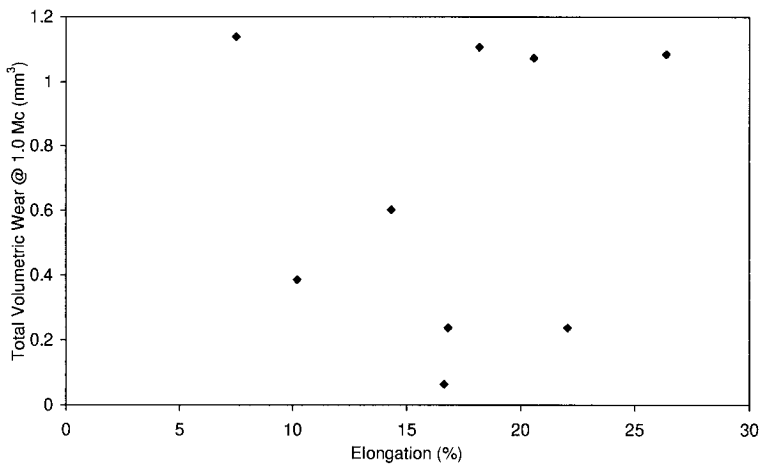

(c)

Figure 6.6. Wear behaviour of as-received and heat treated alloys after 1.0 Mc of testing as a function of (a) yield strength, (b) ultimate tensile strength and (c) elongation

That being said, this study conducted on self-bearing materials proves that relatively hard-on-hard surfaces are not always beneficial against wear and that mechanical properties in general may not be a good indicator of a material's wear behaviour against itself.

6.3.3. Surface characterization

6.3.3.1. Oxide particles

As presented in Section 5.4, several surface features were observed which may shed some light on the wear phenomenon. In the as-polished condition the surfaces of the cast alloys were found to contain spherical particles consistent with another study conducted on a surface analysis of hip implants tested in a hip joint simulator.[103] Compositional analysis of the particles in the cast materials revealed Si and O, and none of the particles were observed in the wrought alloys (in either study).

If a grinding process was used as a finishing step for all the implants, then these SiO_2 particles or "stones" should have been present in all the alloy surfaces. However, the fact that SiO_2 grinding media was not used in the present study suggests that these particles (which were only present in the cast alloys) originated from another source. Both the F1537 and F75 specifications allow for a maximum of 1.0 wt% Si in the alloy compositions. In these alloys, Si is generally used as a deoxidizing element. For the F75 alloy, the material is melted and sand cast under atmospheric conditions. Thus, the Si reacts with O to form inclusions (probably while the metal is melted). The inclusions are found throughout the cast component most likely as a result of the pouring step.

In the case of the F1537 alloy, the processing route is different. The material is first vacuum induction melted followed by a process called electroslag remelting in order to refine the material (both steps minimize any chances for oxidation to occur). Then the product is warm worked into bars, plates or sheets (depending on the application). Finally, the material is ground or machined into the desired component. Thus, SiO_2 inclusions are not found in the wrought materials.

It is clear that inclusions such as those found in the cast Co-based alloys are for the most part undesirable due to their detrimental effect on the mechanical properties of the

material. As a result, much work has been done in other alloy systems to eliminate or minimize the formation of these inclusions during the casting process. The presence of these inclusions may contribute to the relatively poor mechanical properties of the cast Co alloys in comparison to the wrought alloys, since inclusions can act as sites for crack and void initiation during deformation (leading to subsequent failure). In terms of the wear behaviour, it is unclear if non-metallic inclusions would improve the wear resistance even if their hardness is relatively high. In this study, the cast alloys exhibited the best wear behaviour. Whether it can be partly attributed to these inclusions is unknown. However, it may be postulated that inclusions would more likely behave as third-body wear particles due to their relatively poor adherence to the matrix compared to other phases (e.g. carbides). Figure 6.7 is a small example of the differences between matrix-carbide and matrix-inclusion interfaces. The interfaces between the matrix and carbides in Figure 6.7a seem to have been well-defined yet without any visible gaps between them. On the other hand, Figure 6.7b revealed a distinct gap at the matrix-inclusion interface, which may be indicative of the poor adhesion between the two phases.

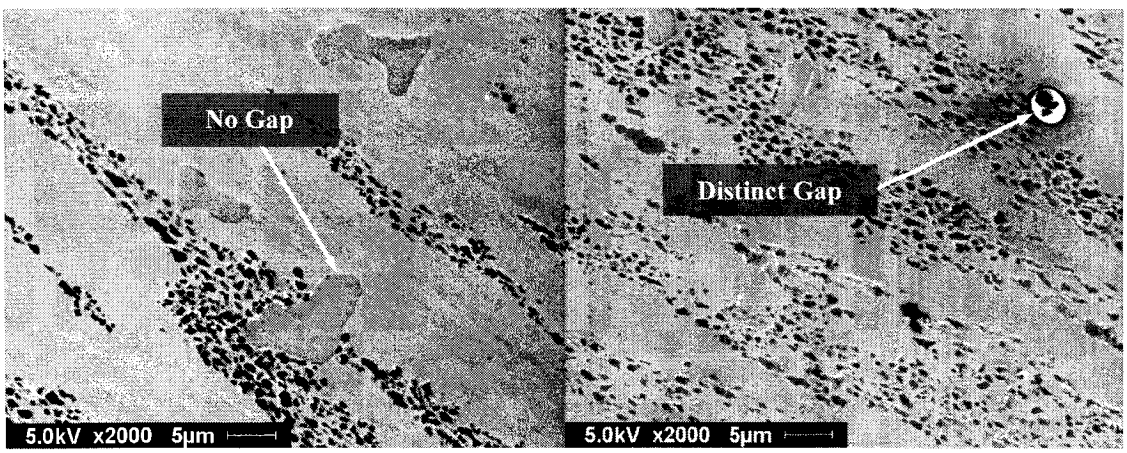

(a) (b)

Figure 6.7. Simple comparison of: (a) matrix-carbide and (b) matrix-inclusion interfaces in the as-cast alloy

6.3.3.2. Fragmentation

The first unique wear feature observed was the appearance of sharp-edged, fragmented groove marks which, at times, were coupled with a dimpled surface as shown in Figure 5.41. Surface fragmentation or fracture in wear is often referred to delamination wear resulting from the cyclical nature of the wear process (i.e. cyclical loading and/or motion). The idea is that repeated contact of two metal surfaces results in deformation of the surface and near-surface material, and over time there is an accumulation of strain (or strain-hardening) leading to crack initiation and subsequent fracture. It is believed that the very large plastic strains and strain gradients close to the contact interface produces a substructure consisting of very fine subgrains in the order of 0.30 μm.[118] The result is an increase in the microhardness due to the formation of this substructure [119] and a loss of ductility (making the material prone to fracture). The brittle nature of the surface and near-surface material may explain the sharp-edged appearance of the groove marks.

In addition, the dimpled surface appearance may be a result of the exposure of these subgrains as described by Rigney (since the dimples in this study seemed to be in the same order of 0.30 μm) or it may be a result of ductile fracture below the wear surface (at some interface separating the strain-hardened and bulk material). It should be noted that the dimpled surface were confined within the grooves and discontinuous along the length of the wear scar. The fact that the fragmentation was limited to the LC plate specimens would suggest that these features may depend on the composition and not so much on microstructure (since other LC microstructures had a similar appearance as shown in Figure 6.8). In addition, the fact that these features were isolated to the plate specimens would imply some dependence on the kinematics of the pin-on-plate tester. This will be further discussed in the following section.

6.3.3.3. Pitting and voids

When metals are exposed to a corrosive environment some form of oxidation is bound to occur, depending on the susceptibility of that metal to the environment. For materials which are naturally passive in acidic solutions (such as Co),[120] this passive behaviour may change when wear is involved.[121,122] Generally, pitting is a form of corrosion that

can be initiated in areas of chemical inhomogeneity, accumulation of dislocations, grain boundaries and non-metallic phases [123] all of which may be influenced by acting wear processes.

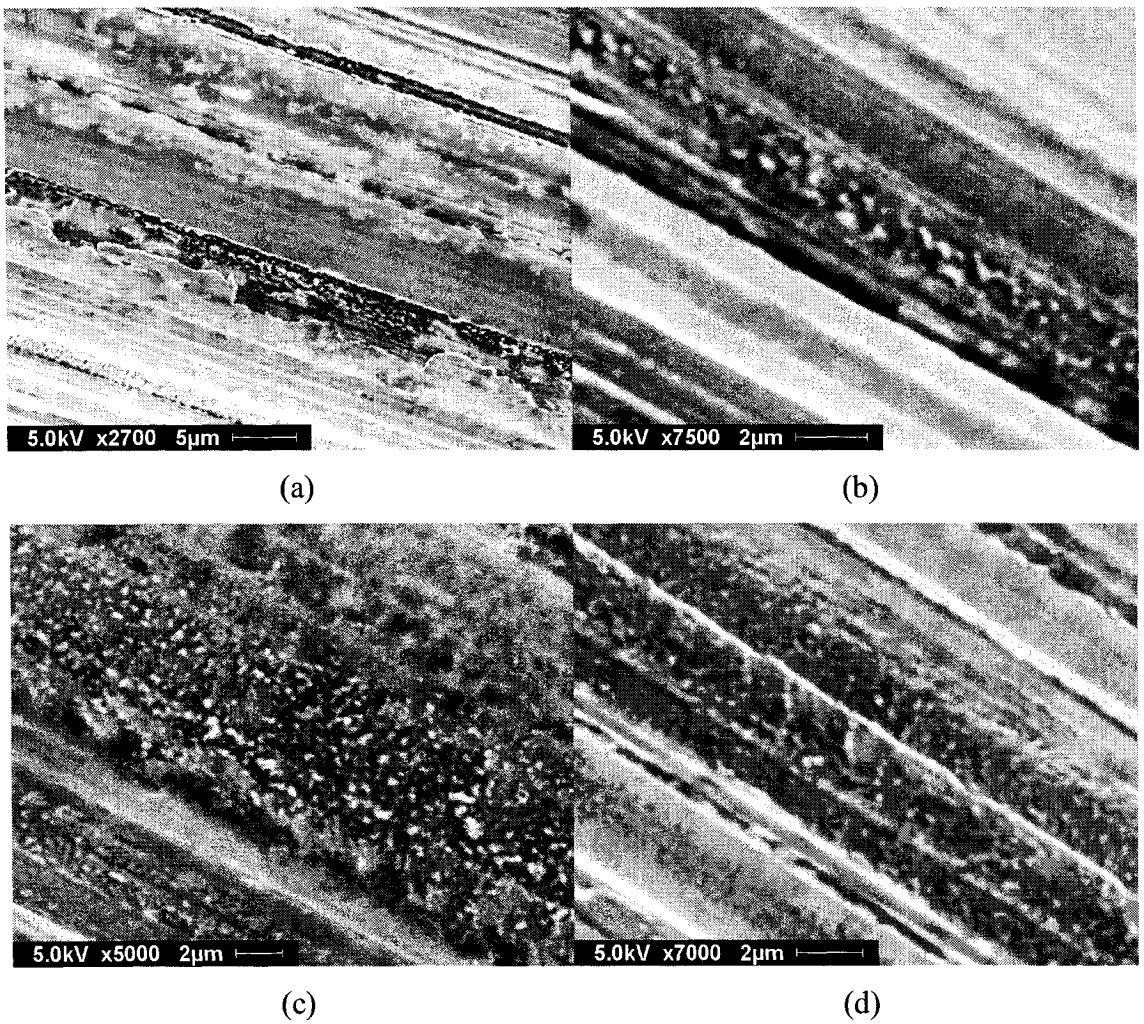

Figure 6.8. Dimpled surface in LC specimens having different microstructures: (a) as-received, (b) solution-annealed, (c) solution-annealed and aged and (d) aged

The Co alloys used in this study were originally designed to withstand the reactive conditions of the human body. As an added measure against corrosion, these alloys were subjected to a passivation process (Section 4.3) in order to promote oxide formation on the component surface. Despite the protective nature of an oxide film, pitting was found

to occur in the wear zone and it occurred more profusely in the HC plate specimens (i.e. as-received F1537 HC, F75 and as-cast alloys).

The fact that more pitting was observed in the HC specimens rather than the LC specimens may be due to the difference in C content. A higher C content would suggest a greater ability for C to tie up more Cr (which would be in solid solution) to form carbide precipitates—thus, lowering the amount of Cr that otherwise would serve to enhance the corrosion resistance of the alloy. In addition, the presence of more carbide precipitates would provide more sites for the initiation of pitting.

Analysis of the pits for the as-received F1537 HC plate specimens revealed two compositional differences. Some of the pits were rich in O as shown in Figure 6.7a, while others were rich in C (Figure 6.9b). Figure 6.9a suggests that the pits were formed by some corrosion mechanism whereas Figure 6.9b suggests that the pits consisted of carbides, which were fractured below the surface of the matrix. This is feasible since the as-received F1537 HC alloy consisted of many carbides in the same size range as the pits observed in the SEM micrographs (Figure 5.43a).

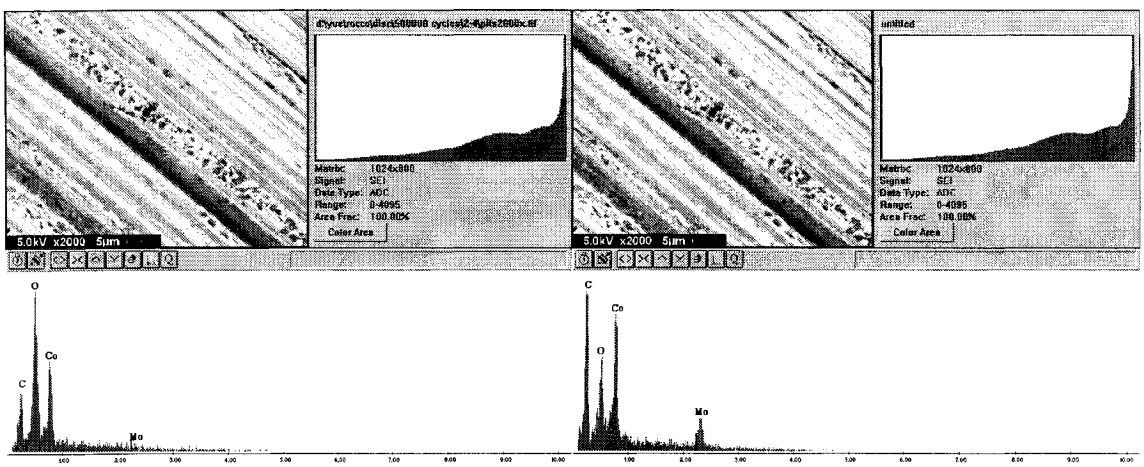

(a) (b)

Figure 6.9. EDS analysis of pits in as-received F1537 HC plate specimen: (a) high O content and (b) high C content

In the case of the cast alloys, EDS analysis of the pits revealed only O-rich areas and no C-rich areas (as in the case of the as-received F1537 HC alloy)—see Figure 6.10. The reason why C was not detected may be due to the fact that the carbides in the as-cast alloys were much greater in size than the observed pits. Based on the nature of cast materials (i.e. possessing inhomogeneous mictrostructures), pitting was most likely a result of local compositional differences between the dendritic and interdendritic regions. This was more observable in the as-cast specimens which exhibited a "branch-like" pitting pattern (Figure 6.11). The F75 had a more regular pattern of pitting along the direction of the wear track with obvious pitting within the carbide lamellae.

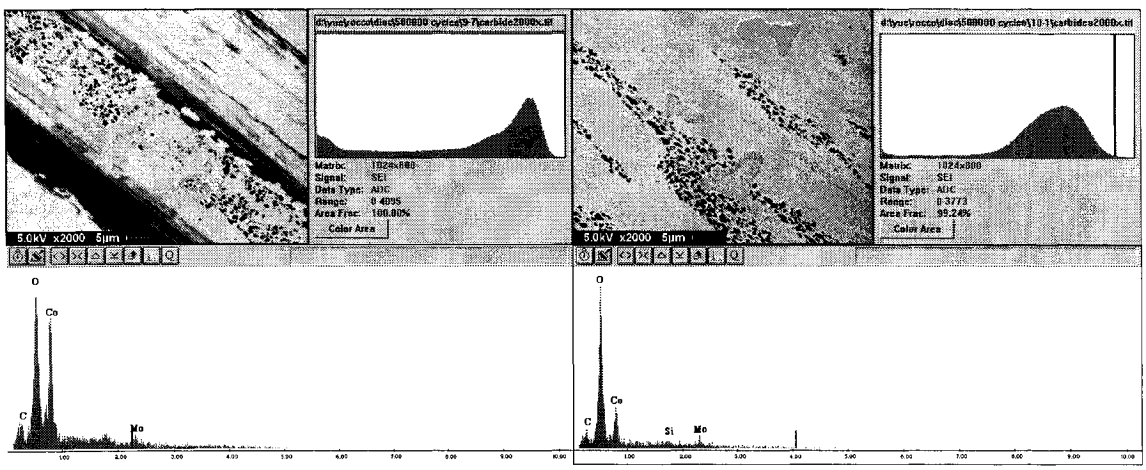

(a) (b)

Figure 6.10. EDS analysis of pits showing high O content: (a) F75 and (b) as-cast plate specimens

Furthermore, the pitting that was seen in the as-received HC plate specimens was less dramatic in the pin specimens. This may be explained by the passivating nature of the alloys and the contact conditions of the pin-on-plate apparatus. Studies have shown that passive metals under wear-corrosion conditions can be paralleled to a passive/active cell in which the wear zone becomes the anode and the rest of the unworn surface is the cathode.[122] The cathode/anode ratio for the plate specimens (based on the ratio of areas) was almost 5.5 times greater than that of the pin specimens, providing a larger driving force for pitting corrosion to occur.

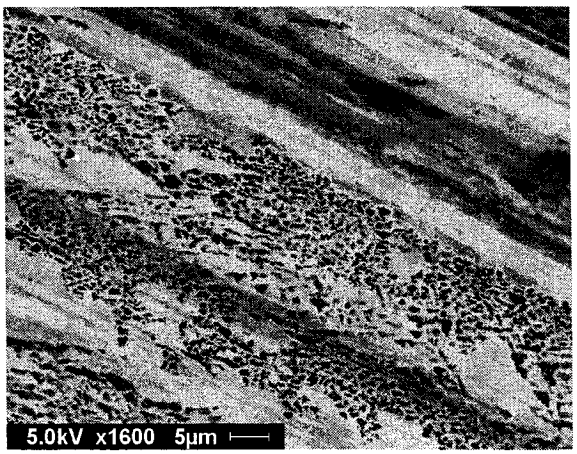

Figure 6.11. SEM micrograph of wear zone for as-cast plate specimen revealing branch-like pitting pattern similar to the dendritic alloy structure

In addition, the contact conditions for the pin-on-plate apparatus were such that the entire wear zone of the pin specimen was in constant contact with plate specimen throughout the length of the stroke. On the other hand, the wear zone of the plate specimen was in contact only partially at any given time (based on the kinematics of the apparatus). Thus, the pin specimens experienced higher amounts of wear than the plate specimens, as expected. The higher pin wear would suggest that the pin contact surface was being removed at a quicker rate than the plate surface and thus, would allow less time for pitting corrosion to occur or would remove any pits that may have formed.

For the surface voids, which were most prevalent in the LC pin specimens, these seemed to be formed by a direct mechanical intervention rather than a chemical attack as was previously discussed with regards to the observed pitting. The basis for this conclusion being that the surface voids differed from pitting with respect to size, morphology and location along the wear zone. While pitting was not always restricted to any particular area on the wear track, the surface voids seem to occur specifically along the wear grooves.

6.3.3.4. Tribofilms

A solution of 25 vol% bovine serum in distilled water was the lubricant of choice for this study (see Section 4.3.5) following the work done by Tipper et al.[74] Although it is unclear what vol% of bovine serum in water would best simulate human synovial fluid, some investigators found that 30 vol% bovine serum in water closely matched the protein content found in healthy human synovial fluid.[124,125] However, in diseased hips, it was found that the protein content was greater and varied from implant couple to implant couple.[126] That being said, it is important that the test lubricant have the same influence on the tribological system to what is found *in vivo*. In some instances, bovine serum has been treated with additives such as EDTA in order to suppress the formation of calcium- and phosphorous-rich films.[96,100] The rationale being that these tenacious films were not so tenacious *in vivo* and they may protect implant surfaces and perhaps lead to an underestimate in the wear observed *in vitro* when compared to *in vivo* results. However, a recent study conducted on the articulating surfaces of retrieved McKee-Farrar MM hip implants [127] found similar tribofilms and they were also with CoCrMo MM pin-on-ball components tested *in vitro*.[98] The tribofilms were found to consist of several layers of which the top most layer was C-rich, followed by an O- and Cr-rich layer and below these two layers was the base material.

In the present study, surface films were also observed in all the specimens which may have been the same tribochemical reaction layers found by Wimmer et al.,[127] even though EDTA was used in the lubricant. Under optical microscopy the films seemed to have a rainbow-like appearance and were most evident with the naked eye on the as-cast surfaces (Figure 6.12). These films could also be observed in the SEM and was distinguishable in both secondary electron (SE) and backscattered electron (BSE) modes, as shown in Figure 6.13.

Compositional analysis of these tribofilms were conducted using EDS at various accelerating voltages in order to detect any changes in composition with increasing penetration below the immediate surface. At low accelerating voltages (5.0 kV) the analysis revealed high peaks for C and O as well as the presence of Si and traces of N and P. At higher accelerating voltages (i.e. 10 kV and 15 kV) the C and O peaks diminish, but the O peak was now greater than the C peak (Figure 6.14). These findings are in

agreement with those of Wimmer et al. in their comparison study between *in vitro* and *in vivo* MM wear.[127] Since these films were found on all the test specimens, their effect on the wear behaviour could not be ascertained. However, the formation of these films in the absence of EDTA may in fact be indicative of some tribochemical reactions occurring on the wear surfaces due to an elevation in temperature generated at contact spots during sliding.[127]

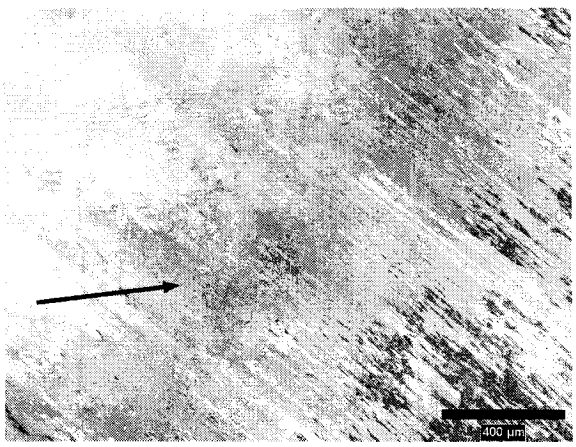

Figure 6.12 Optical micrograph of tribofilm along the edge of the wear scar in the as-cast plate specimen under x50 magnification

6.3.3.5. Grooves

The most obvious evidence of wear on contacting surfaces is the presence of macroscopically visible groove marks. For the reciprocating pin-on-plate apparatus used in this study, the groove marks were, for the most part, linear and parallel to the direction of motion, as expected. The roughness profiles of the contact surfaces normal to the direction of motion revealed a series of peaks and valleys with varying heights and widths. The origin of these grooves is discussed in the following.

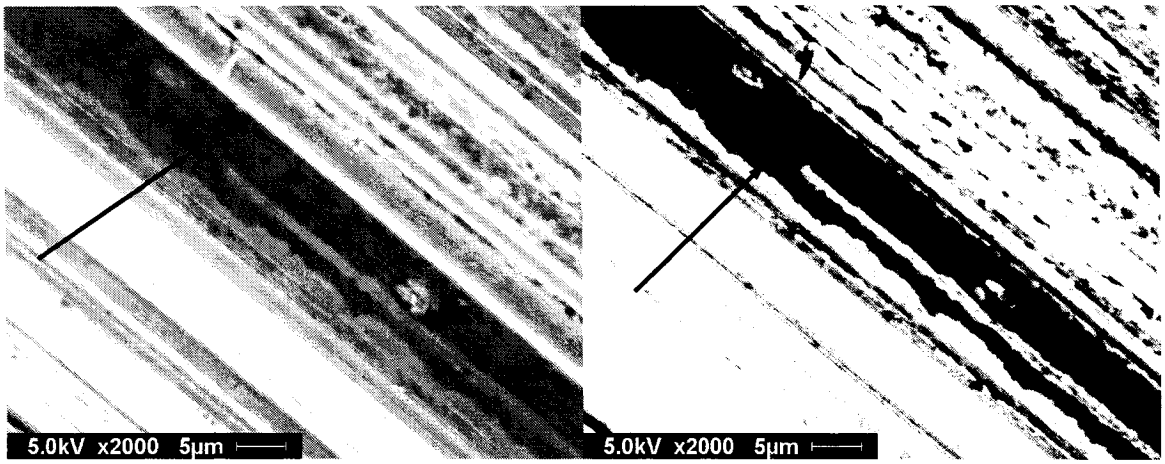

(a) (b)

Figure 6.13. SEM micrographs of tribofilms in F75 alloy: (a) SE image and (b) BSE image

One of the mechanisms of wear mentioned in Section 2.3.1 was adhesive wear. This involves the "sticking" of one surface to another sometimes enhances by frictional heating resulting from applied normal and tangential loads acting on two contacting bodies. The source of frictional heating may be likely due to the local heat of deformation and inelastic collisions between asperities. As the temperature at the contact increases the yield (shear and tensile) strength of the material decreases, allowing for easy plastic flow and diffusion to take place—thus, resulting in the joining and tearing of material due to the high temperature gradients at these points.[128] Typical effects of adhesive wear are: irregularly shaped groove marks and material transfer.

During wear testing it was found that the wear zone was composed of fairly regularly shaped groove marks (Figure 5.40), suggesting that adhesive wear may not have occurred. However, gravimetric analysis did detect a weight gain in the order of 0.010 g after 1.0 Mc cycles of testing for the F75 and as-cast plate specimens (note: the pin specimens did not experience a weight gain for any of the alloys). A weight gain may have resulted from improper cleaning of the surfaces or actual material transfer during wear. The fact that the tribofilms mentioned earlier were present on both the pin and plate surfaces would rule them out as possible sources of weight gain. If material transfer did occur, and since only the plate specimens experienced a weight gain, it may have been due to a gravity issue with regards to the specimen setup (Figure 4.5). In other words,

gravity may have caused preferential transfer from the pin to the plate specimens (the pin being the upper surface and the plate being the lower surface).

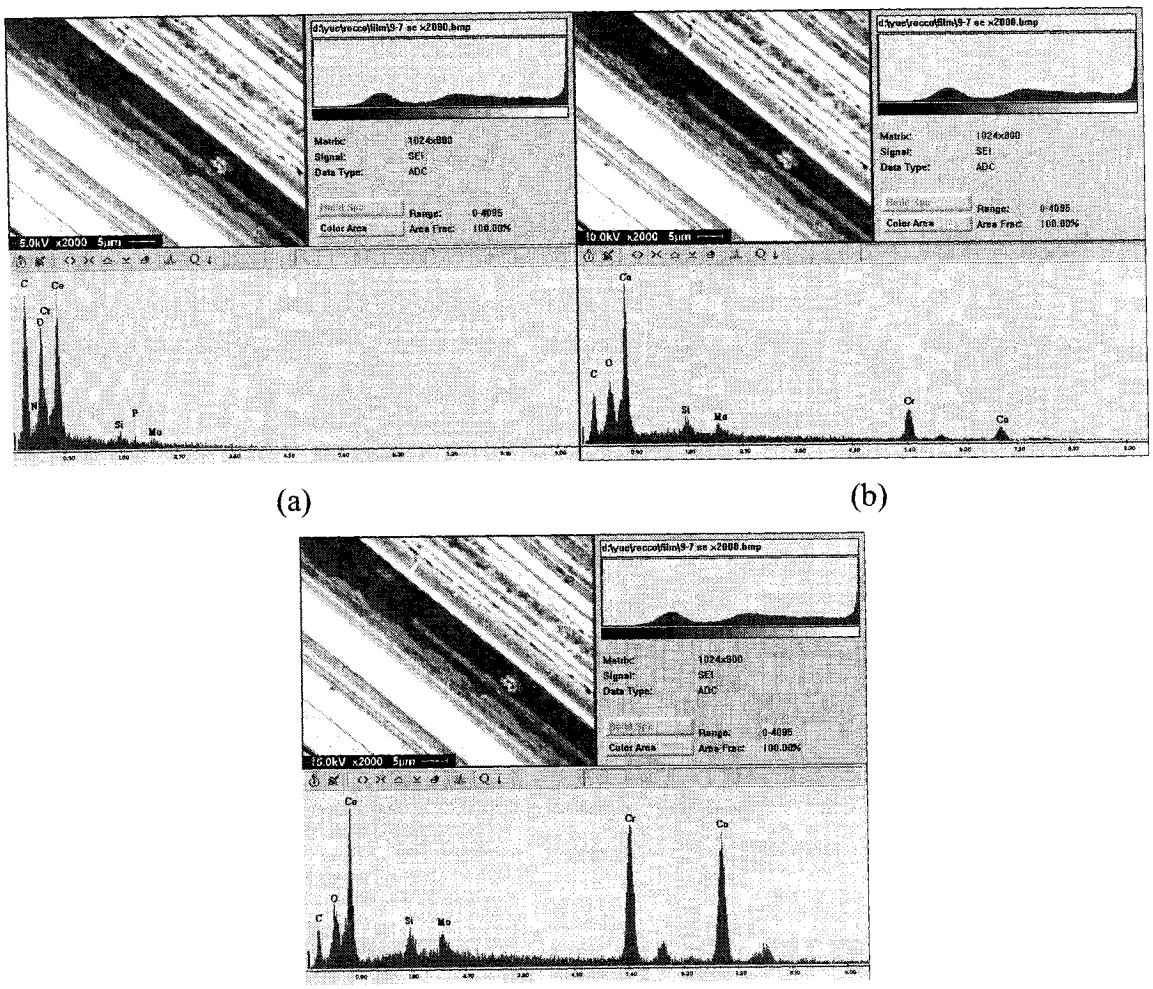

Figure 6.14. EDS analysis of tribofilm shown in Figure 6.12: (a) 5.0 kV, (b) 10 kV and (c) 15 kV

Another mechanism of wear is abrasive wear (Section 2.3.2). This seems to be the most likely source for the wear grooves since abrasive wear involves cutting and ploughing of harder phases against softer ones. An abrasive cutting process could be assessed through debris analysis. If the wear debris had the same microstructure and composition as the base material then it could be postulated that the particles were

formed by direct abrasive cutting. Unfortunately, wear debris could not be collected from this study, also the very fine particle sizes (< 100 nm) would make it difficult to analyze for microstructure. However, in a study conducted by Catelas *et al* [129] on a hip joint simulator, particles were isolated from the test lubricant (95 vol% bovine serum) using an enzymatic protocol in order to minimize any changes to the particles due to reagents. Through transmission electron microscopy and EDS analysis it was found that the majority of the particles were round to oval in shape (but some were distinctly needle in shape) with a Cr-O composition. In another study conducted by Tipper *et al*, using a pin-on-plate apparatus, the particles were also round to oval in the same size range but no needle-shaped particles were found and the composition of their particles was uniformly Co-Cr.[74] In the Tipper study it was not mentioned if prior passivation was done on the test specimens. If not, this would explain the absence of oxide wear particles in their analysis. In any case, the fact that both studies reported round to oval shaped wear particles would suggest that abrasive cutting did not occur (which would likely produce elongated flake-like wear debris—Figure 2.16) or if cutting did occur then some shape change may have taken place after the particle was released due to entrapment within the contact zone. Of the two abrasive mechanisms, abrasive ploughing seems to be the more plausible source for the wear grooves observed, based on the evidence of deformation in and around the wear grooves. A characteristic feature of Co alloys is the appearance of twins resulting from the deformation process. Therefore, these twins are a clear indication that deformation has occurred. And the presence of these twin in and around the contact zone is consistent with the displacement of material due to ploughing. This ploughing in itself may not necessarily lead to wear, although when coupled with the cyclic nature of the wear apparatus used in this study, delamination wear may ensue. The displaced material becomes work hardened and as the contact zone is fatigued, crack initiation occurs and is followed by fracture. Evidence of deformation and fracture at the wear zone is shown in Figures 6.15 and 6.16, respectively.

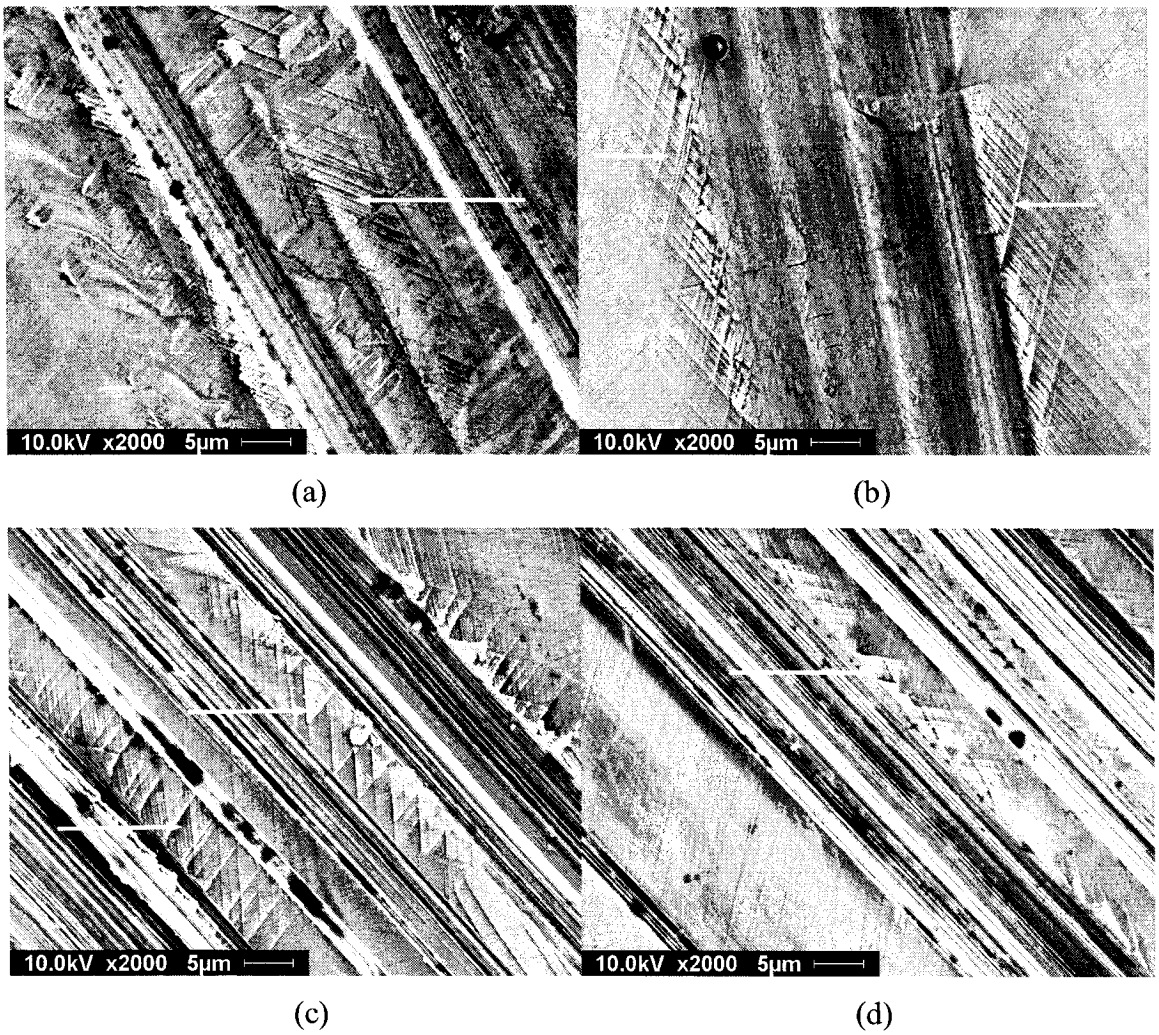

Figure 6.15. Examples of deformation twinning at the contact zones and evidence of crack formation parallel to the direction of motion: (a) F75, (b) as-cast, (c) solution-annealed F1537 LC and (d) solution-annealed F1537 HC alloys

The twin planes were clearly seen in both the LC and HC specimens (mainly in the cast and heat treated alloys due to the large grain sizes) proving that deformation is occurring in conjunction with wear. In addition, the presence of these twin lines show that deformation can extend well beyond the wear zone in every direction. An example of this can be seen in a macrohardness test done on the same CoCrMo alloys used in this study, revealing the extent of deformation around the indentation mark (extending ~ 500 μm radially from the edge of the indentation as shown in Figure 6.17).

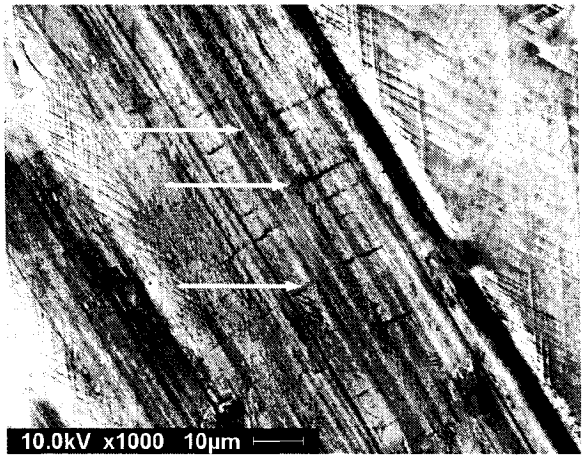

Figure 6.16. Example of surface cracking in the wear zone normal to the direction of motion

Considering the loading conditions of the pin-on-plate apparatus, the resulting surface and near surface deformation caused by the applied normal load from the pin specimens and the tangential load from the motorized baseplate can best be illustrated through Figure 6.18. In a ball-on-flat configuration, such as the pin-on-plate apparatus used in the present study, the applied normal load F_N (prior to any motion) would result in an apparent circular contact area having an initial radius a according to Equation 4.8 (Section 4.3).

Initial contact would cause local flattening of the spherical tip of the pin and perhaps a slight indentation of the plate. Assuming plastic deformation due to asperity-asperity contact (e.g. matrix-matrix, matrix-carbide and carbide-carbide) and conservation of volume, material would be displaced to the perimeter of the individual contact spots. If a reciprocating motion is then added (F_T), the prior contact spots may act as starting points for the groove marks which are readily observed on the wear surfaces. Evidence of material displacement can be seen in the roughness profiles of the pin and plate specimens (Figure 6.19). Superimposed over the roughness profiles are the original surface profiles shown by the dotted lines. The arrows point to the displaced material at the edges of the wear zone.

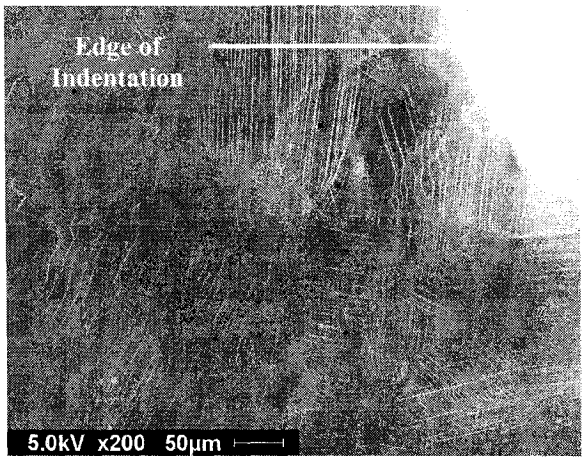

Figure 6.17. Macrohardness test revealing the extent of deformation around indentation mark by the presence of twins

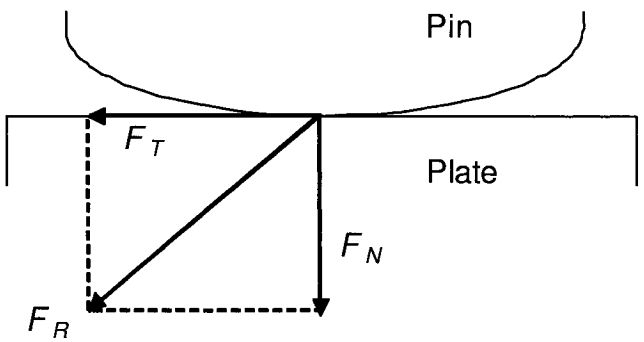

Figure 6.18. Schematic diagram of the applied loads acting on the contact surfaces: F_N = normal load, F_T = tangential load and F_R = resultant load

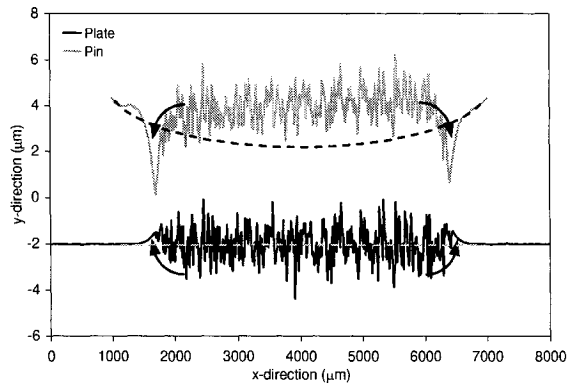

Figure 6.19. Surface roughness profiles of pin and plate specimens normal to the direction of motion revealing bulging at the edges of the wear zone indicative of material displacement.

6.3.4. Carbon content

In regards to wear tests using screening devices involving simple linear reciprocating motion (such as the pin-on-plate wear apparatus), it has been found that the wear performance of CoCrMo alloys was affected by C content.[74,130] Indeed, C plays an important role when considering the wear behaviour of CoCrMo alloys. In the present study a clear distinction in the wear behaviour between LC and HC alloys was also observed in relation to C content regardless of certain microstructural features, such as: grain size and carbide fraction. However, this does not mean that grain size and carbide fraction are not important. In the past, the issue of C content in CoCrMo alloys was centered on the presence of carbides, since carbides are considerably harder than the CoCrMo matrix. Nevertheless, C may also have a solid-solution effect in CoCrMo alloys. From the literature it can be found that C helps to stabilize the FCC-Co crystal structure.[23] This stabilizing effect was also found experimentally.[80] The fact that Co transforms from FCC to HCP through SIT is thought to be beneficial to resist wear since the HCP-Co structure is a higher strength phase (Figure 5.34). However, in self-mating applications the opposite may be true.

Since it was found that a high C content reduced the total volumetric wear and since there was not a strong correlation between carbides and wear, it may be safe to assume that the key to reducing wear under such conditions may lie in the amount of

dissolved C. In order to verify this, the total volumetric wear for each alloy condition was plotted against the dissolved C content for that material. The results, shown in Figure 6.20, reveal a strong dependence of wear on the dissolved C content. This would explain why there was a general decrease in the volumetric wear with larger carbide sizes (Figure 6.3b), since these alloys actually possessed a higher C content.

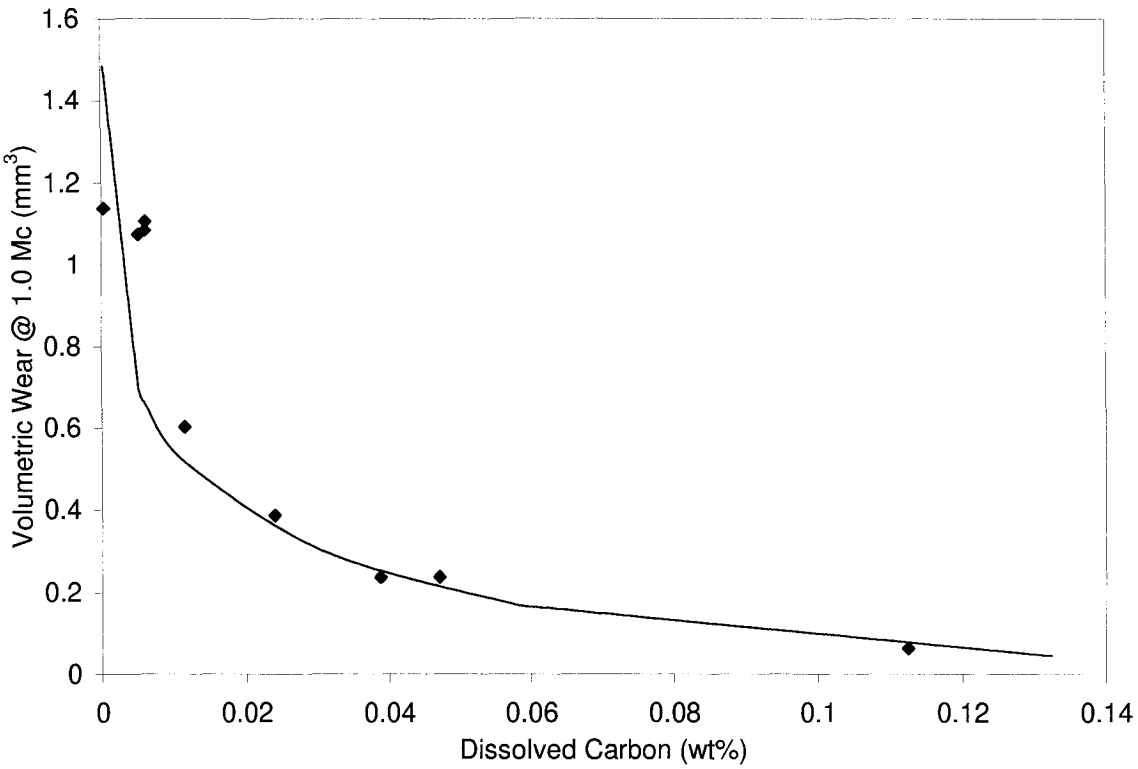

Figure 6.20. Total volumetric wear as a function of dissolved C content (y is the volumetric wear and x is the dissolved C content)

From a materials standpoint the results would suggest that dissolved C is very important in dictating the wear behaviour of CoCrMo alloys, since the C in solution influences the stability of the FCC structure to undergo SIT to HCP. The fact that dissolved C affects SIT and since SIT is a deformation process, it may be further suggested that wear follows a deformation-controlled mechanism. This would be in line

with the observed deformation twinning and the increasing wear rates for the HCP susceptible materials (Figure 6.5).

In addition, a large discrepancy in the wear behaviour was found for the HC specimens which were solution-annealed and aged. For every test condition, three pairs of specimens were tested for the sake of repeatability. In the case of the solution-annealed and aged HC specimens, two pairs exhibited high wear while the third pair experienced very low wear, comparable to the as-cast specimens (Figure 6.21).

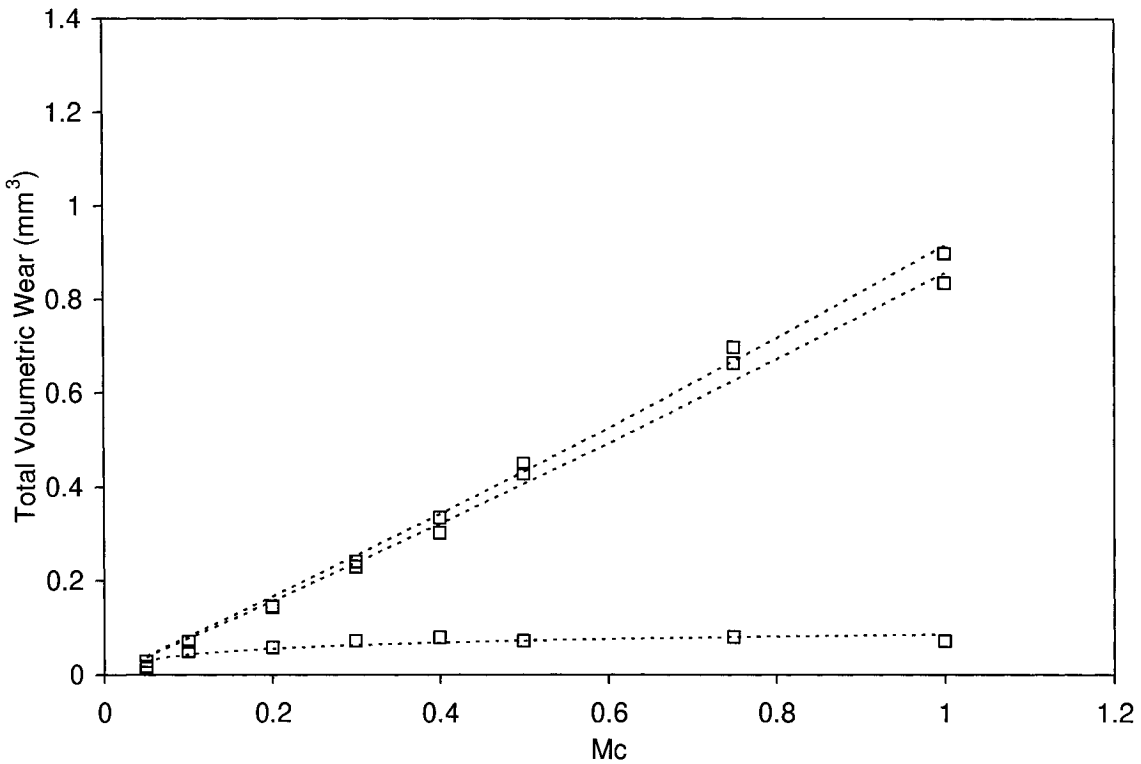

Figure 6.21. Wear behaviour of solution-annealed and age HC specimens. Of the three pairs tested, one pair experienced very low wear

Previously, x-ray diffraction analysis of the worn and as-polished surfaces was presented as part of the wear results (Section 5.3) and in both cases a dual phase structure was revealed for the LC and HC alloys. Although C helps to stabilize the FCC structure,

it does not completely suppress the formation of the HCP phase through SIT. The fact that the HCP phase was observed in both the worn and as-polished surfaces may be explained by surface deformation resulting from the wear process and mechanical polishing, respectively. In order to determine the extent of surface SIT, vibrational polishing of the contact surfaces was done prior to x-ray diffraction analysis. The x-ray results in Figure 6.22 reveal that even after 4 h vibrational polishing the high wear specimens had a strong HCP signal. The x-ray diffraction analysis of the low wear specimens revealed a predominantly FCC structure. These findings are additional evidence of the detrimental effect of the HCP phase on wear.

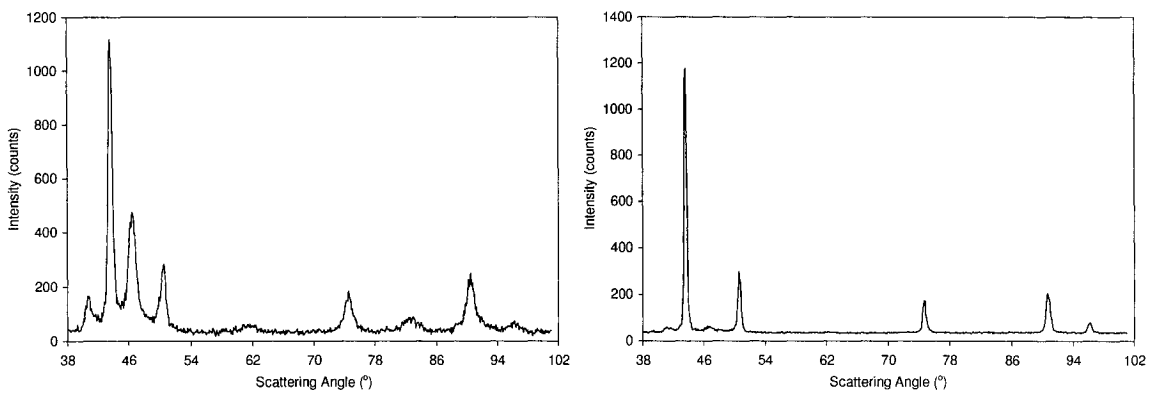

Figure 6.22. X-ray diffraction results of contact surfaces after vibrational polishing for solution-annealed and aged HC specimens: (a) high wear specimens revealing dual phase structure (FCC and HCP) and (b) low wear specimens revealing a predominantly FCC structure

6.3.5. Proposed wear mechanisms

In light of the results attained through this study, the operating wear mechanisms in MM CoCrMo alloys can be divided into two categories: chemical and mechanical. The chemical mechanisms identified in this study and also identified in other *in vitro* [104] and *in vivo* [127] studies are surface pitting corrosion and tribofilms. Surface pitting corrosion was found to be related mainly to alloy composition, since it was predominantly observed in the HC alloys. The fact that the HC alloys exhibited lower wear than the LC alloys

would suggest that surface pitting corrosion may have a negligible affect on the total volumetric wear (under the current test conditions) and thus play a minor role in osteolysis. However, surface pitting corrosion may be a key factor with respect to the question of ion release in MM bearings and their long-term effects.[131]

Tribofilms were also observed as a chemical wear mechanism in MM CoCrMo alloys. Due to elevated contact temperatures, reactions between the bio-lubricant and the metal surfaces seem to form adherent C- and O-rich films incorporating elements from both the serum (e.g. Ca, P) and from the alloy (e.g. Cr). The findings from Wimmer et al.[98,127] would suggest that these films form a protective layer against wear. However, that study was limited to only the HC alloys (both wrought and cast). In this study, tribofilms were also observed on both LC and HC alloys. Since the LC alloys experienced higher wear than the HC alloys, it may be safe to say that tribofilms are only a by-product of wear and not a controlling mechanism.[132]

Eliminating the chemical side of wear as the controlling factor in the overall wear process, there remains the mechanical aspect. Based on surface characterization and the effect of C content, the wear behaviour of MM CoCrMo alloys seem to be controlled by an abrasive ploughing process leading to material displacement and deformation. This further results in twinning and transformation of the surface structure (as shown by the analyses). Considering the nature of the HCP phase that is formed within the FCC lattice, it may be postulated that the very fine particles (in the size range of stacking faults) may behave poorly under fatigue conditions due to the reciprocating motion of the current experimental setup. The high work hardening rate resulting from SIT and the brittle nature of the HCP phase may make it prone to cracking and fracture.

A deformation mechanism of wear would also explain the shape of the wear curves in Section 5.3. Recalling Section 2.3, wear was said to be dependent on the applied normal load. According to linear wear theory, increasing the applied normal load should increase the amount of wear (Equation 5.1). However, when the applied load is constant (as in the present study) then wear may be related to stress, which will decrease as the contact area increases. It was found that in the early stages of testing there was a dramatic increase in the volumetric wear. This may have been due to the high starting stresses at the asperity contact points. As the surface material was deformed plastically and

removed, the contact area increased and the stress was reduced. Eventually, the system arrived at a state of equilibrium or steady state. At this point, the work hardened surface could accommodate the applied load due to the low contact stresses. During steady state wear, the amount of material loss was more gradual and most likely controlled by a fatigue process. This is the general mechanism for the present wear scenario and may be the case for other MM systems. However, for MM CoCrMo alloys the controlling factor dictating the wear behaviour of these materials seems to be the presence and formation of the HCP phase due to surface deformation.

CHAPTER 7

Conclusions

The wear behaviour of MM CoCrMo specimens made from ASTM F1537, ASTM F75 and as-cast alloys was studied in a unidirectional sinusoidally reciprocating pin-on-plate apparatus at room temperature with a particular lubricant, load, speed, stroke length and specimen geometry. All conclusions regarding wear were based on tests with this apparatus. It was considered likely that wear behaviour would change for a different apparatus with different conditions but hopefully these changes would not be enough to significantly distort the findings of the present thesis. The appearances of the worn surfaces of the present study were generally similar to those found in simulator testing and this provided some support for the concept that the wear obtained from the present apparatus was adequately representative of in vivo wear.

In further testing, the ASTM F1537 alloys were subjected to various heat treatments and tested under the same wear conditions. The microstructure, crystallography and mechanical properties of all the specimens were studied in order to explain the observed wear behaviour.

The following conclusions were drawn from the present study:

CONCLUSIONS

1. SiO_2 particles found in the as-received cast alloys were identified as inclusions originating from the casting process
2. The as-received HC alloys had a lower volumetric wear than the LC alloy
3. Of the as-received HC alloys, the as-cast alloy had the lowest wear, followed by the F75 alloy and the F1537 alloy was the highest of the three
4. Solution-annealing reduced the volumetric wear of the HC alloy and changed the wear rate of the LC alloy from increasing to decreasing
5. Solution-annealing and aging increased the volumetric wear of the HC alloy and changed the wear rate of the LC alloy from increasing to decreasing
6. Aging of LC alloy resulted in the highest volumetric wear and wear rate of all the other alloys
7. There was no correlation between grain size and wear
8. There was no correlation between carbide fraction and wear
9. Volumetric wear decreased with increasing dissolved C content
10. The HCP phase is detrimental to the wear behaviour of MM CoCrMo alloys
11. Wear proceeds through several mechanisms: pitting, tribochemical and mechanical
12. The dominant wear mechanism follows a deformation process involving surface twinning and the SIT characteristics of CoCrMo alloys

Recommendations for Future Work

It was the intention of this study to determine the materials effect on the wear behaviour of CoCrMo MM bearings in order to improve their performance and ultimately increase their longevity *in vivo*. From a materials standpoint it was found that dissolved C was a key factor influencing the wear behaviour of these implant couples in that C has a strong effect on the stability of the FCC phase and thus on the transformation behaviour to the HCP phase. Based on the findings of the present work, it was determined that the presence of the HCP phase was detrimental to the wear behaviour of MM bearings.

In the process of determining the optimum material parameters with respect to wear it was found that the as-cast condition of CoCrMo alloys out-performed any of the existing ASTM alloys currently used in MM THA. Further investigation as to why the as-cast condition resulted in the best wear behaviour is required. Overall, the as-cast alloy would seem an excellent choice for MM bearings both from a performance and a manufacturing perspective, since components can be directly cast to the desired shape reducing the cost of post treatments and machining. However, due their poor mechanical properties the as-cast alloys should be confined only to the bearing components (i.e. the head and cup components), whereas the wrought alloys (ASTM F1537) or other alloys

(such as Ti) should be used for the stems, since these materials are more structural sound and less prone to fatigue fracture failure.

Further recommendations for future work would include the modification of the current commercially available ASTM alloys through heat treatments and alloy chemistry. Solution-annealing was found to be beneficial by introducing C into solution and thus promoting the stability of the FCC phase. It would be desirable to achieve full carbide dissolution under vacuum or in an inert atmosphere for longer treatment times (~ 72 h) in order to minimize any C losses that would occur. For this reason, the solution-anneal treatments conducted in the present study were done for shorter times since the atmospheric environment promoted decarburization and oxidation of the metal surfaces. In regards to alloy chemistry, it would be interesting to increase the nominal C contents which are normally found in these alloys to there maximum allowable amounts of 0.35 wt% and even going beyond that in order to observe the effect on the wear behaviour. For future reference direct C measurement in solution using electron probe analysis would be complementary to the findings in this work in order to compare with the indirect C measurements using mass balance techniques.

Finally, it would also be important to wear test these material couples using the present pin-on-plate configuration for longer test cycles. Currently at 1 Mc, it was found that the LC alloys were still in the run-in stage of wear while the HC alloys arrived at the onset of steady-state wear. Therefore, increased cycles of testing (up to 10 Mc) would help to better characterize the different stages of wear that exist.

Contributions to Original Knowledge

An in depth look at the materials issues influencing the MM wear behaviour of CoCrMo alloys were studied for the first time. Of all the microstructural features, it was found that the HCP phase and the susceptibility of the FCC phase to undergo SIT to HCP were detrimental to the wear behaviour of these alloys in self-mating applications.

For the first time, neutron diffraction analysis was conducted on these alloys and several fundamental findings were noted:

1. After quenching from 1200°C, the FCC phase does not undergo an athermal martensitic transformation to HCP as previously reported
2. After solution-annealing at 1200°C for 24 hrs, the FCC phase does not undergo isothermal transformation to the HCP phase even after aging at 650°C for 144 hrs, suggesting thermal stability of the FCC phase at lower temperatures

For the first time, Si-O inclusions were identified in the cast alloys (F75 and as-cast) which were originally identified as residual grinding stones.

For the first time, volumetric wear was correlated to the dissolved C content in CoCrMo alloys (supporting the detrimental nature of the HCP phase in MM wear).

For the first time, proof of surface deformation during MM wear in CoCrMo alloys was presented.

For the first time a stress related deformation mechanism of wear was presented as the controlling factor affecting the MM wear behaviour of CoCrMo alloys based on the susceptibility of the FCC structure to undergo SIT to the HCP phase.

References

1. W. H. Harris, The problem is osteolysis, *Clin. Orthop.*, 311 (1995) 46-53.
2. N. A. Athanasou, J. Quinn and C. J. K. Bulstrode, Resorption of bone by inflammatory cells derived from the joint capsule of hip arthroplasties, *J. Bone Joint Surg.*, 74B (1992) 57-62.
3. W. Murray and N. Rushton, Macrophages stimulate bone resorption when they phagocytose particles, *J. Bone Joint Surg.*, 72B (1990) 988-992.
4. T. P. Schmalzried, M. Jasty and W. H. Harris, Periprosthetic bone loss in total hip arthroplasty polyethylene wear debris and the concept of effective joint space, *J. Bone Joint Surg.*, 74A (1992) 849-863.
5. H. G. Willert, H. Bertram and G. H. Buchhorn, Osteolysis in alloarthroplasty of the hip: The role of ultrahigh molecular weight polyethylene wear particles, *Clin. Orthop.* 258 (1990) 95-107.
6. J. Charnley, *Low friction arthroplasty of the hip—Theory and practice*, Springer-Verlag, New York (1979) 3-15.
7. P. Crook, Cobalt-base alloys resist wear, corrosion, and heat, *Adv. Mater. Process.*, 4 (1994) 27-30.

8. B. D. Ratner, A. S. Hoffman, F. J. Schoen and J. E. Lemons, *Biomaterials science—An introduction to materials in medicine*, Academic Press, Toronto (1996) 41-46.
9. G. K. McKee, Total hip replacement—Past, present and future, *Biomaterials*, 3 (1982) 130-135.
10. P. S. Walker and B. L. Gold, Tribology—Friction, lubrication and wear, *Wear*, 17 (1971) 285-299.
11. Centerpulse Orthopedics, *www.centerpulseorthopedics.com/metasul/index.*
12. L. Z. Zhuang and E. W. Langer, Effects of alloy additions on the microstructures and tensile properties of cast Co-Cr-Mo alloy used for surgical implants, *J. Mater. Sci.*, 24 (1989) 4324-4330.
13. R. S. Young, *Cobalt*, Reinhold Publishing Corporation, New York (1948) 66-70.
14. F. Sebilleau and H. Bibring, The allotropic transformation of cobalt, *Inst. Metals Mono.*, 18 (1956) 209-217.
15. R. E. Reed-Hill and R. Abbaschian, *Physical metallurgy principles*, PWS-Kent Publishing Company, Boston (1992) 561-563.
16. C. M. Wayman, Martensitic transformations and mechanical behavior, *Strength of Metals and Alloys*, 3 (1985) 1779-1804.
17. B. Strauss and F. Frey, Martensitic phase transformation and lattice dynamics, *Phys. Rev. B*, 54 (1996) 6035-6038.
18. Y. Q. Wang, Z. Wang, J. H. Yang and L. C. Zhao, Pseudoelasticity, shape memory effect and FCC→HCP martensitic transformation associated with stacking faults in FCC alloys, *Scr. Mater.*, 35 (1996) 1161-1166.
19. R. W. Hertzberg, *Deformation and fracture mechanics of engineering materials*, John Wiley & Sons, Toronto (1989) 69.
20. E. O. Hall, *Twinning and diffusionless transformations in metals*, Butterworths Scientific Publications, London (1954) 152-155.
21. A. Seeger, Dislocations and allotropic transformations II, *Z. Metallk.*, 47 (1956) 653-660.
22. L. Shi, D. O. Northwood and Z. Cao, Alloy design and microstructure of a biomedical Co-Cr alloy, *J. Mater. Sci.*, 28 (1993) 1312-1316.

23. C. T. Sims, A contemporary view of cobalt-based alloys, *J. Metals*, 21 (1969) 27-42.
24. American Society for Testing and Materials, *Annual book of ASTM standards 1301*, ASTM, West Conshohocken (1997) 4-5.
25. American Society for Testing and Materials, *Annual book of ASTM standards 1301*, ASTM, West Conshohocken (1997) 860-861.
26. M. G. Fontana and N. D. Greene, *Corrosion engineering*, McGraw-Hill, New York (1978) 73-85.
27. N. S. Stoloff, Alloying of nickel, *ASM International* (1988) 371-417.
28. E. F. Bradley, *Superalloys—A technical guide*, American Society for Metals, Metals Park (1988) 32-51.
29. M. J. Jr. Donachie, *Superalloys—Source book*, American Society for Metals, Metals Park (1984) 102-111.
30. C. T. Sims and W. C. Hagel, *The superalloys*, John Wiley and Sons, New York (1972) 153-154.
31. M. G. Fontana and N. D. Greene, *Corrosion engineering*, McGraw-Hill, New York (1978) 63-73.
32. B. Pickering, *Physical metallurgy and the design of steels*, Applied Science, Essex (1978) 226.
33. C. T. Sims and W. C. Hagel, *The superalloys*, John Wiley and Sons, New York (1972) 145-174.
34. R. W. Hertzberg, *Deformation and fracture mechanics of engineering materials*, John Wiley & Sons, Toronto (1989) 125-128.
35. J. W. Weeton and R. A. Signorelli, Structures, microconstituents and hardness of a wrought cobalt base alloy, *Trans. ASM*, 47 (1955) 815-852.
36. D. I. Bardos and H. A. Luckey, Microstructural analysis of biomaterials, *Microstructure Science*, 3B (1975) 951-970.
37. Centre D'information du Cobalt, *Cobalt Monograph*, Centre D'information du Cobalt, Brussels (1960) 210-218.
38. C. T. Sims and W. C. Hagel, *The superalloys*, John Wiley and Sons, New York (1972) 259-284.

39. R. Silverman, W. Arbiter and F. Hodi, Effect of sigma phase on Co-Cr-Mo base alloy, *Trans. ASM*, 49 (1957) 805-822.
40. C. T. Sims, N. S. Stoloff and W. C. Hagel, *Superalloys II*, John Wiley and Sons, New York (1987) 135-164.
41. R. G. Barrows and J. B. Newkirk, A modified system for predicting σ formation, *Metall. Trans.*, 3 (1972) 2889-2893.
42. J. H. Wernick, Topologically close-packed structures, *Intermetallic Compounds* (1967) 197-216.
43. R. G. Barrows and J. B. Newkirk, Phase equilibria in the Co-Cr-W system with special emphasis on the *R*-phase, *Metallography*, 5 (1972) 515-541.
44. F. P. Bowden and D. Tabor, *Friction—An introduction to tribology*, Anchor Press/Doubleday, Garden City (1973) 23-24.
45. F. P. Bowden and D. Tabor, *Friction—An introduction to tribology*, Anchor Press/Doubleday, Garden City (1973) 65.
46. A. D. Sarkar, *Wear of Metals*, Pergamon Press, Oxford (1976) 24-31.
47. D. F. Moore, *Principle and applications of tribology*, Pergamon Press, Oxford (1975) 43-44.
48. R. Lansdown and A. L. Price, *Materials to resist wear*, Pergamon Press, Oxford (1986) 1.
49. R. Lansdown and A. L. Price, *Materials to resist wear*, Pergamon Press, Oxford (1986) 12-13.
50. D. A. Rigney, The roles of hardness in the sliding behavior of Materials, *Wear*, 175 (1994) 63-69.
51. E. Rabinowicz, *Friction and wear of materials—2nd ed.*, John Wiley and Sons, Toronto (1995) 145.
52. E. Rabinowicz, *Friction and wear of materials—2nd ed.*, John Wiley and Sons, Toronto (1995) 144.
53. K. Hokkirigawa, T. Kato, T. Fukuda and M. Shinooka, Experimental and theoretical analysis of wear mechanism of metals in tilted block on plate type sliding, *Wear*, 214 (1998) 192-201.

54. E. Rabinowicz, *Friction and wear of materials—2nd ed.*, John Wiley and Sons, Toronto (1995) 192.
55. K. Kato, Abrasive wear of metals, *Tribol. Int.*, 30 (1997) 333-338.
56. E. Rabinowicz, *Friction and wear of materials—2nd ed.*, John Wiley and Sons, Toronto (1995) 220.
57. S. K. Biswas and S. V. Kailas, Strain rate response and wear of metals, *Tribol. Int.*, 30 (1997) 369-375.
58. T. F. J. Quinn, *NASA interdisciplinary collaboration in tribology—A review of oxidational wear*, NASA Contractor Report 3686, NASA (1983) 1-91.
59. E. Rabinowicz, *Friction and wear of materials—2nd ed.*, John Wiley and Sons, Toronto (1995) 136-140.
60. J. A. Davidson, G. Schwartz and G. Lynch, Wear, creep, and frictional heating of femoral implant articulating surfaces and the effect on long-term performances—Part II: Friction, heating and torque, *J. Biomed. Mater. Res.*, 22 (1988) 69-91.
61. J. B. Medley, J. J. Krygier, J. D. Bobyn, F. W. Chan, A. Lippincott and M. Tanzer, Kinematics of the MATCO hip simulator and issues related to wear testing of metal-metal implants, *Proc. Instn. Mech. Engrs.*, 211 (1997) 1-11.
62. M. Semlitsch and H. G. Willert, Clinical wear behavior of ultra-high molecular weight polyethylene cups paired with metal and ceramic ball heads in comparison to metal-on-metal pairings of hip joint replacements, *Proc. Instn. Mech. Engrs.*, 211 (1997) 73-88.
63. M. E. Müller, The benefits of metal-on-metal total hip replacements, *Clin. Orthop.*, 311 (1995) 54-59.
64. J. B. Medley, J. D. Bobyn, J. J. Krygier, G. E. Roter, N. Y. Cheng and F. W. Chan, Intermittent motion as a simulator protocol for hip implants made from high elastic modulus materials, Engineers & Surgeons—Joined at the Hip, *Trans. IMechE*, London (2002).
65. P. Paré, J. B. Medley, F. W. Chan, S. Young, J. D. Bobyn and J. J. Krygier, The role of the lambda parameter on the simulator wear of metal-metal hip implants, *Presented at the 29th Leeds-Lyon Symposium on Tribology*, Leeds, September 3-6

(2002). Published in *Tribology* Series 41, Elsevier (2003) 281-290. [Written discussion] 877-878.

66. A. Wang, S. Yue, J. D. Bobyn, F. W. Chan and J. B. Medley, Surface characterization of metal-on-metal hip implants tested in a hip simulator, *Wear*, 225-229 (1999) 708-715.
67. P. J. Firkins, J. L. Tipper, M. R. Saadatzadeh, E. Ingham, M. H. Stone, R. Farrar and J. Fisher, Quantitative analysis of wear and wear debris from metal-on-metal hip prostheses tested in a physiological hip joint simulator, *Bio-Med. Mater. Eng.*, 11 (2001) 143-157.
68. K. K. Wang, A. Wang and L. J. Gustavson, Metal-on-metal wear testing of Co-Cr alloys, *Proc. on Cobalt-Based Alloys for Biomedical Applications,* ASTM, Norfolk (1999) 135-144.
69. J. G. Bowsher, J. Nevelos, J. Pickard and J. C. Shelton, Do heat treatments influence the wear of large diameter metal-on-metal hip joints? An in vitro study under normal and adverse gait conditions. *49th Annual Meeting of the Orthopaedic Research Society*, New Orleans (2003.
70. P. J. Blau, Fifty Years of Research on the Wear of Metals, *Tribol. Int.*, 30 (1997) 321-331.
71. J. Schey, Systems view of optimizing metal on metal bearings, *Clin. Orthop.*, 329S (1996) S115-S127.
72. A. A. Besong, Z. M. Jin and J. Fisher, Importance of pin geometry on pin-on-plate wear testing of hard-on-hard bearing materials for artificial hip joints, *Proc. Instn. Mech. Engrs.*, 215 (2001) 605-610.
73. A. Wang, A. Essner, C. Stark and J. H. Dumbleton, A biaxial line-contact wear machine for the evaluation of implant bearing materials for total knee joint replacement, *Wear*, 225-229 (1999) 701-707.
74. J. L. Tipper, J. Firkins, E. Ingham, J. Fisher, M. H. Stone and R. Farrar, Quantitative analysis of the wear and wear debris from low and high carbon content cobalt chrome alloys used in metal on metal total hip replacements, *J. Mater. Sci.-Mater. Med.*, 10 (1999) 353-362.

75. S. C. Scholes and A. Unsworth, Pin-on-plate studies on the effect of rotation on the wear of metal-on-metal samples, *J. Mater. Sci.-Mater. Med.*, 12 (2001) 299-303.
76. D. A. Rigney, Comments on the sliding wear of metals, *Tribol. Int.*, 30 (1997) 361-367.
77. S. Atamert and J. Stekly, Microstructure, wear resistance and stability of cobalt based and alternative iron based hardfacing alloys, *Surf. Eng.*, 9 (1993) 231-240.
78. P. Huang and H. F. López, Athermal ε-martensite in a Co-Cr-Mo alloy—Grain size effects, *Mater. Lett.*, 39 (1999) 249-253.
79. P. Huang and H. F. López, Strain induced ε-martensite in a Co-Cr-Mo alloy—Grain size effects, *Mater. Lett.*, 39 (1999) 244-248.
80. R. Varano, S. Yue, J. D. Bobyn and J. B. Medley, Co-Cr-Mo alloys used in metal-metal bearing surfaces, *Proc. on Alternative Bearing Surfaces in Total Joint Replacement,* ASTM, San Diego (1998) 92-110.
81. A. Roebuck, E. A. Almond and A. M. Cottenden, The influence of composition, phase transformation and varying the relative FCC and HCP phase contents on the properties of dilute Co-W-C alloys, *Mater. Sci. Eng.*, 66 (1984) 179-194.
82. P. Crook and A. V. Levy, *ASM handbook 18*, ASM International, Materials Park (1992) 766-771.
83. H. R. Shetty, T. H. Kosel and N. F. Fiore, A study of abrasive wear mechanisms using diamond and alumina scratch tests, *Wear*, 80 (1982) 347-376.
84. J. D. B. De Mello, M. Durand-Charre and T. Mathia, A sclerometric study of unidirectionally solidified Cr-Mo white cast irons, *Wear*, 111 (1986) 203-215.
85. J. Roylance and S. Raadnui, The morphological attributes of wear particles—Their role in identifying wear mechanisms, *Wear*, 175 (1994) 115-121.
86. A. Frenk and W. Kurz, Microstructural effects on the sliding wear resistance of a cobalt-based alloy, *Wear*, 174 (1994) 81-91.
87. K. L. Johnson, Contact mechanics and the wear of metals, *Wear*, 190 (1995) 162-170.
88. M. Terheci, Wear by surface fatigue on a new foundation—Part II: Particle detachment mechanisms and quantitative aspects, *Wear*, 218 (1998) 191-202.

89. R. W. Hertzberg, *Deformation and fracture mechanics of engineering materials*, John Wiley & Sons, Toronto (1989) 356-357.
90. F. P. Bowden and D. Tabor, *Friction—An introduction to tribology*, Anchor Press/Doubleday, Garden City (1973) 64-66.
91. N. B. Konyer and J. H. Root, *Dualspec powder diffractometer user's guide*, Atomic Energy of Canada Ltd, Chalk River (1992).
92. M. J. Neale, *The tribology handbook—2nd ed.*, Butterworth-Heinemann, Oxford (1995) E24.
93. J. B. Medley, *Tribology course notes—Part 2*, Department of Mechanical Engineering, University of Waterloo, Waterloo (1998) 101.
94. L. Z. Zhuang and E. W. Langer, Effects of alloy additions on the fatigue properties of cast Co-Cr-Mo alloy used for surgical implants, *J. Mater. Sci.*, 25 (1990) 683-689.
95. P. Wanjara, R. A. L. Drew and S. Yue, Shear punch test for strength and ductility measurements of Ti-6Al-4V/TiC particulate reinforced MMC's, *Titanium '96*, 3 (1996) 2851-2858.
96. H. McKellop, B. Lu and P. Benya, Friction, lubrication and wear of cobalt-chromuim, alumina and zirconia hip prostheses compared on a joint simulator, *Trans. Ortho. Res. Soc.* (1992) 402.
97. A. J. Hamrock, *Fundamentals of fluid film lubrication*, McGraw-Hill, New York (1994).
98. M. A. Wimmer, J. Loos, R. Nassutt, M. Heitkemper and A. Fischer, The acting wear mechanisms on metal-on-metal hip joint bearings: In-vitro results, *Wear*, 250 (2001) 129-139.
99. L. Z. Zhuang and E. W. Langer, Carbide precipitation in cast Co-Cr-Mo alloys used for surgical implants, *Z. Metallk.*, 80 (1989) 251-257.
100. F. W. Chan, J. D. Bobyn, J. B. Medley, J. J. Krygier and M. Tanzer, Wear and lubrication of metal-on-metal hip implants, *Clin. Orthop.*, 369 (1999) 10-24.
101. H. L. Anissian, A. Stark, V. Good, H. Dahlstrand and I. C. Clarke, The wear pattern in metal-on-metal hip prostheses, *J. Biomed. Mater. Res.*, 58B (2001) 673-678.

102. F. W. Chan, J. D. Bobyn, J. B. Medley, J. J. Krygier, S. Yue and M. Tanzer, Engineering issues and wear performance of metal on metal hip implants, *Clin. Orthop.*, 333 (1996) 96-107.

103. A. Wang, J. D. Bobyn, S. Yue, J. B. Medley and F. W. Chan, Residual abrasive material from surface grinding of metal-metal hip implants: A source of third-body wear?, *Proc. on Cobalt-Based Alloys for Biomedical Applications*, ASTM, Norfolk (1999) 125-134.

104. A. Wang, Surface characterization of metal-metal hip implants tested in a hip simulator, *Masters of Engineering Thesis*, McGill University (2000) 1-127.

105. R. W. Hertzberg, *Deformation and fracture mechanics of engineering materials*, John Wiley & Sons, Toronto (1989) 94-105.

106. L. Zhuang and E. W. Langer, Carbide precipitation in cast Co-Cr-Mo alloys used for surgical implants, *Z. Metallk.*, 80 (1989) 251-257.

107. A. Salinas-Rodriguez and J. L. Rodriguez-Galicia, Deformation behavior of low-carbon Co-Cr-Mo alloys for low-friction implant applications, *J. Biomed. Mater. Res.*, 31 (1996) 409-419.

108. S. Yue, A. Di Chiro and A. Z. Hanzaki, Thermomechanical processing effects on C-Mn-Si TRIP Steels, *J. Metals*, 49 (1997) 59-61.

109. D. McMinn and T. Band, Hip resurfacing: How metal on metal articulations have come full circle, Engineers and Surgeons—Joined at the Hip, *Trans. IMechE*, London (2002) 1-7.

110. A. J. T. Clemow and B. L. Daniell, Solution treatment behavior of Co-Cr-Mo Alloy, *J. Biomed. Mater. Res.*, 13 (1979) 265-279.

111. A. Sasmal, Mechanism of the formation of lamellar $M_{23}C_6$ at and near twin boundaries in austenitic stainless steels, *Metall. Mater. Trans.*, 30A (1999) 2791-2801.

112. G. B. Olson and M. Cohen, A general mechanism of martensitic nucleation: Part I General concepts and the FCC→HCP transformation, *Metall. Trans.*, 7A (1976) 1897-1904.

113. R. Varano, J. D. Bobyn and S. Yue, Characterization of Co-Cr-Mo alloys used in hip implant articulating surfaces, *Mater. Res. Soc.*, 441 (1996) 481-486.

114. T. Waitz and H. P. Karnthaler, The f.c.c. to h.c.p. martensitic phase transformation in CoNi studied by TEM and AFM methods, *Acta Mater.*, 45 (1997) 837-847.

115. K. Rajan and J. B. Vander Sande, Room temperature strengthening mechanisms in a Co-Cr-Mo alloy, *J. Mater. Sci.*, 17 (1982) 769-778.

116. R. W. Hertzberg, *Deformation and fracture mechanics of engineering materials*, John Wiley & Sons, Toronto (1989) 95.

117. A. V. Shtansky, K. Nakai and Y. Ohmori, Crystallography and interface boundary structure of pearlite with M_7C_3 carbide lamellae, *Acta Mater.*, 47 (1999) 1105-1115.

118. D. A. Rigney, Large strains associated with sliding contact of metals, *Mater. Res. Innov.*, 1 (1998) 231-234.

119. D. A. Rigney, Transfer, mixing and associated chemical and mechanical processes during the sliding of ductile materials, *Wear*, 245 (2000) 1-9.

120. L. Q. Shi, D. O. Northwood and Z. W. Cao, The properties of a wrought biomedical cobalt-chromium alloy, *J. Mater. Sci.*, 29 (1994) 1233-1238.

121. J. L. Gilbert, C. A. Buckley and J. J. Jacobs, In-vivo corrosion of modular hip-prosthesis components in mixed and similar metal combinations—the effect of crevice, stress, motion, and alloy coupling, *J. Biomed. Mater. Res.*, 27 (1993) 1533-1544.

122. N. Latona, P. Fetherston, A. Chen, K. Sridharan and R. A. Dodd, Wear-corrosion comparisons of passivating vs nonpassivating alloys in aerated 3.5% aqueous solutions of sodium chloride, *Corrosion*, 57 (2001) 884-888.

123. Z. Stradomski and S. Stachura, The role of non-metallic inclusions in the pitting corrosion of chromium- and chromium-nickel steels, *Prakt. Metallogr.*, 34 (1997) 300-311.

124. A. Essner, A. Wang, C. Stark and J. H. Dumbleton, A simulator for the evaluation of total knee replacement wear, *Trans. of the Fifth World Biomaterials Congress*, 1 (1996) 580.

125. R. M. Streicher, R. Schoen and M. F. Semlitsch, Investigation of the tribological behaviour of metal-metal combinations for artificial hip joints, *Biomed. Tech.*, 35 (1990) 107-111.

126. P. S. Walker and M. J. Erkman, Metal-on-metal lubrication in artificial human joints, *Wear*, 21 (1972) 377-392.

127. M. A. Wimmer, C. Sprecher, R. Hauert, G. Täger and A. Fischer, Tribochemical reaction on metal-on-metal hip joint bearings: A comparison between in-vitro and in-vivo results, *Wear*, 255 (2003) 1007-1014.

128. L. Fu, L. Y. Duan and S. G. Du, Numerical Simulation of Inertia Friction Welding Process by Finite Element Method, *Welding Journal*, 82 (2003) 65S-70S.

129. I. Catelas, J. D. Bobyn, J. B. Medley, J. J. Krygier, D. J. Zukor and O. L. Huk, Size, shape, and composition of wear particles from metal-metal hip simulator testing: Effects of alloy and number of loading cycles, *J. Biomed. Mater. Res.*, 67A (2003) 312-327.

130. R. M. Streicher, M. Semlitsch, R. Schön, H. Weber and C. Rieker, Metal-on-metal articulation for artificial hip joints: Laboratory study and clinical results, *Proc. Instn. Mech. Engrs.-J. Eng. Med.*, 210 (1996) 223-232.

131. L. Savarino, D. Granchi, G. Ciapetti, E. Cenni, A. Nardi Pantoli, R. Rotini, C. A. Veronesi, N. Baldini and A. Giunti, Ion release in patients with metal-on-metal hip bearings in total joint replacement: A comparison with metal-on-polyethylene, *J. Biomed. Mater. Res.*, 63B (2002) 467-474.

132. R. Büscher, M. A. Wimmer, G. Täger, C. Sprecher, W. Dudzinski and A. Fischer, The origin of nanometer sized debris in metal-on-metal hip joints, *50th Annual Meeting of the Orthopaedic Research Society*, San Francisco (2004).